Boron unlocks silicone recycling pp. 361 & 392

Partisan patterns in how policy draws on science p. 362

Spread of avian influenza in cattle p. 380

Science

$15
25 APRIL 2025
science.org

AAAS

THE LEGACY OF AGENT ORANGE

Fifty years later, is the herbicide still a threat to Vietnam's children? p. 350

Recent PhD?

Science & SciLifeLab PRIZE
For Young Scientists

How about $30,000 US, having your essay published in *Science*, and being celebrated with a week of festivities in Stockholm, Sweden?

Apply now to the *Science* & SciLifeLab Prize for Young Scientists!

A global award aimed at young researchers

Every year, four early-career scientists from across the globe are awarded the *Science* & SciLifeLab Prize for Young Scientists for outstanding research they have conducted as part of their PhD.

The selected winners receive up to $30, 000 US in prize money for their accomplishments. In addition, all four winners are published in *Science* and invited by SciLifeLab to Sweden in December to participate in a unique week filled with events in honor of science. Here, they will be given the opportunity to meet with leading scientists in their field of research and create life-long connections to support their career.

Categories

The award is available in four categories:

- Cell and Molecular Biology
- Genomics, Proteomics and Systems Biology Approaches
- Ecology and Environment
- Molecular Medicine

More information

More information: scienceprize.scilifelab.se
Questions: scilifelabprize@aaas.org
Application deadline: July 15, 2025
Eligibility: applicants must have received their PhD between January 1, 2023 and December 31, 2024.

Enabled by the generous support of the Knut and Alice Wallenberg Foundation.

Knut and Alice Wallenberg Foundation

Science AAAS

SciLifeLab

CONTENTS

25 APRIL 2025 • VOLUME 388 • ISSUE 6745

354
The Vietnam War marked many who survived it, and perhaps later generations.

PHOTO: MANAN VATSYAYANA/AFP VIA GETTY IMAGES

NEWS

IN BRIEF

IN DEPTH

FEATURES

INSIGHTS

PERSPECTIVES

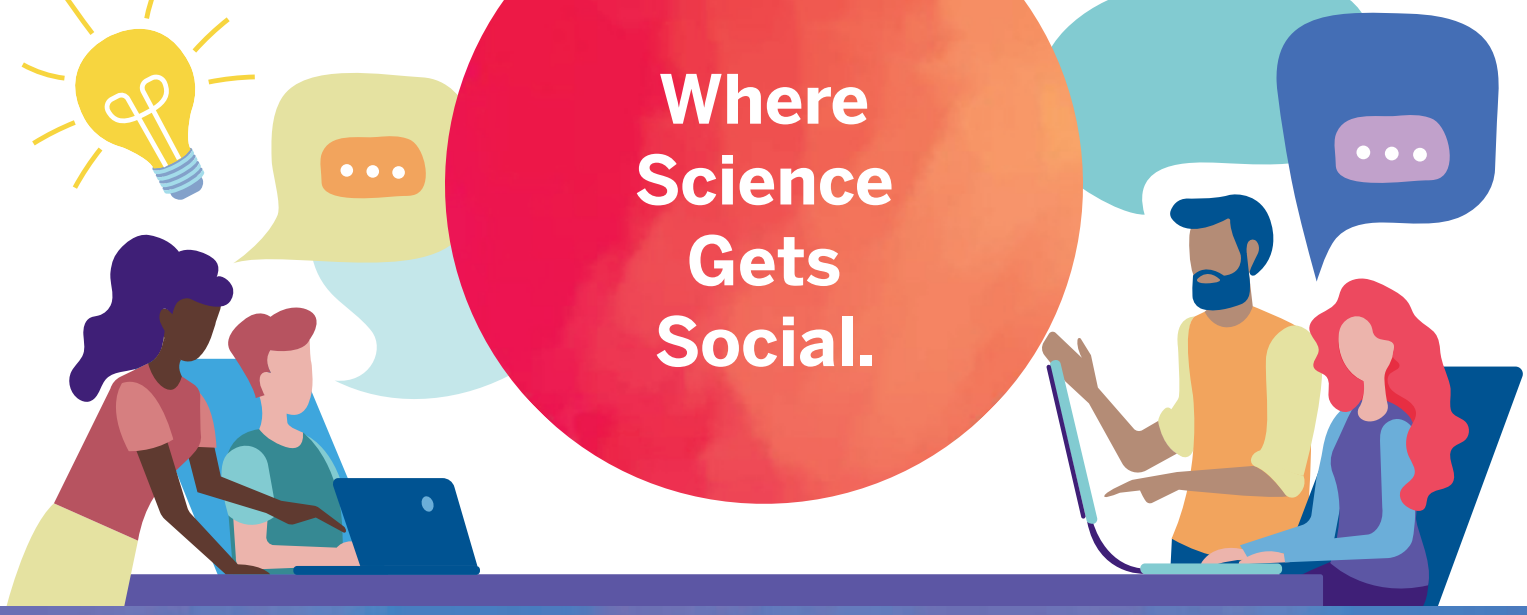

AAAS.ORG/COMMUNITY

AAAS' Member Community is a one-stop destination for scientists and STEM enthusiasts alike. It's "Where Science Gets Social": a community where facts matter, ideas are big and there's always a reason to come hang out, share, discuss and explore.

Member COMMUNITY
AAAS

AMERICAN ASSOCIATION FOR THE ADVANCEMENT OF SCIENCE

ON THE COVER

US aircraft sprayed herbicides over South Vietnam during the Vietnam War. The herbicides contained dioxin, a long-lived toxic chemical that contaminated soils and aquatic sediments and found its way into the food chain. Now, more than 50 years after the spraying ended, researchers are still trying to understand how dioxin exposure has affected human health. See page 350. *Credit: US Air Force*

PHOTO: RON G.M. DE GOEDE

SCIENCE (ISSN 0036-8075) is published weekly on Friday, except last week in December, by the American Association for the Advancement of Science, 1200 New York Avenue, NW, Washington, DC 20005. Periodicals mail postage (publication No. 484460) paid at Washington, DC, and additional mailing offices. The title SCIENCE is a registered trademark of the AAAS. Domestic individual membership, including subscription (12 months): $165 ($74 allocated to subscription). Domestic institutional subscription (51 issues): $2865; Foreign postage extra: Air assist delivery: $135. First class, airmail, student, and emeritus rates on request. Canadian rates with GST available upon request, GST #125488122. Publications Mail Agreement Number 1069624. **Printed in the U.S.A.**
Change of address: Allow 4 weeks, giving old and new addresses and 8-digit account number. **Postmaster:** Send change of address to AAAS, P.O. Box 96178, Washington, DC 20090–6178. **Single-copy sales:** $15 each plus shipping and handling available from backissues.science.org; bulk rate on request. *Science* is indexed in the *Reader's Guide to Periodical Literature* and in several specialized indexes.

Science AAAS

Editor-in-Chief Holden Thorp, hthorp@aaas.org

Executive Editor Valda Vinson

Editor, Research Jake S. Yeston **Editor, Insights** Lisa D. Chong **Deputy Executive Editor** Lauren Kmec

DEPUTY EDITORS Stella M. Hurtley (UK), Phillip D. Szuromi, Sacha Vignieri **SR. EDITORS** Caroline Ash (UK), Michael A. Funk, Angela Hessler, Di Jiang, Priscilla N. Kelly, Marc S. Lavine (Canada), Sarah Lempriere (UK), Mattia Maroso, Yevgeniya Nusinovich, Ian S. Osborne (UK), L. Bryan Ray, H. Jesse Smith, Keith T. Smith (UK), Jelena Stajic, Peter Stern (UK), Yury V. Suleymanov, Valerie B. Thompson, Brad Wible **ASSOCIATE EDITORS** Jack Huang, Sumin Jin, Bianca Lopez, Sarah Ross (UK), Madeleine Seale (UK), Corinne Simonti, Ekeoma Uzogara **SENIOR LETTERS EDITOR** Jennifer Sills **NEWSLETTER EDITOR** Christie Wilcox **RESEARCH & DATA ANALYST** Jessica L. Slater **LEAD CONTENT PRODUCTION EDITORS** Chris Filiatreau, Harry Jach **SR. CONTENT PRODUCTION EDITOR** Amelia Beyna **CONTENT PRODUCTION EDITORS** Anne Abraham, Robert French, Julia Haber-Katris, Nida Masiulis, Abigail Shashikanth, Suzanne M. White **SR. EDITORIAL MANAGER** Beverly Shields **SR. PROGRAM ASSOCIATE** Maryrose Madrid **EDITORIAL ASSOCIATES** Aneera Dobbins, Joi S. Granger, Lisa Johnson, Jerry Richardson, Anita Wynn **SR. EDITORIAL COORDINATORS** Alexander Kief, Ronmel Navas, Isabel Schnaidt, Alice Whaley (UK), Brian White **EDITORIAL COORDINATORS** Clair Goodhead (UK), Kat Kirkman, Samantha Price **ADMINISTRATIVE COORDINATOR** Karalee P. Rogers **ASI DIRECTOR, OPERATIONS** Janet Clements (UK) **ASI OFFICE MANAGER** Victoria Smith **ASI SR. OFFICE ADMINISTRATORS** Dawn Titheridge (UK), Jessica Waldock (UK) **COMMUNICATIONS DIRECTOR** Meagan Phelan **DEPUTY DIRECTOR** Matthew Wright **SENIOR WRITERS** Walter Beckwith, Joseph Cariz, Abigail Eisenstadt **WRITERS** Mahathi Ramaswamy **SENIOR COMMUNICATIONS ASSOCIATES** Zachary Graber, Sarah Woods **COMMUNICATIONS ASSOCIATES** Kiara Brooks, Haley Riley, Mackenzie Williams

News Editor Tim Appenzeller

NEWS MANAGING EDITOR John Travis **INTERNATIONAL EDITOR** David Malakoff **DEPUTY NEWS EDITORS** Rachel Bernstein, Shraddha Chakradhar, Martin Enserink, David Grimm, Eric Hand, Michael Price Kelly Servick, Matt Warren (Europe) **SR. CORRESPONDENTS** Daniel Clery (UK), Jon Cohen, Jeffrey Mervis **ASSOCIATE EDITORS** Jeffrey Brainard, Michael Greshko, Katie Langin **NEWS REPORTERS** Adrian Cho, Jennifer Couzin-Frankel, Phie Jacobs, Jocelyn Kaiser, Rodrigo Pérez Ortega (Mexico City), Robert F. Service, Erik Stokstad, Paul Voosen, Meredith Wadman **CONSULTING EDITOR** Elizabeth Culotta **CONTRIBUTING CORRESPONDENTS** Vaishnavi Chandrashekhar, Dan Charles, Warren Cornwall, Andrew Curry (Berlin), Ann Gibbons, Sam Kean, Kai Kupferschmidt (Berlin), Andrew Lawler, Mitch Leslie, Virginia Morell, Dennis Normile (Tokyo), Cathleen O'Grady, Elisabeth Pain (Careers), Charles Piller, Sara Reardon, Richard Stone (Senior Asia Correspondent), Gretchen Vogel (Berlin), Lizzie Wade (Mexico City) **INTERNS** Alexa Robles-Gil **COPY EDITORS** Julia Cole (Senior Copy Editor), Hannah Knighton, Cyra Master (Copy Chief) **ADMINISTRATIVE SUPPORT** Meagan Weiland

Creative Director Beth Rakouskas

DESIGN MANAGING EDITOR Chrystal Smith **GRAPHICS MANAGING EDITOR** Chris Bickel **PHOTOGRAPHY MANAGING EDITOR** Emily Petersen **MULTIMEDIA MANAGING PRODUCER** Kevin McLean **DIGITAL DIRECTOR** Kara Estelle-Powers **DESIGN EDITOR** Marcy Atarod **DESIGNER** Noelle Jessup **SENIOR SCIENTIFIC ILLUSTRATOR** Noelle Burgess **SCIENTIFIC ILLUSTRATORS** Austin Fisher, Kellie Holoski, Ashley Mastin **SENIOR GRAPHICS EDITOR** Monica Hersher **GRAPHICS EDITOR** Veronica Penney **SENIOR PHOTO EDITOR** Charles Borst **PHOTO EDITOR** Elizabeth Billman **SENIOR PODCAST PRODUCER** Sarah Crespi **SENIOR VIDEO PRODUCER** Meagan Cantwell **SOCIAL MEDIA STRATEGIST** Jessica Hubbard **SOCIAL MEDIA PRODUCER** Sabrina Jenkins **WEB DESIGNER** Jennie Pajerowski

Chief Executive Officer and Executive Publisher Sudip Parikh

Publisher, Science Family of Journals Bill Moran

DIRECTOR, BUSINESS SYSTEMS AND FINANCIAL ANALYSIS Randy Yi **DIRECTOR, BUSINESS OPERATIONS & ANALYSIS** Eric Knott **MANAGER, BUSINESS OPERATIONS** Jessica Tierney **MANAGER, BUSINESS ANALYSIS** Cory Lipman **BUSINESS ANALYSTS** Kurt Ennis, Maggie Clark, Isacco Fusi **BUSINESS OPERATIONS ADMINISTRATOR** Taylor Fisher **DIGITAL SPECIALIST** Marissa Zuckerman **SENIOR PRODUCTION MANAGER** Jason Hillman **SENIOR MANAGER, PUBLISHING AND CONTENT SYSTEMS** Marcus Spiegler **CONTENT OPERATIONS MANAGER** Rebecca Doshi **PUBLISHING PLATFORM MANAGER** Jessica Loayza **PUBLISHING SYSTEMS SPECIALIST, PROJECT COORDINATOR** Jacob Hedrick **SENIOR PRODUCTION SPECIALIST** Kristin Wowk **PRODUCTION SPECIALISTS** Kelsey Cartelli, Audrey Diggs **SPECIAL PROJECTS ASSOCIATE** Shantel Agnew

MARKETING DIRECTOR Sharice Collins **ASSOCIATE DIRECTOR, MARKETING** Justin Sawyers **GLOBAL MARKETING MANAGER** Allison Pritchard **ASSOCIATE DIRECTOR, MARKETING SYSTEMS & STRATEGY** Aimee Aponte **SENIOR MARKETING MANAGER** Shawana Arnold **MARKETING MANAGER** Ashley Evans **MARKETING ASSOCIATES** Hugues Beaulieu, Ashley Hylton, Lorena Chirinos Rodriguez, Jenna Voris **MARKETING ASSISTANT** Courtney Ford **SENIOR DESIGNER** Kim Huynh

DIRECTOR AND SENIOR EDITOR, CUSTOM PUBLISHING Erika Gebel Berg **ADVERTISING PRODUCTION OPERATIONS MANAGER** Deborah Tompkins **DESIGNER, CUSTOM PUBLISHING** Jeremy Huntsinger **SR. TRAFFIC ASSOCIATE** Christine Hall

DIRECTOR, PRODUCT MANAGEMENT Kris Bishop **PRODUCT DEVELOPMENT MANAGER** Scott Chernoff **ASSOCIATE DIRECTOR, PUBLISHING INTELLIGENCE** Rasmus Andersen **SR. PRODUCT ASSOCIATE** Robert Koepke **PRODUCT ASSOCIATES** Caroline Breul, Anne Mason

ASSOCIATE DIRECTOR, INSTITUTIONAL LICENSING MARKETING Kess Knight **ASSOCIATE DIRECTOR, INSTITUTIONAL LICENSING SALES** Ryan Rexroth **INSTITUTIONAL LICENSING MANAGER** Nazim Mohammedi, Claudia Paulsen-Young **SENIOR MANAGER, INSTITUTIONAL LICENSING OPERATIONS** Judy Lillibridge **MANAGER, RENEWAL & RETENTION** Lana Guz **SYSTEMS & OPERATIONS ANALYST** Ben Teincuff **FULFILLMENT ANALYST** Aminta Reyes

ASSOCIATE DIRECTOR, INTERNATIONAL Roger Goncalves **ASSOCIATE DIRECTOR, US ADVERTISING** Stephanie O'Connor **US MID WEST, MID ATLANTIC AND SOUTH EAST SALES MANAGER** Chris Hoag **DIRECTOR, OUTREACH AND STRATEGIC PARTNERSHIPS, ASIA** Shoupeng Liu **SALES REP, ROW** Sarah Lelarge **SALES ADMIN ASSISTANT, ROW** Victoria Glasbey **DIRECTOR OF GLOBAL COLLABORATION AND ACADEMIC PUBLISHING RELATIONS, ASIA** Xiaoying Chu **ASSOCIATE DIRECTOR, INTERNATIONAL COLLABORATION** Grace Yao **SALES MANAGER** Danny Zhao **MARKETING MANAGER** Kilo Lan **ASCA CORPORATION, JAPAN** Rie Rambelli (Tokyo), Miyuki Tani (Osaka)

DIRECTOR, COPYRIGHT, LICENSING AND SPECIAL PROJECTS Emilie David **RIGHTS AND PERMISSIONS ASSOCIATE** Elizabeth Sandler **LICENSING ASSOCIATE** Virginia Warren **RIGHTS AND LICENSING COORDINATOR** Dana James **CONTRACT SUPPORT SPECIALIST** Michael Wheeler

EDITORIAL
science_editors@aaas.org

NEWS
science_news@aaas.org

INFORMATION FOR AUTHORS
science.org/authors/science-information-authors

REPRINTS AND PERMISSIONS
science.org/help/reprints-and-permissions

MULTIMEDIA CONTACTS
SciencePodcast@aaas.org
ScienceVideo@aaas.org

MEDIA CONTACTS
scipak@aaas.org

PRODUCT ADVERTISING & CUSTOM PUBLISHING
advertising.science.org
science_advertising@aaas.org

CLASSIFIED ADVERTISING
advertising.science.org/science-careers
advertise@sciencecareers.org

JOB POSTING CUSTOMER SERVICE
employers.sciencecareers.org
support@sciencecareers.org

MEMBERSHIP AND INDIVIDUAL SUBSCRIPTIONS
science.org/subscriptions

MEMBER BENEFITS
aaas.org/membership/benefits

INSTITUTIONAL SALES AND SITE LICENSES
science.org/librarian

AAAS BOARD OF DIRECTORS
CHAIR Gilda A. Barabino
PRESIDENT Keith R. Yamamoto
PRESIDENT-ELECT Willie E. May
TREASURER Carolyn N. Ainslie
CHIEF EXECUTIVE OFFICER Sudip Parikh
BOARD Cynthia M. Beall, Janine Austin Clayton, Kaye Husbands Fealing, Kathleen Hall Jamieson, Jane Maienschein, Robert B. Millard, Babak Parviz, William D. Provine, Juan S. Ramírez Lugo, Susan M. Rosenberg, Vassiliki Betty Smocovitis

Science serves as a forum for discussion of important issues related to the advancement of science by publishing material on which a consensus has been reached as well as including the presentation of minority or conflicting points of view. Accordingly, all articles published in *Science*—including editorials, news and comment, and book reviews—are signed and reflect the individual views of the authors and not official points of view adopted by AAAS or the institutions with which the authors are affiliated.

EDITORIAL

Convergence and consensus

H. Holden Thorp
Editor-in-Chief,
Science journals.
hthorp@aaas.org

In these days of political instability, geopolitical tensions, and social discontent around the world, there are continued threats to the principles, conduct, and findings of science. This assault on science has been fueled by flooding the public with confusing information from both traditional and digital media. One concept that creates misunderstanding is "scientific consensus." It's time to stop using this shorthand and make clear what it really means.

Scientists take it for granted that the consensus they refer to is not the result of opinion polls of their colleagues or a negotiated agreement reached at a research conclave. Rather, it is a phrase that describes a process in which evidence from independent lines of inquiry leads collectively toward the same conclusion. This process transcends the individual scientists who carry out the research.

"...consensus...is not the result of opinion polls...or a negotiated agreement..."

To make that clear to politicians and to the public, communication scholar Kathleen Hall Jamieson believes that scientists need to talk instead about "convergent evidence." "Unlike declarations that a consensus exists," she told me, "a claim that convergent evidence exists honors science's norms of critique and correction by inviting discussion of the extent of existing knowledge and the multiple ways in which it was developed rather than on what a lay audience is likely to hear as a 'case closed' appeal to authority." When a scientific consensus is overturned, it requires not only introducing new evidence that counters the accepted understanding but also explaining why all the evidence, new and old, is now pointing in a different direction. "To discredit a statement that a consensus exists, one simply cites other respected scientists who disagree," says Jamieson. However, rebutting a claim that convergent evidence exists requires an extra step. Jamieson pointed out that the counterevidence must be assimilated into the evidence that has already been accumulated so that all of it can be interpreted together.

The question of whether vaccines cause autism is a perfect example of this notion. There is a massive amount of convergent evidence that refutes the idea that the measles, mumps, and rubella (MMR) vaccine causes autism. This has been discredited in one study after another. Nevertheless, US Secretary of Health and Human Services (HHS) Robert F. Kennedy Jr. announced that the Centers for Disease Control and Prevention (CDC) will carry out yet another study on this claim, and that "exposures" that cause autism would be known by September, despite the discouragement of many scientists and physicians, including Senator Bill Cassidy who chairs the Senate committee that oversees HHS. Even a report released by the CDC last week describes multiple ways in which better identification has led to higher rates of autism diagnoses. With any subject, one can always do another study but at the cost of diminishing returns. It is certainly the position of many scientists that this issue is settled, including Jay Bhattacharya, director of the US National Institutes of Health, not because of an opinion poll of scientists, but because of evidence converging from numerous directions that has debunked the idea. If another study seems to suggest some kind of correlation between vaccines and autism, it would not suddenly erase all of the solid research that came before it. The outlier would need to be considered along with the overall picture, which would likely still converge on the lack of a meaningful connection unless the large number of previous studies were somehow shown to be flawed.

The yearly poll by the Pew Research Center on trust in science in the United States has consistently showed that although the majority of Democrats agree that scientists should be included in policy decisions that involve science, the majority of Republicans feel that scientists should "focus on establishing sound scientific facts and stay out of public policy debates." Although this view was exacerbated by the passion that many scientists exhibited during the pandemic, the result of the 2024 presidential election in the United States shows that the latter sentiment is prevalent at the moment. A key to reversing this view is to take ever more care in clearly delineating scientific results from scientists' opinions. Taking the further step of correctly portraying scientific consensus as convergent evidence rather than scientists' opinions will further the goal of showing why vetted and validated science is a crucial ingredient of policy decisions around the world.

–H. Holden Thorp

PHOTO: CAMERON DAVIDSON

10.1126/science.ady3211

NEWS

> “Let us put an end to the irresponsible derision that would present this issue as something purely ecological, ‘green,’ romantic.”
>
> **Pope Francis** on climate change, in 2023. Francis died this week.

IN BRIEF

Edited by
Kelly Servick

ASTRONOMY

Life on an exoplanet? Not so fast

Astronomers last week reported hints that the atmosphere of a distant planet contains gases linked to life. They used NASA’s JWST observatory to detect the fingerprints of dimethyl sulfide and dimethyl disulfide in starlight that had passed through the atmosphere of K2-18b, a massive planet 120 light-years away that may have a deep global ocean. Because those gases are produced by marine phytoplankton on Earth, the team heralded this as the strongest evidence yet of life on far-flung worlds.

The atmosphere of an exoplanet (artist’s concept) contains gases linked to marine algal life on Earth, researchers say.

Their report, published in *The Astrophysical Journal Letters*, prompted worldwide headlines. But detecting gases in alien atmospheres is pushing telescope technology to its limit, and this detection is not yet conclusive. Exoplanets and their atmospheres are complex systems so researchers will likely need more than a couple of atmospheric gases to assert the presence of life. “We don’t know what other geological activity could be happening on this planet that might produce the molecules,” Catherine Heymans of the University of Edinburgh told BBC.

Carbon removal projects rewarded

CLIMATE CHANGE | Farming-related strategies were the big winners in a $100 million contest for the most promising technologies to remove climate-warming carbon dioxide (CO_2) from the atmosphere. The $50 million top award from XPRIZE Carbon Removal, announced on 23 April, went to Houston-based Mati Carbon, which has enlisted small-scale farmers in India, Zambia, and Tanzania to spread dust from crushed basalt rock on their fields. The rock speeds up a natural process in which minerals react with CO_2 to create bicarbonate, which remains inert for thousands of years. A similar approach using silicate rocks earned U.K.-based UNDO Carbon the $5 million prize for fourth place. Second place went to the French firm NetZero, which converts agricultural waste into a charcoal-like substance farmers can use as a soil amendment. Vaulted Deep, also based in Houston, earned the $8 million third place prize; it takes slurries of biomass such as livestock manure and injects them deep underground.

Blood pressure and dementia

BIOMEDICINE | A trial of nearly 34,000 people in rural China offers some of the best evidence yet that reducing high blood pressure, alongside lifestyle changes, can lower risk of cognitive impairment and dementia. The study, described this week in *Nature Medicine*, involved 326 Chinese villages; in half, participants ages 40 and older with uncontrolled high blood pressure received antihypertensive medication, home blood pressure monitoring, and healthy lifestyle

ILLUSTRATION: AMANDA SMITH/N. MADHUSUDHAN/UNIVERSITY OF CAMBRIDGE

coaching from community health workers. After 4 years, these participants were 15% less likely to have developed dementia and 16% less likely to have cognitive impairment without dementia, compared with people in the control villages, where health workers didn't provide medication or coaching. In 2019 a U.S. trial in about 9000 people showed blood pressure treatment reduced mild cognitive impairment, but did not show a statistically significant reduction in dementia.

Giant croc family tree revised

EVOLUTION | *Deinosuchus*—a predatory reptile that may have reached 12 meters in length and roamed North American wetlands more than 75 million years ago—was long considered closely related to modern alligators. But a newly revised family tree for *Deinosuchus* and other crocodilians instead places the predator in a separate family from both alligators and crocodiles. The findings, published in *Communications Biology*, may help explain why *Deinosuchus* lived on both sides of an ancient seaway stretching through North America: Alligators and kin don't handle saltwater well, but if *Deinosuchus* was unrelated, it likely retained an ancestral crocodilian tolerance for saltwater and could swim across the sea. The findings also show that, far from being aberrations, giant crocodilians have abounded over the past 130 million years, evolving whenever there was a marine or wetland habitat big enough to sustain their appetites.

Ultracool microscopes advance

MICROSCOPY | Using electron microscopes cooled to near absolute zero, a team of scientists has produced remarkably high-resolution views of the molecular structure of proteins. Researchers have long hoped extremely cold conditions would help sharpen cryogenic electron microscopy, which bombards frozen samples with a powerful beam of electrons to reveal molecular structure. Cooling samples with liquid helium rather than the standard liquid nitrogen reduces radiation damage produced by the microscopes' electron beams, but has until now produced fuzzier images. By redesigning the microscope's thin plate that holds proteins in place, researchers constrained unwanted movements and improved resolution about 1.5-fold, they report this week in the *Proceedings of the National Academy of Sciences*. The result may open new vistas on a variety of proteins, including key cell surface proteins targeted by drug developers.

TRUMP TRACKER

HIV NETWORKS IN SOUTH AFRICA The U.S. National Institutes of Health (NIH) last week restricted South Africa from participating in the four international clinical trial networks it funds to study new medicines to prevent and treat HIV. The U.S. institutions that run the networks were told they may not use funds to start new clinical trials in South Africa or to enroll new patients from the country in studies that are underway. No reason was given for the move, which compounds damage to the country's HIV efforts from earlier cuts in foreign research funding by President Donald Trump's administration and its dismantling of the U.S. Agency for International Development.

JOURNALS TARGETED The Trump-appointed interim U.S. attorney for the District of Columbia has sent letters to the editors of multiple scientific journals asserting their publications are "partisans in various scientific debates" and asking for responses to questions such as "Do you accept articles or essays from competing viewpoints?" The journal *CHEST* confirmed it had received one such letter, and *Science* has learned that another journal has received a nearly identical one. The Trump administration also plans to cut funding for two open-access, peer-reviewed journals published by the Centers for Disease Control and Prevention (CDC)—*Emerging Infectious Diseases* and *Preventing Chronic Disease*—according to a leaked draft of an internal 2026 budget proposal for the Department of Health and Human Services. A spokesperson for CDC says the proposal "is a draft, predecisional document, and CDC won't speculate on the future of publishing" the journals.

NSF SQUEEZE The National Science Foundation (NSF) is likely to lose $234 million this year in funding it planned to use on building and upgrading major research facilities. That's bad news for two major projects: Construction on a $520 million supercomputer at the University of Texas, slated to be completed next year, will almost certainly be delayed, if not eventually halted. And last week NSF ordered the National Center for Atmospheric Research to stop work on a $92 million airborne phased-array radar to be mounted on hurricane trackers flown by the National Oceanic and Atmospheric Administration. The spending crunch stems from Trump's decision to strip out what was labeled emergency spending in NSF's $9 billion budget as part of a governmentwide spending bill passed by Congress last month covering the rest of this fiscal year. Legislators say Trump's move is illegal, however, and the dispute could end up in court.

USGS SCIENCE IMPERILED The White House is expected to ask Congress to zero out the entire biological research program at the U.S. Geological Survey (USGS) in its upcoming 2026 budget request. In an internal email seen by *Science*, Anne Kinsinger, associate director of ecosystems at USGS, notified colleagues that the White House Office of Management and Budget has ordered the agency to design a plan to slow and then cease all activities in its Ecosystems Mission Area in the next fiscal year, which begins in October. This year the $1.6 billion research agency will spend $307 million on the research, which informs conservation of endangered species, state management of wildlife, responses to wildfire and sea level rise, and more.

EPA GRANTS CUT The Environmental Protection Agency (EPA) last week ordered its staff to start canceling grants already awarded to universities and research institutes, according to an agency source and an email seen by *Science*. These grants provide $35 million to $40 million each year to researchers studying the impacts of pollution and ways to reduce them. The termination order includes more than 100 grants from the investigator-initiated Science to Achieve Results program, along with grants from eight other programs. EPA has given no reason for scrapping the grants, but it can legally terminate awards made before 1 October 2024 just by citing changes in administration priorities.

PANDEMIC'S 'TRUE ORIGINS' Last week, two widely viewed federal websites, covid.gov and covidtests.gov, were redirected to a new White House page emblazoned with "Lab Leak" and claiming to reveal the "true origins of COVID-19." It made the oft-repeated but unproven case that the virus emerged from a lab in Wuhan, China, that had been conducting risky virology experiments with U.S. funding. Some scientists who favor the alternative idea that an infected wild animal passed the virus to people at a Wuhan market said the web page is full of unverified or inaccurate claims and lacks any new information on the origin debate.

Harvard University students, faculty, and supporters rallied on its campus last week to protest threats by President Donald Trump's administration.

PHOTO: AP

IN DEPTH

HIGHER EDUCATION

NIH grants caught in crossfire as Harvard and Trump collide

Agency freezes funding to Harvard, four other universities amid debates over antisemitism and government overreach

By **Sara Reardon**

If halting scores of research grants at Columbia University represented the opening shots of the attack on U.S. higher education by President Donald Trump's administration, the war has now escalated on multiple fronts. After freezing all grants to Columbia earlier this month for not doing enough to combat antisemitism on its campus, according to Trump officials, the National Institutes of Health (NIH) is now similarly stopping grant and contract payments to Harvard and four other universities.

The move would both block new funding and halt payments to investigators currently working on NIH projects. But this week Harvard filed a lawsuit against the Trump administration, saying it was illegally withholding federal funding "as leverage to gain control of academic decision making at Harvard."

The NIH grant freeze came in a 16 April email seen by *Science*, in which an official from NIH's Office of Extramural Research told grants managers to halt disbursements to Harvard, Brown, Northwestern, and Cornell universities, as well as Weill-Cornell Medical School. The email also says that, on orders from the Department of Health and Human Services (HHS), NIH's parent agency, NIH staff should not provide any communication to these institutions or to Columbia about whether the funds are frozen or why.

The Trump administration had already announced its intention to freeze $1 billion in funds from multiple federal agencies to Cornell, $790 million to Northwestern, and $510 million to Brown. At Harvard, more than $2.2 billion in multiyear federal funds were at risk, the White House originally said. Last week's NIH email made it clear the administration is following through on its threats, although none of the schools could confirm the total amount of funding that has been frozen or provide a comprehensive list of affected projects.

The fight with these top research universities escalated after Harvard President Alan Garber on 14 April declared the school would not comply with demands by Trump officials to change its hiring and teaching practices and grant the government control of some operations. "The university will not surrender its independence or relinquish its constitutional rights," Garber wrote in an open letter to federal officials. "Neither Harvard nor any other private university can allow itself to be taken over by the federal government."

The Massachusetts Institute of Technology, Stanford University, Princeton University, and others quickly released statements in support of Harvard. And in the following days, Trump and some of his officials voiced new threats to Harvard's finances by questioning its tax-exempt status and scrutinizing its enrollment of foreign students, who typically pay full tuition. Other universities were put on notice, too. "Tax-exempt status, I mean, that's a privilege," Trump said at an Oval Office briefing.

On the morning of 21 April, when Harvard filed its lawsuit, *The Wall Street Journal* reported that the White House planned to halt another $1 billion in unspecified health research at the university. In a statement Harvard released about the lawsuit, Garber said the Trump administration was trying to seize "unprecedented and improper control" of the university's operations and academic decision-making.

The new freeze on ongoing NIH grants means researchers at Harvard and the other affected universities won't be able to receive reimbursements for work already completed. At Harvard, only a few—albeit large—grants and contracts have been publicly confirmed as suspended. Many Harvard scientists remain unsure of the status of their grants, perhaps because NIH has been ordered not to say what's frozen. Still, Harvard has told researchers to pause hiring and limit spending.

How much the Trump administration's actions will harm Harvard's affiliated medical schools, such as Boston Children's Hospital and Massachusetts General Hospital, remains unclear. But more than $6 billion of Harvard's $9 billion total in federal grants and contracts, all of which the administration has threatened to withhold, goes to hospitals in the area.

In principle, researchers whose grants have been frozen can continue to work. But some individual faculty with ongoing contracts through NIH and other agencies have received stop-work orders, the universities told *Science*, which would require them to immediately cease research activities.

At Northwestern, more than 100 projects have received stop-work orders, according to the university, including research on

wearable devices, robotics, nanotechnology, and Parkinson's disease. Cornell received stop-work orders on more than 90 research projects from the departments of Defense and Agriculture, most of which involve military readiness, cancer research, and research on the spread of airborne infectious diseases.

As *Science* went to press, Harvard hadn't confirmed any specific stop-work orders beyond three that were reported by media outlets before the new NIH freeze. The largest by far involves $60 million in NIH funding for immunologist Sarah Fortune, who runs a multicenter network of researchers studying tuberculosis. Fortune had told multiple media outlets that losing the funding might eventually force her lab to euthanize rhesus macaques it uses to test vaccines for the disease. But *The Boston Globe* reported that Fortune last week was promised $500,000 by the nonprofit Open Philanthropy, already a funder of her work, to keep the monkey vaccine trial going.

In another 16 April NIH email seen by *Science*, the agency told Harvard researcher David Walt to immediately stop work on his $650,000 contract studying diagnostics and treatments for amyotrophic lateral sclerosis. And Harvard's Donald Ingber, who is developing computer chip–size devices with fluid channels called "organs-on-chips," which mimic the physiology of human livers and other organs, also received stop orders on two non-NIH contracts. One is a $15.9 million contract from the Biomedical Advanced Research and Development Authority—a division of HHS—to test treatments for radiation exposure using the devices; the other is a $3.2 million contract from NASA to study the health effects of spaceflight, including with devices intended to accompany astronauts scheduled to orbit the Moon in 2026.

Any funding delay "may kill the whole program," Ingber says. He notes that the Trump administration has announced plans to send humans to Mars within a few years. "There's no way we'll ever go to Mars if we can't figure out how to mitigate radiation toxicities," he says.

Walt says his lab may be able to weather losing its NIH contract, but further cuts might force him to lay off staff. Earlier this year, then-President Joe Biden awarded him the National Medal of Technology and Innovation for his work on genetic and proteomic analysis tools and research into neurodegenerative diseases.

"There's no words to describe my disappointment with our government at this point," Walt says. The Trump administration's approach to slashing biomedical research "is going to cost lives." ■

SPACE

Astronomers claim Chinese star catalog is world's oldest

Novel computer analysis of records ascribed to legendary Chinese astrologer dates them to nearly 2400 years ago

By **Joshua Sokol**

The emperor's chariot. A celestial marketplace. A toilet with excrement represented by a single star. Early Chinese astronomers, likely including a legendary one named Shi Shen, at some point grouped stars they saw into depictions of an imperial court in the sky. And for some 2000 years, these and other constellations—and the coordinates that show where to find them—undergirded an astronomical system maintained by Chinese government bureaucrats, who searched for correspondences between heavenly omens and earthly concerns to help emperors keep the cosmos in harmony. Known as the Star Manual of Master Shi, these constellations comprise the oldest surviving star catalog in China. Now, a study from astronomers at the Chinese National Astronomical Observatories (NAO) claims these records aren't just the oldest in China—but the oldest of their kind found anywhere in the world, dating back nearly 2400 years.

The study is the latest volley in a nearly centurylong debate over the provenance of Shi's star measurements, a mystery grounded in both the history of science and the politics of claiming scientific firsts. Already, the research is drawing criticism and praise alike. "This is an excellent study," says David Pankenier, an emeritus historian of Chinese astronomy at Lehigh University. "I hold a totally different perspective," counters Boshun Yang, a historian at the University of Science and Technology of China.

Like modern Chinese and Western star catalogs, Shi's specified star positions using spherical coordinates, much like latitude and longitude specify points on Earth's surface. But those ancient coordinates no longer match current star positions. Year after year, the coordinates within any given star catalog gradually become more inaccurate. Earth's axis of rotation wobbles like a spinning top on a 26,000-year cycle, so over time, the locations of the celestial poles seem to wander across the background of more distant stars, a phenomenon called precession.

So exactly how old is the Shi catalog? In theory, measuring precession's effects on an old star catalog can allow modern researchers to precisely date when the catalog must have been created, just as counting rings in a tree trunk can reveal a tree's age.

That's what Boliang He and Yongheng Zhao at NAO attempted when they fed historical Chinese star catalogs into a computational algorithm based on the Hough transform, an analytical technique often used for image processing. Their algorithm ingests historical star coordinates, attempts to rule out data that may have been erroneously copied down over the centuries, and then estimates a best fit to where the celestial north pole must have been when the coordinates were measured. This inferred location is then translated back into a date.

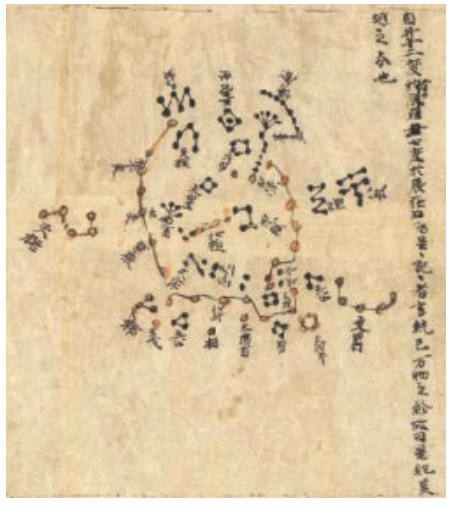

The faded, reddish stars on this seventh century Chinese star chart belong to a catalog created by astronomer Shi Shen.

After testing their method on more recent, better understood Chinese catalogs in a study published last year, He and Zhao tried to look at Shi's catalog. Their new results, soon to be published in *Research in Astronomy and Astrophysics*, argue some star measurements within Shi's catalog were updated around 125 C.E.—but that the other half of the star coordinates date back to about 355 B.C.E., around when Shi was supposed to have lived.

"Our findings align perfectly with these historical accounts, vividly demonstrating the continuity and completeness of ancient

PHOTO: BRITISH LIBRARY ARCHIVE/BRIDGEMAN IMAGES

Chinese historical records," He says. "These discoveries left us deeply surprised."

The analysis suggests Shi's catalog is the world's oldest, beating out a catalog created near the Mediterranean around 130 B.C.E. by the influential Greek astronomer Hipparchus. However, not all outside historians of science are convinced, including Yang, who also studies how to date ancient astronomical records.

Part of the trouble is that Shi's catalog has passed through many hands. Shi is said to have lived during the fourth century B.C.E., serving as a court astrologer to one of the kingdoms during China's Warring States period. That his constellations have survived is nothing short of miraculous: In the third century C.E., another astronomer recopied Shi's data points, or at least data credited to astronomers working in Shi's school of thought. This catalog survived because it was itself recopied during the Tang dynasty in the eighth century, into a catalog known today from only a few surviving manuscripts—one of which was reportedly found in the belly of a Buddha statue 400 years ago.

In the first century B.C.E., Chinese astronomers began using armillary spheres to measure celestial objects' coordinates.

Yang says that if most of the Shi data points are taken at face value, they seem to split into two age clusters, including one that points to the mid-300s B.C.E., a finding that was first established in 1929. But Yang adds that for decades, historians have argued that Shi's data shouldn't be taken at face value.

Following others including Xiaochun Sun at the Chinese Academy of Sciences, Yang has argued that many of Shi's more ancient-looking coordinates can best be explained if they were measured by an instrument that was misaligned from the true celestial north pole by about 1°. This would exaggerate the amount of precession between the coordinates' measurement date and today on one hemisphere of the sky, while underestimating it for the other hemisphere, explaining the two age clusters. Earlier studies, including Yang's own 2023 Ph.D. thesis, found that after accounting for a possible misalignment, the Shi catalog dates to somewhere around or after 103 B.C.E., around the same time as Hipparchus's. That time corresponds to when Han-period scholars were blending the school of Shi and other early Chinese astronomical traditions into a unified whole.

Historians contacted by *Science* also favor this later date for Shi's catalog because it helps explain why the catalog uses spherical coordinates. Historical accounts suggest that during the first century B.C.E., Chinese astronomers both invented the armillary sphere, a globelike device used to measure the sky, and adopted a cosmological model of a spherical universe. Any claim that spherical coordinates were measured before the armillary sphere's arrival, as backdating Shi's catalog implies, would be "like we dug up a receipt from a gas station and somebody wants to say it's from 1700," says Daniel Patrick Morgan, a historian at France's Center for Research on East Asian Civilizations.

The larger context for jostling over the world's oldest star catalog, Morgan adds, is that during the 19th century, Europeans asserted scientific priority over other cultures, kicking off an ongoing fight for bragging rights. Even so, Hipparchus's and Shi's catalogs are both infants when compared with Babylonian records that date at least to the eighth century B.C.E. and specify when a series of stars will rise at dawn.

For his part, He maintains that his algorithm can test whether the data fed into it come from a misaligned instrument. He also suggests the instruments and ideas behind the spherical coordinate system could have been in their early stages before the oldest surviving evidence of their introduction.

Now that He and Zhao have examined China's oldest star catalog, they plan to study records from a later period of Chinese history: the star catalogs after the Ming dynasty, when Chinese and Western astronomical systems first came into contact. He, citing Chinese President Xi Jinping, says these records offer the chance to study China's legacy of cross-cultural exchange, while the country aims to foster new collaborations today. "The concept emphasized by Chinese leaders—that 'civilizations thrive through mutual exchange and learning'—is vividly reflected in this research." ■

Joshua Sokol is a journalist in North Carolina.

GLOBAL HEALTH

World agrees on pandemic treaty—without the U.S.

Health experts hail "victory for multilateralism," but some sticking points remain

By **Kai Kupferschmidt**

After the negotiations come … more negotiations. In the early hours of 16 April, more than 3 years of deliberations culminated when governments around the globe—minus the United States—finally agreed on the text of a treaty to improve how the world prevents, prepares for, and responds to future pandemics. "The nations of the world made history in Geneva today," Tedros Adhanom Ghebreyesus, director-general of the World Health Organization (WHO), said after the talks concluded around 3 a.m. But almost immediately, work started on setting up the next round of negotiations.

That's because delegates agreed to defer resolution of one of the biggest sticking points. The treaty sets up a system called pathogen access and benefit sharing (PABS), which commits countries to sharing samples and genetic sequences of bacteria, viruses, and other potentially pandemic pathogens, but also promises them access to vaccines, drugs, and diagnostics created with that information. The details of the PABS system will have to be worked out in a future annex to the treaty, which will be "very, very challenging," says Jeffrey Valdez, a diplomat on the Filipino negotiating team.

Still, getting this far was a milestone, says Lawrence Gostin, a global health law expert at Georgetown University—especially after U.S. President Donald Trump announced in January that his administration would withdraw from WHO and the treaty negotiations. "The achievement of finding consensus in a world torn asunder by the Trump administration cannot be overstated," Gostin says.

WHO's member states agreed to create a global pandemic treaty in December 2021, just as the Omicron variant of SARS-CoV-2

PHOTO: CHINA IMAGES/ALAMY STOCK PHOTO

French diplomat Anne-Claire Amprou (left), co-chair of negotiations, and WHO head Tedros Adhanom Ghebreyesus after a pandemic treaty was finalized on 16 April.

PHOTO: CHRISTOPHER BLACK/WORLD HEALTH ORGANIZATION VIA GETTY IMAGES

was spreading across the world, producing a massive new COVID-19 surge amid searing inequities in vaccine access. Countries that produced COVID-19 vaccines had hoarded millions of doses, whereas those with no vaccine plants often went without. One study estimated that a fairer sharing system could have prevented hundreds of millions of infections and saved 1.3 million lives. "To prevent what we experienced with COVID from happening again, we needed something drastic," says Precious Matsoso, the South African co-chair of the intergovernmental negotiating body set up to hammer out the treaty.

But the body, which included delegations from all member states, missed the original deadline of May 2024 and negotiations were extended for another year, with several grueling marathon sessions in the very last week. The resulting 30-page treaty covers everything from protecting health workers and strengthening regulation of new drugs and vaccines to reducing risks of pathogens spilling over from animals to humans.

The PABS system was a bone of contention until the end. Countries agreed on the need to share information about pathogens—allowing the world to track how they're evolving—but debates raged about how many vaccine and drug doses should be set aside for use in developing countries, at what cost, and how binding these commitments would be. In the final compromise, manufacturers committed to donating 10% of their production to WHO, with a target of offering another 10% at affordable prices.

That may not be ideal, but it marks huge progress, says Aalisha Sahukhan, Fiji's lead negotiator. "There was a point in the negotiations when there was a real feeling that some developed countries just would not accept any set-asides," she says, "which would have been devastating to the treaty." Still unresolved is exactly how the PABS system will work: how databases will be set up so that information is rapidly accessible to everyone but companies' use of the data can be tracked. "We brokered language that basically defers conclusion of that debate," Valdez says.

Technology transfer was the other major sticking point. Developing countries in particular want to become more self-reliant by pushing drug developers and vaccine companies to share their technology and help build production facilities. (As Sahukhan puts it, the PABS system is about how the cake is divided during a pandemic and tech transfer is about "sharing the recipe so that cake can be made in more places in the world.")

Early drafts described tech transfer as occurring "on mutually agreed terms," a standard phrase in international agreements, but some countries with big pharmaceutical industries pushed for including the word "voluntary." Developing countries worried that could set a precedent for tech transfer under other agreements. "That word, 'voluntary,' was a red line for a number of countries—and in both directions," says Alexandra Phelan, a global health lawyer at Johns Hopkins University who has closely followed the negotiations. In the final hours, countries agreed to use only "mutually agreed terms," with a footnote defining that phrase for this treaty as "willingly undertaken."

The outcome can be seen as disappointing, says Ellen 't Hoen, a Dutch lawyer and public health advocate. "There are few hard new obligations for member states," she says. Still, laying down a new framework on how to collaborate during future pandemics is "no small feat and a victory for multilateralism," she says. But Clare Wenham, a global health expert at the London School of Economics, says the text is "very soft in places" and "doesn't really alter the status quo" on tech transfer. "I don't think this is the big win for multilateralism some are claiming," Wenham says. "I very much hope I'm wrong."

The World Health Assembly, the annual meeting of WHO member states, is set to officially adopt the treaty in May. Countries are now working on a plan for resolving the PABS disputes. An early version calls for establishing a group of experts to come up with a draft of the PABS annex, which could hasten consensus, Matsoso says. "If you want to bring the negotiators … you spend half a day listening to their speeches," she says. "If you want this done quicker, bring scientists." The PABS annex, if it's hammered out, could be adopted at the World Health Assembly in 2026, after which the entire treaty would be opened for signatures. It will enter into force 1 month after 60 countries have ratified it.

The U.S., a major producer of pharmaceutical products, won't be bound by it, which weakens the treaty. But U.S.-based manufacturers are likely to join the PABS system, "even if reluctantly," Gostin predicts. "They will need unimpeded access to pathogen samples and genomic sequencing data as a prerequisite to scientific innovation." ■

Yellow pods were a clue that helped Gregor Mendel figure out patterns of heredity.

PHOTO: KATHY DEWITT/ALAMY

GENETICS

Last of Mendel's seven genetic riddles solved

Massive pea study probes the basis of Mendelian traits and expands breeders' toolbox

By **Erik Stokstad**

Generations of high school students have learned how the 19th century Austro-Hungarian friar Gregor Mendel discovered basic principles of genetics by studying peas, which he planted by the thousands in the garden of his abbey. After cross-pollinating varieties and noting the proportions in which traits such as flower color occurred in their offspring, he revealed the mathematical patterns of recessive and dominant inheritance—a fundamental breakthrough in genetics. But, working decades before genes were identified as the mechanism of heredity, Mendel knew nothing about the molecular basis of his seven traits, which remained "seven riddles," says Shifeng Cheng, an evolutionary geneticist at the Agricultural Genomics Institute at Shenzhen (AGIS).

In recent decades, researchers have gradually mapped those traits onto DNA sequences, identifying the genes behind four of them. Now, in the largest genomic study of peas yet, published this week in *Nature*, Cheng and his colleagues reveal the genes associated with the remaining three, as well as many other genes that pea breeders could use to improve the plants. "This is another milestone in plant genomics," says Aureliano Bombarely, a plant geonomicist at the Institute of Molecular and Cellular Biology of Plants who wasn't involved in the work.

The first of Mendel's traits to be linked to a gene was seed shape. Some pea varieties have seeds that wrinkle if dried and taste sweet when served fresh. Mendel showed they have recessive "wrinkled" alleles. Peas with a dominant "round" allele stay smooth when dry and are less sweet, often going to soup or animal feed. In 1990, researchers at the John Innes Centre (JIC) identified the responsible gene, which codes for an enzyme that helps convert sugars to starch. Its dominant form packs the seeds with starch and keeps them smooth, whereas the recessive allele makes an inactive enzyme that leaves more sugar in the seeds. Scientists at JIC and elsewhere subsequently discovered the genes behind three other traits: plant height, and flower and seed color.

The large size of the pea genome and a general emphasis on higher profile crops such as wheat, maize, and rice slowed further progress. "Peas don't get a whole lot of attention," says Rebecca McGee, a plant scientist at Washington State University. But as sequencing costs fall, that's changing.

The entire pea genome was sequenced in 2019. Researchers in China went on to sequence 237 kinds of peas and compile their genetic differences into a map, published last year. This diversity allowed them to identify 29 million genetic markers, called single nucleotide polymorphisms (SNPs), that pea breeders can use to guide and accelerate crop improvement.

Now, Cheng has partnered with colleagues at JIC to vastly expand the catalog of variations. JIC has a historic connection to Mendel: In the early 20th century its first director, pioneering geneticist William Bateson, helped disseminate Mendel's findings and prioritized research on pea genetics. Since then it has collected several thousand varieties of pea, including from the Middle East, where the crop was domesticated, and from Ethiopia and the Himalayas, two other hot spots of diversity, amassing a large and varied collection.

Together, AGIS and JIC sequenced nearly 700 pea varieties, spanning the diversity of the collection. This yielded 155 million SNPs that they correlated with physical traits of the plants, allowing them to narrow down the location of important genes. "It is a great accomplishment for the pea," says Tom Warkentin, a plant breeder at the University of Saskatchewan.

Among those genes are ones for the three remaining Mendel traits: the color of the pea pod, the arrangement of flowers, and whether the pods are edible. "We have finally provided an answer to this 160-year-old riddle," Cheng says. The new details show, for example, that yellow pods occur in plants with DNA missing next to a gene involved in making chlorophyll. Cheng's group believes the defective RNA transcribed from that DNA region interferes with chlorophyll synthesis, leading to pallid pods.

That particular insight might not lead directly to improved peas, but others likely will. Take the genetic basis for tendrils. By intertwining, these modified leaflets help pea plants stay upright and make harvesting much easier. In the 1980s breeders produced varieties with plentiful tendrils, a trait controlled by a gene called *afila*. But the same *afila* alleles that cause pea plants to grow more tendrils and fewer leaves can also lower yield by somehow deleting adjacent genes that influence the number and weight of seeds. By revealing exactly where on the genome the deletions start and stop, Cheng and colleagues hope to help breeders select *afila* alleles that don't delete the flanking genes.

Many other traits in peas are determined by multiple genes, and there, too, genomic maps with plentiful markers will help breeders build on the heritage of Mendel, Warkentin says. "All these developments add to the toolbox of plant breeders." ■

TRUMP ADMINISTRATION

NSF kills grants to comply with war on woke

Senator's report seen as blueprint for targeting up to $2 billion in funding

By **Jeffrey Mervis**

The National Science Foundation (NSF) has spent billions of dollars over several decades trying to attract more women and members of underrepresented groups into science, technology, engineering, and math (STEM). But President Donald Trump says such efforts "stigmatize" people in the United States based on their race or sex and has ordered the agency to stop funding them. So last week NSF reversed course and began to terminate what could be as much as $2 billion in grants.

An NSF spokesperson declined to comment on how the axed grants were selected, except to say they were "not aligned with agency priorities." The agency's 18 April announcement flagged those relating to "diversity, equity, and inclusion (DEI)" as well as "research with the goal of combating 'misinformation,' 'disinformation,' and 'malinformation' that could be used to infringe on the constitutionally protected speech rights of American citizens."

Sources tell *Science* that NSF's actions were driven by a report issued last fall by Senator Ted Cruz (R–TX), chair of a committee that oversees NSF and other science agencies. The agency had "politicized" its $9 billion research portfolio under former President Joe Biden, according to the report, which listed $2 billion in "questionable projects that promoted [DEI] tenets or pushed onto science neo-Marxist perspectives about enduring class struggle." The report also singled out NSF research in environmental and social justice.

The top Democrat on the committee overseeing NSF in the House of Representatives deplores NSF's moves. "The American people do not want a system where politicians, be they in the Senate or in the White House, decide which scientific projects to fund or defund based on their biases," declared Representative Zoe Lofgren (D–CA), who has rejected Cruz's description of the NSF-funded projects. "I call on the [NSF] director to reverse course immediately and protect the integrity of NSF and the U.S. scientific enterprise."

That's not going to happen, predicts one former NSF director. "The NSF director has no choice but to do what the White House tells him to do, or resign," says Neal Lane, who held the job 30 years ago under then-President Bill Clinton.

In February, NSF began to vet active grants it suspected might run afoul of an executive order issued by Trump on 21 January, which called for "ending illegal discrimination." Although NSF never announced the results of that post-award screening, many program officers assumed they would be talking with grantees to modify offending portions of their grants. But that never happened, according to sources at the agency. Instead, they say, late last week members of Elon Musk's Department of Government Efficiency told NSF officials to terminate the 3483 grants listed in Cruz's report.

After spending billions to increase diversity in science, the National Science Foundation has changed course.

PHOTO: E. BILLMAN/*SCIENCE*

Science educator Tammie Visintainer of San Jose State University had one of those grants. She's been on edge ever since Cruz devoted two pages to her 5-year, $786,000 project to help secondary school teachers prepare classroom units on urban heat islands and guide students in researching the health and environmental effects of such hot spots. Cruz said her project and others like it "allege discrimination in the environmental sciences … and emphasize activism over scientific investigation."

Visintainer says Cruz's critique of her project, which serves teachers and students of all backgrounds and income levels across the San Jose area, makes no sense. "My program is open to anyone, and I don't pick the teachers or the students," she says. "So I don't understand what crime I'm supposed to have committed."

Former top NSF policymakers say they've never heard of such after-the-fact tinkering with NSF's highly regarded system for choosing which proposals to fund, much less the outright cancellation of a grant. "The announcement made me very sad," says Tufts University computer scientist Diane Souvaine, a former chair of NSF's oversight body, the National Science Board. "Once an award is made, the PI [principal investigator] should be free to carry out the research they have proposed."

At the same time, Souvaine says she has told colleagues who have had their grants terminated to rethink their research plans to conform to the new political landscape. "And that means avoiding activities that serve only those with certain characteristics," she says.

A Q&A section on NSF's website says the agency will no longer accept research proposals that "indirectly preference or exclude individuals or groups based on protected characteristics," a phrase that refers to a person's race, sex, religion, age, or disability. But the site also includes a personal note from NSF Director Sethuraman "Panch" Panchanathan that says, "NSF will continue to support basic and use-inspired research in S&E [science and engineering] fields that focus on protected characteristics when doing so is intrinsic to the research question and is aligned with Agency priorities."

Lane thinks that language should offer a ray of hope to scientists dismayed by NSF's decision to retract so much of its research portfolio. "To me, those words are his attempt to stay as close to NSF's statutory mission as he can without violating the president's order," Lane says. "That mission begins with 'promoting the progress of science.' And you can't do that without making sure that everybody has an equal opportunity to participate in STEM. I think Panch's statement is an indication NSF is still committed to doing that." ■

ECONOMIC RESEARCH

Trade war is 'natural experiment' for economists

Rare chance to study tariffs might be "the only silver lining" in Trump policies, one says

By **Dan Charles**

On the morning of 2 April, shortly before U.S. President Donald Trump unveiled his sweeping plan to impose tariffs on most of the nation's trading partners, a research team at the University of Cambridge was debating whether its computer model of global supply chains could accurately predict the effects of trade barriers. How would industrial networks adapt, for instance, if a cluster of "geopolitically friendly" countries required electric vehicle batteries to be manufactured domestically? One student mused that they would have to "wait for a natural experiment" to validate the model's predictions, recalls Alexandra Brintrup, leader of the research group.

Then, "That very evening, the natural experiment began with [Trump's] 'Liberation Day' announcement," Brintrup wrote in an email to *Science*. "So now we are very much watching the events unfold!"

Many economists have condemned the Trump administration's tariff offensive. They argue it will bring disruption and economic hardship to much of the world. Yet it's also presenting researchers with an unprecedented chance to test theories and launch new research projects. "It's an opportunity that I've been waiting for, similar to an epidemiologist waiting for an outbreak, to understand the world," says César Hidalgo, a physicist–turned–economics researcher at the Toulouse School of Economics.

In the days after Trump's announcement, Hidalgo turned to a model of international trade that tracks the flows of thousands of different products, depicting them visually as a weblike structure. "We ran a simulation, using the Liberation Day tariffs," Hidalgo says, and found that "the world basically rewires itself in a way that is not so centered on the United States anymore."

A truck carries goods into the United States from Mexico, which could face much higher U.S. tariffs.

In the computer-generated web of trade, links between the U.S. and other countries weakened. French aircraft exports, meanwhile, grew, as did exports of shoes from Mexico and Central America.

Brintrup's research group, called the Supply Chain AI Laboratory, launched a similar exercise and ran a Trump-tariff scenario through its model of industrial supply chains. In preliminary results, companies ended up buying from a larger number of suppliers, increasing their costs.

Real-world economic data that emerge in coming months or years could, at least in theory, validate these predictions or reveal weaknesses in the assumptions of each model. But the results might not be clear-cut.

For one thing, Trump keeps changing his mind. Since the initial announcement he has rolled back some tariffs, warned of new ones, and exempted certain products, such as mobile phones, from the highest tariff rates. He's also promising negotiations with dozens of individual countries, potentially leading to different deals with each one.

In addition, many changes are happening simultaneously, "so it's actually a horrible setup for a natural experiment," says Jesse Anttila-Hughes, an economist at the University of San Francisco. "Trump is simultaneously implementing tariffs and destroying major federal agencies and assaulting the rule of law and reorganizing geopolitics." As a result, it likely won't be clear what caused any particular outcome.

According to William Ridley, an economist at the University of Illinois Urbana-Champaign, "The only concrete aspect of the current situation seems to be the extreme uncertainty that it's causing."

As it happens, uncertainty itself is increasingly the focus of economic research, and the current crisis is boosting its relevance. "This is an extreme case of uncertainty," says Nuno Limão, an economist at Georgetown University who's among the pioneers of this field.

In earlier research, Limão measured the effects of uncertainty by analyzing what happened when China won entry to the World Trade Organization (WTO). The boom in trade that followed far exceeded what classical theories would have predicted, based on lower tariffs alone. Limão and his colleagues argued that much of the boom resulted instead from greater certainty that WTO membership created about the rules of trade with China.

The Trump administration's trade war, however, "is basically the opposite," Limão says, adding that he and a colleague are weighing whether to update their past models of the economic impacts of uncertainty. "Trade agreements don't really mean anything under this administration."

According to Limão, the lack of clarity caused by the emerging global trade conflict will likely do its part to impair global trade. The chance it offers to learn, he says, "is about the only silver lining." ■

PHOTO: JOSE LUIS GONZALEZ/REUTERS

Science Webinars

AAAS

Science Webinars help you keep pace with emerging scientific fields!

Stay informed about scientific breakthroughs and discoveries.

Gain insights into current research from top scientists.

Take the opportunity to ask questions during live broadcasts.

Get alerts about upcoming free webinars.

Sign up at: scim.ag/wcfq2023

THE FOG OF WAR

Fifty years after the Vietnam War, researchers are still struggling to document the long-term health effects of the massive spraying of Agent Orange and other herbicides

By **Dennis Normile**

Nearly 2 decades ago, more than 240 women who had recently given birth in Da Nang, Vietnam, got an unusual request from visiting nurses checking on their newborns: Could we collect a small sample of your breast milk?

The mothers had volunteered for a study scientists hoped would answer a question that had haunted Vietnam since what it calls the Resistance War Against America ended in 1975: Had the U.S. military's massive aerial spraying of vegetation-killing chemicals during the conflict put children's health at risk?

By the time the milk-collecting effort began in 2008, researchers already knew those herbicides—collectively called Agent Orange, after the orange stripe painted on the barrels holding one formulation—were tainted with a highly toxic dioxin, a long-lived chemical linked to an array of human health problems. Postwar surveys had found that relatively high concentrations of dioxin lingered in some of Vietnam's soils and aquatic sediments, especially near former U.S. air bases—such as the one in Da Nang—that had handled vast volumes of the chemicals. And Agent Orange had been anecdotally linked to reports of birth defects in communities exposed to the spraying, which lasted from 1961 to 1971.

As years went by, Vietnam asserted that those harmed by Agent Orange included the second-, third-, and even fourth-generation relatives of those who experienced the spraying, because of dioxin lingering in the environment or inherited health effects. The country put birth defects at the center of its descriptions of the horrors of Agent Orange. But few studies had attempted to rigorously examine a link, until the Da Nang work. Led by environmental health

PHOTO: HORST FAAS/AP

During the war in Vietnam, the U.S. military sprayed herbicides on an estimated 2.2 million hectares of forest and farmland.

scientist Muneko Nishijo of Kanazawa Medical University and public health specialist Tai Pham-The of the Vietnam Military Medical University, it aimed to document dioxin levels in the milk of new mothers, then follow their children as they matured.

Now, Vietnam is preparing to mark the 50th anniversary of the event that ended the war—the capture of Saigon, now Ho Chi Minh City, by North Vietnamese and Viet Cong forces on 30 April 1975. Yet that study remains one of the few ongoing research efforts on the long-term health effects of the bitter conflict, which cost the lives of some 3.3 million Vietnamese and nearly 60,000 U.S. service members. It did not resolve the birth defects question. But Nishijo and Tai did find evidence that the chemical can affect brain development in exposed children, and others are studying how the conflict is still affecting the physical and mental health of those who lived through it (see sidebar, p. 353).

By now, most Vietnamese have no memory of the war, as the majority of the nation's 101 million people were born after it ended. And finding support for studies to understand the war's continuing impact is proving increasingly difficult, as neither the United States nor Vietnam appears eager to revisit that era. But, "The ongoing burden of disease among exposed populations means that Vietnam's dioxin legacy remains a significant public health challenge," says environmental health scientist Tran Thi Tuyet-Hanh of the Hanoi University of Public Health.

THE VIETNAM WAR marked the biggest deployment of herbicidal warfare the world has ever seen. Between 1961 and 1971, lumbering aircraft sprayed an estimated 74 million liters of the chemicals over South Vietnam as well as border areas of Laos and Cambodia. The goal was to strip foliage from mangrove swamps and dense forests that were providing cover for North Vietnamese and Viet Cong troops, and to destroy crops they relied on for food.

The weapons of choice were called the rainbow herbicides—a half-dozen formulations identified by names such as Agent Pink and Agent White, after the colors used to mark barrels. Agent Orange, which became the most notorious, was a 50-50 blend of two commercially available herbicides, 2,4-dichlorophenoxyacetic acid and 2,4,5-trichlorophenoxyacetic acid (2,4,5-T). The defoliants were believed to be harmless to humans, and U.S. troops typically handled them without wearing protective gear.

By the late 1960s, however, lab experiments showed 2,4,5-T could cause abnormalities and stillbirths in mice, and there were reports of human birth defects in sprayed areas of Vietnam. Later it became clear that the herbicide manufacturing process introduced a particularly toxic dioxin, known as 2,3,7,8-tetrachlorodibenzo-p-dioxin (TCDD), into Agent Orange and other herbicides. Four years before the war ended, the U.S. abandoned its decadelong spraying campaign amid mounting international condemnation and concerns about safety.

Looking for links

A 2018 U.S. National Academies report found "sufficient" or "suggestive" evidence linking 19 conditions to herbicide exposure.

SUFFICIENT EVIDENCE

- Soft-tissue sarcoma
- Non-Hodgkin and Hodgkin lymphoma
- Chronic lymphocytic leukemia
- Chloracne
- Hypertension

SUGGESTIVE EVIDENCE

- Laryngeal, lung, and bladder cancer
- Multiple myeloma
- Parkinson's disease
- Ischemic heart disease
- Stroke
- Hypothyroidism

NO CONSENSUS

- Type 2 diabetes

Today, there is broad consensus that dioxin poses serious health risks to those directly exposed, including Vietnamese citizens and soldiers as well as members of the armed forces of the U.S. and other countries that aided it during the war: South Korea, Australia, and New Zealand. That consensus rests, in part, on efforts by the U.S. government to assess how exposure affected the health of U.S. veterans. In 1992, the Department of Veterans Affairs asked the Institute of Medicine, now part of the U.S. National Academies of Sciences, Engineering, and Medicine (NASEM), to review the scientific literature and provide biennial updates. The last of those reports, *Veterans and Agent Orange*, appeared in 2018 and identified 19 cancers and other conditions with "sufficient" or "suggestive" evidence of an association with exposure to the herbicides (see table, left). Vietnamese investigators separately produced a similar list.

But such studies largely left open one of the most visible and contentious questions surrounding Agent Orange: whether the compounds pose risks not just for those who were directly exposed, but for their children.

THE CONCERN about future generations was prompted, in large part, by the worrisome staying power of TCDD, the dioxin that contaminated Agent Orange. Unlike the herbicide itself, which decomposes within hours to days, TCDD can survive up to 3 years in soil that is exposed to sunlight. If leached into river or pond sediment, it can have a half-life of more than 100 years—more than enough time to be picked up by fish, ducks, and other animals that people eat. (People can also inhale contaminated dust and absorb dioxin through the skin.) Once in the human body, dioxin can lodge in breast and other fatty tissue and have a half-life of 7 to 11 years. It can also contaminate breast milk and be passed to breastfeeding babies.

Since the 1970s, numerous animal studies have found that fetuses exposed to dioxin can exhibit a wide range of birth defects and developmental problems, suggesting an impact on human fetuses is biologically plausible. But documenting it has proved difficult.

Because of the Agent Orange spraying, Vietnam was the obvious place to seek an answer. In 2003, the U.S. National Institute

DATA: NATIONAL ACADEMIES OF SCIENCES, ENGINEERING, AND MEDICINE. 2018. *VETERANS AND AGENT ORANGE: UPDATE 11 (2018)*. HTTPS://DOI.ORG/10.17226/25137

In Vietnam, the government has asserted that contamination from herbicide spraying by the U.S. military is responsible for birth defects.

PHOTO: PAULA BRONSTEIN/GETTY IMAGES

of Environmental Health Sciences (NIEHS) approved a 5-year, $3.5 million study proposed by public health physician David Carpenter of the University at Albany. It planned to analyze dioxin levels in the blood of 300 Vietnamese mothers of babies with birth defects, using 300 mothers of healthy infants as controls. But NIEHS canceled the study in 2005 after failing to agree on research protocols with Vietnam's Ministry of Health.

The next year, a team led by Tuan Van Nguyen, then at the Garvan Institute of Medical Research, published a meta-analysis of 22 studies, including unpublished Vietnamese-language reports, that suggested mothers exposed to Agent Orange were twice as likely to have children with birth defects as those not exposed. But that conclusion, reported in the *International Journal of Epidemiology*, proved controversial. In a commentary in the same journal, toxicologist Arnold Schecter of the University of Texas and surgeon John Constable of Harvard Medical School criticized the paper for relying on old, non–peer-reviewed publications. "We know of no non-Vietnamese studies linking herbicide or dioxin exposure to congenital malformations other than spina bifida and anencephaly," the pair wrote. (In 2014, the NASEM committee that produced that year's update to *Veterans and Agent Orange* reviewed additional evidence and concluded it was "inadequate or insufficient" to link Agent Orange to any birth defects, including spina bifida.)

Nguyen, now at the University of Technology Sydney, says that although their work suggested an association between Agent Orange exposure and birth defects, many of the studies they drew on were observational. As a result, "We avoided causal conclusions." But more rigorous cohort studies that tracked individuals in a way that would rule out confounding factors, such as maternal age and exposure to other chemicals, could yield firmer conclusions, he says.

A good opportunity to launch those studies was missed, Nguyen says. By the mid-2000s, Vietnamese and U.S. researchers had measured the dioxin burdens of a significant number of individuals from across Vietnam, which could have enabled a large-scale study of the birth defects question. But Vietnamese authorities never acted on Nguyen's suggestion to use those data. "The study was entirely feasible, yet it was never conducted, which was deeply disappointing," Nguyen says.

Several factors explain the lackluster support, scientists say. One is that the topic "is extremely political" in both Vietnam and the U.S., Carpenter says. For example, if his 2003 study "had shown what we expected"—that herbicide exposure was linked to birth defects—the U.S. might have been "expected to pay reparations to Vietnamese children." Alternatively, if it had found no link, that might have "embarrassed" the Vietnamese government, which has long highlighted birth defects as Agent Orange's most prominent harm.

At this point, Carpenter says, "It looks increasingly hopeless to think that an adequate study [of the birth defects question] will ever be funded and done."

FOR THE MOMENT, Nishijo's and Tai's breast milk study is the only ongoing epidemiological study focusing on dioxin in Vietnam, Nishijo notes. Launched in Da Nang, it has since expanded to a second cohort near the former Bien Hoa Air Base, another hot spot, and a control group. But the study is unlikely to provide a definitive answer to the birth defects question. "Our cohort is too small to investigate congenital anomalies," because they occur rarely, Nishijo says.

Still, in dozens of papers published over the past 15 years, the team has documented other links. In particular, they have found that a high level of dioxin in a mother's milk—a proxy for fetal exposure—is associated with slower physical growth and lagging neurodevelopment in their children. Boys exhibit learning difficulties, for example, whereas girls show attention deficit hyperactivity disorder and autism.

The papers "provide strong evidence" that living near sites contaminated by Agent Orange can result in high dioxin body burdens that are associated with behavioral disorders in children, says Steven Stellman, an epidemiologist now retired from Columbia University who was long involved in Agent Orange studies.

If funding allows, Nishijo and Tai intend to keep following the children as they age. That could reveal links between dioxin exposure and cancers and other diseases that manifest later in life.

In the meantime, other researchers say there's another issue surrounding the long-term health impacts of Agent Orange that

could still be studied—if funders are willing to step forward. It is the question of whether exposure has caused fundamental biological changes in people that can be handed down from generation to generation.

Vietnamese scientists and officials contend they are seeing such multigenerational effects resulting in birth defects several generations after exposure. And although the authors of the 2018 NASEM report concluded there was "inadequate or insufficient evidence" of epigenetic effects, they strongly encouraged more study of the issue.

Here, too, there is suggestive evidence from animal experiments. Michael Skinner, a biologist at Washington State University, has reported that, in rodents, genetic changes and adult-onset diseases linked to dioxin exposure can be seen in fourth-generation descendants.

Recent human research also lends support to the idea. Cristina Giuliani, a biological anthropologist at University of Bologna, and colleagues at the Hue University of Medicine and Pharmacy and the University of California (UC), Riverside focused on an epigenetic mechanism called DNA methylation and how it affected the expression of one particular gene, *CYP1A1*, which has a role in breaking down toxic compounds, making them easier to be eliminated from the body. "TCDD is different as it cannot be fully detoxified and its presence further stresses the detoxification system," she says. In a 2018 *Environmental Pollution* paper, they reported that the offspring of Vietnamese parents exposed to Agent Orange shared a distinctive *CYP1A1* DNA methylation signature that was not seen in the children of parents with no exposure.

Giuliani is careful to note that the study "does not experimentally demonstrate that exposure to dioxin is transmitted to descendants." And it does not address the question of whether any changes are harmful, beneficial, or neutral.

Getting a firmer grip on those issues, researchers say, would require epigenetic studies comparing several generations of exposed and nonexposed populations. But there are "no studies like that yet," Skinner says. And finding the funding to conduct such studies in Vietnam, he says, "would be difficult … due to the politics of the situation."

THE 50TH ANNIVERSARY of the end of the war is likely to draw renewed attention to the Agent Orange era. But many researchers doubt it will lead to a substantial surge in scientific activity. One obstacle is that Vietnam now has "more pressing environmental health issues," such as increasingly severe air pollution from sources including the widespread burning of plastic waste, says David Biggs, an environmental historian at UC Riverside who has studied the Agent Orange controversy.

Another hurdle is that the impact of Agent Orange is fading. In the early 2000s, the Vietnam Red Cross Society estimated 3 million people were affected by the spraying and lingering contamination. But those who were directly exposed to the spray are dying, and ongoing exposure "will become less and less because this dioxin no longer exists in the environment" as it breaks down, says Le Ke Son, a toxicologist who led the Vietnamese government's efforts to deal with the herbicides. The U.S. has also paid to clean up some contaminated sites, although one or two hot spots still persist. (President Donald Trump's administration recently suspended funding for a cleanup of the Bien Hoa site.) And even if biological changes due to exposure can be inherited, "those born with severe disabilities are less likely to marry and have children," says Charles Bailey, who spearheaded the Ford Foundation's efforts to address Agent Orange issues in Vietnam in the early 2000s.

Still, even 50 years on, Agent Orange casts a dark shadow over Vietnam. And Carpenter, for one, believes "we are missing a very important opportunity to understand more about the risks." ■

With reporting by Le My in Ho Chi Minh City, Vietnam.

Did the United States commit 'ecocide'?

The harm to human health caused by spraying Agent Orange and other herbicides over southern Vietnam was unintended—but not the damage to the environment. The U.S. military's effort to denude an estimated 2 million hectares of forest and 200,000 hectares of farmland was designed to deny Viet Cong and North Vietnamese troops food and protective cover. At the time, critics of the tactic coined a new term—"ecocide"—to describe the widespread destruction.

More than 50 years after the spraying ended, however, little is known about its long-term ecological impacts. In 1983, 12 years after the herbicide campaign ended, *Science* reported that Vietnamese scientists attending a conference in Ho Chi Minh City had found that many sprayed upland forests that villagers tried to convert to agriculture were "unsuitable for growing crops and the land has become covered with a coarse, deep-rooting grass." Another study presented there found only 24 bird and five mammal species in a heavily sprayed forest strip; in contrast, two nearby undisturbed areas held 145 and 170 kinds of birds and 30 and 55 mammal species.

Decades later, few published studies have examined how forests and wildlife have recovered from the spraying, researchers reported in 2021 in *Environmental Science & Technology*. After reviewing hundreds of papers related to Agent Orange, the authors—ecologists Truong Ngoc Kiem of Vietnam National University and Dinh Van Khuong of the University of Oslo—found just one related to wildlife. That paper, which appeared in the *Vietnamese Journal of Primatology* in 2009, reported that fecal samples could reveal dioxin burdens in douc langurs residing in sprayed areas, but did not reach conclusions about the health impacts of the exposure.

The lack of Agent Orange follow-up is unfortunate, Dinh says. "We missed a lot of opportunities to learn if this has a negative impact on ecosystems," he says, "and to find solutions to recover those ecosystems." —*D.N.*

A sign warns passersby of dioxin contamination at the former U.S. Bien Hoa Air Base, which handled vast volumes of herbicides during the Vietnam War.

PHOTO: DAVID WA/ALAMY

A 50-YEAR SHADOW

To understand the lasting effects of conflict, researchers look to those who lived through the Vietnam War as teens

By **Jyoti Madhusoodanan**

Nguyen Minh lived through war for the first 18 years of his life. Growing up in the Quảng Bình province of North Vietnam, a region that experienced some of the most intense bombing and artillery attacks during the Vietnam War, Nguyen recalls times when he and his siblings fled their village to escape the explosions—once to the forest, another time to a canyon in the mountains. Both in the country and in Hanoi, where his family moved when he was 8 years old, bombs killed friends and family members. "I can still recall the heartbreaking moments when some of my classmates were killed in those air raids," Nguyen says.

More than 50 years later, Nguyen is studying the physical and emotional legacy of experiences like his. A sociologist who retired in 2023 from the Vietnamese Academy of Social Sciences's Institute for Family and Gender Studies, he has been helping University of Utah sociologist Kim Korinek understand how experiencing the war early in life, as he did, has influenced the health and well-being of older people in Vietnam today.

Launched in 2018, the Vietnam Health and Aging Study (VHAS) has already yielded new insights into the complicated health

PHOTO: MANAN VATSYAYANA/AFP VIA GETTY IMAGES

Many women didn't fight in the Vietnam War, but their experiences of death and suffering had enduring impacts.

impacts of war. The researchers have found, for instance, that serving in the military is linked to greater resilience in later life, and that people's age when they lived through war can shape its later impacts.

The study is also a corrective. "This was a war that was seen through the lens of Americans," Korinek says. Yet estimates suggest some 60 Vietnamese died for every one U.S. soldier, she says. "We owe it to the community of people in that generation who were affected to attempt to document the lasting consequences."

Most studies of the aftermath of war have surveyed refugees, U.S. veterans, or survivors in Europe, says Patrick Heuveline, a social demographer at the University of California, Los Angeles who studies the impacts of conflict in Cambodia. The Global South has been largely overlooked. "It's important to diversify the experiences we study," he says. And it's rare to examine the impact of war so long afterward, says Harry Minas, a mental health researcher at the University of Melbourne. "It gives us a clearer picture of how the consequences last over time and how they change."

The VHAS team surveyed about 2400 people who were in their late teens or early 20s at the end of the war in 1975 and lived in at least one of four regions in North and north-central Vietnam that saw varying levels of violence. Some, such as Quảng Bình, were bombed so heavily that it's still common for locals to uncover unexploded bombs in their backyards and on beaches.

In their interviews, the researchers asked participants about their personal exposure to the conflict, such as having a caregiver serving in the military, serving in the military themselves, or participating in informal youth brigades that assisted with war efforts such as scouting for hidden explosives.

The interviews proved challenging. Many participants live in rural areas, speak only regional dialects of Vietnamese, and—given their advanced age—struggle to remember their early childhood troubles. Nguyen says conducting the interviews resurfaced many of his own recollections—and the gaps in them: "When I speak with the participants, I also recall what I experienced. [But] I can recall only a few things from when I was 6 or 7, and not much before that."

To correlate survivors' experiences with their physical and mental health, the researchers collected general health information on aging-related conditions including heart disease, diabetes, and cognitive decline as well as on post-traumatic stress as a result of the war. They also drew blood samples to check for cortisol levels and DNA methylation patterns, both of which can signal stress and aging.

How people fared in later life seemed to depend on their age during the war. In a 2023 publication, Korinek and her colleagues reported that among people who lived in areas exposed to similar levels of high intensity bombing, those who were under the age of 15 were more likely to report dizziness, joint pains, stomach issues, and other stress-related conditions later in life than those who were in their late teens or early 20s when the war was unfolding.

Gender also seemed to determine how people processed the war. Few women in the study had served in the military, but they did everything from guiding their families through forced evacuations to caring for the wounded to restocking arms and food at the frontlines. Women "really had a proximity to the death and pain that we don't appreciate," Korinek says. Those experiences left women much more likely to experience high blood pressure and other kinds of heart disease than men who had lived through similar levels of trauma while in the military, the VHAS data reveal.

> **"We owe it to the community of people in that generation who were affected to attempt to document the lasting consequences."**
>
> **Kim Korinek**
> University of Utah

The results could help policymakers expand health care—at present, benefits for survivors only reach veterans, not women or youth who served in these "informal" ways during the war, Nguyen says. Addressing these gaps is particularly important as economic growth and cultural shifts in Vietnam alter how older people are cared for, Minas adds. In the past, older adults may have relied on children or grandchildren as caregivers. Today, they "don't have the kind of family supports that they might have had 20 or 30 years ago," he says.

The VHAS researchers continue to analyze the data at hand. But efforts to collect more data were only funded through 2024, Korinek says. If she secures fresh funding, she hopes to include the children of VHAS participants, who may experience indirect effects of the war. Others to include in the next cohort are people born near the end of the war or in subsequent years, when food shortages and malnutrition were rampant.

The work hits close to home for Toan Khanh Tran, a physician and VHAS investigator at Hanoi Medical University who was 4 years old at the end of the war in 1975. His parents told him he was born in a bomb shelter during a massive "carpet bombing" campaign. Despite losing family members and living through food shortages, he has no strong memories of the war. Working on the VHAS has helped him recognize that for survivors without active memories—or those who try to forget their experiences, as many participants say they do—"The trauma is still there." ■

Jyoti Madhusoodanan is a science journalist based in Portland, Oregon. This reporting was supported by a fellowship from the Journalists in Aging Fellows Program and the Silver Century Foundation.

BIOMEDICINE

Integrating exposomics into biomedicine

Assessing a full range of environmental exposures will improve human health

By **Gary W. Miller**[1] *and* **Banbury Exposomics Consortium**

For the past two decades, the notion that an individual's exposure to multiple factors in the environment can influence health over their lifetime has been steadily maturing into an independent field of study (*1*). How do combined exposures to chemicals in the water, poor nutrition, and social stressors influence metabolism, cardiovascular function, or cognition? Such questions are complicated, and investigative research now spans a range of disciplines, from epidemiology and social science to biochemistry and molecular biology. A major challenge for this expanding field of exposomics has been conceptualizing studies and developing methodologies (*2*, *3*) in ways that connect the relevance of environmental exposures to biomedical research. Strengthening this association could benefit from establishing definitions that guide and unify the systematic analysis of environmental factors affecting health and disease. This would enable discovery-based analysis of the environmental influences on health and potentially improve disease prevention, treatment, and public health policies.

Last year, an operational definition for exposomics and its underlying principles was proposed by researchers from diverse disciplines and areas of expertise to provide a foundation on which concepts, approaches, methods, and results can be

compared across disciplines, studies, and laboratories (*4*). Briefly, the exposome is posited as an integrated compilation of all physical, chemical, biological, and (psycho)social influences that "impact biology." The field of exposomics thus examines the comprehensive and cumulative effects of these factors by integrating data from interdisciplinary methodologies and data streams to drive discovery.

The rationale for including exposomics in biomedical research is straightforward. Only a fraction of chronic diseases can be primarily attributed to genetic factors. Thus, considering factors that constitute the exposome will help achieve a more thorough understanding of a given health condition. Exposomics is distinct from environmental health research in that it involves a longitudinal assessment across multiple environmental domains, ultimately linking them with effects on health. This approach also extends epidemiological studies and toxicological risk assessments that address the effects of specific environmental factors on a phenotype at a given time—such as exposure to solvents in the workplace and cognitive function. Exposomics is therefore, by definition, explicitly multifactorial and is amenable to combining with other large-scale "omics" studies, such as genomics, proteomics, and metabolomics. The merging of exposomics and genomics, for example, is empowering new health research studies focused on the effects of industrial chemicals on cancer (*5*); of air pollution on Alzheimer's and Parkinson's diseases (*6*); of nontobacco exposures on chronic obstructive pulmonary disease (*7*); and of combined lifestyle, dietary, and social factors on diabetes (*8*).

Many research pursuits can benefit from this multifactorial exposomic approach. For example, the changing climate can affect human health through natural disasters (and the consequential disruption of socioeconomic structures) and vector-borne disease. Some chronic diseases are affected by suboptimal nutrition, exposure to chemical pollutants, low physical activity, and lack of access to green space; yet, the details of these relationships are unclear. Although some of these conditions are not amenable to classical biochemical measurement, many responses are, such as altered cellular responses to stress and epigenetic modifications. Exposomics has the potential to improve the ability to identify the environmental drivers, physiological targets, relevant cellular pathways, and molecular transducers of health impacts. Moreover, exposome-related factors associated with a medical disorder may be readily modifiable.

Humans are exposed to multiple dynamic factors throughout their lives, yet research methods and regulatory agencies have not kept pace with this complexity and continue to be overly reliant on a "one exposure at a time" mindset. Exposomics is starting to change this strategy through methods and tools that are currently available. These include low- and high-resolution mass spectrometry for detecting multiple chemicals, nutrients, molecular signals, metabolites, and chemical modifications to the genome (epigenetic changes) caused by exposure to the environment. Geospatial techniques allow mapping of exposure sources spatially and temporally. This includes satellite-based remote sensing of air pollutants and wearable devices that monitor an individual's exposure to pollutants.

"Humans are exposed to multiple dynamic factors throughout their lives, yet research methods...have not kept pace..."

These technologies are uncovering previously unknown linkages between small molecules or lifestyle factors and physiological disruptions or human disease. By using approaches that provide systematic and relatively unbiased associations between external factors, their sources, and their connection to biological perturbations (*3*), the paths to discovery become widened.

Several examples illuminate the promise that exposomics can bring to tackling a broader spectrum of challenges. High-resolution mass spectrometry–based analysis of small molecules identified the nutrient precursor trimethylamine *N*-oxide—a plasma metabolite that enhances thrombosis and is linked to cardiovascular disease (*9*). Related approaches have identified chlorinated metabolites associated with renal carcinoma in the blood of workers exposed to trichloroethylene (*10*). Exposure to pesticides has been connected to altered metabolic pathways in primary sclerosing cholangitis, a complex bile duct disorder (*11*). Geospatial science helped link exposures to particulate matter in the air with a diameter of 2.5 micrometers with biological processes in Alzheimer's disease by using residential address history (*12*). In addition, exposomics approaches extend the research beyond cohort and population studies. The value of deep exposome phenotyping, demonstrated in individuals, elucidated a range of health conditions and the notable gap in knowledge that exists between human exposures and health outcomes. For example, intensive personal monitoring revealed the dynamic nature of chemical and microbial exposures (*13*). A population-scale effort that examined a large database of health insurance claims involving twins discerned both genetic and environmental contributions to more than 500 disease phenotypes (*14*).

How can the field move forward? Several areas deserve attention. Improved measurement and data systems will be essential for exposomics to progress beyond small-scale and candidate studies to become more widely adopted. Increasingly sensitive technologies to interrogate exposure mechanisms and cascading biological responses are needed—lessons learned during the rise of genomics. Fortunately, many of the tools are familiar, and the types of data that come from exposomics are like those from related mass spectrometry–based methods (e.g., metabolomics or proteomics) or resemble geospatial features used in spatial epidemiology.

Efforts are also needed to develop biomedical measurement technologies (for biospecimens and environmental samples) and strategies for combining them with other omic technologies and studies to evaluate their use at the point of care. Another goal is to establish new methods to monitor or estimate individual-level exposures over the life course that can be applied in research, public health, and clinical applications. Creating a human exposome reference using systematic and spatially resolved characterization of exposures in biological systems through life spans would enable analysis and contextualization at the population scale to support epidemiological research and policy decisions. Developing wearable or minimally invasive tools that measure an individual's exposome and strategies for commoditization would be a catalyst for research. And creating a framework for the standardization and harmonization of language, protocols, data collection, and large-scale and high-throughput analysis methods is needed. Quality control and quality assurance will maximize the value of data in a FAIR (findable, accessible, interoperable, and reusable) format. This framework would facilitate the application of machine learning and artificial intelligence to analyze the complex datasets from exposome studies.

As these initiatives are pursued, several high-reward but high-risk research avenues currently exist. Exposomics will complement pharmacogenomics by answering

[1]Columbia University, New York, NY, USA. Banbury Exposomics Consortium members and affiliations are listed in the Acknowledgments. Email: gm2815@cumc.columbia.edu

how combined environmental exposures and dietary factors alter drug metabolism and efficacy. Translational cancer research and clinical trials will benefit from the systematic evaluation of environmental factors on initiation, progression, metastasis, and response to therapy. In addition, its application will provide powerful approaches for identifying nongenetic drivers of health disparities and enhancing occupational health and safety by linking known work-related exposures to disruption of biological pathways and by identifying currently unknown exposures.

All large-scale studies of human disease, whether they are cohort, clinical, or biobank, could incorporate exposomics (*1*). Even if research teams lack expertise in exposomics, merely collecting extra aliquots of blood or geospatial information for future analysis can preserve potential knowledge and enhance reuse of cohort data samples. Moreover, performing exposomics on a population scale will allow the creation of exposure that combines individual-level measures using humans as sentinels with geospatial data from monitoring systems. Such approaches would empower policymakers to make data-driven decisions for mitigation and prevention. It should be noted that improvements in exposomics have been uneven, with more attention paid to chemical exposures and less to social and physical influences. For humans, environmental exposures are undoubtedly associated with social determinants of health, and policy implications are therefore far-reaching.

Exposomics allows researchers to reframe studies from a reactive approach to a predictive and preemptive one. However, this requires attention to the ethical, legal, and social aspects of its use across many sectors (*15*). Issues such as data ownership and privacy, the effects of disparate exposures among socioeconomic groups, and uneven access to healthy environments need to be addressed. In addition, clear guidelines for returning results to study participants must be developed. Inclusion of actionable steps to improve health will help to establish public trust in exposomics studies and outcomes.

The interdisciplinarity that underlies exposomics requires investigators to cultivate a collaborative culture to solve major environmental and societal challenges. This includes engaging with community members who have often been research participants but not directly involved in the planning, formulation, and implementation process. The recently established coordinating centers for exposomics in the United States and Europe provide the foundation to foster the required global collaboration, establish best practices, support data harmonization, and train the next generation in the collaborative skills essential for success.

Human phenotype is determined by the dynamic combination of genetic and environmental factors, with stochastic events adding uncertainty on both sides independently and at the interaction level. Gaps in understanding human health and disease can be filled by integrating exposomics into the biomedical enterprise. Life exists at the interface of genetically encoded processes and environmentally driven realities. So too should the biomedical enterprise that studies it. ■

REFERENCES AND NOTES

1. C. P. Wild, *Cancer Epidemiol. Biomarkers Prev.* **14**, 1847 (2005).
2. R. Vermeulen, E. L. Schymanski, A.-L. Barabási, G. W. Miller, *Science* **367**, 392 (2020).
3. M. K. Chung *et al.*, *Environ. Health Perspect.* **129**, 85001 (2021).
4. Banbury Center, Report from the Integrating Exposomics into the Biomedical Enterprise Banbury Conference (2024); https://www.cshl.edu/banbury/meeting-reports/.
5. Cancer Grand Challenges (2024); https://cancergrandchallenges.org/.
6. A. P. Tamiz, W. J. Koroshetz, N. T. Dhruv, D. A. Jett, *Neuron* **110**, 1286 (2022).
7. Y. He *et al.*, *Nat. Commun.* **14**, 8297 (2023).
8. Y. He *et al.*, *Diabetes Care* **44**, 935 (2021).
9. X. S. Li *et al.*, *JCI Insight* **3**, e99096 (2018).
10. D. I. Walker *et al.*, *Int. J. Epidemiol.* **45**, 1517 (2016).
11. D. I. Walker *et al.*, *Hepatol. Commun.* **6**, 965 (2022).
12. V. Kalia *et al.*, *J. Alzheimers Dis.* **96**, 1025 (2023).
13. C. Jiang *et al.*, *Cell* **175**, 277 (2018).
14. C. M. Lakhani *et al.*, *Nat. Genet.* **51**, 327 (2019).
15. C. W. Safarlou, K. R. Jongsma, R. Vermeulen, A. L. Bredenoord, *Exposome* **3**, osad004 (2023).

ACKNOWLEDGMENTS

Participants of the Banbury Conference on Integrating Exposomics into the Biomedical Enterprise (3 to 6 December 2023, https://www.cshl.edu/banbury/meeting-reports/) included: Gary W. Miller[1], L. Michelle Bennett[2], David Balshaw[3], Robert Barouki[4], Gurdane Bhutani[5], Dana Dolinoy[6], Peng Gao[7]†, David Jett[8], Margaret Karagas[9], Jana Klánová[10], Pamela Lein[11], Shuzhao Li[12], Thomas O. Metz[13], Chirag J. Patel[14], Krystal Pollitt[15], Arcot Rajasekar[16], Fenna Sillé[17], Anne Thessen[18]‡, Sophie Thuault-Restituito[1], Roel Vermeulen[19], Cavin K. Ward-Caviness[20], Robert Wright[21]. [1]Columbia University, New York, NY, USA. [2]L.M. Bennett Consulting, LLC, Potomac, MD, USA. [3]US National Institute of Environmental Health Sciences (NIEHS), Research Triangle Park, NC, USA. [4]Inserm, Paris Cedex 13, France. [5]MBX Capital, New York, NY, USA. [6]University of Michigan, Ann Arbor, MI, USA. [7]University of Pittsburgh, Pittsburgh, PA, USA. [8]National Institute of Neurological Disorders and Stroke, Bethesda, MD, USA. [9]Dartmouth College, Hanover, NH, USA. [10]Masaryk University, Brno, Czechia. [11]University of California, Davis, Davis, CA, USA. [12]The Jackson Laboratory, Bar Harbor, ME, USA. [13]Pacific Northwest National Laboratory, Richland, WA, USA. [14]Harvard University, Cambridge, MA, USA. [15]Yale University, New Haven, CT, USA. [16]University of North Carolina at Chapel Hill, Chapel Hill, NC, USA. [17]Johns Hopkins University, Baltimore, MD, USA. [18]University of Colorado Anschutz, Aurora, CO, USA. [19]Utrecht University, Utrecht, Netherlands. [20]US Environmental Protection Agency (EPA), Washington, DC, USA. [21]Icahn School of Medicine at Mount Sinai, New York, NY, USA. †Present address: Harvard University, Cambridge, MA, USA. ‡Present address: University of North Carolina at Chapel Hill, Chapel Hill, NC, USA. This commentary does not necessarily represent the views or policies of the US EPA or the US NIEHS.

10.1126/science.adr0544

CANCER

Epo-calypse now

Blocking erythropoietin receptor signaling in macrophages promotes antitumor immunity

By **Sana M. Arnouk**[1,2] *and* **Jo A. Van Ginderachter**[1,2]

Cancer cells arise through mutational events, which lead to the appearance of altered proteins that can be recognized by tumor-reactive T cells. To kill cancer cells, T cells need to infiltrate the tumor microenvironment (TME), yet many solid tumors lack immune cells and are therefore categorized as immune excluded, immune desert, or more broadly as "noninflamed" (*1*). On page 376 of this issue, Chiu *et al.* (*2*) report that the hormone erythropoietin (EPO) is a central driver of the noninflamed TME in hepatocellular carcinoma tumors through its direct effect on tumor-associated macrophages (TAMs) that express the EPO receptor. Consequently, these macrophages adopt an immunoregulatory phenotype, promoting the infiltration of immunosuppressive cell types such as regulatory T cells (T_{reg} cells), while decreasing the intratumoral abundance of cytotoxic T cells. These findings elucidate factors contributing to a noninflamed TME and may inspire new therapeutic avenues to optimize antitumor immunity.

To better understand the drivers of the nonpermissive TME in hepatocellular carcinoma, Chiu *et al.* established murine models of the cancer that recapitulate the inflamed and noninflamed subtypes seen in humans. This revealed that EPO was only increased in the plasma of mice bearing noninflamed tumors. The clinical relevance of this finding was corroborated in patients with hepatocellular, colorectal, or breast cancer, with increased EPO amounts correlating with a poorer disease prognosis.

To confirm the role of EPO in promoting a noninflamed TME, Chiu *et al.* deleted the *Epo* gene in noninflamed tumors in mice using gene editing. This largely shifted the TME

[1]Lab of Cellular and Molecular Immunology, Brussels Center for Immunology, Vrije Universiteit Brussel, Brussels, Belgium. [2]Myeloid Cell Immunology Laboratory, VIB Center for Inflammation Research, Brussels, Belgium. Email: jo.van.ginderachter@vub.be

toward an inflamed phenotype with infiltrating cytotoxic T cells, resulting in reduced tumor growth. Conversely, overexpression of *Epo* in a mouse model of spontaneously regressing hepatocellular carcinoma supported tumor progression. This was associated with a notable increase in T_{reg} cells, which has been linked with tumor promotion. These findings agree with other studies (*3, 4*) that point to an immunomodulatory and T_{reg} cell–expanding potential of systemically administered high doses of EPO. However, although EPO is best known as an erythropoietic hormone produced primarily by the kidney, Chiu *et al.* show that the intratumoral production of EPO is sufficient to render the local environment more immunosuppressive.

Chiu *et al.* further discovered that the main cells expressing the EPO receptor in the murine hepatocellular carcinoma environment are monocyte-derived macrophages, including both Kupffer cell–like macrophages and non–Kupffer cell subtypes. In patients with hepatocellular carcinoma, TAMs expressing the EPO receptor were also found, which were like previously described immunoregulatory Kupffer cell–like macrophages with a tolerogenic, anti-inflammatory phenotype (*5*), suggesting similar functions within the hepatocellular carcinoma environment.

The functions of liver macrophages are strongly instructed by niche cells through continuous intercellular interactions and microenvironmental cues (*6*). Although the identity of the niche for TAMs expressing the EPO receptor within the TME is currently unknown, Chiu *et al.* identified EPO as a nonredundant environmental trigger for these cells and showed that macrophages mediate the effects of EPO. For example, the induction of tumor development in mice lacking the EPO receptor specifically in cells bearing the carbohydrate-binding domain lysin motif (LysM), which includes macrophages, caused almost half of the mice to reject tumors, an effect that was dependent on cytotoxic T cells. Furthermore, early activated and effector memory cytotoxic T cells were predominant in these tumors, promoting antitumor immunity.

These findings suggest that the increase in T_{reg} cells due to EPO signaling must be an indirect effect mediated by EPO receptor–expressing macrophages (see the figure). Evidence that macrophages function as indispensable intermediary cells for the T_{reg} cell–promoting activity of EPO has been provided in other disease settings, such as allograft survival (*7, 8*) and asthma (*9*), suggesting a potentially more universal phenomenon. However, how macrophages harness EPO receptor signaling to boost T_{reg} cell activity remains unclear. Chiu *et al* identified NRF2 (nuclear factor erythroid 2–related factor 2) as an important transcription factor downstream of the EPO receptor, as its deficiency in LysM-bearing cells failed to generate an immunosuppressive TME when EPO was overexpressed. NRF2 strongly increased the expression of heme oxygenase–1, an enzyme that degrades heme and produces CO and biliverdin, all of which have been reported as anti-inflammatory (*10*), but a direct link with T_{reg} cell activation is not clear. Alternatively, EPO receptor signaling in macrophages can stimulate the transcription factors CCAAT-enhancer-binding protein β and peroxisome proliferator–activated receptor γ, which are important for the efficient clearance of apoptotic (dying) cells (*11*) and the stimulation of anti-inflammatory macrophages (*12*), creating conditions that are likely permissive for T_{reg} cell activation.

Erythropoietin signaling modulates the tumor microenvironment

In hepatocellular carcinoma, erythropoietin (EPO) produced by tumor cells instructs tumor-associated macrophages expressing the EPO receptor to take on an immunoregulatory phenotype, expanding the presence of suppressive regulatory T cells (T_{reg} cells) and inhibiting the activation of effector memory T cells.

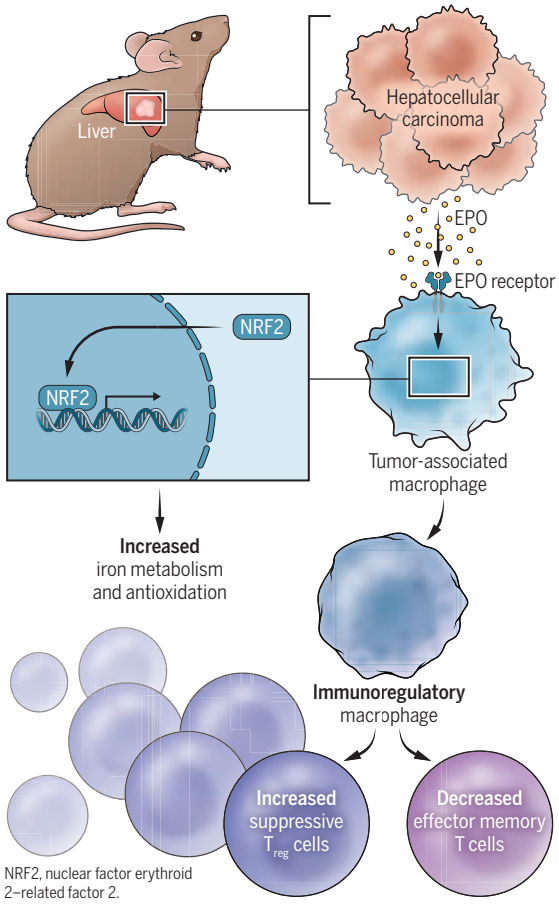

NRF2, nuclear factor erythroid 2–related factor 2.

GRAPHIC: N. BURGESS/*SCIENCE*

The identification of EPO receptor signaling in TAMs as an important modulator of an immunosuppressive TME may have implications for cancer therapy. For example, Chiu *et al.* observed substantial tumor regression in mice upon administering liposomes loaded with small interfering RNAs that block expression of the EPO receptor. These liposomes were predominantly taken up by macrophages, although they were not designed for that purpose. Hence, specific macrophage targeting could be optimized, potentially by using lipid nanoparticles, whose lipid composition and incorporation of macrophage-targeting molecules can direct these vehicles to desired cells (*13, 14*). An alternative therapeutic approach may be the use of recombinant EPO receptor-Fc chimeric proteins to neutralize EPO. This is likely to activate effector memory T cells and remove immunosuppression. Such neutralization could synergize with immune checkpoint inhibitors that remove the immune response brakes in T cells. The combination could boost T cell antitumor activity. Indeed, Chiu *et al.* showed that a recombinant EPO receptor-Fc protein sensitized hepatocellular carcinoma to an immune checkpoint inhibitor in mice. However, given the critical role of EPO in regulating erythropoiesis, it is essential to thoroughly evaluate potential adverse effects of the systemic inhibition of EPO in humans, such as anemia. Future work may also explore strategies for the targeted delivery of the EPO receptor-Fc chimeric proteins to the TME. Regardless of the strategy used, blocking EPO-EPO receptor signaling offers a promising approach to modulate nonpermissive TMEs and tackle tumors that are unresponsive to immune checkpoint blockade, which may improve therapeutic success across various cancer types. ■

REFERENCES AND NOTES

1. G. T. Clifton *et al.*, *J. Immunother. Cancer* **11**, e006773 (2023).
2. D. K.-C. Chiu *et al.*, *Science* **388**, eadr3026 (2025).
3. S. Bessoles *et al.*, *Immunology* **173**, 360 (2024).
4. E. McEachern *et al.*, *J. Autoimmun.* **119**, 102629 (2021).
5. N. Aizarani *et al.*, *Nature* **572**, 199 (2019).
6. M. Guilliams *et al.*, *Cell* **185**, 379 (2022).
7. C. Purroy *et al.*, *J. Am. Soc. Nephrol.* **28**, 2377 (2017).
8. J. K. Horwitz *et al.*, *JCI Insight* **7**, e158856 (2022).
9. G. Wan, B. Wei, *Am. J. Transl. Res.* **7**, 2305 (2015).
10. S. W. Ryter, *Antioxidants* **11**, 555 (2022).
11. B. Luo *et al.*, *Immunity* **44**, 287 (2016).
12. M. Kiss, Z. Czimmerer, L. Nagy, *J. Allergy Clin. Immunol.* **132**, 264 (2013).
13. Q. Fei *et al.*, *ACS Nano* **17**, 16539 (2023).
14. W. Chen *et al.*, *Nat. Rev. Cardiol.* **19**, 228 (2022).

10.1126/science.adx3810

CELL BIOLOGY

The cellular basis for middle-age spread

Age-specific adipocyte progenitors drive visceral adipose tissue expansion in middle age

By **Yong Geun Jeon** and **Jae Bum Kim**

Body fat in humans tends to increase in middle age (approximately 40 to 65 years old), with a preferential expansion of visceral adipose tissue (VAT) around internal organs in the abdominal cavity rather than subcutaneous adipose tissue (SAT) that is stored just beneath the skin (*1*, *2*). This increase in VAT-selective deposits is linked to declines in insulin sensitivity and a heightened risk of metabolic diseases (*3*). Total energy expenditure in humans remains relatively stable from ages 20 to 60 years old (*4*). However, if caloric expenditure is roughly constant, it is unclear how VAT continues to grow with age. On page 378 of this issue, Wang *et al.* (*5*) report that a population of adipocyte progenitor cells (APCs) emerges in middle-aged VAT that drives adipogenesis. This APC subpopulation exhibits a high potential for differentiation into adipocytes, which suggests that adipose tissue in middle age is biologically primed for spread.

Gain of VAT during middle age is of particular concern because it is more strongly associated with metabolic diseases than SAT accumulation (*6*, *7*). Similarly, VAT increase is observed in 12-month-old mice (the equivalent of human middle age), whereas SAT mass remains relatively unchanged (*8*). There are two distinct processes by which adipose tissue increases in size: through the enlargement of existing adipocytes (hypertrophy) and through the formation of new adipocytes from APCs (hyperplasia). Distinguishing these two processes is crucial for understanding the cellular origin or origins of age-driven VAT accumulation. To address this, Wang *et al.* performed elegant cell lineage–tracing experiments by introducing labels to distinguish preexisting adipocytes from newly generated ones. This allowed the authors to track the fates of APCs and adipocytes in young and middle-aged mice. Middle-aged VAT expansion was supported primarily by enhanced differentiation of APCs into new adipocytes, rather than from the enlargement of preexisting adipocytes. Furthermore, middle-aged APCs exhibited a shift toward greater adipogenic and proliferative capacity than their younger counterparts.

Single-cell studies have highlighted the heterogeneity within APC populations, which include multipotent stem cells and committed preadipocytes (CPs) (*9*, *10*). To characterize the population of age-driven APCs, Wang *et al.* performed single-cell RNA sequencing analysis on APCs isolated from young and middle-aged mice. They identified a previously uncharacterized subpopulation of CPs that are highly enriched in middle-aged VAT. Compared with CPs in younger subjects, these age-specific CPs (CP-As) display great capacity for proliferation and differentiation. Furthermore, Wang *et al.* used a range of genetic and pharmacological tools to demonstrate that the activity of a signaling pathway involving leukemia inhibitory factor receptor (LIFR) and signal transducer and activator of transcription 3 (STAT3) is enriched in CP-As, increasing adipogenic activity.

The discovery of CP-As provides a vital clue to understanding the mechanisms governing age-related shifts in VAT mass. In young adults, VAT expansion primarily occurs through hypertrophy rather than hyperplasia, with minimal contribution from progenitor differentiation (*11*). By contrast, Wang *et al.* found that in middle age, VAT expansion is driven by differentiation of CP-As. The adipogenic potential of VAT is transient and declines in late age (18-month-old mice), with a decrease in CP-As. Adipogenesis therefore exhibits notable plasticity, with an inverted U–shaped trajectory: relatively quiescent in early life, hyperplastic in middle age, and progressively exhausted in late age.

The findings of Wang *et al.* raise an intriguing question: What are the spatial (VAT-specific) and temporal (middle-aged) factors that enhance middle age–related adipogenesis? Investigating VAT-specific anatomical features (*3*), cell-type composition (*12*), and molecular properties of APCs (*7*) that constitute the microenvironment of VAT will be important for defining the spatial factors that influence adipogenesis. From a temporal perspective, could there be an "adipose tissue clock"? Elucidating whether temporal adipogenesis activation is bolstered by external adipose tissue stimuli (*13*), cell-to-cell communication within adipose tissue (*5*, *14*), or inherent characteristics of aged APCs (*15*) will be crucial for better understanding the biology of adipose tissue during aging.

The study of Wang *et al.* also points to a new potential framework for treating age-related adiposity in the clinic. The finding that CP-As use LIFR-STAT3 signaling indicates that this pathway could be therapeutically targeted to prevent excessive VAT accumulation before it leads to metabolic disease. Important in this regard, Wang *et al.* demonstrate that VAT from middle-aged humans also contains a CP-A population that expresses LIFR. Nonetheless, demonstrating that adipogenesis is more active in middle-aged humans remains a key challenge in adipose tissue research. Addressing this will require large-scale cohort studies and integrative single-cell analyses to elucidate the heterogeneity of APCs and adipocytes. These efforts will help identify the molecular signatures of differentiating adipocytes and the features of adipocyte differentiation in vivo. Ultimately, elucidating cellular and molecular characteristics of human adipogenesis could lead to breakthrough approaches for preventing and treating middle-aged obesity and metabolic diseases. ■

National Leader Research Initiatives Center for Adipocyte Structure and Function, Institute of Molecular Biology and Genetics, School of Biological Sciences, Seoul National University, Seoul, South Korea. Email: jaebkim@snu.ac.kr

REFERENCES AND NOTES

1. S. S. Guo, C. Zeller, W. C. Chumlea, R. M. Siervogel, *Am. J. Clin. Nutr.* **70**, 405 (1999).
2. A. K. Palmer, J. L. Kirkland, *Exp. Gerontol.* **86**, 97 (2016).
3. A. Sakers, M. K. De Siqueira, P. Seale, C. J. Villanueva, *Cell* **185**, 419 (2022).
4. H. Pontzer *et al.*, *Science* **373**, 808 (2021).
5. G. Wang *et al.*, *Science* **388**, eadj0430 (2025).
6. S. R. Preis *et al.*, *Obesity* **18**, 2191 (2010).
7. I. Hwang *et al.*, *Proc. Natl. Acad. Sci. U.S.A.* **116**, 11936 (2019).
8. J. Park *et al.*, *Nat. Metab.* **4**, 918 (2022).
9. S. Lecoutre *et al.*, *Nat. Rev. Endocrinol.* **21**, 272 (2025).
10. H. Nahmgoong *et al.*, *Cell Metab.* **34**, 458 (2022).
11. Q. A. Wang, C. Tao, R. K. Gupta, P. E. Scherer, *Nat. Med.* **19**, 1338 (2013).
12. M. P. Emont *et al.*, *Nature* **603**, 926 (2022).
13. J. Tang *et al.*, *Nat. Metab.* **7**, 166 (2025).
14. N. Schaum *et al.*, *Nature* **583**, 596 (2020).
15. A. Krtolica, S. Parrinello, S. Lockett, P. Y. Desprez, J. Campisi, *Proc. Natl. Acad. Sci. U.S.A.* **98**, 12072 (2001).

ACKNOWLEDGMENTS

The authors thank N. Hahn for comments and acknowledge support from the National Research Foundation of Korea (RS-2020-NR049402 and RS-2023-00218616 to J.B.K.; RS-2022-NR072211 to J.Y.G.).

10.1126/science.adx1198

CHEMISTRY

Reimagining silicone's life cycle

Synchronized catalysis breaks down silicone polymer waste into starting monomers

By **Koushik Ghosh**

Annual global production of silicone—a synthetic polymer with a long chain of silicon and oxygen atoms—exceeds 2.6 million metric tons (*1*). Its manufacturing is anchored in energy-intensive processes. More than 70% of silicone's carbon footprint stems from elemental silicon production from raw minerals (*2*). Compounding this issue, postconsumer silicone waste often ends up in landfills or is incinerated (*3*). Because of the strong silicon-oxygen bond and many additives such as organic fillers and catalysts in its formulation, decomposition of silicone into smaller molecules is challenging. On page 392 of this issue, Vũ *et al.* (*4*) report a method that breaks down postconsumer and industrial silicone waste from a cross-linked network into chlorosilane, which is a key intermediate molecule in silicone production. This depolymerization chemistry could potentially be used in large-scale silicone manufacturing processes.

Quartz, a mineral that is critical to elemental silicon production, faces increasing pressure for mining because of the growing demand for silicon in the electronics, solar panel, and construction industries (*5*). Silicon is extracted from mined quartz by energy-intensive metallurgical processes. This is followed by the Müller-Rochow process, which performs a copper-catalyzed reaction to produce chlorosilane. This method supplies 90% of silicone precursors but suffers from inefficiencies rooted in mid–20th century chemistry (*6*). For example, the energy-intensive method requires a temperature of 300°C and produces a silicon-copper alloy by-product from catalyst degradation as well as waste containing heavy metal and chlorinated hydrocarbon that harm the environment. Silicone recycling could solve these issues by conserving the already strained natural resources and minimizing energy consumption.

Vũ *et al.* introduce a chemistry that depolymerizes silicone waste into chlorosilanes by using gallium chloride and boron trichloride (see the figure). Performing this reaction in a solvent at 40°C for 2 hours transformed the strong silicon-oxygen bond in silicone to a silicon-chlorine bond, thereby breaking up the long polymeric chain. This produced quantitative amounts (nearly 97% yields) of dimethyldichlorosilane with a level of purity that is required for use in the petrochemical industry. Conventional recycling chemistries generate large molecules called siloxanes with closed, ring-like structures (*7*, *8*) that require further breakdown to produce chlorosilanes. By contrast, the method of Vũ *et al.* produces this key intermediate molecule in a single reaction. This simple chemistry allows for the reintegration of the recycled chlorosilanes into the existing manufacturing process, which could potentially bypass energy-intensive metallurgical processes and the Müller-Rochow process for silicone production.

Vũ *et al.* examined the mechanism underlying the synergistic action of boron trichloride and gallium chloride to overcome the thermodynamic barrier of exchanging a silicon-oxygen bond with a silicon-chlorine bond. Calculations showed that gallium chloride alone cannot lower the activation energy, but adding boron trichloride made the reaction thermodynamically favorable. The authors showed that the high affinity of boron to oxygen reduces the energy barrier by weakening the silicon-oxygen bond, whereas gallium chloride enhances the reaction rate. This synergy facilitates chlorine transfer from boron to silicone, promoting efficient formation of chlorosilane. In addition, Vũ *et al.* demonstrated that the carcinogenic solvent (dichloromethane) used in the reaction can be replaced with a less hazardous alternative. Performing the reaction in toluene produced a quantitative amount of chlorosilane at 90°C. Other solvents, which are known to increase the volume of cross-linked silicone networks, promoted effective diffusion of catalysts to achieve a good yield with a slightly longer reaction time. These findings highlight the feasibility of transitioning to environmentally friendly solvents without compromising efficiency.

What is needed to move the reaction of Vũ *et al.* to industry? Gallium is a critical metal that suffers from scarcity. Developing a closed-loop recovery system for used gallium chloride could address this issue. In addition, testing the robustness of the reaction in a complex mixed-waste stream is needed to expand its application. Rigorous life-cycle analyses and carbon footprint assessments are also essential to confirm the projected environmental benefits that come from prioritizing the use of chlorosilane instead of producing silicone from quartz. Incentivizing manufacturers through circular economy metrics could ensure that recycled chlorosilanes are valued equally as raw materials. ■

Silicone recycling

Silicone production from raw materials involves energy-intensive processes. Synergistic catalysis of boron trichloride (BCl_3) and gallium chloride ($GaCl_3$) can overcome the thermodynamic barrier to break strong silicon-oxygen bonds, resulting in chlorosilane intermediates that are used to produce silicone.

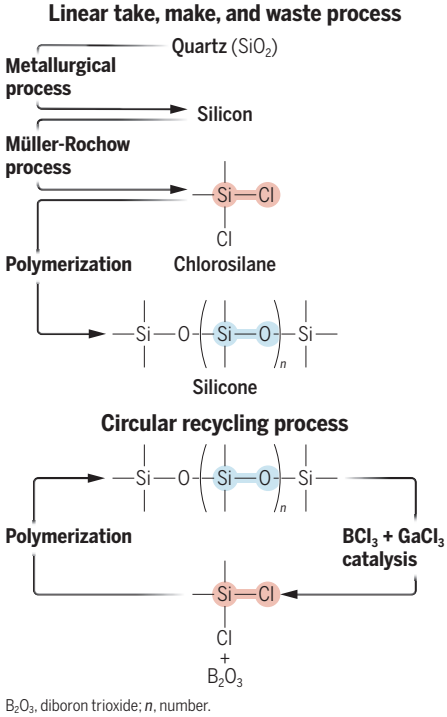

B_2O_3, diboron trioxide; *n*, number.

GRAPHIC: A. FISHER/*SCIENCE*

Sandia National Laboratories, Albuquerque, NM, USA.
Email: kghosh@sandia.gov

REFERENCES AND NOTES

1. Freedonia Group, "Global silicones" (Freedonia Group, 2024); https://www.freedoniagroup.com/industry-study/global-silicones.
2. Global Silicone Council, "Silicone research: An industry commitment" (Global Silicone Council, 2017); https://globalsilicones.org/resources.
3. A. T. Wolf, A. Stammer, *Polymers* **16**, 2220 (2024).
4. N. Đ. Vũ *et al.*, *Science* **388**, 392 (2025).
5. H. Mirletz, S. Ovaitt, S. Sridhar, T. M. Barnes, *PLOS ONE* **17**, e0274351 (2022).
6. Y. Zhang *et al.*, *ChemCatChem* **11**, 2757 (2019).
7. B. Rupasinghe, J. C. Furgal, *Polym. Int.* **71**, 521 (2022).
8. M. J. Warner *et al.*, *Chem. Commun.* **60**, 1188 (2024).

ACKNOWLEDGMENTS

The author thanks J. Grey for helpful discussions and support from the Laboratory Directed Research and Development program at Sandia National Laboratories, which is managed and operated by National Technology and Engineering Solutions of Sandia, LLC, a wholly owned subsidiary of Honeywell International, Inc.; and the US Department of Energy's National Nuclear Security Administration under contract DE-NA-0003525.

10.1126/science.adx1728

POLICY FORUM

SCIENCE AND POLICY-MAKING

Partisan disparities in the use of science in policy

Documents from Congress and think tanks reflect differences in how science is cited

By **Alexander C. Furnas**[1,2,3,4], **Timothy M. LaPira**[5], **Dashun Wang**[1,2,3,4,6]

Science has long been regarded as essential to policy-making, serving as one of the primary sources of evidence that informs decisions (*1, 2*) with its particular epistemic authority (*3*). Its role has become especially vital, as many pressing societal challenges today—from climate change to public health crises to technological advancement—are intricately linked with scientific progress. However, amid rising political polarization (*4*), a fundamental question remains open: Is science used differently by policy-makers in different parties? Here we combine two large-scale databases capturing policy, science, and their interactions to examine the partisan differences in citing science in policy-making in the United States. Overall, we observe systematic differences in the amount, content, and character of science cited in policy by partisan factions in the United States. These differences are strikingly persistent across fields of research, policy issues, time, and institutional contexts.

Understanding any potential partisan differences in the application of science to policy-making is not only of great interest to the scientific community itself, probing the role and impact of science in shaping societal outcomes, but also crucial for understanding the integrity and effectiveness of the policy-making process, promoting evidence-based decision-making (*1*), upholding public trust in science, and fostering bipartisan cooperation [see supplementary materials (SM) 18].

Our first dataset comes from Overton (*5*) and tracks 641,894 policy documents published by both the federal government and think tanks in the United States from 1995 to 2021, as well as the scientific papers and other policy documents referenced therein (see SM 1.1). There has been long-standing interest in quantifying the use of science in policy, and recent work suggests that Overton currently offers the most comprehensive tracking of policy documents and their citations to scientific papers (*2*) (see SM 1.1). We focus on the complete set of all congressional committee reports since 1995 and committee hearings since 2001 (n = 49,345), in addition to the 191,118 policy documents published by 121 US-based ideological think tanks after 1999 (see SM 4). We further match the scientific references (n = 424,199) in these policy documents to our second dataset, Dimensions (*6*), a large-scale publication and citation database that captures 122 million scientific publications across all disciplines. Dimensions offers us paper-level covariates for cited science, including the publication date, scientific citation counts, field- and year-normalized measures of scientific impact [e.g., hit paper and field citation ratio (FCR, reflecting citations of a paper relative to average citations of papers in the same field)], field of research labels, and whether a paper is a preprint. Linking these two databases gives us an opportunity to examine the partisan differences in the use of science in policy.

The predicted percent of policy documents that include at least one scientific reference in our data corpus is plotted here from mixed effects logistic regression models (see the first figure, left panel, and SM 7 for details). Policy citations of science have increased steadily over the 25-year period, growing from less than 20% in 1995 to >35% in 2020, with the increase being especially pronounced among think tank documents (see SM 7 and fig. S2). Yet, as we show next, this growth masks systematic partisan differences in policy citations of science.

To understand partisan differences in the propensity to cite science, we first focus on policy documents produced by congressional committees, with granular measures of political control at the committee level (see SM 1.1). These documents include reports and committee meeting documents, which primarily consist of hearing transcripts and prepared witness statements. Committees, often seen as the institutional workhorses of Congress, play an important role in information gathering, but are also a site of partisan competition to frame issues, making them well suited to study partisan uses of science (see SM 18). We calculate the probability of a committee policy document citing science separately for Republican- and Democratic-controlled committees. Although both have increased their use of science over time, the growth patterns differ depending on which party is in control (see the first figure, middle panel). Estimating the overall partisan differences with year and committee fixed effects, we find that policy documents from Democratic-controlled committees are nearly 1.8 times more likely to cite science than those from Republican-controlled committees (see SM 8 and table S9). These results are robust when accounting for indicator variables for chamber, document type, and whether there is a copartisan president. We find that this effect is most pronounced in the House and in committee meeting documents and does not vary by committee versus subcommittee status (see SM 8).

To further validate our findings, we estimate this effect using changes in party at the committee level as a fixed-effects counterfactual estimator for difference-in-differences designs with heterogeneous treatment effects and treatment switching on a panel of 80 groups (committees) and 13 periods (Congresses). We find that committees that undergo a change from Republican to Democratic party control see an average increase of 196 additional citations to science per committee in the congressional term after the switch, an increase of 0.58 standard deviations. We find no equivalent effects in placebo tests of preceding Congresses or the Congress after a party switch occurs, supporting the identifying parallel trends assumption (see SM 10 for testing, discussion, and alternative estimators).

Although think tanks operate outside of government, many align with the ideological positions of the two major parties (*7*), allowing us to differentiate think tanks by this ideological alignment (see SM 4 for details regarding our coding procedure). These ide-

[1]Kellogg School of Management, Northwestern University, Evanston, IL, USA. [2]Center for Science of Science and Innovation, Northwestern University, Evanston, IL, USA. [3]Northwestern Innovation Institute, Northwestern University, Evanston, IL, USA. [4]Ryan Institute on Complexity, Northwestern University, Evanston, IL, USA. [5]Department of Political Science, James Madison University, Harrisonburg, VA, USA. [6]McCormick School of Engineering, Northwestern University, Evanston, IL, USA. Email: dashun.wang@northwestern.edu

ological think tanks serve as key resources for partisan policy-makers in extended party networks, providing "legislative subsidies" (information and support for policy-makers), setting agendas (*8*), and incubating policy alternatives. They are staffed by party operatives and researchers who frequently move back and forth between government, party, and campaign organizations (see SM 18). Focusing our analysis on think tanks that have a particular ideological bent allows us to better assess our primary question—differentiating the science-citing behavior of policy-makers with partisan or ideological commitments. However, it also excludes think tanks with centrist, ambiguous, bipartisan, or nonideological perspectives, thereby limiting our ability to make inferences about the entire think tank community.

mittees across 20 of the 23 scientific fields and 15 of the 17 issue areas, and left-of-center think tanks citing science more than right-of-center think tanks across all 23 scientific fields and 17 issue areas we study (see SM 8).

These systematic partisan differences that we observe raise an important next question: Do Democratic- and Republican-leaning policy-makers draw from the same science? To answer this question, we first assess the degree of overlap in the science cited, asking what fraction of all the science cited in policy documents was cited by both parties. We find that only 5 to 6% of scientific citations are shared by Republicans and Democrats (see the second figure). It is important to note, however, that this low degree of overlap is partly driven by single-cited papers, which by construction cannot be bipartisan.

(see the second figure). We further vary the threshold for the minimum number of policy citations for inclusion, to assess how bipartisan citation varies as science receives more attention from policy-makers. In Congress, only among the science that is most widely cited in policy—publications that have at least 14 policy citations (top 99.9th percentile of policy citations)—does the rate of observed bipartisan citation ever reach parity with the expectation that, if citation patterns were uncorrelated with partisanship, it would be cited at least once by both Republicans and Democrats (see the second figure, left panel). Even more starkly, among think tanks, at no point does the observed rate of bipartisan citation ever converge with the expected rate, even as we examine papers with increasingly greater policy citations. Instead, the rate of

The increasing use of science in policy documents over the past 25 years

The estimated share of US policy documents citing science at least once has grown (left). Documents are nearly 1.8 times more likely to cite science when from Democrat-controlled committees (center), and more than five times more likely when produced by left-leaning think tanks (right). See supplementary materials.

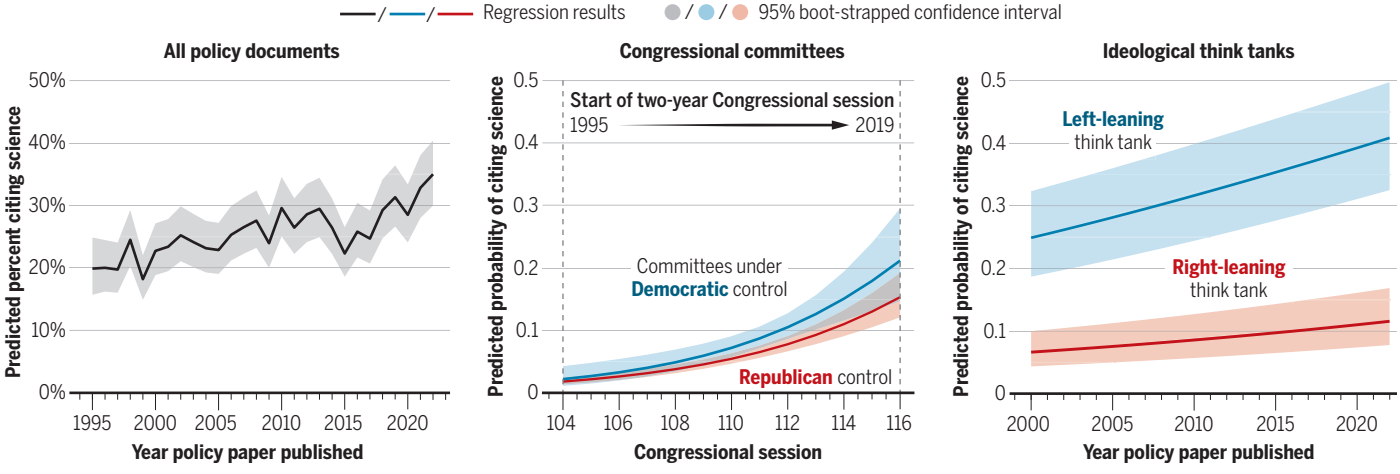

The predicted probability of a think tank policy document citing science for left- and right-leaning think tanks separately is estimated here by logistic regression with a linear time trend (see the first figure, right panel). Given that think tanks' ideological alignments are generally static, we address time-invariant unobserved heterogeneity at the unit level, using think tank random effects. We find that, overall, policy documents from left-leaning think tanks are more than five times as likely to cite science than those produced by right-leaning think tanks (see SM 8 and table S15), revealing an even starker partisan difference in the propensity to cite science among ideological think tanks than in the government.

Moreover, this observed tendency appears widespread across fields and policy issues, with Democratic committees citing science distinguishably more than Republican com-

To account for this, we construct an expected baseline for bipartisan citations using a permutation test that preserves the marginal distribution of citations by party and paper, to estimate what one might expect if citation patterns were uncorrelated with partisanship. Our estimate suggests that we would expect ~12 to 13% of papers with bipartisan engagement (see the second figure and SM 11). In other words, the expected level of bipartisan citation is more than double the level that is observed in the data.

To provide a more conservative test, we further restrict our analyses to papers that receive two or more policy citations—those that could potentially have been cited by both Democrats and Republicans. Under these conditions, we observe 31.1% bipartisan citation in Congress and 20.5% bipartisan citation from think tanks, compared to expected shares of 58.7% and 50.6%, respectively

overlap plateaus at less than 70% of the expected rate above at least 20 policy citations (see the second figure, right panel). Simply put, regardless of the measure we deploy, the policy citation of science appears to feature a low degree of bipartisan engagement with the scientific literature, with partisans consistently less likely to cite the same science.

Given the rising political polarization in the United States in recent years (*5*), we examine the temporal changes in the rate of bipartisan-cited science. We find that the degree of overlap has stayed rather stable over time (see SM 11 and figs. S13 to S16), suggesting that the low degree of bipartisan engagement with science is a long-standing but previously unknown feature of the US policy landscape. We further find that for both the US Congress and think tanks, this low degree of overlap is remarkably universal across scientific fields and policy issues (see SM 11 and figs. S17 and S18).

The fact that Republican and Democratic policy-makers rarely draw on the same scientific papers raises another important question: Do they cite substantively similar papers to inform their policy? To explore this, we assess the topical differences between the science they cite. Here we use deep-learning methods to represent scientific papers in a high-dimensional space. Specifically, we use SPECTER embeddings to represent each scientific article as a vector in a 768-dimensional space, allowing us to quantify the topic similarity between cited science (see SM 3). SPECTER is a transformer model trained on a large corpus of scientific text and citations.

Take, for example, the House Energy and Commerce Committee. We analyze the scientific papers cited by the committee reports in our embedding space, apply a clustering algorithm to group these cited papers, and visualize them in two dimensions using t-distributed stochastic neighbor embedding (t-SNE) (see SM 5). Clusters of science are shown cited by the committee under Democratic and Republican control, respectively (see the third figure). Although there are some common areas of focus, the two plots reveal many distinctive clusters of science drawn by the committee, depending on which party is in control. Under Democratic control, the committee is much more likely to cite science on abortion, drunk driving, youth and e-cigarettes, energy production and infrastructure, or violence, guns, and mental health (see the third figure, left panel). By contrast, under Republican control, the committee is much more likely to cite science about health care insurance costs, air pollution, opioids, or high-school athletic injuries, among other topics (see the third figure, right panel). Extended results, including a example of think tank documents on the topic of weather, are shown in SM 12 (see fig. S20). Of course, these differences may be driven by partisans' differing agendas and goals when in power, a point to which we will return later.

We find similar, systematic differences across nearly all congressional committees and all issue areas for ideological think tanks. The data consistently demonstrate that partisan factions draw from the different distributions of scientific topics (see SM 12 and fig. S20). Overall, the large partisan disparity that we observe appears rather universal across time, policy institutions, and issue areas.

Partisans are consistently less likely to cite the same science

Only among scientific publications cited at least 14 times in congressional committee documents does the rate of observed bipartisan citation ever reach parity with the expectation that, if citation patterns were uncorrelated with partisanship, the science would be cited at least once by both Republicans and Democrats (left). Among think tanks, at no point does the observed rate of bipartisan citation ever converge with the expected rate (right). See supplementary materials.

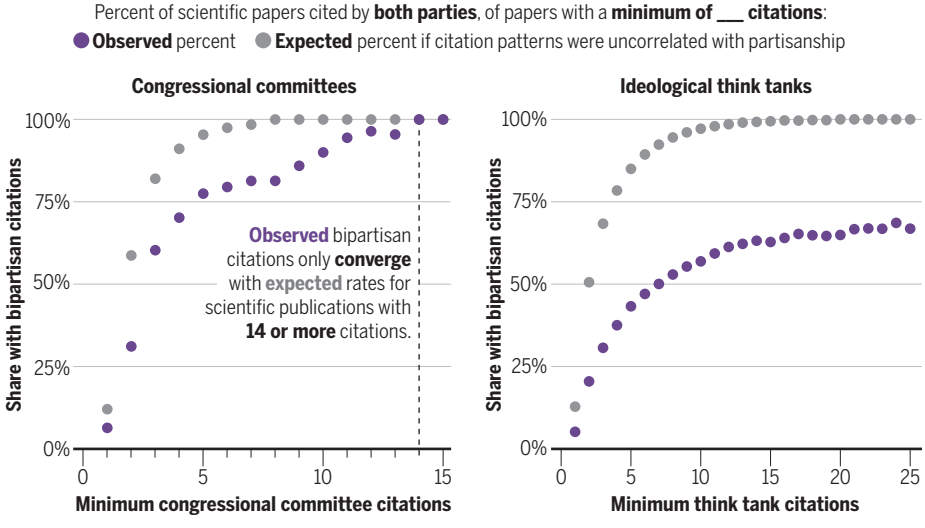

One explanation for these persistent partisan differences is that they may simply reflect the different policy focus and priorities between the two parties. Indeed, although science can serve as a common knowledge base to inform policy on critical issues facing society, partisans are known to have differing agendas (*8*). This discrepancy prompts us to perform tests that simulate the following thought experiment: If the two parties focus on the same policy, do they still differ in the science they cite?

To this end, we use GloVe embeddings to examine policy document titles and generate matched pairs of science-citing policy documents that are highly similar to each other (see SM 13.1). GloVe is a learning algorithm trained to obtain vector representations of words. We find that even when Democratic and Republican policy-makers produce policy documents with nearly identical titles, the overlap in cited science remains not only consistent with our findings above but also of a similar magnitude, with an overlap between ⅓ and ½ of the expectation from our permutation-based null model (see SM 11 and fig. S19).

To illustrate this, we explore an example of two matched minimum-wage policy documents, one by the left-of-center Urban Institute and one by the right-of-center Employment Policies Institute. The Urban Institute's policy document cites multiple papers about the distributional effects of minimum wage, whereas the one from the Employment Policies Institute cites science almost exclusively about the employment and labor supply effects of minimum wage increases. Indeed, although the two policy documents focus on the same issue, of the 62 papers they cite, only one is cited by both. When projecting these cited papers onto the SPECTER embedding space, the science cited by the left- and right-of-center think tanks is nearly perfectly separated. SM 13.1 presents this example (fig. S21A), as well as a similar example of two congressional hearings on paid family leave (fig. S21B).

We use a set of matched pairs of highly similar policy documents, like the minimum wage example discussed above, written by Democrats and Republicans—referred to as "out-partisan pairs"—to further test whether partisans cite different science when working on the same policy issues. We ask whether these out-partisan pairs cite science that is more different than that cited by comparable copartisan pairs (see SM 13.2 and figs. S23 and S24). Here we follow the same procedure described above to construct copartisan pairs of highly similar policy documents using GloVe embeddings of their titles, generating sets where both documents are produced by Democrats (Republicans) in Congress or left-of-center (right-of-center) think tanks. Our results indicate that in both congressional committee documents and ideological think tank documents, the copartisan documents cite science that is more similar to each other than the out-partisan pairs. These results are robust to regression analyses conditioning on dyadic policy document similarity (see SM 13.2 and tables S29 and S30). We reach the same conclusion by comparing the topical distributions of cited science (see SM 13.2 and fig. S22). We also use these matched pairs to test whether our earlier finding of large partisan differences in the rate of citing science can be explained by Democrats and Republi-

Partisan factions draw from different distributions of scientific topics

Many distinctive clusters of science are drawn upon by the House Energy and Commerce Committee, depending on which party is in control. SPECTER embeddings are used to represent each scientific article cited in policy documents as a vector in a 768-dimensional space (visualized here in two dimensions). See supplementary materials.

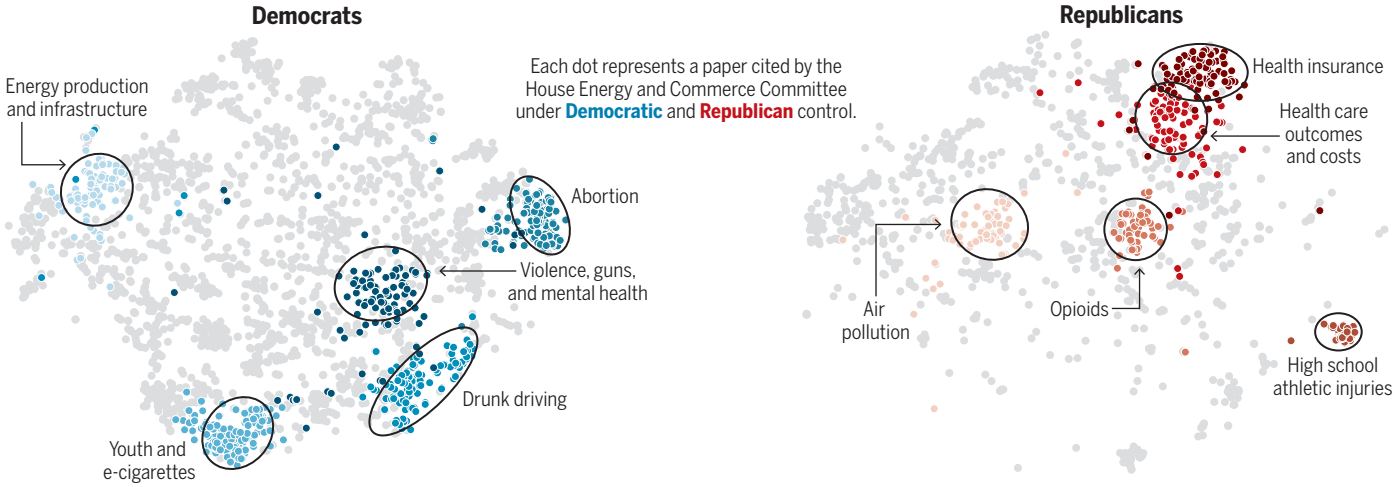

cans focusing on different issues. We confirm that policy documents written by Democrats consistently tend to cite more science than those produced by Republicans, even when accounting for differences in the issues they work on (see SM 13.3 and tables S27 and S28).

Overall, although differences in issues partisans work on may drive some of the observed differences in the sets of science that partisans cite, our results demonstrate that these differences alone do not fully account for the partisan differences in either content or volume of science cited in policy. Another explanation is that policy-makers are citing different science because they hold different positions on the same issues. The lack of overlap in the science they cite, however, implies that politicians and ideological think tanks are not considering all the relevant science to a particular policy. Evidence-based policy-making in its idealized form synthesizes all relevant arguments and evidence (*1, 3*). By contrast, our analysis suggests that committees in Congress and ideological think tanks do not appear to create these broad syntheses, instead focusing on different sets of impacts for the same policy, and citing substantively different sets of science when working on the same policy issue. The observed partisan disparities hence may not necessarily reflect a different willingness to engage with science, but instead may reflect their differing priorities, goals, or stances within issues (*9*).

To further unpack whether the partisan disparity that we uncover is solely due to differing positions, we move beyond comparing the two factions and instead compare their use of science with a third, common reference point: science itself. We compare the characteristics of the scientific papers cited by either only left-leaning or only right-leaning policy-makers, measuring their scientific impact in science, recency, and whether they have passed peer review (see SM 6 for metric construction). We find that papers cited by only Democratic committees are more likely than those cited by only Republican committees to be hit papers in science, defined as the top 5% of the most cited papers in their field and year (μ_D = 0.48 versus μ_R = 0.44, t = 7.50, df = 27468, P < 0.0001; see fig. S25A). Democratic committees' documents are also more likely to cite science that has passed peer review (measured as percent preprint; μ_D = 0.0138 versus μ_R = 0.0184, t = –3.60, df = 28109, P < 0.001; see fig. S25C), and tend to cite slightly older science than Republican committees (μ_D = 8.22 versus μ_R = 7.93, t = 3.16, df = 36945, P < 0.01; see fig. S25D). However, we find no difference in the field citation ratio (FCR) between Republican and Democratic committee document cited papers (μ_D = 30.3 versus μ_R = 31.1, t = –0.598, df = 26540, P = 0.55; see fig. S25B) (these results are robust to log-transforming FCR; see SM 14 and fig. S26). We see slightly greater differences for think tanks, with papers cited by only left-of-center think tanks more likely to be hit papers in science (μ_L = 0.444 versus μ_R = 0.382, t = 19.4, df = 50320, P < 0.0001; see fig. S25E), have a higher field citation ratio, be published substantially more recently (μ_L = 27.2 versus μ_R = 23.4, t = 5.06, df = 28554, P < 0.0001; see fig. S25F), and be more likely to have passed peer review than those cited by only right-of-center think tanks (measured as percent preprint; μ_L = 0.0165 versus μ_R = 0.0344, t = –17.5, df = 47367, P < 0.0001; see fig. S25G), and cite more recent science (μ_L = 8.20 versus μ_R = 10.9, t = –44.7, df = 61822, P < 0.0001; see fig. S25H). In other words, Democratic and left-of-center organizations tend to cite science that is more in line with the work that scientists themselves consider important, which is true for both Congress and think tanks.

There are several possible explanations for the more pronounced differences among think tanks than Congress. Policy-makers in Congress might be especially concerned about the unintended consequences of the policies they enact in a way that think tankers are not, and this universal incentive for all congresspeople—regardless of party—may induce them to cite more highly cited science. Moreover, the selection process for including think tanks in our analysis sample includes only partisan or ideological think tanks, excluding nonpartisan or centrist think tanks. This sampling strategy may also lead to more pronounced differences in our think tank sample.

Of the myriad factors that may influence the use of science in policy-making (*1*), trust is often understood to be a key mediator governing the use of information (see SM 18), raising the question of whether differential levels of trust in scientists and scientific institutions may play a role. Although there is scarce empirical evidence assessing the level of trust in science among policy-makers or political elites, our hypothesis here is partly motivated by evidence that among the general public, there has been a marked decline in conservatives' trust in science in recent decades, suggesting that the rising political polarization during this period in the United States may be threatening confidence in science (see SM 18). We fill this gap to directly assess partisan differences in trust in science among policy-makers by fielding a survey of roughly 3500 US political elites and public servants (e.g., congressional staffers, bureaucrats, political journalists, lobbyists, nonprofit advocates and association leader-

Partisan disparities in the trust of science among political elites

Survey data reflect that political elites exhibit higher levels of trust in scientists than copartisan likely voters, regardless of party identification; elite attitudes toward science cannot be assumed to match those in the general public. Democratic elites trust scientists substantially more than their Republican counterparts. See supplementary materials.

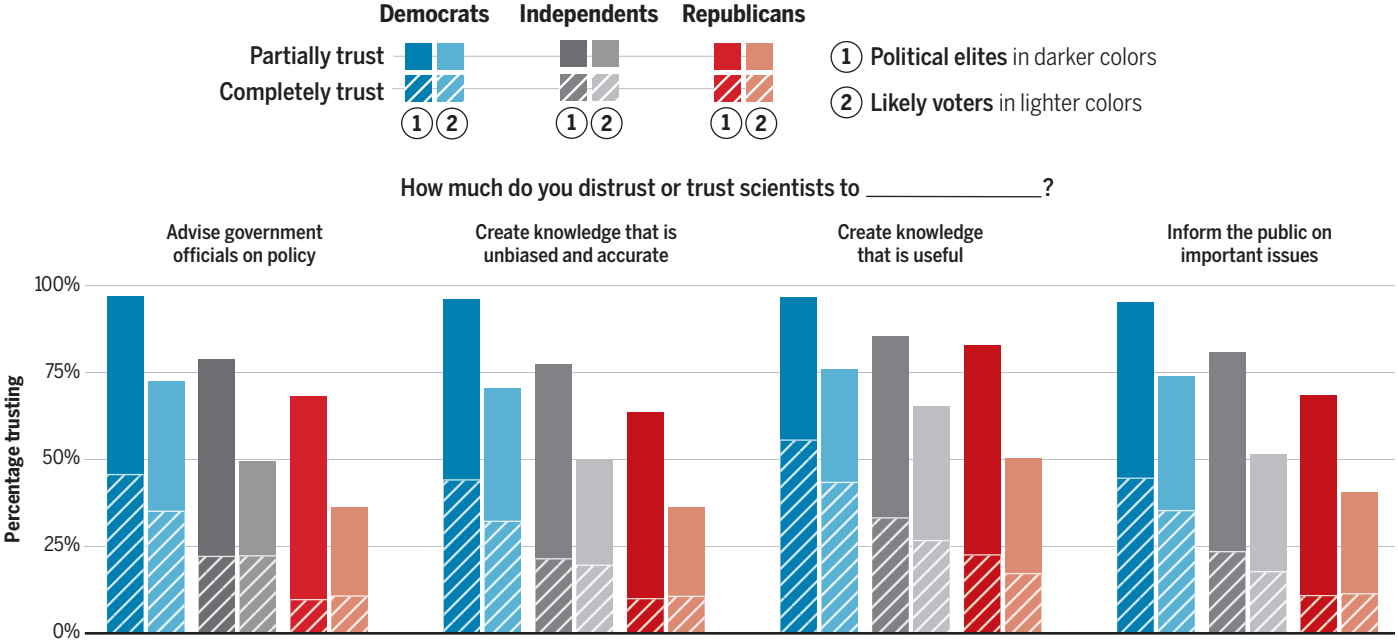

ship, corporate C-suite executives, judges and clerks, and state and local government officials). By surveying the professionals who are actively involved in setting policy agendas and drafting policy documents, we can quantitatively probe their attitudes toward science (see SM 2.1). For comparison, we also conducted a contemporaneous survey of roughly 1000 likely voters (see SM 2.2). We used a standard party identification battery, as well as a series of questions about trust in scientists and scientific organizations (see SM 2).

We first asked political elites to rate how much they "trust or distrust scientists" along four different dimensions, uncovering three primary findings (see the fourth figure). First, regardless of party identification, political elites exhibit substantially higher levels of trust in scientists than copartisan likely voters, suggesting that political elite attitudes toward science cannot merely be assumed to match those in the general public. Second, Democratic elites trust scientists substantially more than their Republican counterparts (μ_D = 1.42 versus μ_R = 0.65, t = 25.86, df = 1188.50, $P < 0.001$), showing large, systematic partisan differences in attitudes toward scientists. For example, 96.0% of Democratic elites either completely or partially trust scientists to "create knowledge that is unbiased and accurate" compared with only 63.7% of Republican elites. The partisan differences are especially stark among those with the highest level of trust. Of Democratic elites, 44.1% completely trust scientists to create unbiased and accurate knowledge, compared with only 9.9% of Republican elites. Third, despite the differences between the four dimensions that we surveyed, ranging from the knowledge scientists create to their roles in informing the public and government officials, the partisan differences we uncover are remarkably consistent across all four dimensions.

To assess the level of trust in scientific institutions, we asked political elites to rate the trustworthiness of the National Academies of Sciences, Engineering, and Medicine (NASEM) and the American Association for the Advancement of Science (AAAS, the publisher of *Science*)—two of the most prominent scientific organizations in the world—on matters of public policy (fig. S27). Nearly three times as many Democratic elites (61.2%) rate NASEM as "very trustworthy" as Republican elites (22.8%) (χ^2 = 427.43, df = 8.00, $P < 0.0001$). The difference is even more pronounced for the AAAS, which Democratic elites rate "very trustworthy" five times more than Republican elites (40.7% versus 8.2%, χ^2 = 444.43, df = 8.00, $P < 0.0001$). These partisan differences are robust after controlling for a range of attributes (see SM 14). Overall, these findings support the proposition that the differential attitudes toward science may partly explain the observed partisan differences in the use of science in policy.

DISCUSSION

These findings must be interpreted with care. First, despite the importance of scientific evidence to policy-making, it is only one of many information sources available to policy-makers, who may also draw from regulators, industry, news media, trade publications, interest groups, and lobbyists (*10*). Although each source has its own potential biases and agendas, science is often seen as holding a relatively privileged position partly owing to its commitment to Mertonian norms like organized skepticism. Nevertheless, although we find that Republicans use science less than Democrats, this does not necessarily mean that Republicans use less evidence overall. To test this possibility, we conduct a preliminary analysis (see SM 16) using witness data from congressional hearings (*10*) to investigate whether Republicans tend to rely more on nonuniversity, nonresearch witnesses than Democrats. Our preliminary findings reject the hypothesis that Republicans in Congress rely more on such information sources. It is still possible, however, that partisans rely on sources of evidence that our data do not capture, and exploring how different information sources, especially those beyond science, are used in policy-making represents an important avenue for future research, both empirically and theoretically.

It is also possible that Republicans and Democrats use science in roughly equal measure when they are "information seeking" in committee, but Republicans may use hearings or committee activity more often as tools for partisan messaging and

GRAPHIC: M. HERSHER/*SCIENCE*

less often for information seeking. This differential use of committee time could cause their overall use of science to be lower. To test this hypothesis, we conduct several additional analyses incorporating data on partisan voting patterns and speech records to identify highly politicized issues, which we expect to serve as potential venues for grandstanding. We then measure the partisan disparities in the use of science in congressional hearings focused on these highly politicized issues, where we expect more or less "grandstanding" activity. We find that partisan differences in citing science are consistent regardless of how politicized the issues are, and partisans hold hearings on highly politicized issues at similar rates (see SM 17.1). Moreover, a hearing-level analysis finds no differences in association between grandstanding speech and citations to science conditional on party control of committees (see SM 17.2). Together, these results suggest that partisan messaging or grandstanding is unlikely to explain the differences we observe, although we believe more study is needed for dispositive results.

It is also possible that scientists, who among the US voter population are predominantly Democrats (*11*), may be more likely to focus on issues or policies favored by left-of-center policy-makers. As a result, these policy-makers might have a larger pool of relevant scientific findings to cite, potentially contributing to the partisan differences we observe. More broadly, understanding whether and how the political leaning of scientists may influence both the production and uptake of their work is an important avenue for future investigation.

The increasing reliance on science that we observe over a 25-year period among both parties is encouraging, especially given that many societal challenges today, from climate change to technological advancement, are deeply intertwined with the latest scientific development. This increase in citing science coincides with broader changes in committee operations, such as a decline in the number of hearings and, more notably, witnesses (*10*). These changes, along with a shift from proactive lawmaking to reactive oversight and an overall broadening of the congressional agenda, have challenged Congress to address more issues on shorter timescales with less in-house expertise (see SM 18). As such, the increased citation of science aligns with expectations that committees would rely more on external expertise, including scientific sources, on a per-document or per-hearing basis, rather than on expertise developed by staffers themselves.

Yet at the same time, this paper uncovers systematic partisan differences in the use and trust of science, which may have wide-ranging implications for science and society at large. If different political parties cite different scientific sources to back their claims, it raises the question of whether science is being used selectively to support preexisting beliefs or agendas (*12*). This line of thinking can erode public confidence in both science and government and undermine the foundational principles of scientific inquiry and its role in informing public policy and personal choices. Above all, our findings underscore the threat to the perception of science as a politically neutral, trusted source of information.

Further, the low degree of overlap in the science cited by policy-makers across the two sides of the aisle raises concerns about the extent to which policies are always drawing on all of the best available scientific evidence. Although some of this is naturally driven by partisans' differing positions, stances, or approaches to issues, our results demonstrate that policy-makers, both those left and right of center, are not generating broad syntheses of scientific evidence accounting for multiple perspectives on relevant issues. A failure to engage all of the appropriate, relevant science in policy-making could result in policies that fall short of their intended objectives or, worse, precipitate unintended adverse outcomes. Furthermore, the systematic disparity in the science cited by different parties then raises concerns about the efficacy of the policies and their ability to serve shared societal goals.

More broadly, in a robust democratic society, although partisans might diverge on their priorities, values, and normative judgments, their capacity for effective cooperation—and the integrity of democratic institutions—is premised on maintaining a broadly shared set of facts. The partisan differences in the use and trust of science among policy-makers suggest a potential erosion of this shared factual foundation, thereby undermining bipartisan efforts toward constructive solutions. Amid rising political polarization, the intertwining of science and partisan politics may impede constructive dialogue, hinder bipartisan cooperation, and stymie our collective ability to address many pressing societal challenges.

The results presented in this paper suggest many areas for future research. For example, although the very public nature of citations in persuasive policy documents suggests that they may be suited to capturing policy-makers' revealed preferences regarding whether science is beneficial to their policy arguments (*12, 13*), future work may attempt to further unpack the purpose of those citations, helping us discern between "substantive" and "strategic" uses of science or explore the broader "conceptual" use of science in shaping policy-makers' perspectives (*14*). Moreover, although our focus has been predominantly on the US, the challenges highlighted here transcend national boundaries. All governments need accurate information to govern effectively, underscoring the need to broaden the geographical ambit of such studies. Lastly, although this paper focuses on the partisan citation of science, it also uncovers an important—albeit small—set of papers that consistently see bipartisan citation. A better understanding of this core of bipartisan-cited science could further demonstrate the value of science across the political spectrum and reveal new avenues for fostering mutual understanding in a polarized political climate.

Ultimately, science is a crucial public good and depends on both sustained public support and long-term commitments (*2*). By contrast, the American political landscape is characterized by inherent volatility and periodic shifts in political control. Despite recent instances of bipartisan support for science, the uncovered partisan differences in the use and trust of science highlight a profound tension at the nexus of science and politics.

REFERENCES AND NOTES

1. National Research Council, *Using Science as Evidence in Public Policy* (The National Academies Press, Washington, DC, 2012); https://nap.nationalacademies.org/catalog/13460/using-science-as-evidence-in-public-policy.
2. Y. Yin, J. Gao, B. F. Jones, D. Wang, *Science* **371**, 128 (2021).
3. H. Douglas, *Science, Policy, and the Value-Free Ideal* (Univ. of Pittsburgh Press, 2009).
4. N. McCarty, K. T. Poole, H. Rosenthal, *Polarized America: The Dance of Ideology and Unequal Riches* (MIT Press, 2016).
5. M. Szomszor, E. Adie, *Quant. Sci. Stud.* **3**, 624 (2022).
6. D. W. Hook, S. J. Porter, C. Herzog, *Front. Res. Metr. Anal.* **3**, 23 (2018).
7. J. M. Crosson, A. C. Furnas, G. M. Lorenz, *Am. Polit. Sci. Rev.* **114**, 1117 (2020).
8. E. Fagan, *Party Polit.* **27**, 149 (2021).
9. M. van Hulst, D. Yanow, *Am. Rev. Public Adm.* **46**, 92 (2016).
10. P. Ban, J. Y. Park, H. Y. You, *Am. Polit. Sci. Rev.* **117**, 122 (2023).
11. A. A. Kaurov, V. Cologna, C. Tyson, N. Oreskes, *Humanit. Soc. Sci. Commun.* **9**, 368 (2022).
12. E. Suhay, J. N. Druckman, *Ann. Am. Acad. Pol. Soc. Sci.* **658**, 6 (2015).
13. A. Lupia, *Proc. Natl. Acad. Sci. U.S.A.* **110** (suppl. 3), 14048 (2013).
14. C. H. Weiss, "The many meanings of research utilization" in *Social Science and Social Policy* (Routledge, 1986).
15. A. C. Furnas, T. M. LaPira, D. Wang, Data and code for "Partisan disparities in the use of science in policy" Harvard Dataverse (2025); https://doi.org/10.7910/DVN/3KVKVH.

ACKNOWLEDGMENTS

The authors thank J. Druckman, P. Rutland, T. Kim, E. Adie, A. Tamame, all members of the Center for Science of Science and Innovation, the seminar audiences at Northwestern University's Institute for Policy Research Colloquia and Wesleyan University for comments and feedback, and A. Freilich for editing. The authors acknowledge support from the Alfred P. Sloan Foundation G-2019-12485, Tides Advocacy, Data for Progress, and the Peter G. Peterson Foundation. All data and code used in this analysis can be found at (*15*).

SUPPLEMENTARY MATERIALS

science.org/doi/10.1126/science.adt9895

10.1126/science.adt9895

Fuentes argues that just as average differences in height contain some overlap, so too do other traits.

BOOKS *et al.*

BIOLOGY

The variable nature of sex

An anthropologist shows why we should think beyond the binary

By **Malin Ah-King**

In the current political moment, the question of how we understand sex is even more pressing than when anthropologist Agustín Fuentes started writing his latest book, *Sex Is a Spectrum: The Biological Limits of the Binary*, which advocates for problematizing definitions of sex and a more nuanced understanding of the interweaving of nature and nurture in gender and sex differences. Elaborating on his 2023 argument against "politicians, pundits and even a few scientists" who maintain that human sex is binary (*1*), this new book is Fuentes's full-length refutation of such claims. He structures his case on scientific understandings of the evolution of sex and of variation in sex and behavior, offering readers a comparative perspective between human biology and primates and exploring what we know about human evolutionary history and variation in contemporary human biological features.

Fuentes does a good job of summarizing what we know about the evolution of sex and writes accessibly about the variability in sex and sex behaviors among animals, carefully documenting examples such as the genetics of sex development in bees, sex-changing fish, and the caring patterns of crocodilians. Moving to humans, his main argument against binary sex frameworks is that humans are biocultural and that "the totality of the human experience cannot be reduced to either specific innate (biological) or external (environmental/cultural) influences. It is a synthesis of both." Cultural context, he maintains, is a factor that helps form people's bodies and their experiences of their sex biology.

Sex Is a Spectrum: The Biological Limits of the Binary
Agustín Fuentes
Princeton University Press, 2025. 216 pp.

In his description of current understandings of human gender and sex differences, Fuentes uses the example of how average differences in human height also contain overlapping distributions to make the case that other human traits vary in the same way. Here, too, he explains how the evolution of helpless human infants that necessitate cooperation among multiple caretakers reveals how culture is entwined in the development of each human from the start.

Not all humans align with typical biological patterns of sex, and throughout the book, Fuentes is sensitive to this, referring to males and females whose genes, gonads, and genitals do align as "3G" and to females as "large gamete producers" and males as "small gamete producers." Although a bit cumbersome to read, the latter decision helps make the point that we need not assume that the production of small or large gametes is directly connected to any other feature in an organism.

For the most part, I agree with Fuentes, yet I sometimes wished that his argumentation was less polemical. I fear that he might lose some of his potential audience with his assertive claims, for example, that there is "no biological battle of the sexes" in humans. This assertion is based on the author's debunking of the sex binary and his observation of the relatively small size difference between the sexes. Yet other scholars, such as primatologist Sarah Blaffer Hrdy, have argued that the threat to women's reproductive rights is based in sexual conflict.

Another overly broad generalization occurs when Fuentes summarizes critiques of the 20th-century biologist Angus Bateman's pioneering experiments in sexual selection to argue that "Bateman was mostly wrong." Although the criticism of Bateman's work is valid, my guess is that most biologists would disagree with this statement, because, for example, he correctly predicted that male variation in reproductive success is greater than that of females in most species.

Furthermore, I have some trouble with Fuentes's discussion of intersex conditions. Fuentes rightly states that the term "hermaphrodite" is no longer used when discussing humans, but then he claims that "the term 'intersex' is used for individuals that produce both types of gamete at the same time." This is the definition of a hermaphrodite in biology, and Fuentes's attempt to make the vocabulary more inclusive risks making the discussion of the phenomenon even more confusing. Earthworms are not "all intersex," and fish are not "sequentially intersex."

I also felt uneasy with Fuentes's detailed descriptions of intersex athlete Caster Semenya's body, which felt reminiscent of other texts that have presented Semenya as an object, rather than a subject with a voice of her own. I much preferred Amanda Lock Swarr's depiction of Semenya's agency in *Envisioning African Intersex*. In that book, Lock Swarr recounts how Semenya and other intersex activists are resisting imposed pharmaceutical treatments to conform to medical norms and creating new decolonizing ways to conceptualize intersex.

Ultimately, however, I think *Sex Is a Spectrum* will be important for introducing a wide readership to the nuances of scientific understandings of variability in sex and of the biocultural constitution of humans, and I believe that there is much for biologists to appreciate in the book as well. ■

REFERENCES AND NOTES

1. A. Fuentes, "Here's why human sex is not binary," *Scientific American*, 1 May 2023.

The reviewer is at the School of Humanities, Education and Social Sciences and the Centre for Feminist Social Studies at Örebro University, Örebro, Sweden.
Email: malin.ah-king@oru.se

10.1126/science.adv3113

PHOTO: MONTI SPRY/CENTRAL PRESS/HULTON ARCHIVE/GETTY IMAGES

MICROBIOLOGY

Missed connections

Early investigators struggled to link contagious diseases and their causative agents

By **Tara C. Smith**

Scientific advancements are often portrayed in popular culture as "eureka!" moments—incredible breakthroughs that result in a "before" and an "after." Often, the advance comes from a lone genius outside of the mainstream. Although it is rare that discoveries happen in this way, what is even rarer is our consideration of moments poised for a "eureka" that never comes—of investigators who had all the information in front of them but did not quite make that revolutionary finding. In *So Very Small*, Thomas Levenson takes readers through an entertaining, if frustrating, journey of missed opportunities in microbiology and the eventual advances that arose in this field as humanity moved from ideas rooted in the "great chain of being," humoral balance, and miasma theory toward more rigorous and evidence-based ideas of disease causation.

The stories and characters Levenson highlights will likely be familiar to those who have a background in microbiology or the history of medicine. They include Antonie van Leeuwenhoek's studies of "animalcules"; the move from smallpox variolation, championed by Boston physician Zabdiel Boylston and preacher Cotton Mather, to Edward Jenner's cowpox inoculation and the subsequent development of a smallpox vaccination; John Snow's tracking of cholera deaths in London's Soho neighborhood and the removal of the Broad Street pump handle from which the outbreak originated; and Ignaz Semmelweis's experiments demonstrating that hand hygiene was lifesaving in maternity wards. Here, too, are Louis Pasteur's and Robert Koch's respective breakthroughs, which finally proved that microorganisms, including many of the same species seen in van Leeuwenhoek's drawings two centuries ago, were the root cause of infectious disease.

While Levenson retells the now-famous tales, he also is careful to point out some of the myths that have traveled with these lauded stories. Yes, Snow did yeoman's work while deciphering the source of the 1854 cholera outbreak, but the removal of the Broad Street pump handle probably did not end the outbreak, and Snow had more doubters than believers in the immediate aftermath of the epidemic. Yes, Pasteur was a genius who saw what many others missed, but he was wrong about the identity of the rabies pathogen and incorrect in his theory of how his rabies vaccine invoked immunity. An important throughline emerges with each incremental step toward germ theory: "What took so long?" What was it about the mindset of investigators at the time that allowed for some discovery but stymied the final connection between contagious diseases and the causative organisms that were readily observable? Why did so many brilliant thinkers miss what we now think of as the obvious link between organisms "so very small" and their role in sickness? Even the language used during this period suggested that investigators were on the right track, with many employing terms such as "particles of infection" and describing diseases as having been "seeded."

Once the connection was made, however, vaccines for various infectious agents quickly followed, as investigators used techniques such as the isolation and attenuation of pathogens or the cultivation of their toxins to develop antisera. The holy grail of infectious disease containment—cures—soon followed in the form of antibiotics. But those interventions are not unassailable.

Levenson ends *So Very Small* with cautionary contemporary accounts of the ways we risk losing many of the practical benefits provided by understanding germ theory. Here, he notes that the success of germ theory hinged not only on it being "strictly scientific" but also on its ability to deliver what older attributions of causation could not: "a direct intervention in the course of a disease, based on a theory of infection that had passed repeated experimental tests." He repeatedly returns to the idea of the "metastasis of disinformation and the stubborn clinging to false ideas," arguing that this phenomenon is not restricted to the distant past. Antibiotics have been used unwisely, as Alexander Fleming—the discoverer of penicillin—warned against in his 1945 Nobel prize acceptance speech. Vaccines are actively rejected, fueling outbreaks of measles and leading to preventable deaths from severe acute respiratory syndrome coronavirus 2 and influenza, among others.

Although Levenson did not write a chapter specifically on this topic, the scientist in me could not help but wonder while reading his book: What groundbreaking discoveries are staring us in the face right now that we are unable to see? What breakthrough will emerge in a few decades' time that was in front of us all along? What errors, as Pasteur suggested of his contemporaries, might we be currently unable to perceive nor know how to avoid? Levenson concludes that "we aren't smarter than the microcosmos," and despite centuries of advances, it is clear that he is correct. ■

The reviewer is at the College of Public Health, Kent State University, Kent, OH, USA. Email: tsmit176@kent.edu

So Very Small: How Humans Discovered the Microcosmos, Defeated Germs—and May Still Lose the War Against Infectious Disease
Thomas Levenson
Random House, 2025. 448 pp.

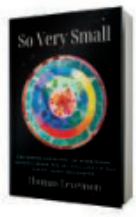

10.1126/science.adv9772

SCIENCE OF DEATH

PHOTO: JAN SOCHOR/GETTY IMAGES

Grave decorations honor the dead in Xalpatláhuac, Mexico.

PODCAST

In 2025, *Science* will present a limited podcast series featuring books that delve into the science of death, exploring the topic through the lenses of biology, sociology, technology, and even astrophysics. On the 24 April episode of the *Science* podcast, series host Angela Saini and *Science*'s books and culture editor, Valerie Thompson, offer listeners a sneak preview of the six books and authors that will be discussed in the months to come. https://bit.ly/4jdSsWU

10.1126/science.adx9075

LETTERS

Edited by **Jennifer Sills**

Editor's note

On 15 September 2022, *Science* published the Research Article "Structural basis for strychnine activation of human bitter taste receptor TAS2R46" by W. Xu *et al.* (*1*). On 22 November 2022, an Editorial Expression of Concern alerted readers to concerns regarding fig. S10D (*2*). The authors have now corrected the paper, and the Editorial Expression of Concern has been replaced by an Erratum (*3*). As described in the Erratum, the authors repeated bioluminescence energy transfer experiments that were the basis for figs. S9, C to F, and S10D. The new data did not provide strong functional support for the structure-based suggestion of precoupling between TAS2R46 and the G protein gustducin. In the corrected version of the Research Article, Xiaoling Cao is no longer an author; figs. S9, C to F, and S10D have been removed; and the conclusions on precoupling are weaker than in the original version. The editors remain confident in the key findings of the paper: the cryo–electron microscopy structures of human TAS2R46 complexed with chimeric mini–G protein gustducin, in both strychnine-bound and apo forms.

H. Holden Thorp
Editor-in-Chief, *Science* journals

REFERENCES AND NOTES

1. W. Xu *et al.*, *Science* **377**, 1298 (2022).
2. H. H. Thorp, *Science* **378**, 1180 (2022).
3. *Science* **388**, eadx9419 (2025).

10.1126/science.adx7164

Science, not silence: Save US economic growth

Scientists in the US are under siege. The Trump administration has placed a stranglehold on federal funding of research and development (*1*, *2*). Yet there has been hardly any public denouncement of the Executive Branch's slash-and-burn strategy from scientific leaders, the national academies, or university presidents. The US has had a long track record of science driving economic strength (*3*, *4*), and scientific leaders must push back against the administration's efforts to dismantle the support that enables scientific success.

Each dollar of federal funding to the National Institutes of Health contributes US$2.46 to economic growth (*3*), and

A US National Science Foundation grant made commercial web browsers and e-commerce possible.

each dollar of investment in the National Science Foundation (NSF) generates about US$2 of economic growth (*4*). A prime example of this economic outgrowth is the birth of the internet, which arose from a US$55 million grant from the NSF for a supercomputer center (*5*). The explicit goal of this unsolicited grant was to establish a National Center for Supercomputing Applications (*6*) to solve scientific problems that required large-scale computing. One by-product of this investment was the first web browser, Mosaic (*7*), which led to Netscape, the first commercially available browser (*8*), ultimately giving rise to the current landscape of e-commerce.

As shown by this example, US scientists have traditionally enjoyed the freedom to engage in idea-driven rather than product-driven research, and that innovation has driven the US economy. Yet as of 2024, the US ranks second to China on the Nature Index for high-impact research (*9*), indicating the need for even more investment and continued support for scientists' pursuit of research unfettered by state mandates. Rather than making "America first," the Trump administration's plans to decrease science funding are likely to result in the country falling even further behind its global competitors. Scientists at the highest, most public levels must denounce the administration's funding cuts and antiscience policies if the US scientific enterprise is to thrive.

Philip Phillips[1,2]
[1]Department of Physics, University of Illinois at Urbana–Champaign, Urbana, IL, USA. [2]Anthony J. Leggett Institute of Condensed Matter Theory, University of Illinois at Urbana–Champaign, Urbana, IL, USA. Email: dimer@illinois.edu

REFERENCES AND NOTES

1. P. Nagarkatti, M. Nagarkatti, "NIH funding cuts will hit red states, rural areas and underserved communities the hardest," *The Conversation*, 7 March 2025.
2. J. Davalos, "Trump's funding cuts threaten America's AI competitiveness," *Bloomberg*, 3 March 2025.
3. H. Floersh, "Report: Every dollar of NIH research funding doubles in economic returns," Fierce Biotech, 25 March 2024.
4. Society for Neuroscience, Funding for the National Science Foundation (2023); https://www.sfn.org/-/media/SfN/Documents/NEW-SfN/Advocacy/2023-Fact-Sheets/2023-NSF-Fact-Sheet.pdf.
5. M. Bowden, "The measured man," *The Atlantic*, July-August 2012.
6. National Center for Supercomputing Applications, History; https://www.ncsa.illinois.edu/about/history/.
7. National Science Foundation, Birth of the commercial internet; https://www.nsf.gov/impacts/internet.
8. R. McGuire, "Thirty years ago this week, the world changed," *Medium*, 17 October 2024.
9. Nature Index, Country/territory tables; https://www.nature.com/nature-index/country-outputs/generate/all/global.

10.1126/science.adx7500

US scientists must stand together

US federal support for science is eroding (*1*), and the future of US scientific agencies and institutions is uncertain. Simultaneously, the Trump administration is scapegoating minority groups, including immigrants, trans people, people of color, and disabled people (*2*–*4*). In the face of this federal onslaught, scientists may feel uncertain about how to respond. Speaking up may feel risky or even futile, but the risk of backlash grows with each day that silence becomes the norm (*5*, *6*). Now is the time for scientists to ask more of each other and demand more from our institutions.

Scientists have a responsibility to care for each other as members of labs, departments, unions, and professional societies. We must collectively demand that our institutions safeguard our personal and professional

PHOTO: ARLAWKA AUNGTUN/ISTOCK PHOTO

well-being. Institutional actions should include protecting those targeted by the Trump administration (*4*, *7*) and pushing back against unjustified funding cuts (*8*, *9*).

Even in the absence of strong institutional response, labs and departments can model leadership by making space for open discussion of federal decisions. Conversations about the material consequences of the Trump administration's actions (*10*, *11*) can serve as valuable guides for collectively identifying suitable responses. Sharing accurate information about the limits of federal policies is also crucial. Overestimating the power and scope of federal decisions could inadvertently lead to scientists ceding unnecessary ground (*5*). For example, preemptively removing content related to diversity, equity, and inclusion from lab materials may be a freely given concession at many institutions. Frank and frequent conversation can help assess the risks and benefits of potential action.

Scientific institutions face immense federal scrutiny, but this pressure cannot serve as an excuse for silence or inaction. In the face of unreliable federal support, scientists must raise, not lower, expectations of each other and of our leaders (*12*).

Anita Simha* and Gaurav Kandlikar
Department of Biological Sciences, Louisiana State University, Baton Rouge, LA, USA.
*Corresponding author. Email: asimha@lsu.edu

REFERENCES AND NOTES

1. J. Travis, K. Langin, J. Kaiser, M. Wadman "Mass firings decimate U.S. science agencies," *Science*, 18 February 2025.
2. A. J. Connelly, "Federal government's growing banned words list is chilling act of censorship," *PEN America*, 21 March 2015.
3. M. Casey, R. Ngowi, "Transgender Americans aim to block Trump's passport policy change," *AP News*, 25 March 2025.
4. "Trump administration arrests Turkish student Rumeysa Ozturk at Tufts," *Al Jazeera*, 26 March 2025.
5. C. Robin, *Fear: The History of a Political Idea* (Oxford Univ. Press, 2005).
6. J. McAlevey, *No Shortcuts: Organizing for Power in the New Gilded Age* (Oxford Univ. Press, 2016).
7. V. B. Chaudhary *et al.*, *Science* **387**, 937 (2025).
8. B. Pierson, J. Allen, "Columbia faculty groups sue Trump administration over funding cuts, academic demands," *Reuters*, 25 March 2025.
9. W. F. Tate IV, *Science* **387**, 1333 (2025).
10. A. Simha, G. Kandlikar, "Caring for our colleagues amidst backlash: A conversation guide," Zenodo (2025); https://doi.org/10.5281/zenodo.15101435.
11. A. Aguilar *et al.*, "How should staff and mentors discuss the recent U.S. election with youth: Leading experts have answers," *The Chronicle of Evidence-Based Mentoring*; https://www.evidencebasedmentoring.org/lets-chat-politics-tips-for-staff-and-mentors-on-discussing-the-u-s-election-with-youth/
12. J. McAlevey, B. Ostertag, *Raising Expectations (and Raising Hell): My Decade Fighting for the Labor Movement* (Verso Books, 2012).

10.1126/science.adx1220

Peaceful protesters stand up for science at the Lincoln Memorial in Washington, DC on 7 March 2025.

PHOTO: KENT NISHIMURA/REUTERS

OUTSIDE THE TOWER

Rallying for US science

I was sitting with my son on a step leading up to the Lincoln Memorial in Washington, DC, which, on this sunny March afternoon, also served as stage right for a massive rally. "Remember," one of the event organizers told me, "speak loudly and directly into the microphone." I heard my name announced, and goosebumps rose on my arms. Suddenly, I was standing before a crowd of 5000 energized people. A sign held by one of the attendees caught my eye: "Girls just want to have funDING FOR SCIENCE." I began to speak, surprised by how different it felt compared with giving my usual talks as a professor and biologist. I quickly learned, in real time, to pause between sentences—like politicians do—allowing space for the crowd's enthusiastic cheers.

The Stand Up for Science 2025 rally, organized by four PhD students and one recent PhD graduate (1), united scientists across the US with simultaneous rallies in nearly every state, as well as in France and Germany. I first learned about the event 3 weeks earlier and immediately decided to go. When I asked my 12-year-old son if he would join me, he agreed—on one condition: I had to be one of the speakers.

At my son's urging, I reached out to the organizers. I offered to speak about how science delivers breakthroughs even though its path is unpredictable. I wanted to emphasize the importance of investing in science and warn that trust in science is under threat. I have been championing creative, exploratory thinking in research for a long time, and the organizers agreed that the message was important.

The Stand Up for Science team brought together those who feel a crisis looming in how the US government funds science. Throughout the day, I engaged in conversations about the importance of building on this momentum and maintaining public trust. The rally was an opportunity to challenge misconceptions and show why investment in science is vital for our health, our economy, and our future. I hope that its success inspires scientists across the country and the world to participate in efforts to communicate with the public and demonstrate the crucial role of government funding for science.

Itai Yanai
Institute for Systems Genetics, NYU Langone Health, New York, NY, USA.
Email: itai.yanai@nyulangone.org

REFERENCES AND NOTES

1. Stand Up for Science; https://standupforscience2025.org/.

10.1126/science.adx5622

Call for submissions

Outside the Tower is an occasional feature highlighting scientists' advocacy experiences. Submit your advocacy story at http://cts.sciencemag.org.

RESEARCH

IN *SCIENCE* JOURNALS

Edited by **Michael Funk**

NATURAL HISTORY

The bone collector

The vast majority of lepidopteran caterpillars are herbivorous. Those that break this rule tend to do so in unexpected ways, such as the Hawaiian inchworm, which is an ambush predator. Rubinoff *et al*. describe another unusual caterpillar, also from Hawaii, that scavenges discarded insect parts. The "bone collector" caterpillar lives in spider webs and feeds on the discarded bits of the spider's insect prey. Perhaps to avoid detection, these caterpillars construct portable cocoons decorated with inedible discarded parts. This species is 5 million years older than the oldest Hawaiian island but is now highly endangered, being found in only a single population on O'ahu. —Sacha Vignieri *Science* p. 428, 10.1126/science.ads4243

Bone collector caterpillars, seen here, evade detection by forming a portable case made of discarded insect body parts.

CRISPR

Viruses inhibit CRISPR by RNA mimicry

CRISPR-Cas systems confer antiviral immunity to their bacterial hosts using RNA-guided Cas nucleases, which mediate sequence-specific destruction of viral DNA or RNA. In response, viruses evolved counterdefenses, usually proteins, called anti-CRISPRs that inhibit activities of Cas proteins to overcome immunity. Some viruses also produce RNA anti-CRISPRs, which resemble CRISPR guide RNAs in sequence but induce malfunction of CRISPR machinery. Hayes *et al*. identified one such system that acts as an RNA inhibitor of the RNA-targeting CRISPR-Cas13 system. Analysis of the RNA in complex with Cas13 revealed that it bears little sequence similarity to guide RNAs but mimics their structure to inhibit Cas13. —Di Jiang

Science p. 387, 10.1126/science.adr3656

CHEMICAL PHYSICS

Probing EDL dynamics

The electrical double layer (EDL), which is formed when an electrolyte solution comes into contact with a solid surface, is an important concept in many fields. However, understanding its dynamics at high concentrations remains difficult, particularly because traditional electrical measurements are constrained by response times and complex interactions with the probing system. Moreover, classical mean-field models have not been validated for this regime. Greco *et al*. developed an all-optical method to induce and monitor EDL dynamics at the air-electrolyte interface at arbitrary concentrations. Classical Debye-Falkenhagen theory accurately predicted EDL relaxation times at high concentrations, suggesting its applicability beyond traditional limits. This insight into EDL dynamics highlights the complex interplay between specific interactions and classical electrostatic forces at high concentrations. —Yury Suleymanov

Science p. 405, 10.1126/science.adu5781

TOLERANCE

Regulatory T cells in miscarriage

During pregnancy, a tolerogenic microenvironment is established in the decidua, the inner lining of the uterus, to prevent fetal rejection. Regulatory T (T_{reg}) cells play a key role in fetal-maternal tolerance, but further understanding of T_{reg} cell function in the decidua is needed. Li *et al*. performed single-cell RNA sequencing on decidual $CD4^+$ T cells during early pregnancy. They identified a population of immunosuppressive $CCR8^+$ T_{reg} cells enriched in the decidua (dT_{reg} cells) that were reduced in women with recurrent pregnancy loss. Depletion of $CCR8^+$

PHOTO: UNIVERSITY OF HAWAII INSECT SYSTEMATICS AND BIODIVERSITY LAB

dT$_{reg}$ cells in abortion-prone mice increased cytotoxic T cells and natural killer cells in the decidual microenvironment and increased susceptibility to fetal loss. These findings indicate that CCR8$^+$ dT$_{reg}$ cells are required for fetal tolerance during early pregnancy. —Hannah Isles

Sci. Immunol. (2025) 10.1126/sciimmunol.ado2463

EXOPLANETS

Microlensing exoplanets on wide orbits

Gravitational microlensing occurs when a foreground star passes between Earth and a background star, focusing light and causing an apparent increase in brightness. If the foreground star has an orbiting planet, then a second, briefer brightness increase can occur. Zang *et al*. identified a microlensing event due to an exoplanet with a planet/star mass ratio between those of Earth and Neptune. They combined this object with a larger sample of planets detected using microlensing to constrain the abundance and population distribution of planets on Jupiter-like orbits. They found a bimodal distribution, which they interpreted as reflecting the formation mechanisms. —Keith T. Smith

Science p. 400, 10.1126/science.adn6088

METABOLISM

How fasting hits differently in obesity

Obesity perturbs many metabolic processes. Morita *et al*. constructed a network revealing regulatory relationships between different types of molecules based on omics data collected from the livers of normal and obese mice during food deprivation. The starvation-responsive metabolic network had a similar structure in normal and obese mouse liver. However, the metabolic network in obese mouse liver was wired around different key molecules and showed temporal and pattern disruptions. These defects may help to explain how obesity negates the beneficial effects of intermittent fasting. —Wei Wong

Sci. Signal. (2025) 10.1126/scisignal.ads2547

AGRICULTURE

Tending the soil

High-intensity, high-yield "conventional" agriculture uses practices that can reduce soil health and have other negative environmental impacts. Organic farming generally has a lower environmental impact because it avoids synthetic pesticides and fertilizers, but both organic and conventional farms can vary widely in practices that affect soil. van Rijssel *et al*. assessed soil biota and functions, including a measure of multifunctionality, in 53 organic and conventional fields across the Netherlands. They found no significant difference in soil multifunctionality between broader agriculture types, but specific practices positively (cover cropping) or negatively (inversion tillage) affected soil functions. Adopting specific practices might thus improve the sustainability of both organic and conventional farms. —Bianca Lopez

Science p. 410, 10.1126/science.adr0211

ELECTROCHEMISTRY

Metal cooperation for water splitting

Splitting water electrochemically is an appealing method for sustainable and environmentally friendly hydrogen production. However, current catalysts still lack the stability and activity to cost-effectively scale the process for the envisioned applications. Yue *et al*. report an earth-abundant multimetallic catalyst for the oxygen evolution side that exhibits high stability under alkaline conditions. The catalyst assembly combines an iron and cobalt metal organic framework with nickel and tungsten polyoxometalate clusters, which the authors posit facilitates efficient electron transfer in a stable structure. —Jake S. Yeston

Science p. 430, 10.1126/science.ads1466

IN OTHER JOURNALS

Edited by **Corinne Simonti** *and* **Jesse Smith**

NEUROSCIENCE

You see what you expect

Visual recognition is thought to start with basic object features in the primary visual cortex, reaching the level of object representation at higher cortical areas after processing. However, there is increasing evidence for top-down influences in these pathways. Altavini *et al.* recorded from electrode arrays in several rhesus monkey cortical areas during a delayed match-to-sample task, which measured the effect of cued objects on neuronal responses to a range of objects. Top-down influences were involved in object recognition at several visual pathway stages. Many neurons changed their selectivity with different cues even at the earliest processing stages. This indicates that internal representations of object identity are continually being fed back to all cortical areas in the ventral visual stream. —Peter Stern

Proc. Natl. Acad. Sci. U.S.A. (2025) 10.1073/pnas.2406684122

Feedback from higher-level visual processing centers in the brain influences the early stages of object recognition.

DISEASE GENOMICS

Detangling ancestry effects on disease

Recent progress in human genomics has resulted in vast databases of genetic and clinical data that are then used to inform the diagnosis and treatment of medical conditions. Unfortunately, most of the individuals included in these databases are of European descent, making it more difficult to apply precision medicine for individuals of other ancestries. To overcome this challenge, Smith *et al.* developed a machine learning method called PhyloFrame, which can distinguish ancestry-specific and disease-specific genetic

PHOTO: EYEEM MOBILE GMBH/ISTOCK PHOTO

The ancestors of the Fijian banded iguana likely originated from western North America, a journey requiring a 5000-mile transoceanic voyage.

MIGRATION

I'm sailing away

Speciation can result from long-distance migrations, particularly those that cross geographic barriers such as mountains or bodies of water. In cases of extreme distances, such as crossing oceans, it can be difficult to determine the source population and thus the dynamics surrounding the speciation event. Scarpetta *et al.* analyzed 4441 loci from across the genomes of 14 species of iguanas to determine the nearest living relative of the Fijian banded iguana (*Brachylophus bulabula*). The closest was the North American desert iguana (*Dipsosaurus dorsalis*), suggesting that the ancestral populations of modern-day Fijian iguanas rafted a staggering 5000 miles across the Pacific Ocean rather than island hopping from Southeast Asia. —Corinne Simonti

Proc. Natl. Acad. Sci. U.S.A. (2025) 10.1073/pnas.2318622122

signatures and help identify ancestry-specific genetic variants that affect disease risk. This approach avoids reliance on self-identification and the assumption that individuals come from uniform ancestral backgrounds, which is particularly important in a world of increasingly admixed populations. —Yevgeniya Nusinovich

Nat. Commun. (2025) 10.1038/s41467-025-57216-8

SIGNAL TRANSDUCTION

Tracking PIP_3 at the lysosome

Phosphatidylinositol (3,4,5) trisphosphate (PIP_3) is a critical signaling molecule generated in response to growth factors and is considered to function primarily at the cell membrane. Sahan *et al.* developed a fluorescence resonance energy transfer (FRET)–based sensor for PIP_3 that features tunable affinity and can be targeted to lysosomes, which are now recognized as being important hubs for cell signaling. The sensor detected rapid accumulation of PIP_3 at lysosomes in cultured mouse embryonic fibroblast NIH3T3 cells stimulated with platelet-derived growth factor. The PIP_3 appeared to be generated at the cell membrane and required dynamin-dependent endocytosis for internalization and delivery to the lysosomes. These sensors may enable a better understanding of the spatiotemporal control of PIP_3 signaling in health and disease. —L. Bryan Ray

Proc. Natl. Acad. Sci. U.S.A. (2025) 10.1073/pnas.2426929122

PLASMONICS

High-speed plasmonic modulator

While mobile communications continue to expand 5G coverage across their networks, the desire for even faster data rates and higher capacity will require the development of 6G components for deployment in 5 to 10 years. These devices typically would operate at terahertz frequencies and require integrated photonics to bridge the operational frequencies from electronics to optical fiber carriers. Horst *et al.* have developed ultrafast plasmonic modulators that can meet these requirements. Demonstrating the ability to modulate an input signal from megahertz to terahertz that is compatible with photonic integrated circuitry will be important for developing the next generation of wireless technology. In sensing mode, the broadband plasmonic modulator should also find application in biological and security imaging. —Ian S. Osborne

Optica (2025) 10.1364/OPTICA.544016

STEM WORKFORCE

Perceived realities for women in physics

Women remain underrepresented across all levels of physics. Previous research suggested that women both perceive and receive less recognition about their abilities as physicists than men do, but it is not well understood whether these facts are related. Sundstrom and Holmes tested three models by surveying more than 1700 undergraduate physics students. Results showed that for men and women receiving the same recognition (and having the same demographics), women, on average, reported their perceived recognition as 0.25 points (on a 5-point Likert scale) lower than men. Therefore, a woman would need to receive three more nominations (received recognition) to increase their perceived peer recognition by this amount. This study identifies correlational findings, laying the foundation for identifying causal mechanisms to answer the ultimate question of why men and women in physics internalize recognition differently. —Melissa McCartney

Nat. Phys. (2025) 10.1038/s41567-025-02789-w

ION SEPARATIONS

Capturing the larger cations

Functionalization of covalent organic frameworks (COFs) with crown ethers enables the selective electrochemical capture of alkali ions. Jiang *et al.* synthesized COFs with a Schiff-base reaction between terphenyl dicarbaldehydes bearing 12-, 15-, or 18-crown ethers as struts with 1,3,5-tris(4-aminophenyl)-benzene as the linker. When used as the cathode for alkali ion capture, the 18-crown ether material showed high selectivity for larger cations (~14 for K^+ over Na^+ and ~22 for Rb^+ over Na^+) and high selectivity and capacity with mixed-cation feeds. —Phil Szuromi

J. Am. Chem. Soc. (2025) 10.1021/jacs.4c16346

PHOTO: JOEL SARTORE/PHOTO ARK/MINDEN PICTURES

REVIEW SUMMARY

CONSERVATION

A well-connected Earth: The science and conservation of organismal movement

Jedediah F. Brodie*, Andrew Gonzalez, Jayasilan Mohd-Azlan, Cara R. Nelson, Gary Tabor, Divya Vasudev, Katherine A. Zeller, Robert J. Fletcher Jr.

BACKGROUND: New global biodiversity targets focus on the importance of protecting connectivity, the unimpeded flow of organisms and natural processes across landscapes and seascapes, as a foundational component of biodiversity conservation. The Kunming–Montreal Global Biodiversity Framework presents humanity's most ambitious conservation strategy to date: setting aside 30% of Earth as networks of "well-connected" protected areas by 2030. But the term "well connected" has not been defined and is difficult to quantify, making it problematic to ascertain whether actions will result in the protection and restoration of well-connected land- and seascapes. Because ecological connectivity varies across environmental contexts and scales, precise definitions and measurements have been elusive, rendering it difficult to quantify connectivity in robust and comparable ways that span multiple species and ecosystems. The clear challenge is to transform the concept of well connected from ambiguous to a scientifically grounded, robust, and quantifiable concept that is ecologically and socially meaningful across biomes, taxa, and scales.

ADVANCES: Recent advances allow the measurement and prediction of organismal movements and connectivity at multiple scales and highlight relationships between connectivity and ecological integrity. Connectivity influences population dynamics, with meta-analyses of natural and experimental corridors demonstrating their efficacy at enhancing organismal dispersal, which in turn affects fitness, abundance, and community diversity. By helping maintain populations and metapopulations, connectivity supports the ecological functions that species' movements provide, including provisioning of ecosystem services that benefit humanity. For example, models and empirical data show that loss of connectivity can affect pollination and the natural control of crop pests. Accumulating evidence also highlights ongoing and severe losses of connectivity globally, which now require action to bring connectivity back for nature and society.

We propose an operational definition of "well connected" that can be adapted to nearly any ecosystem or set of focal species (or focal ecological functions) for which data are available. Specifically, a landscape, seascape, or protected-area network is well connected if organismal movement is sufficient to maintain the long-term persistence of focal taxa, maintain ecological functions, and/or sustain the provisioning of ecosystem services relative to counterfactuals with the same amount of intact habitat and no barriers to movement. This definition allows flexibility in assessing counterfactuals based on real-world scenarios (for example, nearby undisturbed study areas) or computer simulations. A variety of existing metrics allow the measurement of particular aspects of connectivity across space and over time, but there is a pressing need for additional indicators that go beyond measuring structural connectivity to estimate the long-term persistence of species and the ecological functions they provide. Policy-driven action needs robust evidence provided by a detection and attribution framework demonstrating that connectivity change results in positive outcomes for biodiversity conservation.

OUTLOOK: Advances in connectivity science can guide biodiversity conservation, ecological restoration, and climate adaptation. But although connectivity has been incorporated into recent conservation plans, much of connectivity science and science-informed planning is not well implemented. Perhaps most critically, connectivity is not well integrated into the designation of protected-area networks, as evidenced by only ~10% of global protected areas being structurally connected. As we expand from ~15% global protected area coverage in 2020 toward 30% by 2030, incorporation of structural and functional connectivity will be critical to avoid extinctions in isolated parks and reserves. In addition, a coordinated international effort to produce and share data on the movement of animals, plants, and other taxa will help ensure that investments in climate resilience and large-scale conservation and restoration will result in anticipated biodiversity gains. Viewing connectivity as the conceptual link between biological, economic, and societal objectives provides a foundation for a strong connectivity science that informs conservation planning. ■

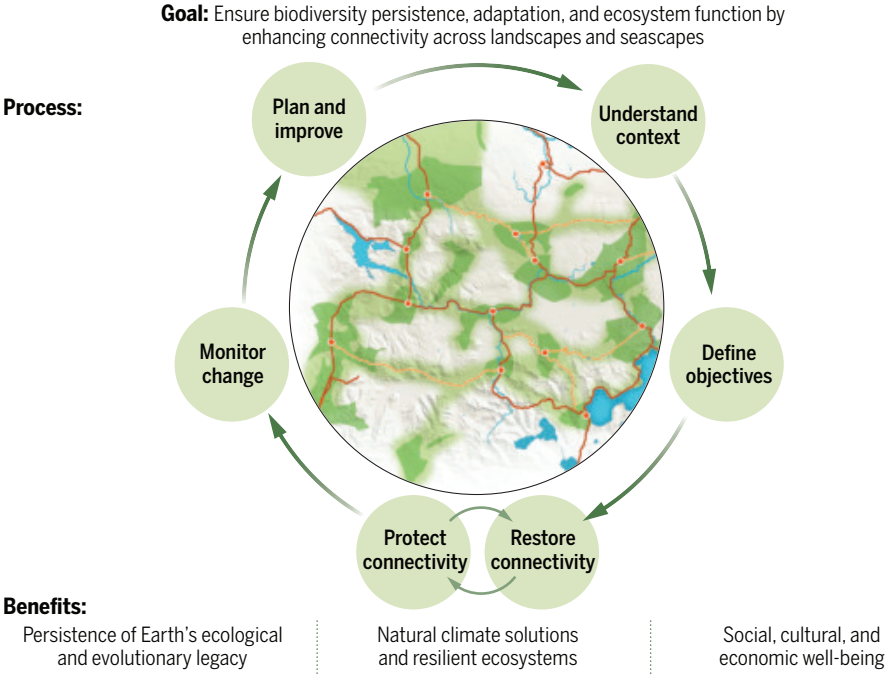

Connectivity enables organisms to move and facilitates ecological processes across scales.

The list of author affiliations is available in the full article online.
*Corresponding author. Email: jedediah.brodie@gmail.com (J.F.B.)
Cite this article as J. F. Brodie *et al.*, *Science* **388**, eadn2225 (2025). DOI: 10.1126/science.adn2225

READ THE FULL ARTICLE AT
https://doi.org/10.1126/science.adn2225

RESEARCH ARTICLE SUMMARY

CANCER

Tumor-derived erythropoietin acts as an immunosuppressive switch in cancer immunity

David Kung-Chun Chiu*, Xiangyue Zhang, Bowie Yik-Ling Cheng, Qiang Liu, Kazukuni Hayashi, Bo Yu, Ryan Lee, Catherine Zhang, Xiuli An, Jayakumar Rajadas, Nathan E. Reticker-Flynn, Erinn B. Rankin, Edgar G. Engleman*

INTRODUCTION: Cancer patients with inflamed (T cell–rich) tumors, indicative of an active antitumor immune response, often benefit from immune checkpoint blockade (ICB) therapy. However, despite the presence of tumor mutations that should theoretically trigger an immune response, most patients have noninflamed (T cell–deprived) tumors and do not benefit from ICB. These noninflamed tumors are typically replete with immunosuppressive macrophages and neutrophils that hinder T cell priming, activation, and homing—critical processes for fostering antitumor immunity. Yet, the mechanisms that determine the immune cell profile or immunotype of tumors remain poorly understood.

RATIONALE: To investigate the factors that govern antitumor immunity and tumor immunotype, using somatic gene editing, we developed and compared spontaneous mouse models of hepatocellular carcinoma (HCC) with either an inflamed or a noninflamed tumor microenvironment (TME). Notably, elevated plasma erythropoietin (EPO) and splenomegaly were observed exclusively in noninflamed tumor models, independent of tumor size and without signs of anemia. EPO, a glycoprotein hormone known for stimulating red blood cell production, has recently been implicated in other biological processes involving resolution of inflammation. Clinically, high expression of EPO is linked to poor prognosis in several cancers, including HCC, and accumulation of immunosuppressive cells such as regulatory T cells (T_{reg} cells) and regulatory macrophages. Therefore, we hypothesized that EPO may play a key role in promoting an immunosuppressive, noninflamed TME.

RESULTS: Using both gain-of-function (EPO overexpression in inflamed tumors) and loss-of-function (EPO ablation in noninflamed tumors) approaches, we established that tumor-secreted EPO autonomously shapes the immune landscape of the TME by promoting T_{reg} cells while reducing $CD8^+$ effector memory T cells (T_{EM} cells), thereby facilitating immune evasion. Because we observed that immunoregulatory macrophages constitute the predominant EPO receptor–positive ($EPOR^+$) population in human and mouse HCC, we hypothesized that $EPOR^+$ macrophages directly mediate the effects of EPO and are indispensable for preventing immunosurveillance in HCC. We found that EPOR reduction in macrophages—achieved either through genetic deletion or macrophage-targeted small interfering RNA treatment—significantly inhibited noninflamed tumor growth, even leading to spontaneous regression of some established tumors. This effect was primarily driven by a robust $CD8^+$ T_{EM} cell response, which synergized with ICB. A similar therapeutic synergy was also observed in established noninflamed tumors treated with either tamoxifen-induced EPOR deletion in macrophages or pharmacological inhibition of EPO/EPOR signaling using an EPOR-Fc chimera decoy receptor to neutralize EPO. Mechanistically, we showed that EPO reprograms proinflammatory macrophages—responsible for chemokine production and antigen presentation to recruit and activate effector T cells—into immunoregulatory macrophages with Kupffer cell–like characteristics. Finally, we identified NRF2 (nuclear factor erythroid 2-related factor 2) as a critical downstream mediator of the EPO/EPOR axis, driving heme depletion and antioxidant production in macrophages, which are key events in immunoregulatory macrophage reprogramming.

CONCLUSION: Using spontaneous preclinical models of HCC with distinct immunotypes, we show that the EPO/EPOR axis functions as an immunosuppressive switch in macrophages that maintains a T cell–deprived TME, thus posing a major barrier to effective antitumor immunity. Inactivation of EPO/EPOR reprograms macrophages to initiate a robust antitumor immune response, converting a noninflamed TME into an inflamed one. These findings point to the EPO/EPOR axis as a promising therapeutic target in HCC. Given that high EPO expression is associated with a poor prognosis across various solid tumors, targeting this axis may prove effective in the treatment of other tumors as well. ■

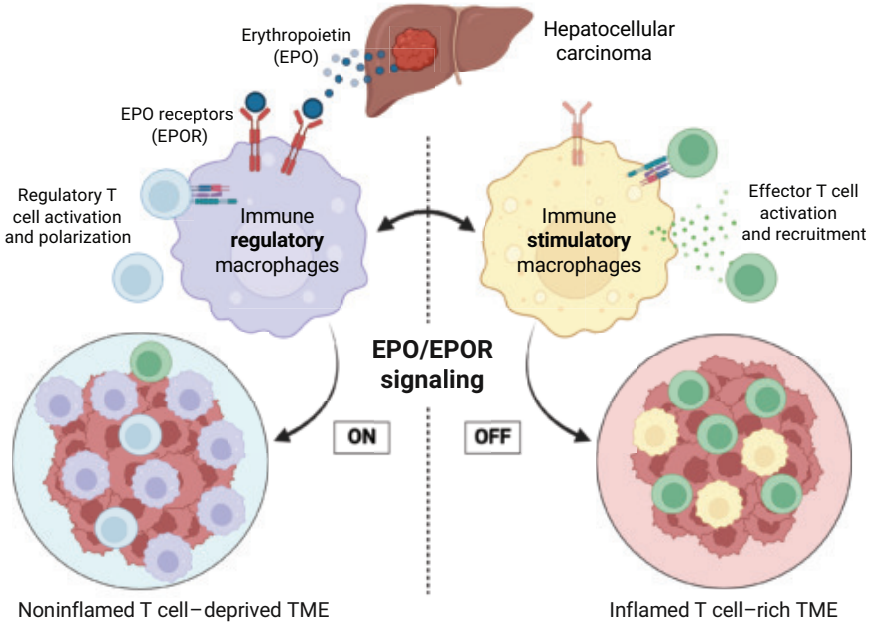

EPO/EPOR signaling in macrophages imposes a noninflamed tumor immunotype. Tumor-derived EPO binds to EPOR on tumor-associated macrophages, preventing their differentiation into immune-stimulatory macrophages that drive effector T cell (green) activation and recruitment. Instead, EPO-stimulated macrophages are immunoregulatory, promote T_{reg} cell (blue) activation, and sustain a noninflamed, T cell–deprived TME. Targeting the EPO/EPOR axis in macrophages converts a noninflamed TME into an inflamed, immune-active state.

The list of author affiliations is available in the full article online.
*Corresponding author. Email: edgareng@stanford.edu (E.G.E.); kcchiu@stanford.edu (D.K.-C.C.)
Cite this article as D. K.-C. Chiu *et al.*, *Science* **388**, eadr3026 (2025). DOI: 10.1126/science.adr3026

READ THE FULL ARTICLE AT
https://doi.org/10.1126/science.adr3026

RESEARCH ARTICLE SUMMARY

TRANSPOSON

Structural mechanism of LINE-1 target-primed reverse transcription

George E. Ghanim*, Hongmiao Hu, Jerome Boulanger, Thi Hoang Duong Nguyen*

INTRODUCTION: Long interspersed element–1 (LINE-1) retrotransposons are the most abundant and the only active autonomous transposable element in humans, accounting for ~17% of the human genome. LINE-1 activity can have profound effects on genomic integrity and has been strongly linked to cancers and various other diseases. The propagation of LINE-1 occurs through a mechanism called target-primed reverse transcription (TPRT). During TPRT, the open reading frame 2 protein (ORF2p), encoded by LINE-1, cleaves the target DNA and reverse transcribes LINE-1 messenger RNA (mRNA) into a new genomic location. To complete the insertion, a second cleavage on the opposite DNA strand and DNA synthesis of this second strand are necessary. The staggered nature of the two cleavages leads to the duplication of the target sequence at both ends of the insertion, a feature known as target site duplication (TSD). However, how ORF2p reorganizes the target DNA for reverse transcription, whether ORF2p nicks both target DNA strands, the factors influencing the variable length of the TSDs, and the involvement of host factors in this process remain largely unknown.

RATIONALE: In this study, we aimed to dissect the molecular mechanisms underlying LINE-1 retrotransposition. We sought to understand how ORF2p handles nucleic acids during TPRT by biochemically and structurally capturing a LINE-1 TPRT complex, which includes ORF2p, a substrate RNA, and an authentic target DNA derived from the human factor VIII gene. Using AlphaFold3 structure prediction, we also explored potential interactions with host factors to elucidate their roles in LINE-1 retrotransposition.

RESULTS: We biochemically stalled ORF2p during TPRT by bypassing the first nicking step and resolved four structures of the TPRT complex using cryo–electron microscopy (cryo-EM). Our structures show that ORF2p bends and unwinds the target DNA, inserting the nicked 3′ end into its active site to prime reverse transcription. We observe that the second DNA strand is also nicked in the TPRT structures. Biochemical experiments confirmed that the endonuclease domain of ORF2p is responsible for second-strand nicking, either before or concurrently with the reverse transcription of the first strand. Structural analysis suggests that the flexibility of the endonuclease domain, along with target DNA unwinding, may contribute to the variability in TSD length.

Notably, the identified nicking sites are close to but do not coincide with the putative nicking site from the patient-derived target DNA sequence. This discrepancy could be attributed to interactions between the LINE-1 ribonucleoprotein (RNP) and other cellular factors. Alphafold3 predictions identify previously unknown interaction sites on ORF2p for proliferating cell nuclear antigen (PCNA) and cytoplasmic poly(A)-binding protein 1 (PABPC1). These binding sites are highly conserved and are critical for retrotransposition. The predicted binding site for PCNA aligns with the position of target DNA in our cryo-EM structure. The predicted interaction with PABPC1 may explain a phenomenon known as cis-preference, in which ORF2p preferentially associates with its encoding mRNA.

Together with structure predictions, our structure and associated experiments allow us to expand on the model of LINE-1 retrotransposition. First, cotranslational interaction between ORF2p and PABPC1 may facilitate ORF2p association with its own mRNA. Upon RNP formation and nuclear import, LINE-1 RNP may be recruited to a target DNA by interaction with PCNA. ORF2p cleaves the first strand, remodels the target DNA, and cleaves the second strand before or during first-strand synthesis. Once the first strand is copied, ORF2p synthesizes the second strand by priming from the nicked second strand, resulting in a new LINE-1 insertion. In this model, premature initiation of second-strand synthesis would result in 5′ truncated insertions.

CONCLUSION: We present the structure of a human LINE-1 TPRT complex, providing insights into the extensive remodeling of the target DNA by ORF2p and clarifying the mechanism of second-strand nicking. We describe previously unidentified PCNA and PABPC1 binding sites on ORF2p, highlighting their potential involvement in LINE-1 retrotransposition. Together, our findings propose a revised model for LINE-1 retrotransposition, detailing an updated sequence of events for TPRT. ■

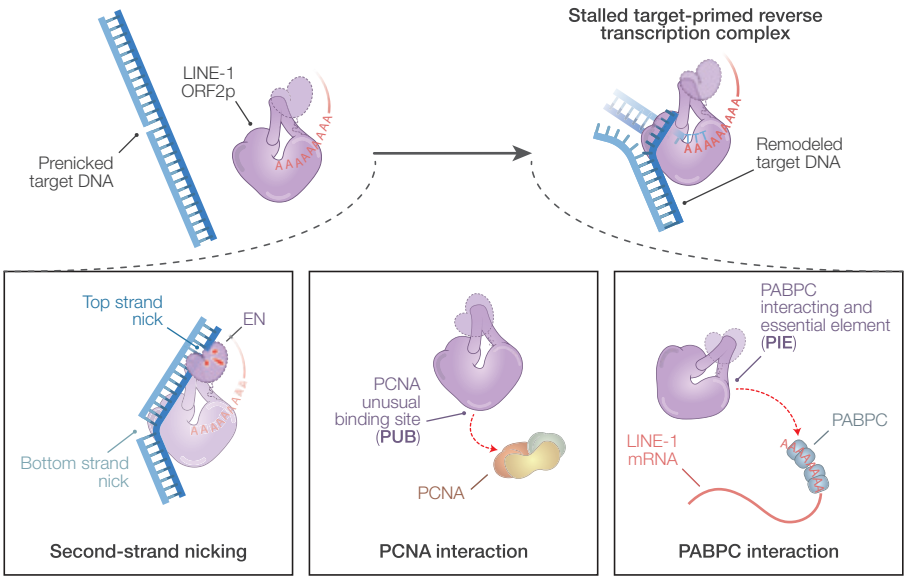

Structural insights from the LINE-1 ORF2p TPRT complex. ORF2p remodels the target DNA in the LINE-1 TPRT complex and nicks the second strand before or with reverse transcription of the first strand. Structure predictions suggest roles for two LINE-1–associated factors, PCNA and PABPC, in the retrotransposition process. EN, endonuclease.

The list of author affiliations is available in the full article online.
*Corresponding author. Email: gghanim@princeton.edu (G.E.G.); knguyen@mrc-lmb.cam.ac.uk (T.H.D.N.)
Cite this article as G. E. Ghanim *et al.*, *Science* **388**, eads8412 (2025). DOI: 10.1126/science.ads8412

READ THE FULL ARTICLE AT
https://doi.org/10.1126/science.ads8412

RESEARCH ARTICLE SUMMARY

PHYSIOLOGY

Distinct adipose progenitor cells emerging with age drive active adipogenesis

Guan Wang†, Gaoyan Li†, Anying Song, Yutian Zhao, Jiayu Yu, Yifan Wang, Wenting Dai, Martha Salas, Hanjun Qin, Leonard Medrano, Joan Dow, Aimin Li, Brian Armstrong, Patrick T. Fueger, Hua Yu, Yi Zhu, Mengle Shao, Xiwei Wu, Lei Jiang, Judith Campisi, Xia Yang*, Qiong A. Wang*

INTRODUCTION: Adipose tissue plays a crucial role in regulating various hormonal and metabolic processes and demonstrates substantial compositional and phenotypic plasticity. From middle age to early aging, adults often experience a notable increase in visceral adipose tissue mass. Visceral adiposity is believed to be an important risk factor for various metabolic disorders. The accumulation of adipose tissue occurs through two primary mechanisms: adipocyte hypertrophy and adipogenesis. However, the mechanisms by which early aging contributes to adipose tissue accumulation remain poorly understood.

RATIONALE: Adipogenesis is the process by which new adipocytes are generated through the proliferation and differentiation of adipose progenitor cells (APCs). Previous reports suggested that APCs exhibit a reduced capacity for adipogenesis in aged humans or rodents in an in vitro, two-dimensional (2D) culture setting. In this work, we used in vivo lineage tracing mouse models, 3D profiling of APC transplants to monitor adipogenesis of APCs up to middle age, and single-cell RNA sequencing to identify distinct types of APCs generated during this life stage. Functional assessments of these age-specific APCs provide insights into how adipogenesis contributes to visceral adipose tissue accumulation during middle age and early aging.

RESULTS: At 12 months old, male mice gained body weight due to increased adipose tissue mass, especially in the visceral site. By contrast, female mice only had moderate body weight gain. Tracking adipogenesis in lineage-tracing mouse models revealed that in contrast to the low turnover rate of adipocytes in young adults, more than 80% of adipocytes were newly generated in the visceral adipose tissue of 12-month-old male mice fed a standard chow diet. Along with this massive adipogenesis, middle-aged mice developed adipocyte hypotrophy, visceral adiposity, reduced energy expenditure, and insulin resistance. 3D profiling of APC transplants quantitatively showed that APCs in middle-aged mice had a much higher adipogenic rate than those in young mice, indicating that these APCs cell-autonomously obtain higher adipogenic potential. Single-cell RNA sequencing of APCs then identified a new committed preadipocyte population that is age enriched (CP-A), both in mice and humans. CP-As displayed high proliferation and differentiation capacities, both in vitro and in vivo. The number of CP-As in the visceral adipose tissue increased when mice were 9 months old, peaked when they were 12 months old, and then sharply declined when they were 18 months old. Leukemia inhibitory factor receptor (LIFR) was identified as a functional marker of CP-A. Pharmacological inhibition and genetic manipulations indicated that LIFR is indispensable for CP-A adipogenesis. The inhibition of LIFR did not affect the adipogenesis of young APCs, indicating that LIFR signaling is specifically required for CP-As. Lastly, chronic treatment with a LIFR inhibitor during early aging prevented the expansion of visceral fat in mice.

CONCLUSION: Integrating in vivo lineage-tracing, 3D profiling of transplants, and single-cell RNA sequencing, our work reveals that adipogenesis of APCs contributes greatly to the visceral adipose tissue expansion during middle age. The discovery of CP-A as an age-specific APC population, along with the validation of its high adipogenic capacity both in vitro and in vivo, and the identification of LIFR signaling as a CP-A–specific adipogenic mechanism enhance our understanding of the early aging process in fat tissue. A key finding from our work is that despite the low turnover rate of adipocytes in young adults, adipogenesis is unlocked during middle age. The increase of adipogenic capacity in APCs distinguishes these cells from most other adult stem cells, which typically exhibit a reduced capacity to proliferate and differentiate with age. Moreover, as the enhancement of adipogenesis and emergence of the CP-A population happens primarily in the male visceral adipose tissue and only during middle age and early aging, these events are location, stage, and sex specific. Our findings offer a fundamental understanding of the pathophysiology of age-related metabolic disorders, which may have critical implications for preventing and treating age-related diseases, thereby promoting healthy aging. ■

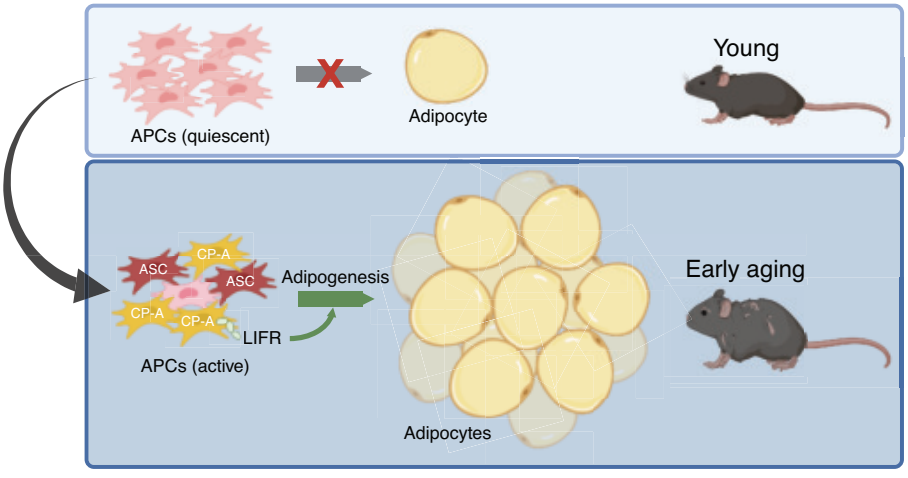

Adipogenesis contributes to age-related visceral adipose tissue accumulation. Male mice gain a large amount of body weight during middle age owing to increased visceral adipose tissue mass. APCs in young adult mice exhibit low adipogenesis activity unless stimulated by metabolic stresses. However, adipogenesis in visceral adipose tissue becomes markedly active during middle age. APCs from middle-aged mice display a cell-autonomous increase in adipogenic potential, generating a distinct committed preadipocyte population that is age enriched (CP-A). CP-As possess high proliferation and differentiation capabilities. LIFR serves as a functional marker that is essential for CP-A adipogenesis. ASC, adipocyte stem cell. [Figure created with BioRender.com]

The list of author affiliations is available in the full article online.
*Corresponding author. Email: xyang123@ucla.edu (X.Y.); qwang@coh.org (Q.A.W.)
†These authors contributed equally to this work.
Cite this article as G. Wang *et al.*, *Science* **388**, eadj0430 (2025). DOI: 10.1126/science.adj0430

READ THE FULL ARTICLE AT
https://doi.org/10.1126/science.adj0430

RESEARCH ARTICLE SUMMARY

BACTERIAL IMMUNITY

Base-modified nucleotides mediate immune signaling in bacteria

Zhifeng Zeng†, Zeyu Hu†, Ruiliang Zhao†, Jikai Rao†, Mario Rodríguez Mestre, Yanqiu Liu, Shunhang Liu, Hao Feng, Yu Chen, Huan He, Nuo Chen, Jinshui Zheng, Donghai Peng, Min Luo, Qunxin She, Rafael Pinilla-Redondo*, Wenyuan Han*

INTRODUCTION: All living organisms must defend themselves against viruses. To do so, they rely on immune systems that detect infections and activate defensive responses, often by producing signaling molecules. Immune systems across bacteria, animals, and plants use similar immune signaling molecules, including cyclic (oligo)nucleotides and adenine diphosphate ribose (ADPR) variants. However, it remains unclear whether other types of immune signals exist.

RATIONALE: To uncover bacterial antiphage systems, researchers often mine "defense islands," genomic regions where immune systems cluster. By using this approach, we identified a previously uncharacterized three-gene system providing broad and robust antiphage protection. Investigating the underlying mechanisms revealed an immune strategy wherein the system hijacks a phage enzyme to produce a base-modified nucleotide signal. We named the system Kongming, after a Chinese strategist known for using the enemy's resources against them.

RESULTS: Kongming encodes three proteins: KomA, an adenosine deaminase; KomB, a modified HAM1-family purine pyrophosphatase; and KomC, a SIR2-like enzyme with nicotinamide adenine dinucleotide (oxidized form; NAD^+)–degrading activity. The system is activated by phage deoxynucleotide monophosphate kinases (DNKs), which are introduced by infecting phages to facilitate their own replication. However, in the presence of Kongming, this phage enzyme instead contributes to the production of deoxyinosine triphosphate (dITP), a base-modified nucleotide that acts as an immune signal.

dITP binds to the KomBC complex, triggering the rapid depletion of NAD^+, a molecule essential for metabolism. This depletion halts cellular activity, preventing phage replication and safeguarding the bacterial population by sacrificing infected cells. Structural and biochemical analyses indicate that KomB has lost its original enzymatic function and now serves as a specialized dITP sensor, enabling activation of KomC's NAD^+-degrading activity.

Kongming generates dITP through two distinct pathways, both requiring collaboration between KomA and phage DNKs. This dual-route synthesis suggests that Kongming has evolved to counter diverse phage replication strategies. In response, some phages have developed a counter-defense enzyme, deoxyribonucleoside 5′-monophosphatase, which depletes deoxyadenosine monophosphate (dAMP), the precursor needed for dITP production, effectively inhibiting immune activation. This ongoing molecular arms race highlights the coevolution of bacterial defenses and phage countermeasures.

Comparative genomic analysis indicates that Kongming has evolved through modular rearrangements, with KomB and KomC consistently found together across bacterial species, whereas their association with KomA is more variable. This suggests the existence of an unexplored diversity of this immune strategy in which Kongming has diversified to combat different viral threats.

CONCLUSION: This study expands the known repertoire of immune signaling by introducing a nucleobase-modified nucleotide as an immune messenger. Unlike other immune pathways, which generate signaling molecules relying on their own enzymatic activities, Kongming hijacks a phage enzyme to complete its immune response, illustrating an unexpected strategy in host-virus interactions. These findings deepen our understanding of bacterial immunity and the molecular battle between bacteria and their viruses. ■

The list of author affiliations is available in the full article online.
*Corresponding author. Email: rafael.pinilla@bio.ku.dk (R.P.-R.); hanwenyuan@mail.hzau.edu.cn (W.H.)
†These authors contributed equally to this work.
Cite this article as Z. Zeng *et al.*, *Science* **388**, eads6055 (2025). DOI: 10.1126/ads6055

READ THE FULL ARTICLE AT
https://doi.org/10.1126/science.ads6055

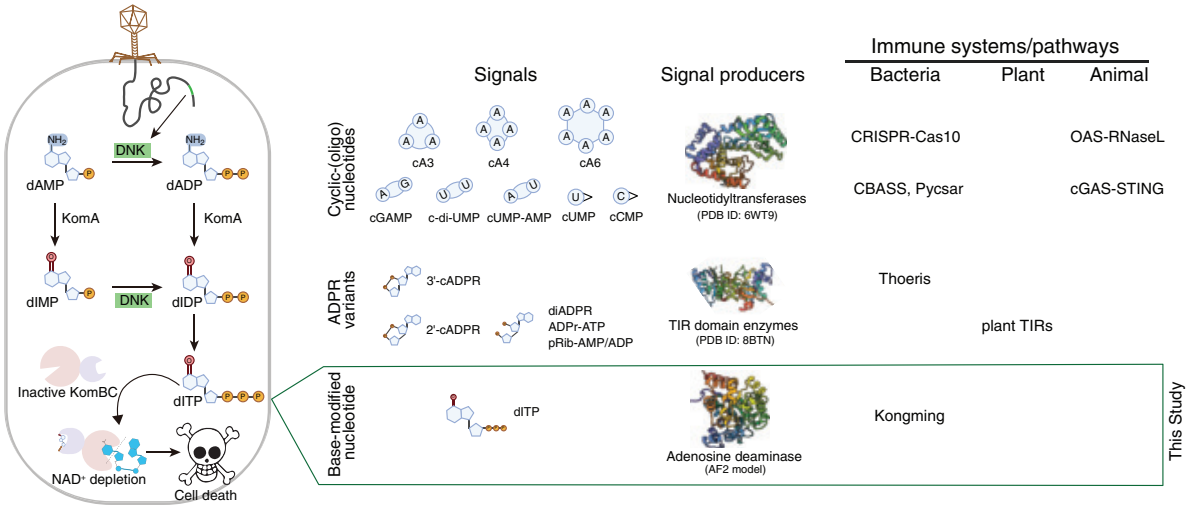

Mechanism of a nucleobase-modified nucleotide immune signaling in bacteria. (Left) Defense mechanism of the Kongming antiphage system. KomA and phage DNKs mediate synthesis of the dITP signal, which activates the KomBC effector complex for NAD^+ depletion. (Right) Comparison of Kongming signaling with the immune pathways across bacteria, plants, and animals that utilize cyclic-(oligo)nucleotides and ADPR variants as signaling molecules. dADP, deoxyadenosine diphosphate; dIMP, deoxyinosine monophosphate; dIDP, deoxyinosine diphosphate; dITP, deoxyinosine triphosphate; cADPR, cyclic ADPR; ATP, adenosine triphosphate; UMP, uridine monophosphate; CMP, cytidine monophosphate; TIR, Toll/interleukin-1 receptor; RNase, ribonuclease.

RESEARCH ARTICLE SUMMARY

AVIAN INFLUENZA

Emergence and interstate spread of highly pathogenic avian influenza A(H5N1) in dairy cattle in the United States

Thao-Quyen Nguyen†, Carl R. Hutter†, Alexey Markin, Megan Thomas, Kristina Lantz, Mary Lea Killian, Garrett M. Janzen, Sriram Vijendran, Sanket Wagle, Blake Inderski, Drew R. Magstadt, Ganwu Li, Diego G. Diel, Elisha Anna Frye, Kiril M. Dimitrov, Amy K. Swinford, Alexis C. Thompson, Kevin R. Snekvik, David L. Suarez, Steven M. Lakin, Stacey Schwabenlander, Sara C. Ahola, Kammy R. Johnson, Amy L. Baker, Suelee Robbe-Austerman*, Mia Kim Torchetti*, Tavis K. Anderson*

INTRODUCTION: Highly pathogenic avian influenza (HPAI) viruses have critical consequences for animal health and the agricultural economy—and may have pandemic potential. HPAI related to the goose/Guangdong 2.3.4.4 hemagglutinin (HA) H5NX phylogenetic clade has spread to nearly 100 countries, and it is recognized as a panzootic. HPAI virus circulation is ongoing in North America, and after a trans-Atlantic incursion in late 2021, the HPAI H5N1 clade 2.3.4.4b virus caused widespread outbreaks. The outbreaks resulted in extensive mortality events, culling of poultry when detected in agricultural systems, and interspecies transmission events into mammals. It is critical to determine how HPAI clade 2.3.4.4b evolves in wild birds and in nonhuman mammals after spillover to assess the potential for human infection and transmission.

RATIONALE: In late January 2024, veterinarians observed dairy cattle displaying decreased feed intake and changes in milk quality and production. On 25 March 2024, HPAI H5N1 clade 2.3.4.4b was confirmed in dairy cattle in Texas. Shortly thereafter, the virus was identified in cattle in eight other United States (US) states by members of the National Animal Health Laboratory Network. The goal of this study was to analyze genetic sequence data collected after the introduction of HPAI H5N1 in late 2021 into the Atlantic flyway of North America and its onward circulation and reassortment with North American wild bird–origin low-pathogenicity viruses. These data were combined with whole-genome sequence data and epidemiological information from the HPAI H5N1 outbreak among US dairy cattle to help us understand when the interspecies transmission event to cattle occurred and the consequences of animal movement for virus spread.

RESULTS: H5N1 clade 2.3.4.4b genotype B3.13 influenza A virus was confirmed in milk with limited detections in nasal swabs. The initial outbreak included samples from 26 dairy cattle premises across eight states and six poultry premises in three states. The sequences isolated from cattle clustered within a single group in phylogenetic analyses, supporting a single spillover event in late 2023. A reassortment event preceded the spillover, and after introduction, the virus persisted in cattle with evidence for transmission from cattle into poultry and peridomestic animal species. Epidemiological records and phylodynamic modeling documented that the movement of asymptomatic or presymptomatic dairy cattle resulted in the dissemination of the virus across the US. We identified low-frequency within-host sequence variants across the genome that were associated with changes in virulence, host-range specificity, and mammalian adaptation.

CONCLUSION: A single wild bird-to-cattle transmission event of HPAI H5N1 clade 2.3.4.4b occurred in late 2023. The spillover was likely preceded by a reassortment event in wild bird populations followed by the movement of cattle that spread HPAI within the US dairy herd. Molecular markers that may lead to changes in transmission efficiency and phenotype were detected at low frequencies. Continued transmission of H5N1 HPAI within dairy cattle increases the risk for infection and subsequent spread of the virus to humans and other host populations. ■

The list of author affiliations is available in the full article online.
***Corresponding author. Email: tavis.anderson@usda.gov (T.K.A.); mia.kim.torchetti@usda.gov (M.K.T.); suelee.robbe-austerman@usda.gov (S.R.-A.)**
†These authors contributed equally to this work.
Cite this article as T.-Q. Nguyen *et al.*, *Science* 388, eadq0900 (2025). DOI: 10.1126/science.adq0900

READ THE FULL ARTICLE AT
https://doi.org/10.1126/science.adq0900

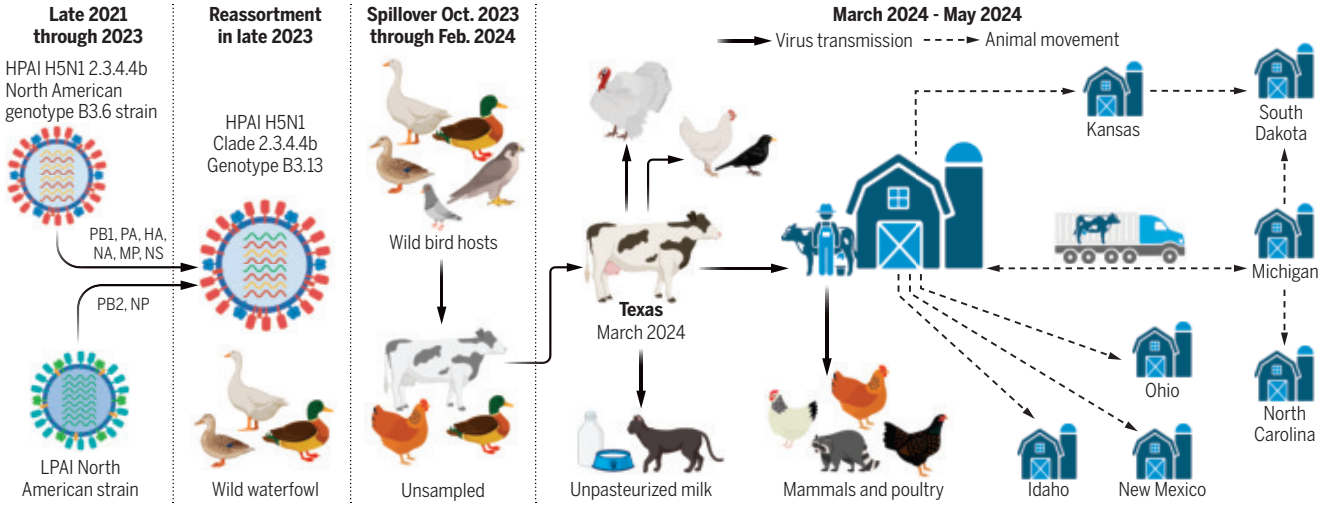

The emergence and spread of highly pathogenic avian influenza virus H5N1 clade 2.3.4.4b in dairy cattle in the US. Highly pathogenic avian influenza (HPAI) H5N1 was detected in North America in late 2021, and epidemiological information and genomic analysis demonstrated a single spillover into dairy cattle by a reassorted HPAI H5N1 genotype B3.13 virus. The virus disseminated across the US through the movement of asymptomatic or presymptomatic animals and was subsequently reintroduced from dairy cattle back into other host species.

RESEARCH ARTICLES

QUANTUM SIMULATION

Observation of generalized *t-J* spin dynamics with tunable dipolar interactions

Annette N. Carroll[1]*, Henrik Hirzler[1]†, Calder Miller[1], David Wellnitz[1], Sean R. Muleady[1,2], Junyu Lin[1], Krzysztof P. Zamarski[1,3], Reuben R. W. Wang[1]‡§, John L. Bohn[1], Ana Maria Rey[1], Jun Ye[1]*

Long-range and anisotropic dipolar interactions profoundly modify the dynamics of particles hopping in a periodic lattice potential. We report the realization of a generalized *t-J* model with dipolar interactions using a system of ultracold fermionic molecules with spin encoded in the two lowest rotational states. We independently tuned the dipolar Ising and spin-exchange couplings and the molecular motion and studied their interplay on coherent spin dynamics. Using Ramsey spectroscopy, we observed and modeled interaction-driven contrast decay that depends strongly both on the strength of the anisotropy between Ising and spin-exchange couplings and on motion. This study paves the way for future exploration of kinetic spin dynamics and quantum magnetism with highly tunable molecular platforms in regimes that are challenging for existing numerical and analytical methods.

The *t-J* model, which arises from the more general Fermi-Hubbard model in the limit of large onsite interactions U, fundamentally describes a competition between motion via tunneling between lattice sites, t, and spin interactions, J, caused by superexchange through virtual tunneling of particles in adjacent lattice sites. The model has long been proposed to explain unconventional phases, including high-temperature superconductivity (*1*–*3*). Ultracold atoms with contact interactions have recently emerged as a controllable system to study the behavior of this model, but the $J \sim t^2/U$ scaling of superexchange has limited the range of accessible phases to $J \ll t$ and imposes stringent low temperature requirements to observe interaction-induced phase transitions (*4*–*6*).

Adding long-range anisotropic dipolar interactions, where J can be tuned independently of t, softens the low-temperature constraints on phase transitions and generates a generalized *t-J* model that is predicted to produce exotic phases, including an enhanced superfluid state (*7*, *8*). Magnetic atoms provide access to dipolar interactions that, while relatively weak, have recently produced a variety of quantum phase transitions (*9*, *10*) and out-of-equilibrium spin dynamics in optical lattices (*11*–*15*). Ultracold polar molecules offer the advantage of stronger, tunable dipolar interactions (*16*–*21*). With electric field ($\boldsymbol{E}$)–tunable interactions between pseudo-spins encoded in rotational states, effective spin and spin-motion models can be implemented with high controllability (*22*) if two-body loss is suppressed by either strong confinement into lower dimensions (*23*) or collisional shielding with microwaves (*24*–*30*) or static electric fields (*31*–*35*). The extended lifetime of these itinerant molecules enables the combination of motion and strong dipolar interactions to study exotic spin-motion phenomena. Here, we report the realization of a generalized *t-J* model using ultracold dipolar molecules and the exploration of the system's out-of-equilibrium dynamics with independent control over both the motion and the interaction anisotropy $\chi = J_Z - J_\perp$ between spin-exchange ($J_\perp$) and Ising (J_Z) couplings in an XXZ spin model.

Dipolar interactions between molecules in optical lattices

We prepared degenerate gases of ^{40}K and ^{87}Rb in a crossed optical dipole trap and loaded these atoms into the ground band of a three-dimensional (3D) lattice with spacing a_y = 540 nm in the vertical direction and $a_x = a_z$ = 532 nm in the horizontal directions. The atoms were then converted to fermionic KRb molecules (*36*) in their rovibrational ground state $|0\rangle$, where $|N\rangle$ is the rotational state with $\boldsymbol{E}$-dressed quantum number N and projection $m_N = 0$ onto the quantization axis set by $\boldsymbol{E}$. The highest observed average molecular filling fraction was about 13%. For the spin measurements throughout this work, we used the two lowest rotational states of the molecule $|0\rangle$ and $|1\rangle$ as our spin-1/2 manifold, referred to as $|\downarrow\rangle$ and $|\uparrow\rangle$, respectively.

Heteronuclear molecules intrinsically have field-tunable dipolar interactions. The rotational states have induced dipole moments $d_\downarrow = \langle\downarrow|d_y|\downarrow\rangle$ and $d_\uparrow = \langle\uparrow|d_y|\uparrow\rangle$ and transition dipole moment $d_{\downarrow\uparrow} = \langle\downarrow|d_y|\uparrow\rangle$, where d_y is the dipole operator along $\hat{y}$, the quantization axis set by $\boldsymbol{E}$. These dipole moments depend on $|\boldsymbol{E}|$, with $d_\downarrow \approx d_\uparrow \approx 0$ at $|\boldsymbol{E}| \approx 0$ and $|d_\downarrow|, |d_\uparrow| > 0$ at $|\boldsymbol{E}| > 0$, as other rotational states get mixed into the field-dressed state $|N\rangle$. The dipolar interactions and the motional confinement provided by optical lattices are illustrated in Fig. 1, A and B.

Dipolar interactions are described by

$$\hat{H}_{\text{int}} = h\int d^3\boldsymbol{r}\int d^3\boldsymbol{r}'\frac{[1-3\cos^2(\theta)]a_x^3}{2|\boldsymbol{r}-\boldsymbol{r}'|^3}\times \left\{\begin{array}{l}\frac{J_\perp}{2}\left[\hat{s}^+(\boldsymbol{r})\hat{s}^-(\boldsymbol{r}')+\hat{s}^+(\boldsymbol{r}')\hat{s}^-(\boldsymbol{r})\right]+J_Z\hat{s}^Z(\boldsymbol{r})\hat{s}^Z(\boldsymbol{r}')+\\ V\hat{n}(\boldsymbol{r})\hat{n}(\boldsymbol{r}')+W\left[\hat{n}(\boldsymbol{r})\hat{s}^Z(\boldsymbol{r}')+\hat{s}^Z(\boldsymbol{r})\hat{n}(\boldsymbol{r}')\right]\end{array}\right\} \quad (1)$$

where $\hat{\psi}_\sigma(\boldsymbol{r})$ is the fermionic field operator at position $\boldsymbol{r}$ with spin σ (*7*, *8*, *36*), $\hat{n}(\boldsymbol{r}) = \sum_\sigma \hat{\psi}_\sigma^\dagger(\boldsymbol{r})\hat{\psi}_\sigma(\boldsymbol{r})$ is the density, $\hat{s}^Z(\boldsymbol{r}) = \left[\hat{\psi}_\uparrow^\dagger(\boldsymbol{r})\hat{\psi}_\uparrow(\boldsymbol{r}) - \hat{\psi}_\downarrow^\dagger(\boldsymbol{r})\hat{\psi}_\downarrow(\boldsymbol{r})\right]/2$ is the local magnetization, and $\hat{s}^+(\boldsymbol{r}) = \hat{\psi}_\uparrow^\dagger(\boldsymbol{r})\hat{\psi}_\downarrow(\boldsymbol{r})$ ($\hat{s}^-(\boldsymbol{r}) = \left[\hat{s}^+(\boldsymbol{r})\right]^\dagger$) raises (lowers) the spin. θ is the angle between $\boldsymbol{E}$ and $\boldsymbol{r}-\boldsymbol{r}'$. $hJ_\perp = 2d_{\downarrow\uparrow}^2/\left(4\pi\epsilon_0 a_x^3\right)$ is the spin-exchange interaction, $hJ_Z = \left(d_\downarrow - d_\uparrow\right)^2/\left(4\pi\epsilon_0 a_x^3\right)$ is the Ising interaction arising from differential dipole moments of the two states, $hV = \left(d_\downarrow + d_\uparrow\right)^2/\left(16\pi\epsilon_0 a_x^3\right)$ is the density-density interaction due to average dipole moments, and $hW = \left(d_\uparrow^2 - d_\downarrow^2\right)/\left(8\pi\epsilon_0 a_x^3\right)$ is the residual spin-density interaction arising from the cross-term of differential and average dipole moments. The relationship between dipole moments and $J_\perp$, J_Z, V, and W is illustrated in Fig. 1C. The full Hamiltonian is $\hat{H} = \hat{H}_{\text{sp}} + \hat{H}_{\text{int}}$ (*36*), where $\hat{H}_{\text{sp}} = \int d^3\boldsymbol{r}\sum_\sigma \hat{\psi}_\sigma^\dagger(\boldsymbol{r})H_0\hat{\psi}_\sigma(\boldsymbol{r})$ and $H_0 = -\frac{\hbar^2}{2m}\nabla^2 + \sum_{\alpha=x,y,z} V_{\text{L},\alpha}\sin^2\left(\frac{\pi r_\alpha}{a_\alpha}\right)$ describe the kinetic and lattice potential energies, respectively (for simplicity, we neglect an external confining potential). Here, $\hbar = h/2\pi$ is the reduced Planck constant, m is the mass of ^{40}K^{87}Rb, and $V_{\text{L},\alpha}$ is lattice depth in the $\alpha \in (x, y, z)$ direction.

In a deep 3D optical lattice, molecules cannot move, and the Hamiltonian becomes a spin model of frozen dipoles. In contrast, in the absence of horizontal lattices ($V_{\text{L},x} = V_{\text{L},z} = 0$), molecules are fully itinerant, so the Hamiltonian describes quasi-2D dipolar collisions

[1]JILA, National Institute of Standards and Technology, and Department of Physics, University of Colorado, Boulder, CO, USA. [2]Joint Center for Quantum Information and Computer Science, Joint Quantum Institute, National Institute of Standards and Technology, and University of Maryland, College Park, MD, USA. [3]Institut für Experimentalphysik und Zentrum für Quantenphysik, Universität Innsbruck, Innsbruck, Austria.
*Corresponding author. Email: annette.carroll@colorado.edu (A.N.C.); ye@jila.colorado.edu (J.Y.)
†Present address: Institute for Quantum Electronics, ETH Zürich, Zürich, Switzerland.
‡Present address: ITAMP, Center for Astrophysics | Harvard & Smithsonian, Cambridge, MA, USA.
§Present address: Department of Physics, Harvard University, Cambridge, MA, USA.

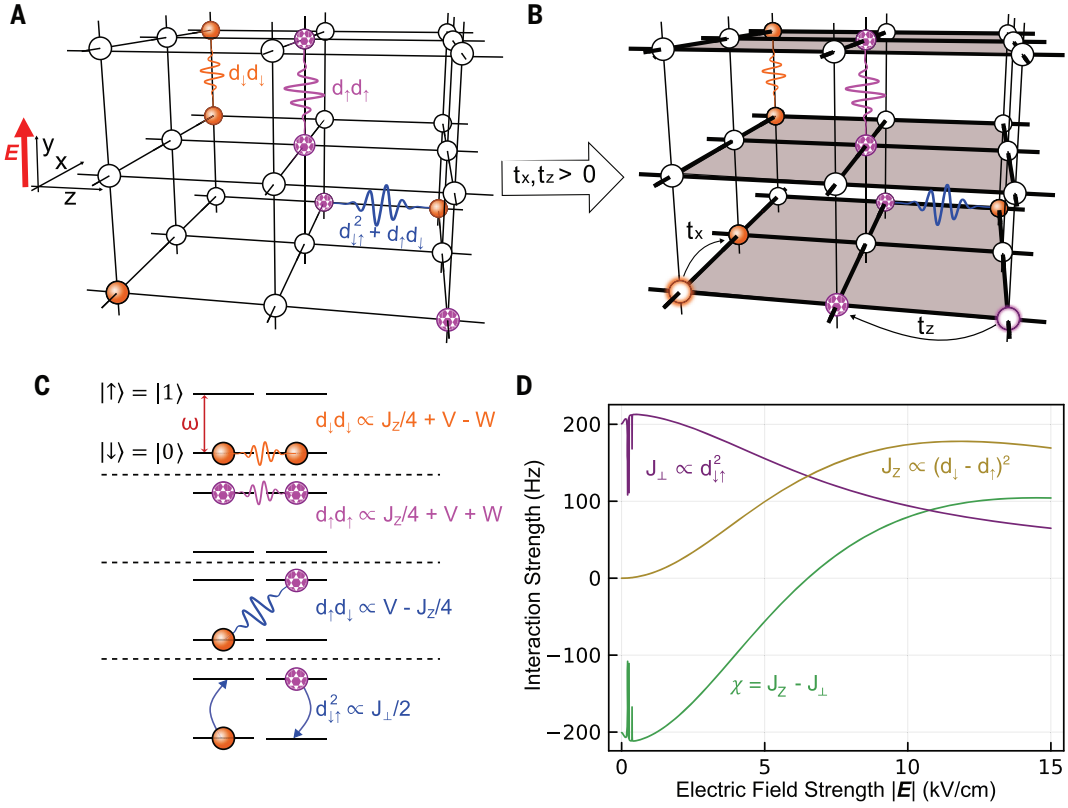

Fig. 1. Field-tunable dipolar interactions between lattice-confined molecules. (**A**) Molecules sparsely occupy a deep 3D optical lattice. Sites are shaded white if unoccupied, pink patterned if in the $|\uparrow\rangle$ state, and solid orange if in the $|\downarrow\rangle$ state. Molecules interact through induced dipole moments and transition dipole moments represented by squiggly lines between lattice sites. (**B**) Lowering the lattice depth in the horizontal directions allows tunneling between sites within layers, represented by the black arrows t_x and t_z. For most of our experiments, $t_x = t_z$. (**C**) Molecular interactions arising from dipole moments can be rewritten in terms of $J_\perp$, J_Z, V, and W, the spin-exchange, Ising, density-density, and spin-density interactions, respectively, which are used in a spin-basis Hamiltonian. The interactions set by $d_\downarrow^2$, $d_\uparrow^2$, $d_\uparrow d_\downarrow$, and $d_{\downarrow\uparrow}^2$, and their associated Hamiltonian terms, are drawn schematically from top to bottom. The two lowest rotational states of the molecules, $|\downarrow\rangle$ and $|\uparrow\rangle$, are split by microwave frequencies ω (red arrow between spin levels in the top row) between 2.2 GHz and 4.2 GHz, depending on electric field strength ($|\boldsymbol{E}|$). (**D**) Calculated dipolar interaction strengths for KRb molecules separated by 532 nm perpendicular to the dipole orientations as a function of $|\boldsymbol{E}|$. Purple represents the spin-exchange interaction $J_\perp$ arising from the transition dipole moment between a $|\downarrow\rangle$ molecule and a $|\uparrow\rangle$ molecule, which decreases with increasing electric field magnitude. Gold represents the Ising interaction J_Z from induced dipole moments, which increases with increasing field strength. Green represents the interaction-type anisotropy $\chi = J_Z - J_\perp$, which crosses zero at around 6.5 kV/cm. Hyperfine structure of the molecules produces interaction strengths that change drastically with small changes in $|\boldsymbol{E}|$ for small electric fields of <1 kV/cm.

where the motion is confined to two dimensions, but the interaction potential remains 3D (*37*). Between these two extremes, both motion and interactions become discretized on a lattice, and the full Hamiltonian reduces to a generalized *t-J* Hamiltonian, the *t-J-V-W* model (*7*, *8*)

$$\hat{H}_{tJVW} = -h\sum_{\langle i,j\rangle,\sigma} t_{ij}\left[\hat{c}_{i\sigma}^\dagger \hat{c}_{j\sigma} + h.c.\right] + h\sum_{i\neq j}\frac{V_{ij}}{2}\left[J_\perp(\hat{\boldsymbol{s}}_i\cdot\hat{\boldsymbol{s}}_j) + \chi\left(\hat{s}_i^Z\hat{s}_j^Z\right) + V\hat{n}_i\hat{n}_j + W\left(\hat{n}_i\hat{s}_j^Z + \hat{n}_j\hat{s}_i^Z\right)\right] + hU\sum_i \hat{n}_{i\downarrow}\hat{n}_{i\uparrow} \quad (2)$$

where $\hat{c}_{i\sigma}^\dagger$ is the fermionic creation operator at lattice site i for spin σ, and we have $\hat{n}_{i\sigma} = \hat{c}_{i\sigma}^\dagger\hat{c}_{i\sigma}$, total site occupation $\hat{n}_i = \sum_\sigma \hat{n}_{i\sigma}$, and magnetization $\hat{s}_i^Z = \left(\hat{c}_{i\uparrow}^\dagger\hat{c}_{i\uparrow} - \hat{c}_{i\downarrow}^\dagger\hat{c}_{i\downarrow}\right)/2$. t_{ij} characterizes the hopping rate of molecules between neighboring sites i and j, denoted $\langle i,j\rangle$. V_{ij} captures the geometric $(1 - 3\cos^2\theta)a_x^3/r^3$ component of the interactions. Strong kilohertz-scale on-site interaction U, rapid on-site two-body loss, and low filling fractions prohibit double occupancy of lattice sites and suppress superexchange interactions. The spin interaction anisotropy χ parameterizes rich spin dynamics that were previously studied at the mean field level (*22*) and produces one-axis twisting that can be used to generate entangled states (*38*, *39*). The $\boldsymbol{E}$-tunability of the interactions for molecules on neighboring lattice sites in the $\hat{x}-\hat{z}$ plane is shown in Fig. 1D. We note that V is spin independent and small compared with spin-spin interactions and thus not expected to appreciably affect the spin dynamics observed here (*36*).

Coherent spin dynamics probed with Ramsey spectroscopy

To explore the out-of-equilibrium coherent dynamics of the molecules in different interaction regimes and geometries of the generalized *t-J* model, we measured the Ramsey contrast decay (Fig. 2A). First, an applied microwave pulse prepared an equal superposition of the $|\downarrow\rangle$ and $|\uparrow\rangle$ states. In a Bloch sphere picture, the collective Bloch vector was prepared along $\hat{X}$ with maximal length $N_{\mathrm{mol}}/2$ for total molecule number N_{mol}. The system was allowed to evolve for a variable time T before a microwave pulse of area $\pi/2$ about variable axis $\hat{R} = \cos\varphi\hat{X} + \sin\varphi\hat{Y}$ was applied. The number of molecules in each spin state was then measured (*36*). By repeating the measurement several times while varying the phase φ of the second pulse and taking the standard deviation of the fraction in the excited state, the contrast, or the equatorial length of the Bloch vector, $C = \frac{2}{N_{\mathrm{mol}}}\sqrt{\left\langle\sum_i \hat{s}_i^X\right\rangle^2 + \left\langle\sum_i \hat{s}_i^Y\right\rangle^2}$ at wait time T was extracted (*36*). Because $\left\langle\sum_i \hat{s}_i^Z\right\rangle = 0$ is conserved during the dynamics, C describes the magnetization of the sample. During T, a KDD pulse sequence (*40*) suppresses single-particle dephasing by frequently swapping the populations in the $|\downarrow\rangle$ and $|\uparrow\rangle$ states (*36*). Dynamical decoupling also removes the W term in the *t-J-V-W* Hamiltonian. The contrast evolution was then fit to a stretched exponential via $C(T) = e^{-(\Gamma T)^\nu}$, where Γ is the dephasing rate and ν is the stretching parameter. We observed $\nu < 1$ for all parameters analyzed in this work, describing subexponential decay, possibly associated with glassy dynamics (*41*) and number loss (*36*).

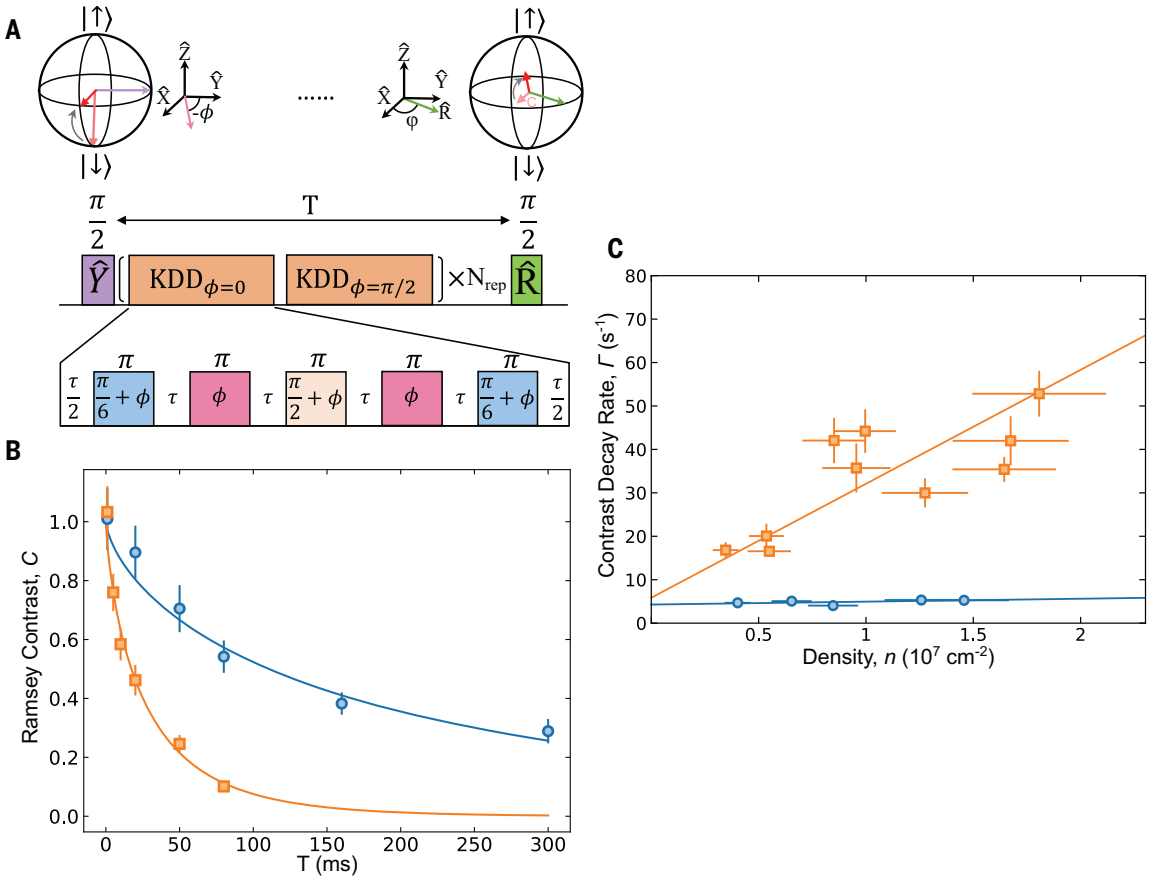

Fig. 2. Dynamical magnetization of interacting pinned molecules. (**A**) Ramsey spectroscopy is used to measure the dynamical magnetization of the molecules. The top row shows the orientation of the collective spin in the Bloch sphere representation, and the middle and bottom rows show the pulse sequence. A $\pi/2$ pulse about the $\hat{Y}$ axis prepares the molecules in a coherent superposition of $1/\sqrt{2}(|\downarrow\rangle + |\uparrow\rangle)$. A KDD pulse sequence (shown as the bottom row) removes single-particle dephasing and is repeated a variable number of times N_{rep} to extend the total interrogation time to T. A final $\pi/2$ pulse about variable axis $\hat{R}$ reads out the projection of the Bloch vector orthogonal to $\hat{R}$. By repeating the measurements varying $\hat{R}$, the equatorial length of the Bloch vector, which is the Ramsey contrast (dynamical magnetization) C, at time T is extracted. (**B**) Measured contrast decay $C(T)$ for χ = 0 (blue circles) and χ = 102 Hz (orange squares) for initial 2D average densities (n) of roughly 1.5 × 10^7 cm^{-2} of molecules confined in a deep 3D optical lattice. Solid lines are stretched exponential fits to the experimental data. Error bars are 1 SD from bootstrapping (*36*). (**C**) Extracted Ramsey contrast decay rates versus initial density for χ = 0 (blue circles) and χ = 102 Hz (orange squares). Solid lines are linear fits to the data whose slopes measure density-dependent decoherence rate κ. Error bars are 1 SE from fits (stretched exponential fit for contrast decay rates, one-body loss for densities).

To examine the effect of field-tunable interactions on spin coherence, we first froze the motional degree of freedom by confining the molecules in a deep 3D optical lattice ($t_{ij} \approx 0$ in all directions). At zero electric field, $d_\downarrow \approx d_\uparrow \approx 0$, molecules interact predominately through spin exchange, realizing the XY model $\hat{H}_{XY} = h\sum_{i\neq j} \frac{V_{ij}}{2} J_\perp \left(\hat{s}_i^X \hat{s}_j^X + \hat{s}_i^Y \hat{s}_j^Y\right)$. The coherent spin dynamics in this regime at low fillings have been studied (*16*, *17*, *42*), revealing density-dependent Ramsey contrast decay from long-range interactions, with periodic revivals in contrast arising from spin exchange between nearest neighbors. Turning on static $\boldsymbol{E}$ to add Ising interactions realizes the XXZ model $\hat{H}_{XXZ} = h\sum_{i\neq j} \frac{V_{ij}}{2}\left[J_\perp(\hat{\boldsymbol{s}}_i \cdot \hat{\boldsymbol{s}}_j) + \chi\left(\hat{s}_i^Z \hat{s}_j^Z\right)\right]$. Previous works have studied the coherent dynamics of this model in the presence of strong disorder using Floquet engineering on platforms such as nitrogen-vacancy centers in diamond (*43*) and Rydberg atoms (*44*). In this study, we utilized polar molecules to probe these lattice spin models beyond the pure spin-exchange regime. At the Heisenberg point (χ = 0 at $|\boldsymbol{E}|$ = 6.5 kV/cm), the Hamiltonian reduces to the isotropic XXX model $\hat{H}_{XXX} = h\sum_{i\neq j} \frac{V_{ij}}{2} J_\perp(\hat{\boldsymbol{s}}_i \cdot \hat{\boldsymbol{s}}_j)$, where the interactions are independent of spin orientation, making all points on the collective Bloch sphere eigenstates of the Hamiltonian. As such, there should be no interaction-induced dephasing. Figure 2B shows contrast decay traces and fits to stretched exponentials for average 2D densities of roughly 1.5 × 10^7 cm^{-2} at two different values of $\boldsymbol{E}$ where χ = 0 (blue circles) and χ = 102 Hz (orange squares, $|\boldsymbol{E}|$ = 12.72 kV/cm). We observed an order of magnitude slower contrast decay at the Heisenberg point than at χ = 102 Hz.

If interactions limit the coherence time, higher densities should lead to faster contrast decay. To extract the effect of many-body processes, the contrast decay measurement was repeated for different initial average 2D densities n (*36*). The contrast decay rates for each n were fit to a linear function $\Gamma(n) = \kappa n + \Gamma_0$, where Γ_0 is the single-particle dephasing rate after dynamical decoupling and κ is the many-body dephasing rate. This density-normalization procedure is shown in Fig. 2C for χ = 0 (blue circles) and χ = 102 Hz (orange squares). Prominently, in the χ = 0 case, we measured κ = 0.07(7) × 10^{-6} cm^2 s^{-1}, consistent with no density-dependent contrast decay, as expected in the XXX model with a single-body dephasing rate, determined from the linear slope offset, of Γ_0 = 4.3(7) s^{-1}. By contrast, for χ = 102 Hz, we observed contrast decay rates that depend strongly on density, with κ = 2.6(4) × 10^{-6} cm^2 s^{-1} and Γ_0 = 6(3) s^{-1}.

Interaction-limited decoherence dynamics

Repeating the measurement at several values of $|\boldsymbol{E}|$ in the pinned configuration, we observed a roughly linear dependence of κ on $|\chi|$, with a slight dependence on the sign of χ (Fig. 3A). κ depends approximately linearly on $|\chi|$ because dephasing in our lattice originates from couplings with strength proportional to χ within local clusters of molecules. We attribute the observed slower decay in

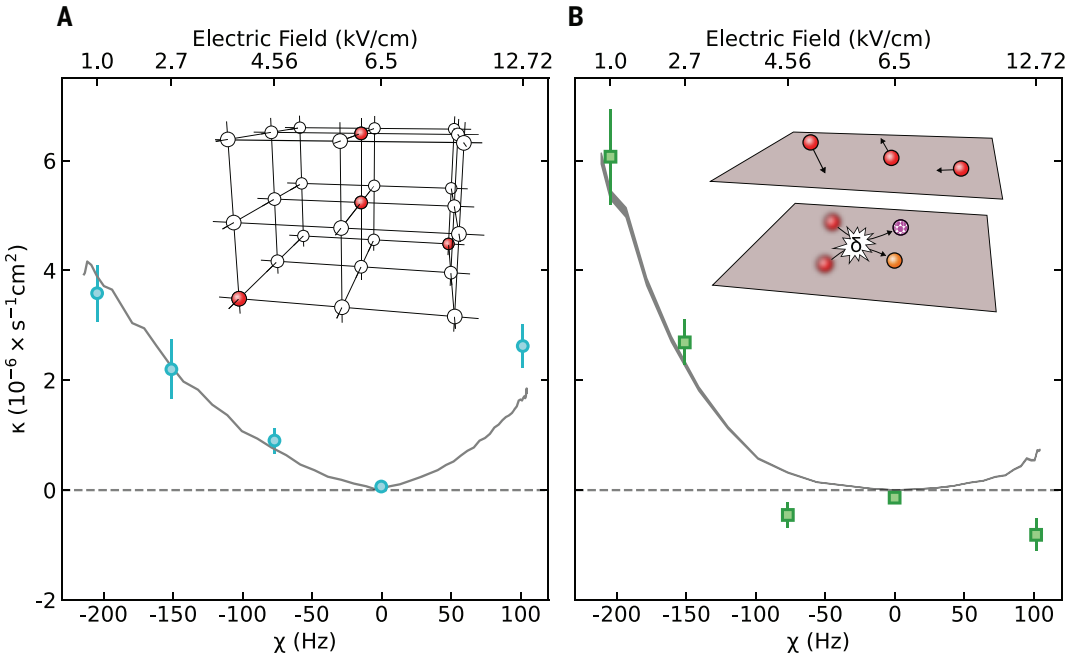

Fig. 3. Field-tunable density-dependent decoherence rates. (**A**) Density-normalized contrast decay rates κ for pinned molecules tuned with interaction anisotropy χ. Blue circles are experimental data extracted from slopes in Fig. 2C. Error bars are 1 SE from linear fits. Gray line is a MACE simulation (*36*) with the same density-normalization procedure as experimental data with no scaling. (Inset) 3D lattice with fully pinned molecules, with white circles representing unoccupied sites and red circles denoting sites occupied by a molecule initially in $1/\sqrt{2}(|\downarrow\rangle + |\uparrow\rangle)$. (**B**) As in (A), but for molecules confined to 2D layers without horizontal corrugation. Green squares are experimental data. Error bars are 1 SE from linear fits. Gray shaded band is from Monte Carlo coherent collision simulations with no scaling (*36*), with the band halfwidth representing 1 SE of linear fit. (Inset) 2D geometry of the system, with molecules (red circles) free to move within 2D layers. In the bottom 2D layer, collisional dephasing occurs when a collision leads to a relative phase shift $\delta = \delta_{\leftrightarrow} - \delta_{\updownarrow}$, making the molecules no longer identical after the collision, illustrated as one molecule becoming pink and the other turning orange.

the $J_\perp$-dominated ($\chi < 0$) regime to periodic self-rephasing from spin exchange within local clusters that is suppressed in the J_Z-dominated ($\chi > 0$) regime (*36*). We also modeled the contrast dynamics using a moving-average cluster expansion (MACE) (*36*, *42*). In this approximation, the dynamics for a given molecule are solved exactly in the presence of its M most strongly coupled neighbors. The global contrast dynamics are then obtained by averaging these "cluster" dynamics for every molecule in the system, with reasonable convergence being obtained for clusters as small as $M = 6$. This convergence for a small particle number is an indicator of the local nature of the spin dynamics under anisotropic dipolar interactions in three dimensions, whereas the spin dynamics for isotropic interactions can depend collectively on all particles in the system in certain geometries (*45*–*47*). The results of the MACE simulation (Fig. 3A, gray trace) show excellent agreement between theory and experiment and confirm that pinned dipolar spin dynamics are well described by the XXZ model.

Next, we observed modifications to the many-body dephasing rates from collisions of fully itinerant molecules. To probe the interplay of motion with spin-dependent dipolar interactions, we confined the molecules to 2D layers formed by a vertical lattice of $65E_r$ depth, where $E_r \approx h \times 1.4$ kHz is the photon recoil energy for KRb. In these experiments, without any horizontal lattice potential ($V_{L,x} = V_{L,z} = 0$), radial harmonic confinement was provided predominantly by a crossed optical dipole trap, which was also maintained for all other experiments. We then extracted the density-normalized dephasing rate κ as a function of χ, as in the pinned molecule case (Fig. 3B, green squares). In prior work (*22*), the short-time mean-field dynamics were well described by an XXZ spin model with spins pinned in a harmonic oscillator mode space lattice (*36*). At longer times relevant for the current measurements, the thermal occupation of our sample enabled molecules to delocalize in mode space caused by mode-changing collisions, invalidating the pinned mode picture. Although collisional decoherence was previously observed in ultracold molecules (*22*), the dependence on dipolar interactions was not completely understood, and modeling dipolar collisional dephasing of coherent superpositions has been challenging.

We systematically measured that κ depends more strongly on $|\chi|$ than in the pinned case, and we present a scattering approach to study the $V_{L,x} = V_{L,z} = 0$ limit of the molecular Hamiltonian to explain our observations. We adopted two methods of theoretical analysis (*36*): collisional Monte Carlo simulations and a simplified analytic model. Data obtained from Monte Carlo simulations (Fig. 3B, gray trace) show agreement with the experimental data, apart from experimentally measured negative values of κ. We attribute these negative values to the preferential two-body loss of decohered molecules (*36*). The agreement between theory and experiment suggests that our theoretical model captures the relevant physics from collisional dephasing of molecular superpositions.

The simplified analytic model provides a more intuitive understanding of the observed stronger, approximately cubic dependence of κ on $|\chi|$. With the molecular spins initially prepared in the state $|X\rangle = (|\uparrow\uparrow\rangle + |\downarrow\downarrow\rangle + |\uparrow\downarrow\rangle + |\downarrow\uparrow\rangle)/2$, their first collision would only involve states in the symmetric spin sector: $|\downarrow\downarrow\rangle$, $(|\uparrow\downarrow\rangle + |\downarrow\uparrow\rangle)/\sqrt{2}$, and $|\uparrow\uparrow\rangle$, which each accrue a scattering phase shift. Collisions in this sector are predominantly elastic, as Fermi statistics suppresses close contact of the molecules, implying that long-ranged dipolar interactions dominate these phase shifts. We therefore expect that completed collisions are slow compared with the dynamical decoupling pulses that rapidly flip molecules between $|\downarrow\rangle$ and $|\uparrow\rangle$. The result is that the aligned $(\updownarrow)|\downarrow\downarrow\rangle$ and $|\uparrow\uparrow\rangle$ spin states will both incur the same scattering phase shift $\delta_\updownarrow$ proportional to dipole length (*48*): $a_D^{\updownarrow} \propto d_\downarrow^2 + d_\uparrow^2 \propto V + \frac{J_\perp}{4} + \frac{\chi}{4}$. The remaining anti-aligned triplet state ($\leftrightarrow$) will, in general, develop a different phase shift $\delta_\leftrightarrow$ proportional to the dipole length $a_D^{\leftrightarrow} \propto d_{\downarrow\uparrow}^2 + d_\downarrow d_\uparrow \propto V + \frac{J_\perp}{4} - \frac{\chi}{4}$. Each single collision thus causes the scattered molecules to decohere, with a change in contrast $\Delta C = 2\sin^2(\delta_\leftrightarrow - \delta_\updownarrow) \propto \chi^2$ for small $\delta_\leftrightarrow - \delta_\updownarrow \propto \chi$ (see inset of Fig. 3B for schematic). The total dephasing rate is approximated by the product of the change in contrast for each collision and the elastic collision rate:

$\kappa \propto \Delta C \beta_{el}$. For 2D motion, ultracold identical spin-polarized fermionic molecules scatter elastically at a rate proportional to their threshold cross section $\sigma \approx 8\pi k a_D^2$, where k is the relative momentum of the colliding pair (*23*, *37*, *48*). Molecules in superpositions should also elastically scatter from both aligned and anti-aligned channels, so that $\beta_{el} = (\beta_{\updownarrow} + \beta_{\leftrightarrow})/2 = 4\pi\hbar k^2 \left[\left(a_D^{\updownarrow}\right)^2 + \left(a_D^{\leftrightarrow}\right)^2\right]/\mu$, where μ is the reduced mass of the pair. Evaluating the product for κ captures the dominant $\kappa \propto |\chi|^3$ scaling seen to arise in the Monte Carlo simulations (*36*). Notably, we find that this scaling is sensitive to the trap frequency of the tight confining axis and is thus relevant to our current experiment but not universal.

Spin dynamics of the generalized *t-J* model

We next explored the more complex generalized *t-J* model regime by tuning tunneling within 2D layers. Experimentally, we studied the effect of motion on contrast by measuring κ of molecules confined in a deep vertical lattice with variable corrugation in the $\hat{x}$ and $\hat{z}$ directions, for different values of χ. The measured values of κ as a function of tunneling rate t in both the $\hat{x}$ and $\hat{z}$ directions are plotted in Fig. 4A, with black circles, blue squares, and orange triangles representing χ = −205, 0, and 102 Hz ($J_\perp$ = 211, 133, and 75 Hz), respectively. For χ = 0 Hz, we observed no density-dependent contrast decay (that is, κ was consistent with 0) over the entire range of t explored, as intuitively expected at the Heisenberg point. For χ = 102 Hz, we saw a smooth transition between the two motional extremes, with κ gradually decreasing for increasing t. For χ = −205 Hz, we observed stronger decoherence in general, with a peak in decoherence rate around t = 70 Hz. Similar to the fully itinerant case, and as a result of the nonlinear dependence of collisional dephasing on $|\chi|$, it is not surprising that the behavior for χ = −205 Hz can be qualitatively different than for χ = 102 Hz.

To understand the observed peak when χ = −205 Hz, we first examined the rise in κ as the lattice depth was reduced from the pinned molecule case. Intuitively, increasing tunneling will couple the internal and external degrees of freedom of the molecules, leading to increased dephasing. This mechanism is well captured by simulations with an extended MACE (EMACE) (*36*), which adds molecular motion to the standard MACE and is shown as a light gray (orange) band for χ = −205 Hz (χ = 102 Hz) in Fig. 4A.

We next examined the enhanced contrast decay as the lattice depth was increased from zero. From a band structure perspective, increasing the lattice depth shrinks the width of each motional band, increasing its density of states and allowing more channels for mode-changing collisions, generally leading to faster spin decoherence (*36*) (Fig. 4B). From a scattering perspective, in the lattice, molecules

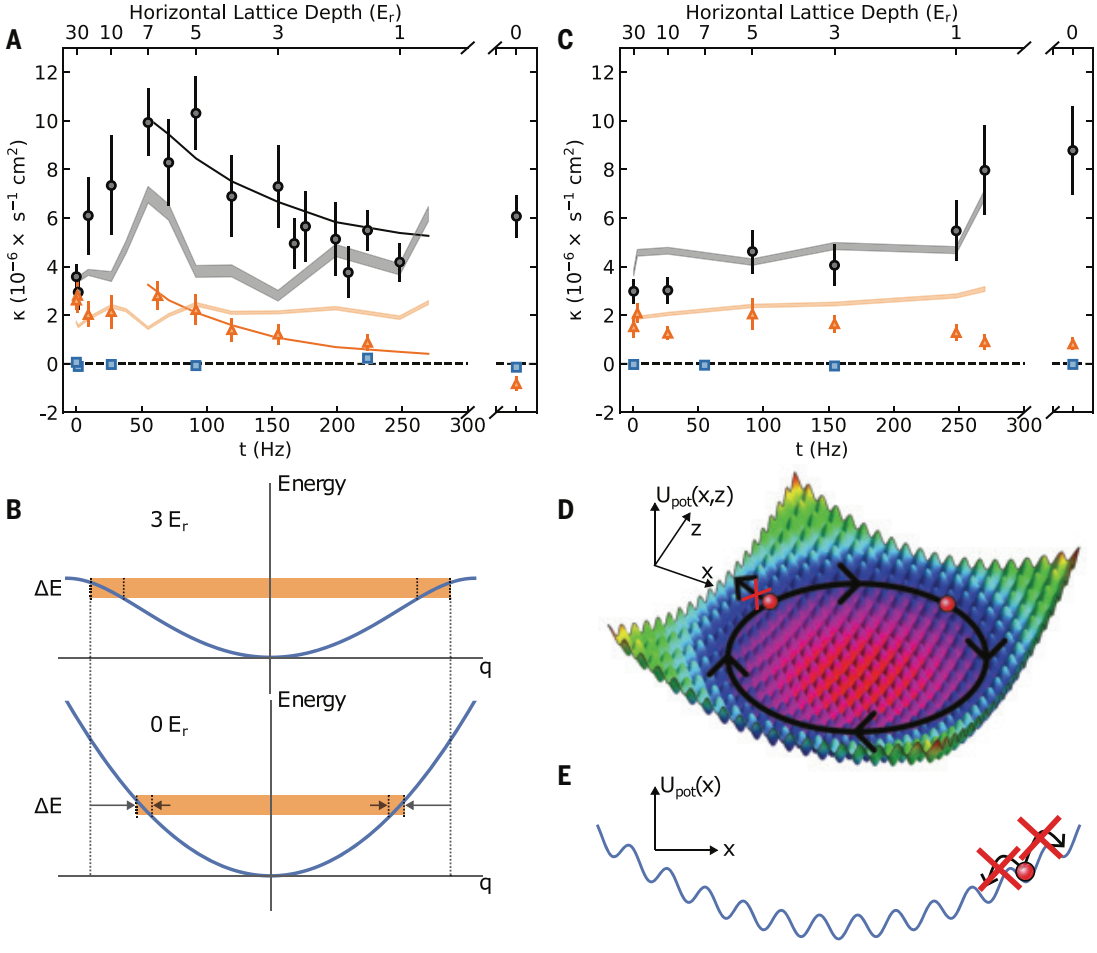

Fig. 4. Tuning coherent *t-J* dynamics. (**A**) Density-dependent contrast decay rates κ versus tunneling rate t in two directions. Black circles, blue squares, and orange triangles represent experimental data for χ = −205, 0, and 102 Hz, respectively. Horizontal axis break occurs when transverse lattices are turned off (case of Fig. 3B). Error bars are 1 SE from linear fits. Light gray (orange) bands are EMACE simulations (*36*) for χ = −205 Hz (χ = 102 Hz) with no scaling, with the band halfwidth representing 1 SE of linear fit. Black (orange) solid lines shown for t > 50 Hz are two-body simulations (*36*) with a rescaling by 0.75 for χ = −205 Hz (χ = 102 Hz). (**B**) (Top row) Kinetic energy of two particles in a $3E_r$ lattice as a function of relative quasi-momentum q. (Bottom row) Kinetic energy in the absence of a lattice where $q = k$. Shaded orange regions show the range of momentum states within a given energy interval, showing the increased density of states in a shallow lattice compared with the no-lattice case. (**C**) As in (A), but for tunneling only in one direction. (**D**) 3D rendering of the single-molecule potential energy U_{pot} in the $\hat{x}$ and $\hat{z}$ directions arising from a weak 2D optical lattice and a crossed optical dipole trap. Colors indicate equipotential surfaces. Because of the site-to-site energy shift, molecular tunneling along the radial directions is suppressed, and tunneling instead occurs along azimuthal rings. (**E**) Schematic of the localization of molecules within a potential landscape U_{pot} produced by a weak 1D optical lattice in the $\hat{x}$ direction and a crossed optical dipole trap [equivalently, by taking a 1D slice of the 2D lattice potential shown in (D)] because of site-to-site energy shifts, when the motion is also frozen in the other two directions by deep optical lattices.

move slower because of larger effective mass (*49*), increasing the phase shifts accrued in each collision, enhancing contrast decay. In addition, molecular losses from inelastic collisions increase as the lattice depth is reduced (*36*), and the losses are largest for molecules that have already decohered, suppressing contrast decay in the remaining sample (*36*). While the EMACE simulation qualitatively captures the peak structure, quantitative differences arise owing to neglected molecular loss and limited cluster sizes. To further understand the role of mode-changing collisions and molecular loss in shallow lattices, a two-body simulation based on Hamiltonian trotterization (*36*) is included for $t > 50$ Hz as a black (orange) solid line for $\chi = -205$ Hz ($\chi = 102$ Hz) in Fig. 4A, which agrees well with the experimental data with an empirical rescaling of 0.75.

Finally, we studied the role of motional dimensionality on the spin dynamics by measuring the dependence of κ on t for molecules allowed to tunnel in only one direction (Fig. 4C). Whereas the $\chi = 0$ Hz and $\chi = 102$ Hz dynamics are almost identical to the 2D case, the peak in contrast decay around $t \approx 70$ Hz for $\chi = -205$ Hz disappears when the kinetic dimensions are reduced from two to one. In one dimension, we instead only observed a rise in κ at very shallow lattices ($t \gtrsim 200$ Hz). We attribute the different $\chi = -205$ Hz dynamics in the 1D case to the interplay of the confining harmonic trap with the lattice. For tunneling in only one direction, the combined potential leads to quasi-localization of the molecules owing to potential energy differences between neighboring lattice sites (*50*, *51*), schematically shown in Fig. 4E. In the 1D configuration, most of the molecules are localized along all three axes of motion (*36*), leading to dynamics qualitatively similar to the motionless case as the lattice depth is lowered. In contrast, for the 2D case, the additional tunneling dimension allows these particles to delocalize within a quasi-1D azimuthal ring (Fig. 4D).

An EMACE simulation [gray (orange) band for $\chi = -205$ Hz ($\chi = 102$ Hz)] in Fig. 4C shows favorable agreement with experimental values of κ as t is varied in one direction. Note that the number of available tunneling sites is smaller in one dimension than in two, enabling more-controlled EMACE simulations for shallow lattices in the 1D case than in the 2D case (*36*). As shown in both the experimental data and EMACE simulations, the 1D dynamics remain relatively flat between the pinned and fully itinerant cases, consistent with the quasi-localization picture. We attribute the slight disagreement between theory and experiment at very shallow lattices ($t \gtrsim 200$ Hz) for $\chi = 102$ Hz to molecular loss not included in EMACE and to the breakdown of the single-band tight-binding model.

Discussion and outlook

Here, we present a systematic study of the out-of-equilibrium dynamics of a generalized *t-J* system of interacting polar molecules. By increasing molecular filling fractions and using single-site detection (*6*, *17*) or spectroscopic signatures (*52*, *53*), it should be possible to study equilibrium states of these dipolar Hamiltonians. Using similar experimental techniques, a future out-of-equilibrium investigation could probe spin diffusion in lattice-confined polar molecules, potentially observing many-body localized states (*54*). Additionally, with an isolated single layer (*18*) and improved detection, the generalized *t-J* model is predicted to dynamically generate highly entangled spin-squeezed states with applications to precision measurement (*38*, *39*). Recently, we demonstrated Floquet engineering of XYZ spin models, including a two-axis twisting Hamiltonian (*55*), which could enable more-scalable spin squeezing than that produced with native XXZ models. Ultracold molecules, whose dipolar interactions can be tuned independently of motion, have thus emerged as a versatile platform to study a broad range of itinerant spin problems in many-body physics.

REFERENCES AND NOTES

1. P. A. Lee, N. Nagaosa, X.-G. Wen, *Rev. Mod. Phys.* **78**, 17–85 (2006).
2. B. Keimer, S. A. Kivelson, M. R. Norman, S. Uchida, J. Zaanen, *Nature* **518**, 179–186 (2015).
3. P. W. Anderson, *Science* **235**, 1196–1198 (1987).
4. U. Schneider *et al*., *Science* **322**, 1520–1525 (2008).
5. D. Greif, T. Uehlinger, G. Jotzu, L. Tarruell, T. Esslinger, *Science* **340**, 1307–1310 (2013).
6. A. Mazurenko *et al*., *Nature* **545**, 462–466 (2017).
7. A. V. Gorshkov *et al*., *Phys. Rev. Lett.* **107**, 115301 (2011).
8. A. V. Gorshkov *et al*., *Phys. Rev. A* **84**, 033619 (2011).
9. L. Chomaz *et al*., *Rep. Prog. Phys.* **86**, 026401 (2022).
10. L. Su *et al*., *Nature* **622**, 724–729 (2023).
11. A. de Paz *et al*., *Phys. Rev. Lett.* **111**, 185305 (2013).
12. P. Fersterer *et al*., *Phys. Rev. A* **100**, 033609 (2019).
13. S. Baier *et al*., *Science* **352**, 201–205 (2016).
14. A. Patscheider *et al*., *Phys. Rev. Res.* **2**, 023050 (2020).
15. Y. Tang *et al*., *Phys. Rev. X* **8**, 021030 (2018).
16. B. Yan *et al*., *Nature* **501**, 521–525 (2013).
17. L. Christakis *et al*., *Nature* **614**, 64–69 (2023).
18. W. G. Tobias *et al*., *Science* **375**, 1299–1303 (2022).
19. C. M. Holland, Y. Lu, L. W. Cheuk, *Science* **382**, 1143–1147 (2023).
20. Y. Bao *et al*., *Science* **382**, 1138–1143 (2023).
21. P. D. Gregory *et al*., *Nat. Phys.* **20**, 415–421 (2024).
22. J.-R. Li *et al*., *Nature* **614**, 70–74 (2023).
23. G. Valtolina *et al*., *Nature* **588**, 239–243 (2020).
24. A. Schindewolf *et al*., *Nature* **607**, 677–681 (2022).
25. N. Bigagli *et al*., *Nature* **631**, 289–293 (2024).
26. L. Anderegg *et al*., *Science* **373**, 779–782 (2021).
27. J. Lin *et al*., *Phys. Rev. X* **13**, 031032 (2023).
28. A. V. Avdeenkov, *Phys. Rev. A* **86**, 022707 (2012).
29. L. Lassablière, G. Quéméner, *Phys. Rev. Lett.* **121**, 163402 (2018).
30. T. Karman, J. M. Hutson, *Phys. Rev. Lett.* **121**, 163401 (2018).
31. K. Matsuda *et al*., *Science* **370**, 1324–1327 (2020).
32. J.-R. Li *et al*., *Nat. Phys.* **17**, 1144–1148 (2021).
33. G. Quéméner, J. L. Bohn, *Phys. Rev. A* **93**, 012704 (2016).
34. M. L. González-Martínez, J. L. Bohn, G. Quéméner, *Phys. Rev. A* **96**, 032718 (2017).
35. B. Mukherjee, M. D. Frye, C. R. Le Sueur, M. R. Tarbutt, J. M. Hutson, *Phys. Rev. Res.* **5**, 033097 (2023).
36. Materials and methods are available as supplementary materials.
37. G. Quéméner, J. L. Bohn, *Phys. Rev. A* **83**, 012705 (2011).
38. T. Bilitewski *et al*., *Phys. Rev. Lett.* **126**, 113401 (2021).
39. D. Wellnitz, M. Mamaev, T. Bilitewski, A. M. Rey, *Phys. Rev. Res.* **6**, L012025 (2024).
40. A. M. Souza, G. A. Álvarez, D. Suter, *Phys. Rev. Lett.* **106**, 240501 (2011).
41. A. Signoles *et al*., *Phys. Rev. X* **11**, 011011 (2021).
42. K. R. A. Hazzard *et al*., *Phys. Rev. Lett.* **113**, 195302 (2014).
43. L. S. Martin *et al*., *Phys. Rev. Lett.* **130**, 210403 (2023).
44. S. Geier *et al*., *Science* **374**, 1149–1152 (2021).
45. M. P. Kwasigroch, N. R. Cooper, *Phys. Rev. A* **96**, 053610 (2017).
46. M. Block *et al*., *Nat. Phys.* **20**, 1575–1581 (2024).
47. M. A. Perlin, C. Qu, A. M. Rey, *Phys. Rev. Lett.* **125**, 223401 (2020).
48. C. Ticknor, *Phys. Rev. A* **80**, 052702 (2009).
49. N. W. Ashcroft, N. D. Mermin, *Solid State Physics* (Holt, Rinehart and Winston, 1976).
50. M. Rigol, A. Muramatsu, *Phys. Rev. A* **70**, 043627 (2004).
51. A. M. Rey, G. Pupillo, C. W. Clark, C. J. Williams, *Phys. Rev. A* **72**, 033616 (2005).
52. J. T. Stewart, J. P. Gaebler, D. S. Jin, *Nature* **454**, 744–747 (2008).
53. H.-J. Shao *et al*., arXiv:2402.14605 [cond-mat.quant-gas] (2024).
54. N. Y. Yao *et al*., *Phys. Rev. Lett.* **113**, 243002 (2014).
55. C. Miller *et al*., *Nature* **633**, 332–337 (2024).
56. A. N. Carroll *et al*., Data for "Observation of Generalized t-J Spin Dynamics with Tunable Dipolar Interactions" [Data set], Zenodo (2025); https://doi.org/10.5281/zenodo.14941807.

ACKNOWLEDGMENTS

We thank N. Darkwah Oppong and A. V. Gorshkov for a careful review of this manuscript and for providing useful comments. We acknowledge experimental contributions from J.-R. Li and J. S. Higgins and helpful discussions with P. J. D. Crowley and N. Y. Yao. **Funding:** This material is based on work supported by National Science Foundation grant QLCI OMA-2016244. Additional support is acknowledged from the US Department of Energy, Office of Science, National Quantum Information Science Research Centers, Quantum Systems Accelerator; ARO and AFOSR MURIs; JILA Physics Frontier Center grant PHY-2317149; National Science Foundation grant PHY-2110327; ARO single investigator award W911NF-24-1-0128; and the National Institute of Standards and Technology. A.N.C. acknowledges support from the National Science Foundation Graduate Research Fellowship under grant DGE 2040434. C.M. acknowledges support from the US Department of Defense through the NDSEG Graduate Fellowship. S.R.M. acknowledges support from the National Science Foundation under grant QLCI OMA-2120757. K.P.Z. acknowledges support from the Austrian Science Fund (FWF) under grant W1259-N27. R.R.W.W. acknowledges partial support from the National Science Foundation through a grant from ITAMP at Harvard University. **Author contributions:** A.N.C., H.H., C.M., J.L., K.P.Z., and J.Y. conducted the experiments and analyzed the data. D.W., S.R.M., R.R.W.W., J.L.B., and A.M.R. developed the theoretical models. All authors contributed to interpreting results and writing the manuscript. **Competing interests:** The authors declare that they have no competing interests. **Data and materials availability:** All data needed to evaluate the conclusions in this paper are available in Zenodo (*56*). This research was funded in whole or in part by the Austrian Science Fund (FWF) (W1259-N27), a cOAlition S organization. The author will make the Author Accepted Manuscript (AAM) version available under a CC BY public copyright license.

SUPPLEMENTARY MATERIALS

science.org/doi/10.1126/science.adq0911
Materials and Methods
Supplementary Text
Figs. S1 to S16
Table S1
References (*57*–*73*)

Submitted 25 April 2024; accepted 27 February 2025
10.1126/science.adq0911

CRISPR

RNA-mediated CRISPR-Cas13 inhibition through crRNA structural mimicry

Victoria M. Hayes[1]†, Jun-Tao Zhang[2]†, Mark A. Katz[1], Yuelong Li[2], Benjamin Kocsis[1], David M. Brinkley[1], Ning Jia[2,3]*, Alexander J. Meeske[1]*

To circumvent CRISPR-Cas immunity, phages express anti-CRISPR factors that inhibit the expression or activities of Cas proteins. Whereas most anti-CRISPRs described to date are proteins, recently described small RNAs called RNA anti-CRISPRs (rAcrs) have sequence homology to CRISPR RNAs (crRNAs) and displace them from cognate Cas nucleases. In this work, we report the discovery of rAcrVIA1—a plasmid-encoded small RNA that inhibits the RNA-targeting CRISPR-Cas13 system in its natural host, *Listeria seeligeri*. We solved the cryo–electron microscopy structure of the Cas13-rAcr complex, which revealed that rAcrVIA1 adopts a fold nearly identical to crRNA despite sharing negligible sequence similarity. Collectively, our findings expand the diversity of rAcrs and reveal an example of immune antagonism through RNA structural mimicry.

Bacteriophage and foreign genetic elements subvert CRISPR immunity by producing anti-CRISPRs (Acrs), which inhibit Cas nucleases to enable invasion (*1*). Because Cas nucleases are extremely diverse in sequence, the spectrum of inhibition by a given Acr is typically limited to a single CRISPR type. Although most identified Acrs are proteins, small RNA anti-CRISPRs (rAcrs) inhibit the DNA-targeting type I-C, I-E, I-F, and V-A CRISPR systems (*2*). Owing to their strong resemblance to CRISPR RNAs (crRNAs) in sequence, bioinformatic efforts have identified predicted rAcrs for five of the six major CRISPR types. However, whether additional noncoding RNAs play roles in antagonism of prokaryotic immune systems remains unclear. Furthermore, the structural mechanisms underlying CRISPR-Cas inhibition by rAcrs have not been explored.

A noncoding RNA inhibits CRISPR-Cas13 target interference

The CRISPR-Cas13 inhibitor AcrVIA2 is encoded as part of a 14-kb *acr* locus within an integrated plasmid in *Listeria seeligeri* strain LS21 (Fig. 1A and fig. S1A) (*3*). We introduced a plasmid-borne copy of *acrVIA2* into *L. seeligeri* strain LS1 and tested its ability to inhibit Cas13-mediated restriction of a targeted plasmid (Fig. 1B). When we initially cloned the *acrVIA2* gene, we included the 140–base pair (bp) intergenic region separating it from the upstream gene (Fig. 1A). Although this construct inhibited plasmid targeting by Cas13, introduction of an early stop codon in the *acrVIA2* coding sequence did not diminish the inhibitory effect (Fig. 1B). When we truncated the intergenic region to retain only the 18 bp immediately upstream of the *acrVIA2* start codon, the construct still displayed Cas13 inhibition, but this was abolished upon introduction of the same nonsense mutation (Fig. 1B). Accordingly, we tested a construct containing the 140-bp intergenic region along with only the first 50 bp of the *acrVIA2* coding sequence, which exhibited potent Cas13 inhibition (Fig. 1B). Collectively, these results indicate that an *acr* locus of *L. seeligeri* strain LS21 harbors two adjacent Cas13 inhibitors: one encoded by the *acrVIA2* gene and another encoded just upstream of it.

The 140-bp region between *acrVIA2* and its upstream gene does not encode any predicted open reading frames (ORFs), and constructs in which the AcrVIA2 coding sequence was truncated to 10 bp, contained frameshift mutations, or contained a mutant start codon retained Cas13 inhibition (Fig. 1B and fig. S1B). When we analyzed the transcriptional products of the Acr constructs using small RNA sequencing, we detected reads corresponding to RNAs between 37 and 60 nucleotides (nt) in length, which mapped to the reverse strand of the intergenic region upstream of *acrVIA2* (Fig. 1C). We identified putative -10 and -35 elements of a reverse-facing promoter downstream of the small RNA transcriptional start site (Fig. 1A), which we found to be essential for Cas13 inhibition (Fig. 1B). We confirmed the Acr-specific production of a 60-nt RNA matching this region using Northern blot (Fig. 1D). These results suggest that a small RNA divergently transcribed from *acrVIA2* acts as a Cas13 inhibitor. On the basis of the following analysis, we refer to this factor as rAcrVIA1, in accordance with recently established nomenclature

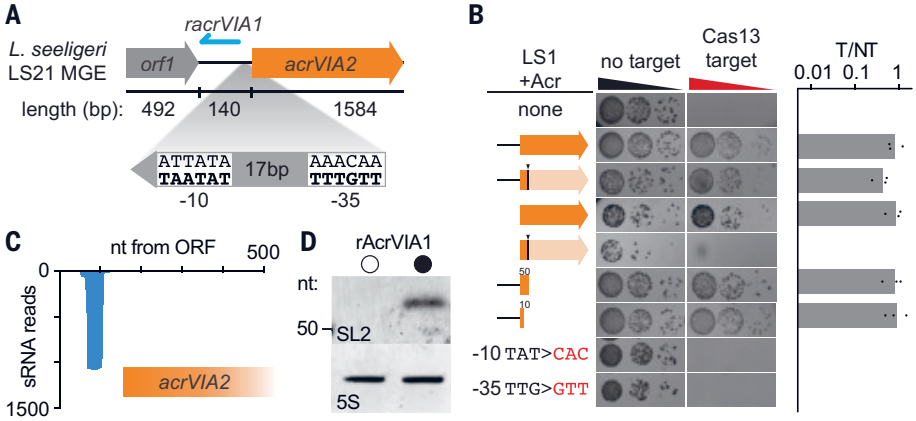

Fig. 1. A small noncoding RNA (rAcrVIA1) inhibits type VI CRISPR interference. (**A**) Schematic of genetic locus encoding AcrVIA2 (orange) and rAcrVIA1 (blue) found in integrated plasmid of *L. seeligeri* strain LS21. Predicted promoter -10 and -35 elements driving rAcrVIA1 transcription. (**B**) Plasmid targeting assay demonstrating Cas13 inhibition. Conjugative plasmids expressing a Cas13 target (or not) were introduced into *L. seeligeri* strains harboring the indicated Acr constructs. Black arrows and lines indicate nonsense mutations. Numbers indicate number of *acrVIA2* coding DNA sequence (CDS) nucleotides left after truncation. Quantification of three biological replicates is shown. T/NT, ratio of transconjugants observed with target plasmid to that with nontarget plasmid. (**C**) Small RNA (sRNA) sequencing reads mapped to the racrVIA1 locus when expressing *racrVIA1-acrVIA2* in strain LS1. Combined reads from two biological replicates are shown. (**D**) Northern blots using probe antisense to *racrVIA1* or 5S ribosomal RNA (rRNA).

[1]Department of Microbiology, University of Washington, Seattle, WA, USA. [2]Department of Biochemistry, SUSTech Homeostatic Medicine Institute, School of Medicine, Southern University of Science and Technology, Shenzhen, Guangdong, China. [3]Shenzhen Key Laboratory of Cell Microenvironment, Guangdong Provincial Key Laboratory of Cell Microenvironment and Disease Research, Key University Laboratory of Metabolism and Health of Guangdong, Institute for Biological Electron Microscopy, Southern University of Science and Technology, Shenzhen, Guangdong, China.
***Corresponding author. Email: meeske@uw.edu (A.J.M.); jian@sustech.edu.cn (N.J.)**
†These authors contributed equally to this work.

for rAcrs (*2*). However, unlike previously described rAcrs, rAcrVIA1 does not bear sequence homology to type VI crRNAs (fig. S1, C and D). In contrast to its effects on type VI CRISPR immunity, rAcrVIA1 did not affect plasmid interference by the DNA-targeting type II-A or II-C CRISPR systems of *L. seeligeri*, although we observed modest yet reproducible inhibition of type I-B CRISPR immunity (fig. S1E).

Secondary structural features of rAcrVIA1 are required for Cas13 inhibition

Secondary structure prediction of rAcrVIA1 using RNAfold (*4*) suggests it forms two stem loops (SLs) with a 2-nt bulge in SL1, similar to that formed by crRNA (Fig. 2A and fig. S2A) (*5*). To test the contribution of these predicted structural features to Cas13 inhibition, we generated a series of mutant rAcrVIA1 alleles. First, we found that removal of either SL abolished Cas13 inhibition by rAcrVIA1 (fig. S2B). We observed similarly strong requirements for specific base pairs within each SL, as disruption of complementarity at 2 or 3 bp eliminated rAcrVIA1 activity (Fig. 2B). Furthermore, restoration of complementarity by compensatory mutation of the other strand of the SL rescued rAcrVIA1-mediated inhibition of Cas13 in both cases, validating the formation of these predicted base pairs and underscoring the importance of the stem structure (but not the sequence) for Cas13 inhibition. Next, we investigated the contributions of various predicted structural features in rAcrVIA1 to its inhibitory activity (fig. S2, A and B). Shortening the length of either SL by 1 bp largely eliminated rAcrVIA1 activity, as did lengthening SL1 by 1 bp. By contrast, lengthening SL2 by 1 bp had no effect on rAcrVIA1-mediated Cas13 inhibition.

Cas13 interacts with rAcrVIA1

Next, we investigated the mechanism of Cas13 inhibition by rAcrVIA1. To test whether rAcrVIA1 physically associates with Cas13, we coexpressed a functionally tagged plasmid-borne dCas13-his6 allele and CRISPR array harboring a single spacer, along with rAcrVIA1, mutant derivatives, or an empty vector control in a ΔCRISPR-Cas13 mutant strain of *L. seeligeri* (Fig. 2, C and D). We used nuclease-inactive dCas13 to avoid confounding effects from potential RNA cleavage products. We then affinity purified dCas13-his6 from both strains by nickel–nitrilotriacetic acid agarose pulldown, extracted RNA from the purified protein, and analyzed dCas13-associated RNAs by denaturing gel electrophoresis. In the absence of rAcrVIA1, we detected two bands corresponding to the expected 50- to 51-nt crRNA normally associated with dCas13 (Fig. 2C). However, in the presence of rAcrVIA1, we observed an additional 60-nt RNA, along with diminished intensity of the crRNA bands. We performed similar experiments with an *apo* form of dCas13 lacking a CRISPR array, which resulted in coprecipitation of Cas13 with mature rAcrVIA1 but no crRNA (Fig. 2C). We determined using small RNA sequencing that the 60-nt band bound to *apo*-dCas13 corresponded to the rAcrVIA1 sequence (Fig. 2D). These results indicate that rAcrVIA1 physically interacts with Cas13 in a manner that does not require the presence of crRNA and suggest that rAcrVIA1 competes with crRNA for binding to Cas13. To investigate this, we tested whether Cas13 immunity could be rescued from rAcrVIA1-mediated inhibition by overexpressing crRNA, through ectopic integration of a copy of the CRISPR array under a strong P_{hyper} promoter. When we challenged this strain with a CRISPR-targeted plasmid, we observed reduced numbers and size of transconjugant colonies, consistent with much weaker rAcrVIA1 activity (Fig. 2B). Cas13 is responsible for processing type VI-A crRNAs (*6*), raising the possibility that it could also process rAcrVIA1 precursors. Consistent with this idea, we observed no coimmunoprecipitation of rAcrVIA1 (or crRNAs) with a mutant allele of dCas13 lacking crRNA processing activity (R1048A and K1049A) (Fig. 2C) (*5*); however, this mutant could be impaired in binding of crRNAs and/or rAcrVIA1.

We then performed dCas13 pulldowns in the presence of the mutant rAcrVIA1 derivatives tested (fig. S2C). Whereas wild-type (WT) rAcrVIA1 and all of the mutant alleles that retained Cas13 inhibition coimmunoprecipitated with dCas13, several of the mutants that lost function failed to associate with dCas13. Notably, although the SL2 Δ1bp mutant largely lost the ability to inhibit Cas13, it remained associated with dCas13, suggesting that the interaction between rAcrVIA1 and Cas13 is necessary but may be insufficient for inhibition. However, this mutant resulted in the formation of numerous small target plasmid–containing transconjugant colonies, suggesting that it retains partial function (fig. S2B, asterisk). That rAcrVIA1 interacts with Cas13 raised the possibility that rAcrVIA1 itself functions as a crRNA. Accordingly, we tested whether a

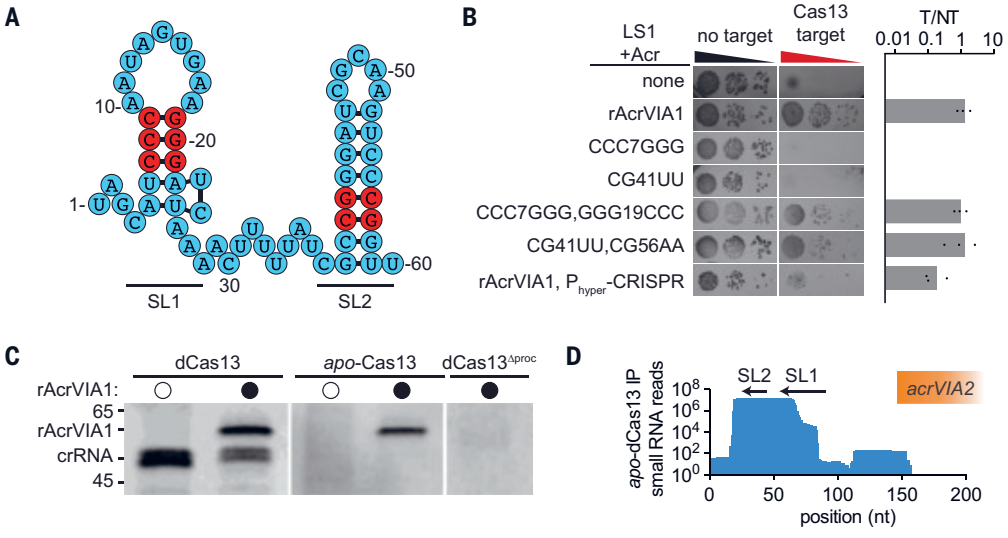

Fig. 2. Secondary structure, processing, and Cas13-binding activity of rAcrVIA1. (**A**) Predicted secondary structure of rAcrVIA1, with SLs (SL1 and SL2). Red nucleotides indicate positions mutated in (B). (**B**) Plasmid-targeting assay demonstrating that mutations in each SL abolish Cas13 inhibition, whereas compensatory mutations that restore complementary rescue inhibition. Quantitation of three biological replicates. (**C**) Denaturing gel analysis of RNA associated with the indicated Cas13 allele in the presence or absence of rAcrVIA1. RNA molecular weight markers in nucleotides. (**D**) sRNA sequencing reads mapping to *racrVIA1* locus from RNA extracted from purified apo-dCas13 in the presence of rAcrVIA1. IP, immunoprecipitation.

plasmid encoding a transcript complementary to rAcrVIA1 was restricted in the presence of rAcrVIA1 or a mutant in which SL2 was disrupted to allow target RNA engagement (fig. S2D). We observed no rAcrVIA1-dependent restriction with either construct and argue that the rAcr does not function as a crRNA, which may be explained by sequence differences in the crRNA handle (SL1) portion.

Cryo–electron microscopy structure of the Cas13-rAcrVIA1 complex

To investigate the mechanism of rAcrVIA1-mediated Cas13 inhibition, we coproduced *apo*-Cas13 with rAcrVIA1 in *L. seeligeri*. Size exclusion chromatography analysis demonstrated the formation of a homogeneous complex between Cas13 and rAcrVIA1 (fig. S3A). We determined its cryo–electron microscopy (cryo-EM) structure at a resolution of 2.85 Å (Fig. 3, A and B, and fig. S3, B to F). The Cas13-rAcrVA1 complex adopts a bilobed architecture, consisting of recognition [N-terminal domain (NTD) and helical-I domain] and nuclease [helical-II and two higher eukaryotes and prokaryotes nucleotide-binding (HEPN) domains connected by a linker element] lobes. Notably, we observed RNA densities corresponding to

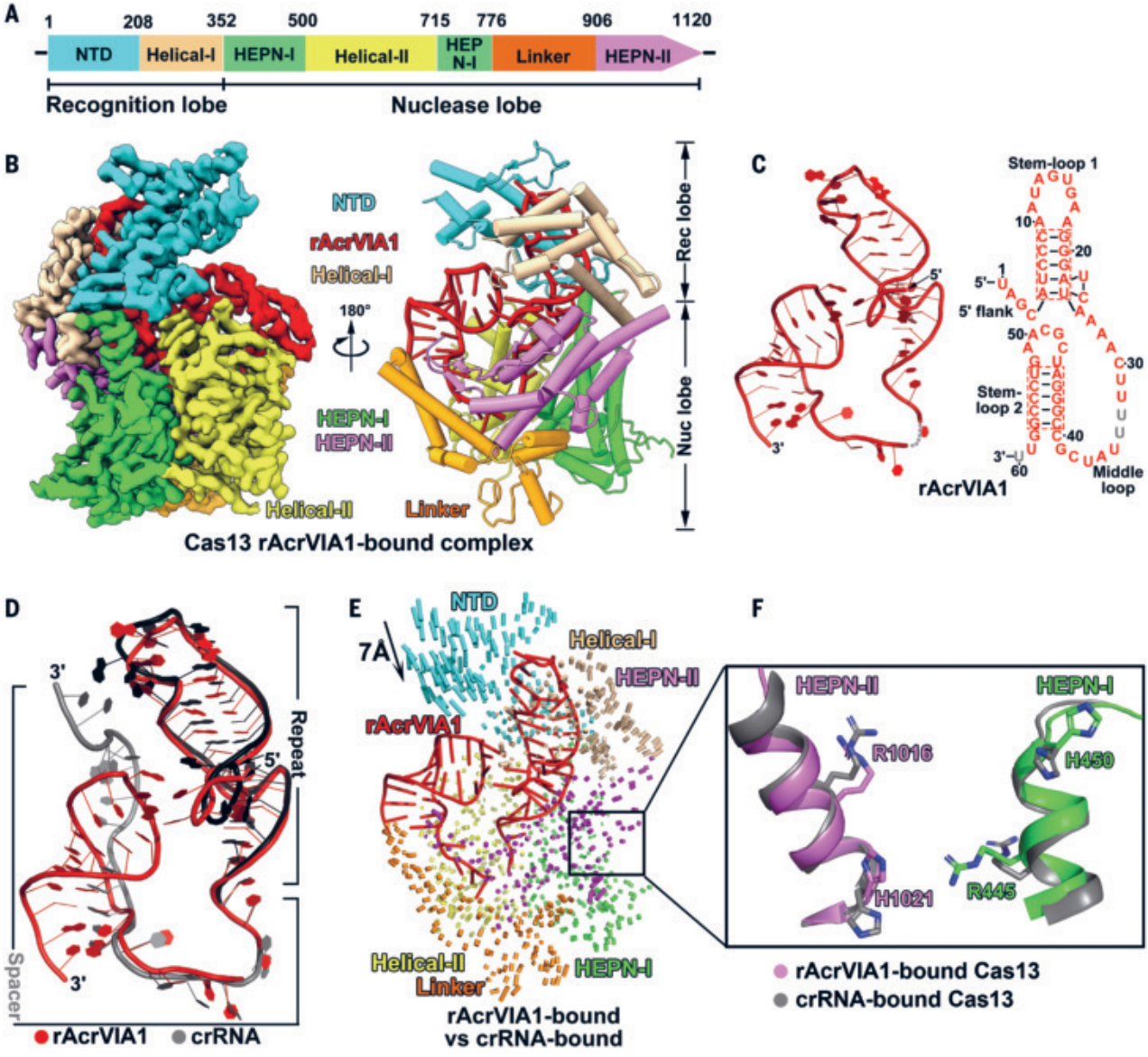

Fig. 3. Overall architecture of the Cas13-rAcrVIA1 complex. (**A**) Domain organization of Cas13. (**B**) Surface (left) and ribbon (right) representation of the cryo-EM structure of Cas13-rAcrVIA1 complex in different orientations. Domains are colored as in (A). (**C**) Ribbon representation (left) and schematic drawing (right) of the sequences and secondary structure of rAcrVIA1. Segments that could be traced are in color, and disordered segments are in gray. (**D**) Structural comparison of Cas13-bound rAcrVIA1 (red) and crRNA (gray). The repeat and spacer regions of the crRNA are colored in black and gray, respectively. (**E**) Structural comparison of Cas13-rAcrVIA1 complex and the Cas13-crRNA complex. The vector length correlates with the scale of domain movement. Domains are colored as in (A). (**F**) Comparison of the positions of the four catalytic residues from HEPN-I and HEPN-II domains between rAcrVIA1-bound and crRNA-bound Cas13. Single-letter abbreviations for the amino acid residues are as follows: A, Ala; C, Cys; D, Asp; E, Glu; F, Phe; G, Gly; H, His; I, Ile; K, Lys; L, Leu; M, Met; N, Asn; P, Pro; Q, Gln; R, Arg; S, Ser; T, Thr; V, Val; W, Trp; and Y, Tyr.

the 60-nt rAcrVIA1, which consists of two SLs (SL1: A5-U25; SL2: C41-G57), a 4-nt 5′ flank (U1-C4), and a 15-nt middle loop (A26-C40) (Fig. 3C). The 5′ flank protrudes from SL1 and inserts into a surface-exposed groove formed by the helical-I and HEPN-II domains (Fig. 3B and fig. S4A). The 5′ hydroxyl group of U1 is anchored near the conserved residues R1041, R1048, and K1051, which are responsible for crRNA maturation (fig. S4B) (*5*, *7*), suggesting that the 5′ end of rAcrVIA1 might be processed similarly to mature crRNA. The 3′ end of rAcrVIA1 is exposed to the solvent (Fig. 3B and fig. S4C), suggesting a potential alternative nuclease-mediated processing mechanism for this region.

SL1 is stabilized primarily through sequence-independent interactions with the NTD and helical-I domains (fig. S4D). Nucleotides A5 and U6 base pair with U25 and A22, respectively, forming a 2-nt bulge (U23 and C24), as in crRNA bound to *L. seeligeri* Cas13 (fig. S4E) (*5*). The middle loop undergoes a 90° turn and is positioned in the crRNA-target RNA binding channel through sequence-independent interactions mediated by the HEPN-II, helical-II, and linker domains (fig. S4, D and F). SL2, adopting an A-form helical conformation, is situated in the cleft formed by NTD and linker domains (Fig. 3B). Few interactions are involved in maintaining the structure of SL2, including nucleotide G48 stacking with residues K306 in the helical-I domain and nucleotides G48, A50, and A51 stacking with nucleotides C4 and G3 of the 5′ flank (fig. S4D). Consistent with our mutagenesis experiments, these structural analyses indicate that Cas13 binds rAcrVIA1 in a shape-dependent rather than sequence-dependent manner. Next, we superimposed the Cas13-rAcrVIA1 complex with the Cas13-crRNA complex. The structure of rAcrVIA1 closely resembles that of crRNA, except for the differences in their 3′ region (Fig. 3D). Whereas the 3′ end of crRNA extends outward and inserts into the NTD domain (fig. S4G) (*5*), rAcrVIA1 forms a SL structure that sits in the cleft between NTD and linker domains (Fig. 3B), similar to the structure formed by crRNA bound to *Leptotrichia buccalis* Cas13 (fig. S4H) (*7*). When Cas13 binds to rAcrVIA1, its structure undergoes minor rearrangements compared with its crRNA-bound form, with a Cα root mean square deviation value of 1.9 Å over 865 atoms (Fig. 3E). Notably, upon binding rAcrVIA1, the NTD domain of Cas13 shifts nearly 7 Å toward the helical-I domain, forming a narrow cleft to accommodate SL2 (Fig. 3E).

We compared the conserved HEPN catalytic site of the rAcrVIA1-bound *L. seeligeri* Cas13 with the crRNA-bound form, which revealed minimal conformational changes in the catalytic ribonuclease residues (Fig. 3F). These catalytic sites have been shown to undergo substantial conformational changes upon target RNA binding to perform RNA cleavage (fig. S4I) (*7*). Because Cas13-rAcrVIA1 cannot bind target RNA, rAcrVIA1 effectively locks Cas13 in a catalytically inactive state. Structural analysis using a protein-ligand interaction profiler tool indicated that rAcrVIA1 and crRNA form a similar number of hydrogen bond interactions with Cas13 (76 hydrogen bonds for rAcrVIA1 and 72 hydrogen bonds for crRNA) (*8*). To further assess the binding ability of rAcrVIA1 and crRNA to Cas13, we incubated fluorescently labeled rAcrVIA1 and crRNA with increasing concentrations of the Cas13-rAcrVIA1 complex. The results showed that both rAcrVIA1 and crRNA bind to Cas13 with similar affinities (fig. S5), consistent with our in vivo observations that overexpression of crRNA can rescue rAcrVIA1-mediated Cas13 inhibition (Fig. 2B). Taken together, these findings suggest that rAcrVIA1 mimics the structure of crRNA and competes with it for binding, thereby preventing Cas13 from recognizing and cleaving target RNA.

AcrVIA2 and rAcrVIA1 contribute independently to Cas13 inhibition

AcrVIA2 is encoded downstream of rAcrVIA1 and inhibits type VI CRISPR immunity by affecting crRNA levels, either by mediating their direct cleavage or by enabling their degradation by other nucleases (Fig. 4A) (*3*). Thus, both rAcrVIA1 and AcrVIA2 affect crRNA:Cas13 stoichiometry, suggesting they may synergize in Cas13 inhibition. To investigate this possibility, we analyzed dCas13-associated RNA during expression of rAcrVIA1, AcrVIA2, or both factors (Fig. 4B). As previously demonstrated, AcrVIA2 expression resulted in reduced crRNA levels but did not affect dCas13 levels. During rAcrVIA1 expression, bands corresponding to both crRNA and rAcrVIA1 were detected in the dCas13-bound RNA fraction. When we coexpressed rAcrVIA1 and AcrVIA2, the rAcrVIA1 band represented the predominant dCas13-bound RNA, indicating the activities of rAcrVIA1 and AcrVIA2 are not mutually exclusive, and despite its mimicry of crRNA, rAcrVIA1 is not susceptible to AcrVIA2-mediated degradation.

During natural invasion of *L. seeligeri* by mobile genetic elements (MGEs) encoding rAcrVIA1 and AcrVIA2, the cell would presumably be equipped with active Cas13 ribonucleoprotein (RNP) complexes available for target RNA recognition before either Acr is expressed, making immunity difficult to suppress. To model this scenario, we introduced type VI spacers, recognizing the kanamycin resistance mRNA encoded on the same conjugative plasmid harboring rAcrVIA1, AcrVIA2, or both, and measured conjugation efficiency (Fig. 4C). Whereas expressing AcrVIA2 alone had a negligible ability to suppress Cas13 targeting, expressing rAcrVIA1 or both Acrs completely inhibited Cas13, suggesting rAcrVIA1 is capable of neutralizing immunity during natural invasion of *L. seeligeri* equipped with preexisting Cas13 targeting complexes. In support of this hypothesis, preincubation of Cas13-crRNA with a molar excess of rAcrVIA1 inhibited target RNA cleavage in vitro (Fig. 4D).

Regulatory control of rAcrVIA1

The rAcrVIA1 locus is naturally found immediately downstream of another gene (*orf1*), encoding a protein with a predicted helix-turn-helix (HTH) domain (Fig. 4A). Thus, we sought to investigate whether this gene affects rAcrVIA1 function. We cloned the locus from the native *orf1* promoter through the *acrVIA2* gene, which abolished Cas13 interference in plasmid-targeting assays (Fig. 4E). Furthermore, AcrVIA2 was dispensable for Cas13 inhibition, suggesting that rAcrVIA1 is functional in this construct. Next, we tested an in-frame deletion of *orf1*, which had no impact on Cas13 inhibition when both *racrVIA1* and *acrVIA2* remained intact. When we deleted *orf1* from the construct solely expressing rAcrVIA1, Cas13 inhibition was abolished and could be rescued by the expression of *orf1* in *trans*. We observed a similar loss of rAcr function when we installed an early nonsense mutation in *orf1*, disrupting ORF1 function but preserving sequence architecture. A construct expressing *orf1* alone did not affect Cas13 activity, suggesting ORF1 is not itself an Acr. Because rAcrVIA1 is functional in the absence of both *orf1* and its promoter (P_{orf1}), we tested whether mutating P_{orf1} could relieve the requirement of ORF1 for rAcrVIA1 function. Indeed, ablation of the predicted P_{orf1}-10 element restored Cas13 inhibition by rAcrVIA1 in the absence of *orf1*. As ORF1 is a predicted nucleic acid–binding protein, we investigated whether it influences rAcrVIA1 activity by affecting the transcriptional activity of its own promoter (P_{orf1}). We ectopically integrated a transcriptional fusion of this promoter to the fluorescent protein mStayGold into the LS1 chromosome and measured fluorescence in the presence and absence of a plasmid encoding ORF1 (Fig. 4F). Whereas we observed strong reporter activity from P_{orf1} alone, the addition of ORF1 reduced the activity by 100-fold, similar to the levels observed after ablation of the P_{orf1}-10 element, indicating that ORF1 is a transcriptional autorepressor. We hypothesized that P_{orf1} drives strong transcription that conflicts with the convergently transcribed rAcrVIA1; thus, rAcrVIA1 can only be produced when P_{orf1} is silenced by ORF1. To investigate this, we generated an mStayGold reporter to measure P_{orf1}-driven readthrough transcription downstream of the *orf1* stop codon, antisense with respect to rAcrVIA1 (Fig. 4F). The reporter construct

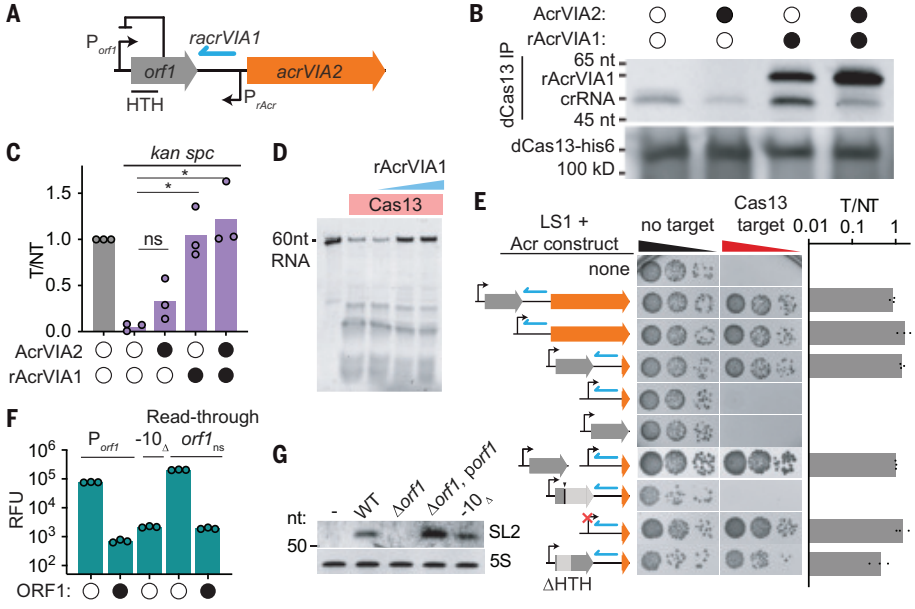

Fig. 4. rAcrVIA1 acts independently of AcrVIA2 and is regulated by ORF1. (**A**) Schematic of genetic locus encoding HTH-containing ORF1, rAcrVIA1, and AcrVIA2. (**B**) (Top) Analysis of dCas13-associated RNA in presence of the indicated Acrs. (Bottom) dCas13-his6 Western blot. (**C**) Plasmid-targeting assay in which plasmids encoding Acrs were directly targeted by preexisting Cas13 RNP complexes. Acr plasmids were conjugated into strain LS1 with or without a targeting spacer, and transconjugants were enumerated. T/NT, targeted to nontargeted transconjugants ratio. Quantification of three biological replicates. Asterisks indicate statistical significance ($P < 0.05$, Student's t test). ns, not significant. (**D**) RNA cleavage assay with purified 3xFlag-tagged Cas13-crRNA and Cy3-labeled target RNA substrate, with rAcrVIA1 added in 1:8, 1:2, and 2:1 molar ratios. Representative of three biological replicates. (**E**) Plasmid-targeting assay. Conjugative plasmids expressing a Cas13 target (or not) were introduced into *L. seeligeri* strains harboring the indicated Acr constructs. Quantification of three biological replicates. (**F**) Transcriptional activity of the indicated promoters in the presence and absence of ORF1. RFU, relative fluorescence units. (**G**) Northern blots using probes antisense to rAcrVIA1 or 5S rRNA sequence.

contained an early nonsense mutation in *orf1* to prevent silencing. Using this reporter, we observed strong transcriptional activity downstream of *orf1*, which was silenced when ORF1 was supplied in *trans* (Fig. 4F). We found that rAcrVIA1 levels were undetectable by Northern blot when *orf1* was mutated in the presence of P_{orf1} but were restored upon mutation of the P_{orf1}-10 element or by expressing ORF1 in *trans*, indicating that convergent transcription from P_{orf1} interferes with rAcrVIA1 production (Fig. 4G). Deletion of the ORF1 HTH only weakly affected rAcrVIA1 activity in plasmid-targeting assays, indicating that it is not strictly required for rAcrVIA1 production (Fig. 4E). Taken together, our results indicate that ORF1 is a transcriptional autorepressor whose activity is required to repress convergent transcription that influences rAcrVIA1 production.

Discussion

Our analyses support the conclusion that rAcrVIA1 is a structural mimic of type VI crRNA that inhibits Cas13 by competing with crRNA for Cas13 binding. Previously described rAcrs share a high degree of sequence homology with the crRNAs of their cognate CRISPR types (*2*). By contrast, rAcrVIA1 has negligible sequence similarity to type VI crRNA, yet the two RNAs adopt a notably similar fold. Our results suggest there may be more structural mimic rAcrs or RNA inhibitors of other defense systems to be discovered, yet their identification poses a challenge to homology-based bioinformatic approaches. Accordingly, few examples of RNA-based structural mimicry in immune antagonism have been identified. One parallel mechanism in viral counter defense against eukaryotic immunity is the adenoviral RNA VAI, a double-stranded RNA that mimics the natural substrate of the immune sensor protein kinase R (PKR) (*9*). VAI functions as a pseudoactivator, binding PKR and inhibiting rather than stimulating its immune activities.

Why is rAcrVIA1 encoded just upstream of another Cas13 inhibitor, AcrVIA2? This arrangement is paralleled for several rAcrs, which are encoded alongside protein-based inhibitors of the same CRISPR type (*2*). Although in all cases tested so far, the RNA and protein Acrs can function independently when produced in advance of CRISPR targeting, our experiments demonstrated that rAcrVIA1 functions more efficiently during initial invasion by the MGEs that encode it. We speculate that rAcrs may serve to neutralize preexisting CRISPR-Cas complexes, and their cognate protein Acrs such as AcrVIA2 serve to maintain immune suppression by inhibiting biogenesis of new CRISPR machinery.

REFERENCES AND NOTES

1. J. Bondy-Denomy, A. Pawluk, K. L. Maxwell, A. R. Davidson, *Nature* **493**, 429–432 (2013).
2. S. Camara-Wilpert *et al.*, *Nature* **623**, 601–607 (2023).
3. M. A. Katz *et al.*, *Nature* **634**, 677–683 (2024).
4. R. Lorenz *et al.*, *Algorithms Mol. Biol.* **6**, 26 (2011).
5. A. East-Seletsky *et al.*, *Nature* **538**, 270–273 (2016).
6. A. J. Meeske *et al.*, *Science* **369**, 54–59 (2020).
7. L. Liu *et al.*, *Cell* **170**, 714–726.e10 (2017).
8. M. F. Adasme *et al.*, *Nucleic Acids Res.* **49**, W530–W534 (2021).
9. M. G. Katze, D. DeCorato, B. Safer, J. Galabru, A. G. Hovanessian, *EMBO J.* **6**, 689–697 (1987).

ACKNOWLEDGMENTS

We are grateful to all members of the Meeske and Jia laboratories for helpful discussions. We thank the staff at Southern University of Science and Technology (SUSTech) Cryo-EM Center for assistance in data collection on the SUSTech Titan KRIOS cryo-EM. **Funding:** This study received support from the National Institutes of Health (grant R35GM142460 to A.J.M.); the National Science Foundation (grant FAIN2235762 to A.J.M.); the Rita Allen Foundation (to A.J.M.); the National Natural Science Foundation of China (32270050 to N.J.); a Guangdong Provincial Science and Technology Innovation Council grant (2017B030301018 to N.J.); and the SUSTech Institute for Biological Electron Microscopy (to N.J.). **Author contributions:** Conceptualization: A.J.M., N.J.; Cryo-EM sample preparation; data collection, processing, and analysis; and structure refinement: J.-T.Z.; Genetics and pulldown experiments: V.M.H., M.A.K., B.K., A.J.M.; Protein purification: J.-T.Z., Y.L., D.M.B.; Writing – original draft: A.J.M., N.J.; Writing – review & editing: V.M.H., J.-T.Z., M.A.K., Y.L., B.K., D.M.B., N.J., A.J.M. **Competing interests:** A.J.M. is a cofounder of Profluent Bio. The other authors declare that they have no competing interests. **Data and materials availability:** The cryo-EM density map of Cas13-rAcrVIA1 complex has been deposited in the Electron Microscopy Data Bank (EMDB) under accession number EMD-60476. The atomic coordinate of Cas13-rAcrVIA1 complex has been deposited in the Protein Data Bank (PDB) with accession number 8ZTY. All other data are available in the main text or the supplementary materials.

SUPPLEMENTARY MATERIALS

science.org/doi/10.1126/science.adr3656
Materials and Methods
Figs. S1 to S5
Table S1
References (*10*–*23*)
MDAR Reproducibility Checklist
Data S1 to S5

Submitted 27 June 2024; accepted 7 March 2025
10.1126/science.adr3656

INORGANIC CHEMISTRY

Gallium-catalyzed recycling of silicone waste with boron trichloride to yield key chlorosilanes

Nam Đức Vũ[1], Aurélie Boulegue-Mondière[2], Nicolas Durand[2], Joséphine Munsch[2], Mickaël Boste[3], Rudy Lhermet[3], David Gajan[4], Anne Baudouin[5], Steven Roldán-Gómez[5], Marie-Eve L. Perrin[5], Vincent Monteil[1]*, Jean Raynaud[1]*

Chemical recycling to monomers is a key strategy for a sustainable circular polymer economy. However, most efforts have focused on polymers with carbon backbones. Recycling of silicone polymers and corresponding materials, featuring a robust inorganic backbone and tunable properties, remains in its infancy. We present a general method for depolymerization of a very wide range of silicone-based materials and postconsumer waste, including end-of-life cross-linked polydimethylsiloxane-based networks within formulated materials. The reaction proceeds at 40°C, harnessing an efficient gallium catalyst for a million-fold rate enhancement and boron trichloride as the chlorine source, to produce nearly quantitative yields of (methyl)chlorosilanes, key intermediates in the Müller-Rochow process that anchors the silicone industry.

Silicone polymers are ubiquitous materials in our daily lives owing to their exceptional mechanical and thermal stability, chemical resistance, and low toxicity, which are properties that are advantageous across a span of household, automotive, and medicinal care applications, among others (*1*). In 2022, the world production of silicone polymers reached >8 million metric tons, representing a market value at ~20 billion USD (*2*). Owing to an upstream hydrometallurgical process step, the production of silicones is energy intensive. The metallurgy required to produce elemental silicon from mined quartz, and to a lesser extent the Müller-Rochow process to yield chlorosilanes, represents >70% of the CO_2 footprint of silicones. Silicone recycling is therefore key to conserve already depleted or strained resources (such as quartz) and minimize energy consumption.

Silicone waste (oils and elastomers with and without fillers) is presently either incinerated or placed in landfills. Although such wastes have so far been considered mostly benign for our environment (eventual degradation in soil to CO_2, H_2O, and SiO_2), their reuse would be advantageous from an energy and resource standpoint, as noted earlier. In addition, some silicone-based compounds have recently come under scrutiny, motivating strategies such as ecodesign for silicones (*3*) and biocatalytic pathways to deal with volatile methylsiloxanes (*4*). In contrast to plastics such as polyethylene terephthalate (PET) and polyolefins (*5*–*8*)—for which recycling methods are applied or in development, mechanical in particular (*9*) but more recently chemical (*10*–*14*)—the recycling of silicone-based polymers is underexploited, and few examples exist (*15*). Chemical recycling could prove particularly efficient for silicones in sidestepping the power-hungry metallurgy and Müller-Rochow processes. According to studies from Elkem Silicones, the chemical recycling of silicone wastes could reduce up to 65% of energy consumption and 75% of greenhouse gas emissions relative to the present baseline for silicone production (*16*, *17*).

A main barrier to chemical recycling of silicone materials, particularly elastomers (cross-linked networks), is their sophisticated multicomponent formulations. These elastomers or rubbers often exist as a mixture of cross-linked polysiloxanes, inorganic and organic fillers, technical additives, and catalysts (*15*–*17*). Because they are cured or cross-linked in the presence of a catalyst, they can no longer be melted or reshaped. Therefore, mechanical recycling entails only downcycling to rubber powder or crumbs and thus has rather limited applications. Chemical upcycling to recover key industrial intermediates (*15*–*19*) would be more productive.

The chemical recycling of waste silicones has long been studied yet was mainly focused on the conversion of silicone polymers to cyclosiloxanes (method 1, cyclic monomers; see Fig. 1). Very rarely has upcycling to halogenated and, in particular, chlorinated organosilanes been considered an efficient strategy for chemical recycling (method 2, Cl-based monomers; see Fig. 1). Both cyclosiloxanes and chlorinated organosilanes are key intermediates of the silicone industry (see Fig. 1).

With method 1, a strong alkaline base with or without complexing molecules or fluorine derivatives could be used as an efficient catalyst (to generate a propagating silanolate) for the deconstruction of silicone polydimethylsiloxane (PDMS) chains to cyclosiloxanes through successive backbiting nucleophilic attacks (*15*–*17*, *20*–*22*). This is a desirable short recycling loop: "back-to-cyclic monomers." We recently provided a straightforward strategy for several silicone wastes: a back-to-cyclics methodology with a very efficient, readily available, and recyclable catalyst, harnessing the equilibrium between linear and cyclic PDMS through choice of reactive distillation process (*18*). However, the strategy lacks universality and compatibility with moieties supporting Si-H bonds. More detrimentally, it cannot properly handle formulated elastomers and highly cross-linked resins, which account for a large fraction of all silicone waste (>40%), particularly postconsumer waste products (*15*–*17*).

The conversion of silicone polymer to Si-F products as an upcycling strategy is very favorable thermodynamically (analogous to method 2 but yielding less ubiquitous fluorosilanes). Enthaler has presented a synthetic method for the depolymerization of silicone oils and elastomers to produce the corresponding fluorosilanes (*23*). An excess of benzoyl fluoride was used as the fluorine source, and the reaction often proceeds in the presence of a zinc catalyst at elevated temperatures (120° to 190°C). However, there are drawbacks to this method, which involve the price, availability, and/or lack of atom economy of fluorine and fluoride sources and the release of some volatile and hazardous fluorosilanes during the process. Moreover, use of those fluorosilanes is rather limited industrially and is outside the loop of the silicon and silicone main industrial cascade of processes (see Fig. 1).

By contrast, chlorosilanes (method 2) are the most important intermediates in silicone industrial production. They are conventionally produced through the Müller-Rochow process, which involves a copper-catalyzed reaction of methyl chloride and metallurgic silicon in a fluidized bed reactor (300°C, 2 to 5 bar) (*24*). However, the chemical recycling of silicone polymers to (methyl)chlorosilanes is seldom reported owing to unfavored thermodynamics of Si-Cl bond formation from Si-O bonds in silicone backbones (*25*). Döhlert and Enthaler reported the conversion of silicone oils to chlorosilanes (*26*), but the reaction conditions (high catalyst loading [Fe], excess of unsustainable acyl chloride, high temperature of ~190°C) and narrow scope with waning reactivity have limited its application in silicone recycling.

Herein, we present an effective method for depolymerization of nearly any silicone polymers—including functional oils, block copolymers, or industrial and end-of-life elastomers,

[1]Université Claude Bernard Lyon 1, CNRS, CPE Lyon, UMR 5128, Laboratory of Catalysis, Polymerization, Processes and Materials (CP2M), 43 Bd du 11 Nov. 1918, Villeurbanne, France. [2]Elkem Silicones, R&D Chemistry, R&I Centre "ATRiON," 9 rue Spécia, Saint-Fons, France. [3]Activation, Chemical Process Research and Catalysis, 10 rue Jacquard, Chassieu, France. [4]CNRS, ENS Lyon, Université Claude Bernard Lyon 1, UMR 5082, Centre de RMN à très hauts champs de Lyon (CRMN), Villeurbanne, France. [5]Université Claude Bernard Lyon 1, CNRS, CPE Lyon, UMR 5246, Institut de Chimie et de Biochimie, Moléculaires et Supramoléculaires (ICBMS), 1 rue Victor Grignard, Villeurbanne, France.
*Corresponding author. Email: vincent.monteil@univ-lyon1.fr (V.M.); jean.raynaud@univ-lyon1.fr (J.R.)

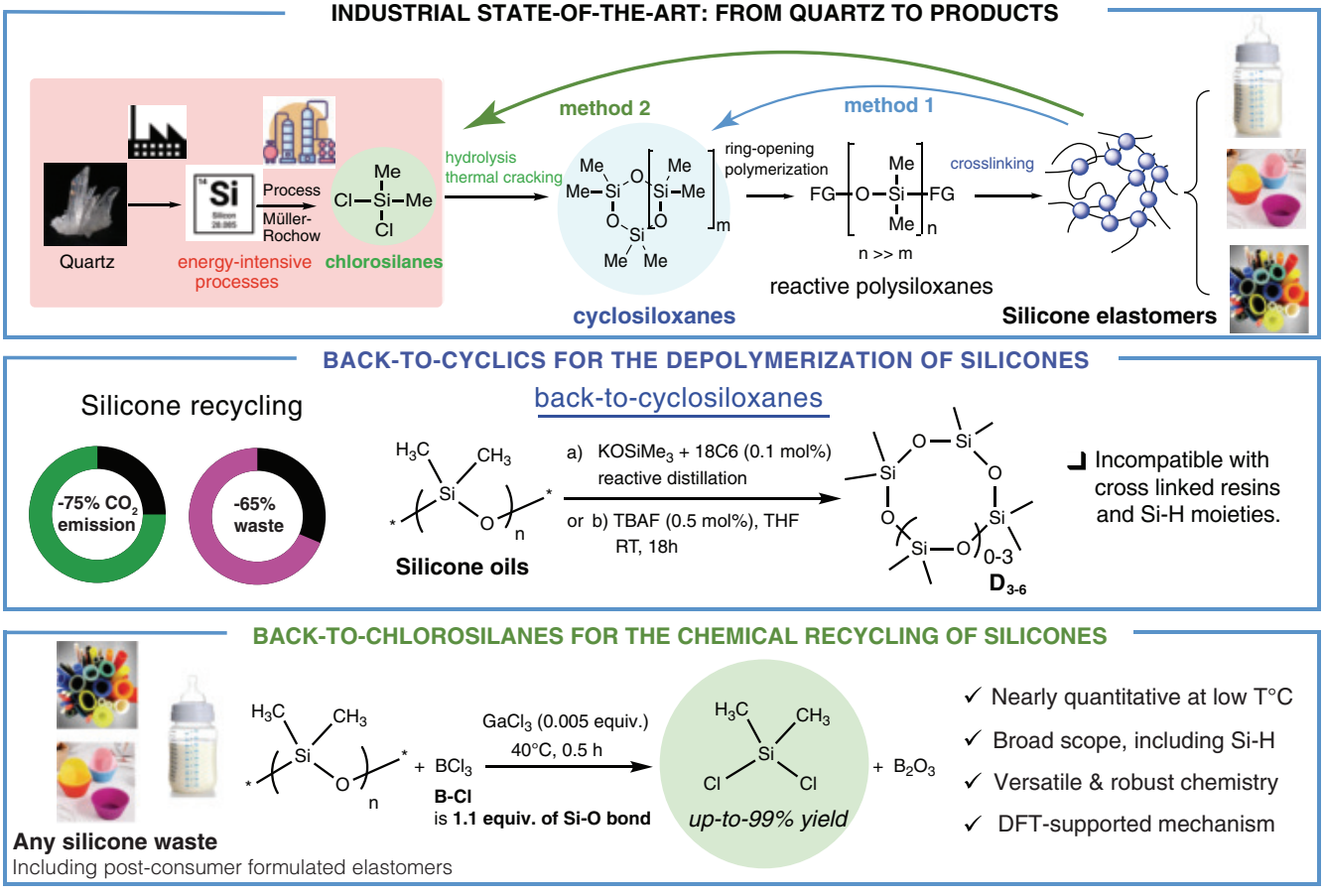

Fig. 1. General strategies for the chemical recycling of silicone polymers. (a) Conditions produce a mixture of $D_3/D_4/D_5$, whereas (b) conditions yield mainly $D_4/D_5/D_6$. RT, room temperature; TBAF, tetra *n*-butylammonium fluoride; THF, tetrahydrofuran.

and filled cross-linked materials—to produce (methyl)chlorosilanes as key commodities of the silicone industry. The reaction is performed at low temperature (40°C) in the presence of low catalyst loadings [typically 0.5 mol % down to 0.02 mol %, i.e., from 0.005 equivalents (equiv.) down to 0.0002 equiv. of Si-O bonds] using boron trichloride as a depolymerizing reagent. The heterobimetallic ion pairs resulting from an Si-O-Si bond, BCl_3 (as Lewis acid and source of Cl) and $GaCl_3$ (as a catalyst), promote Si-O and B-Cl scrambling from BCl_3 and the Si-O-Si silicone backbone. The boron oxide B_2O_3 coproduct can be used by the borosilicate glass industry or looped back into boron trichloride (*27*, *28*). Among various Lewis acids, $GaCl_3$ exhibited superior performance as a catalyst but not as a chloride source when compared with far-superior BCl_3 (see Table 1). The [BCl_3•$GaCl_3$] combination in the presence of the Si-O-Si based backbone can yield up to 99% chlorosilanes. Although this type of Lewis acidic behavior is not extensively documented (see supplementary text section "Literature precedents for the homo/hetero-bimetallic reactivities"), multinuclear nuclear magnetic resonance (NMR) spectra of the active species elucidate and confirm prior findings. With the support of molecular modeling performed using density functional theory (DFT), we unveiled the atypical mechanism of this depolymerization reaction.

The depolymerization of silicone polymers was first studied at 40°C for 24 hours using a 1 M solution of boron chloride in dichloromethane as a source of chloride. BCl_3 was selected to counterbalance the thermodynamically disfavored formation of Si-Cl bonds from Si-O bonds. Silicone oil **1** [$Me_3SiO(SiMe_2O)_{70}SiMe_3$ ($MD_{70}M$); number average molar mass (M_n) = 5340 g/mol; viscosity 100 cSt] was used as a model substrate. Treating BCl_3 in the absence of catalyst evidenced Si-O-Si backbone cleavage (see entry 1 in Table 1). Some Si-O bond cleavage was observed along with the formation of Si-Cl bonds through the formation of product **4**, but no volatile (methyl)chlorosilanes **2** and **3** were detected. To favor the chlorination process, catalysis by an additional Lewis acid was required and thus evaluated. Combining BCl_3 with a second Lewis acid seemed promising to enhance reactivity and Si-O bond cleavage.

Heterobimetallic reactivity was discovered decades ago, but its application through the combination of two Lewis acidic molecules is rarely reported. One key example was reported by Sugasawa and co-workers, using a stoichiometric BCl_3 and $GaCl_3$, to realize a specific ortho-substitution for acylation of aniline derivatives (*29*). This concept was later exploited by Negishi to elucidate what governs or induces ate complexation, transmetallation, or dynamic polarization (see fig. S6 and, more generally, supplementary text section "Literature precedents for the homo/hetero-bimetallic reactivities"); they concluded that the new metal center in the putative heterobimetallic complex must be more electrophilic than the original nonactivated one (*30*). Recently, Schindler and co-workers found that heterobimetallic species, harnessing Fe and Al Lewis acid character, could be used as excellent catalysts for carbonyl-olefin ring-closing metathesis (*31*, *32*). Interestingly, these reports reinforce the idea that the superelectrophilic character arising from such species can unlock unconventional reactivity. Although the experimental data were meticulously interpreted by a computed mechanism, spectroscopy studies

did not reveal conclusive evidence of active species. More recently, Klare, Oestreich, and co-workers reported a halodealkylation of alkylsilanes, harnessing the superelectrophilic character of arenium cations and corresponding chlorenium and silylium intermediates (*33*, *34*). The main goal here was to unlock a valuable, yet thermodynamically unfavorable, formation of Si-Cl bonds from Si-O bonds. We sought to capitalize on the heterobimetallic [BCl_3•Lewis acidic catalyst] combination to induce chlorosilane formation from Si-O-Si backbones.

Lewis acid optimization

To that effect, we tested a wide range of Lewis acids (MCl_x, 0.5 mol % of repeated siloxane unit) as catalysts for the depolymerization reaction (see entries 2 to 9 in Table 1). Limited reactivity was observed using $ZnCl_2$, $MnCl_2$, and $CoCl_2$ (some chain scissions, similar to BCl_3 working alone), whereas dichlorodimethylsilane **2** was obtained, albeit in low yield (12%), in the presence of $FeCl_2$. Conversely and interestingly, the depolymerization with $FeCl_3$ gave an excellent yield of **2** (up to 97%), albeit after 24 hours. More interestingly, the reaction using $AlCl_3$ or $GaCl_3$ provided excellent reactivity in a shorter time frame. The chlorosilane **2** was obtained in 85 and 98% yield, respectively, after only 30 min. We hypothesized that the increased chlorophilicity of these Lewis acids leads to the formation of a superelectrophilic reagent [O-BCl_2^+] from BCl_3, with Si-O-Si behaving as the Lewis base (coordination to stabilize) and $GaCl_3$ harvesting the Cl^- to generate the favorable [$GaCl_4^-$] anion, thus promoting the cleavage of Si-O-Si bonds (see discussion about the mechanism in a following dedicated section). Moreover, Me_3SiO-functionalized chain ends (where Me is methyl) could, for instance, be recovered with this process as corresponding functionalized chlorosilanes (Me_3SiCl, 99% yields). Furthermore, other gallium precatalyst species were also evaluated for the depolymerization reaction. The reactions with $GaBr_3$ and $Ga(OTf)_3$ (where OTf is trifluoromethanesulfonate) gave 95 and 70% of **2**, whereas no desired product was observed when Ga_2O_3 was used as a catalyst precursor, likely owing to immiscibility issues. In the Ga-based series, $GaCl_3$ was thus selected for further investigation, including temperature effect and catalyst loading on the performance of the depolymerization reaction (table S1). Lowering the temperature down to 0° or 25°C resulted in a good but nonquantitative yield of **2** of 67 to 70% along with the formation of silyl ether product ***3*** (10 to 11% yield). When the catalyst loading was decreased further to 0.02 mol %, the reaction time had to be consequently increased to achieve complete depolymerization. Considering all these factors, $GaCl_3$ (0.5 mol %, 40°C) was chosen for further investigation, in particular, with respect to the choice of solvent or diluent (swelling in the case of cross-linked materials).

Solvent screening

We verified that our depolymerization strategy did not require the use of dichloromethane (DCM) as a solvent. We investigated alternative

Table 1. Catalysts and reagent screening for depolymerization of model substrate. *Reaction conditions: silicone oil **1** (300 mg, 4 mmol Si-O), BCl_3 in dichloromethane 1 M (3 ml, 9 mmol Cl-, 2.2 equiv. of siloxane units), catalyst (0.5 mol %); †Yield of chlorosilanes **2**, **3**, and **4** were determined by ^{1}H-NMR analysis using mesitylene as an internal standard; ‡Yield of **5** was determined by ^{1}H-NMR analysis based on the ratio between the amount of TMSCl we observed through cleavage and the amount of trimethylsilyl in the starting material, thus corresponding to recovery of chain ends, and should be treated as a separate yield; §$GaCl_3$ was used as a catalyst.

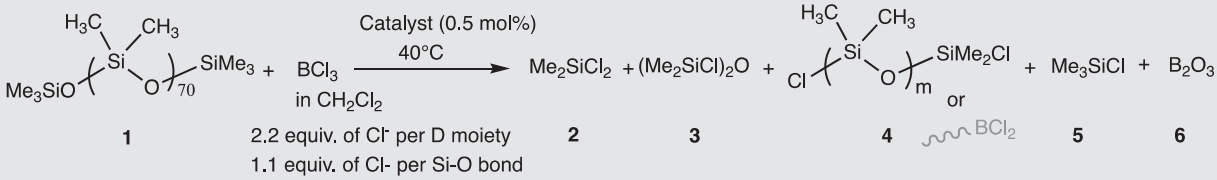

1 2 3 4 5 6

Entry	Conditions*	Time (h)	Yield of 2†	Yield of 3†	Yield of 4†	Yield of 5‡
1	No catalyst	24	0	0	100	22
2	$ZnCl_2$ or $CoCl_2$ or $MnCl_2$	24	0	0	100	20-44
3	$FeCl_2$	24	12	15	77	99
4	$FeCl_3$	24	97	3	0	99
5	$AlCl_3$	0.5	85	12	3	99
6	$GaCl_3$	0.5	98	2	0	99
7	$GaBr_3$	0.5	95	5	0	99
8	$Ga(OTf)_3$	0.5	70	9	21	99
9	Ga_2O_3	24	0	0	100	20
10§	BCl_3 in *n*-heptane	0.5(5)	60(75)	24(16)	16(9)	99(99)
11§	BCl_3 in toluene	0.5(2)	62(95)	17(5)	21(0)	99(99)

appealing solvents, either for the dilution (linear PDMS waste) or for the necessary swelling of any silicone waste (including mixed elastomers), such as toluene and heptane (see entries 10 and 11 in Table 1 and entry 1 in table S2). Because BCl_3 has a low boiling point (12°C) and it is hard to handle in a neat state, we evaluated its dissolution in different solvents (CH_2Cl_2, heptane, or toluene). When the reaction was performed at 40°C for 30 min, the depolymerization in DCM yielded 98% of **2,** whereas using BCl_3 in *n*-heptane or toluene solutions provided yields of **2** at 60 and 62%, respectively. Besides chlorinated solvents, toluene and aromatics as well as heptane and alkanes are known to efficiently swell PDMS-based materials (*35*).When the reaction time was increased, a better conversion of **1** was also observed. After 2 hours, the depolymerization in toluene gave an excellent dichlorosilane yield (95%), whereas the depolymerization in *n*-heptane provided 75% yield of **2** after 5 hours. Furthermore, the temperature could also be increased when higher boiling toluene was used. After 1 hour at 90°C, nearly quantitative yield of **2** was obtained (see entry 1 in table S2) with very little percentage of silyl ether ***3***. Thus, both more sustainable and ecofriendly solvents provided good to excellent yields of desired (methyl)chlorosilanes, albeit using slightly longer reaction times (see entries 10 and 11 in Table 1).

Source of chloride

$AlCl_3$ was tested as an alternative chloride source for the depolymerization, as previously reported by Mair and co-workers (*36*) (see entries 3 and 4 in table S2). Of note, $AlCl_3$ is a by-product of the Si industry (after the Müller-Rochow and subsequent hydrolysis processes). We carried out the reaction at different temperatures (40°C for CH_2Cl_2 and 90°C for $ClCH_2CH_2Cl$ as solvents or swelling agents) for 24 hours. However, only a low yield of chlorosilane **2** (10 to 12%) was observed. We suspect that although the first Al-Cl bond of $AlCl_3$ is reactive, the subsequent –O-$AlCl_2$ and further oxygenated counterparts are far-less-efficient chlorinating reagents. Additionally, $GaCl_3$ was ruled out as the chlorinating reagent, owing to its favored transmethylation (*37*). Finally, we also investigated other metallic or metalloid-based chloride sources such as $TiCl_4$, $SiCl_4$, $CuCl_2$, or even a solution of HCl in dioxane (4M) as alternative chloride sources, but no reactivity was detected in any of these cases (see entries 5 to 9 in table S2), highlighting the advantageous role of boron trichloride as a source of chloride.

Recycling of functional waste oils

After optimization with PDMS oil **1** with viscosity of 100 centistokes (cSt), we selected the conditions for the depolymerization of other silicone waste as follows: BCl_3 as the Cl source (2.2 equiv. of Cl per Si atom to convert, mainly targeting Me_2SiCl_2 as product, which corresponds to 1.1 equiv. of B-Cl bond per Si-O bond) and $GaCl_3$ (0.5 mol%) as the catalyst at 40°C for 30 min. We applied these conditions to a series of silicone oils with different chain-end functionalities (Fig. 2 and table S3). First, we examined several trimethylsilyl end-capped polysiloxanes with higher viscosities **7** and **8** (respectively 1000 cSt and 10^6 cSt). All of them gave an excellent yield of chlorosilane **2** (95 to 97%) upon recycling, indicating that the molar masses of the linear PDMS or silicone gum (very-high–molar mass linear PDMS) do not affect the efficiency of the depolymerization method. We also probed the seemingly very fast kinetics of our depolymerization by attempting to monitor the chain scission using size exclusion chromatography (SEC) (see supplementary text section "Kinetic partial study on the depolymerization of the silicone gum") by quenching the chloro-capped oligomers with absolute ethanol (EtOH). The experiment confirmed that 45% of chlorosilane **2** and 32% of silyl ether ***3*** could be obtained after only 5 min of reaction, indicating extremely fast kinetics for this depolymerization (see fig. S23). Only very-low–molar mass oligomers remained to be recycled back to chlorosilanes.

We then also tested the vinyl-terminated silicone oils **9** and **10** under standard conditions. A good yield of **2** (93 and 96%) was also afforded. Additionally, we also investigated silanol-terminated polysiloxanes **11** and **12**, which gave the desired product **2** in very good yields (93 to 97%). Moreover, we tested the resin **13**, which consists of 75% D moieties, 20% T moieties, and 4% M moieties, under the reaction conditions (*38*). Yields of 90% of **2** and 10% of ***3*** were obtained after the deconstruction. Some advantageous depolymerization products of the T fraction such as $MeSiCl_3$ and $(MeSiCl_2)_2O$ were detected in 10 and 50% yields, respectively. T moieties are particularly challenging for silicone recycling because their accumulation in back-to-cyclics depolymerization strategies often yields a cross-linked insoluble fraction that requires process discontinuity and extensive cleaning [(*15*–*17*), and see discussion on demethylation in (*18*) in particular].

Furthermore, and to showcase the robustness and universality of the method, we also investigated waste silicone block copolymer **14**, which has phenyl content (5 mol %) and a viscosity of 60,000 cSt, under optimized depolymerization conditions. After 30 min, chlorosilane **2** was produced in a yield of 97% based on D moieties (*39*). Dichlorodiphenylsilane was obtained as the major product from depolymerization of diphenylsiloxane moieties within the copolymer. It was identified with its characteristic doublet of doublets (dd) appearing at 7.75 parts per million (ppm) [dd, scalar coupling (*J*) = 8.1 and 1.5 Hz] [see also fig. S36 and supplementary materials (SM)]. Eventually, we evaluated silicone oil **15** containing numerous Si-H moieties—which is extremely challenging to recycle compared with fully methylated silicone oils regarding both safety (H_2 generation and hydride redistribution leading to explosive molecules) and chemical instability—for the depolymerization. Excellent yields of methyldichlorosilane (Me(H)$SiCl_2$) (>95%) and minor silyl ether (Me(H)$SiCl)_2O$ (<5%) were observed. In all examples, chain end–derived chlorosilanes (M moieties) were recovered almost quantitatively (see gray column for product **5**, separated with doubled line in table S3), except for silanol-terminated substrates, which were logically lost during chlorination. These chain blockers [e.g., trimethylsilyl chloride (TMSCl)] are particularly valuable to the Si industry.

Scale-up

Finally, we conducted a scale-up of the method first using 2 g of silicone oil **1** and then using ~80 g of **1** (see supplementary text section "Scale-up experiment for depolymerization of silicone oil") in a dedicated semibatch process. We applied a distillation setup to separate the volatile fraction (containing Me_2SiCl_2 and CH_2Cl_2) and solid coproduct (B_2O_3). We analyzed the side product by solid-state ^{11}B-NMR spectroscopy, and it mainly comprised the boron oxide with some B-Cl residual bonds. Chlorosilane **2** was observed in a high yield of 97%, and boron oxide was isolated as a white solid (95% yield) at the 2-g scale; then, for the promising 80-g-scale experiment, the yields were 95 to 97% (D moieties in liquid distillate plus leftovers in boiler) and ~99%, respectively (see SM for details). The latter allowed for monitoring of the depolymerization reaction (see see supplementary text section "Scale-up experiment for depolymerization of silicone oil"), which we exploited in the mechanistic investigation that follows. Additionally, we could achieve more precise characterization of the B_2O_3 coproduct at this larger scale, revealing minimal contamination by B-Cl bonds (<7%, confirmed by ^{11}B-ss-NMR), likely because of the slight excess used to ensure full transformation to chlorosilanes (figs. S59 and S60). This side product of chemical recycling could therefore be recycled in another industrial loop (*40*), harnessing, for instance, $SiCl_4$ (a presently unwanted by-product of the Müller-Rochow process), or be reused by the borosilicate glass industry.

Recycling of waste elastomers, industrial waste, and postconsumer waste

Silicone elastomers are more challenging substrates for depolymerization processes because manufacturers often formulate complex mixtures of fillers and additives, cross-linked

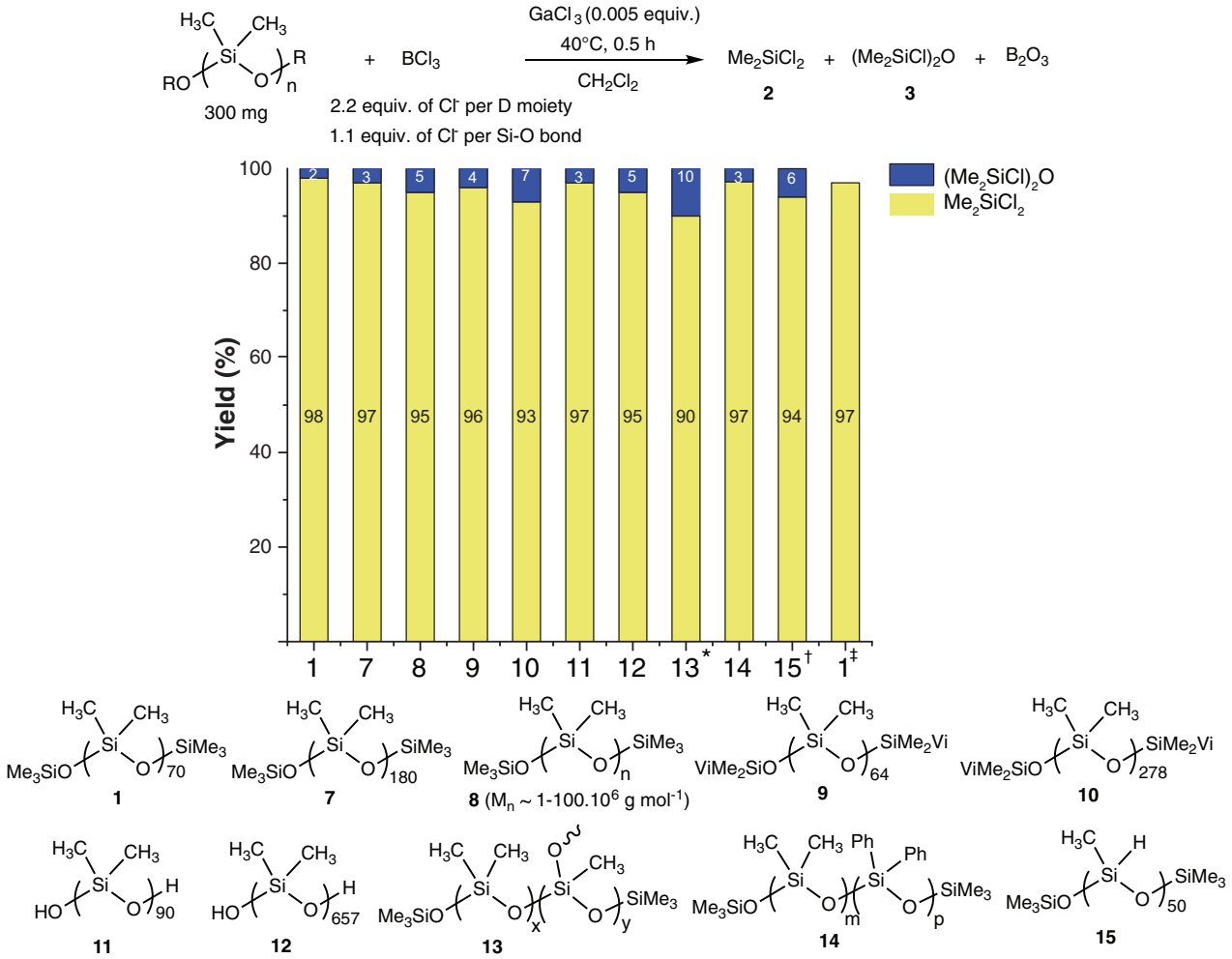

Fig. 2. Scope for the chemical recycling of silicone oils or copolymer to corresponding chlorosilanes. *$MeSiCl_3$ (10% yield) and $(MeSiCl_2)_2O$ (50% yield) were observed as the depolymerization of T units; †Observed corresponding chlorosilanes are $Me(H)SiCl_2$ and $(Me(H)SiCl)_2O$; ‡Scale-up experiment for 2 g of **1**. Vi, vinyl (–CH=CH2); Ph, phenyl (–C6H5).

silicone elastomers, and catalysts. These mixtures are even more challenging at their end of life, with life-span contamination that includes many organic and inorganic contaminants, rendering their formulation even more complex. Polysiloxanes often account for 60 to 70 wt %, whereas fillers (inorganics often based on silica or chemically modified SiO_2), pigments, and catalyst often fall within a range of 30 to 40 wt %. Several representative postconsumer silicone waste items—nipple pads, cupcake molds, silicone sheets, and water or liquid tubing—were used as starting materials for the depolymerization process (Fig. 3 and table S4). No pretreatment was used (aside from obvious dirt removal by wiping), because these postconsumer wastes did not undergo trash disposal and mixing, collecting, and sorting at facilities that could lead to a more complex mix of polymers [polyolefins, PET of even polyvinylchloride (PVC) contaminants]. Desired product **2** was obtained in high yields (90 to 99%, based on theoretical Si-O-containing moieties) (entries 1 to 4 in table S4). Then, we also tested industrial wastes, supplied by our industrial partner Elkem Silicone, under optimized conditions (entries 5 to 8 in table S4). First, we subjected RTV1- and RTV2-formulated elastomers (room-temperature vulcanizates, with fillers), which are obtained through cross-linking using tin (Sn) or platinum (Pt) catalysts, to the depolymerization conditions. Desired product **2** was obtained in an excellent yield (95%). Moreover, we also evaluated high-temperature vulcanization (HTV) elastomer (with fillers) that was cross-linked at elevated temperature in the presence of peroxide initiators. After 30 min, chlorosilane **2** was again obtained in a quantitative yield. We extended this protocol to a more challenging HTV elastomer (formulation with additives and fillers densely cross-linked by peroxide and hydrosilylation at 170°C rather than ~120°C for classical HTV elastomers). By recycling this waste, 80% of **2** and 20% of **3** were recovered after depolymerization, even for this densely cross-linked silicone material. The chlorination of cross-linking knots was also detected in the crude mixture as the appearance of characteristic signals in ^{1}H-NMR spectra at 0.66 and 0.62 ppm (characteristic of Cl_2MeSi-CH_2CH_2-$SiMeCl_2$). Finally, we subjected a mixture of all elastomers without sorting (3 g) to these recycling conditions (see also movie S1 of this experiment and corresponding selected frames in fig. S69). After 2 hours, we distilled the crude mixture under reduced pressure (40°C, 200 mbar) to yield chlorosilane **2** and silyl ether **3** at 83 and 6%, respectively. A mixture of B_2O_3, SiO_2 (2.2 g), and minimal silicone residues was also isolated after the distillation as a gray fine solid (see figs. S61 and S62). This B_2O_3-rich mixture could be used as base material in the production of borosilicate glass, boron nitride, or boron carbide (*27*). These positive results demonstrate that this chemistry is highly selective and robust. Chain-end functionalities and network connectors (T moieties or chlorosilanes

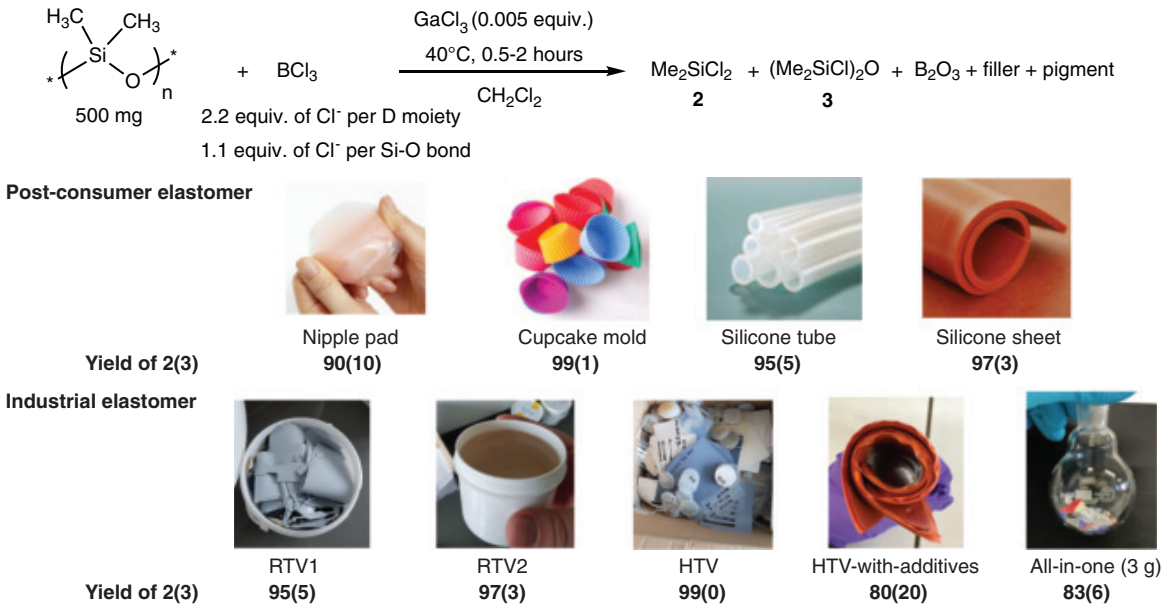

Fig. 3. Scope for the chemical recycling of silicone elastomers to corresponding chlorosilanes.

from hydrosilylation bridges) could be recovered once again as valuable chlorosilanes or chain-capping agents for regeneration of catalog oils for the Si industry.

Mechanistic investigation by NMR

To enhance our understanding and potentially tackle future challenges in silicon chemistry, we sought insight into the active species resulting from the combination of chlorinated Lewis acids and $GaCl_3$ using multinuclear NMR spectroscopy (Fig. 4). First, we analyzed the mixture of BCl_3 and $GaCl_3$ (1:1 ratio) in CD_2Cl_2, but the evidence of an anticipated Cl-bridged dimer was hard to detect (see SM for a detailed analysis). We beneficially added triphenylphosphine (PPh_3) to the mixture in CD_2Cl_2 in a molar ratio of 1:1:2 (BCl_3:$GaCl_3$:PPh_3) and recorded the in situ NMR analyses (^{11}B, ^{31}P, and ^{71}Ga) at room temperature. The substantial difference between the initial BCl_3 signal at 46.5 ppm and the new resonance at 3.91 ppm [doublet (d), J = 154.6 Hz for the $J^1\{^{11}B\text{-}^{31}P\}$ coupling] (Fig. 4A) was attributed to the signal of a stabilized electrophile $[BCl_2(PPh_3)_2]^+$. This reveals the likely halide abstraction using 1 equiv. of $GaCl_3$ and 2 equiv. of PPh_3, which agrees with tetracoordinate boronium species in solution (*41*). Moreover, the main resonance at −1.03 ppm [quadruplet (q), 154.6 Hz for the $J^1\{^{31}P\text{-}^{11}B\}$ coupling] was observed in the ^{31}P-NMR spectrum (Fig. 4B), indicating the interaction of triphenylphosphine with BCl_2^+. Additionally, the overlap of the characteristic quadruplet of $J^1\{^{31}P\text{-}^{11}B\}$ and minor septuplet of $J^1\{^{31}P\text{-}^{10}B\}$ can be identified. The quaternization of the gallium center was also confirmed by ^{71}Ga-NMR spectroscopy (Fig. 4C). The ^{71}Ga-NMR spectrum of active species exhibited a broad feature with two maxima at 250 and 270 ppm, consistent with analogous species $[GaCl_4]^-$ and $[Ga_xCl_{3x+1}]^-$ to those identified for the P-donors (*42*, *43*). For the ^{71}Ga-NMR reference, [bmim$^+GaCl_4^-$] was synthesized. Its main resonance was observed at ~250 ppm as a narrow signal, which corresponds to a nearly centrosymmetric tetracoordinate anion $[GaCl_4]^-$. Similar species can also be identified with $AlCl_3$ instead of $GaCl_3$, which bolstered our assignment (centrosymmetric tetracoordinate anion $[AlCl_4]^-$ and polymeric analogs; fig. S58). In agreement with our spectroscopic study, we postulate a first cycle in the mechanism of the unusual electrophile depolymerization as described in Fig. 4D.

To raise our understanding of the key steps of the depolymerization mechanism, we performed selective cleavages of hexamethyldisiloxane (HMDS) and hexamethylcyclotrisiloxane (D_3) using stoichiometric amounts of BCl_3 and/or $GaCl_3$ as chlorinating reagents in CD_2Cl_2. HMDS and D_3 were selected to best represent the chain ends and main moieties (D) of the silicone waste to recycle while retaining a manageable molecular dimension for the DFT calculation. We performed those model reactions in 5-mm NMR tubes under inert atmosphere and analyzed the corresponding multinuclear NMR spectra to detect key intermediate species. BCl_3 can efficiently produce TMSCl from HMDS (50% yield using 1 equiv. BCl_3 with concomitant formation of TMS-O-BCl_2). Initially, boron trichloride was also able to cleave the D moieties of D_3 (Si-O-Si bond) to yield Si-Cl and Si-O-B bonds (see figs. S63 to S66). Moreover, it favored the redistribution between mono-, di-, and tri-alkoxy borate derivatives (**B1a**, **B2a**, and **B3a**). However, it was not possible to cleave and chlorinate the corresponding O-Si-Cl bond to give Me_2SiCl_2. To obtain the dimethyldichlorosilane **2**, another metal-chloride-based Lewis acid such as $GaCl_3$ (Fe- or Al-based analogs can be used as well; see Table 1) must be involved in the catalytic cycle to break Cl-$(Me_2SiO)_x$-BCl_2 derivatives into Me_2SiCl_2 and its corresponding Cl-B-O derivatives, which could further yield B_2O_3 with the help of catalysis (see supplementary text section "NMR spectra: f. Further deciphering putative mechanisms on the depolymerization of model substrates"). $GaCl_3$ can also cleave HMDS to yield 0.5 equiv. of TMSCl and full conversion when using 2 equiv. with respect to HMDS. However, $GaCl_3$ by itself is unable to cleave D_3. Only by adding the resulting mixture of HMDS/2 equiv. $GaCl_3$ to D_3/$GaCl_3$ can we observe the formation of desired product **2**, albeit not quantitatively. These model reactions already suggest the need for a prerequisite complexation of a Lewis base to allow the formation of [LB-$BCl_2^+GaCl_4^-$]-type species, with a Si-O-Si bond acting as the in situ Lewis base.

As a first approach, we estimated the thermochemical driving force for these transformations by using tabulated bond dissociation energies, that is, enthalpies of formation for Si-Cl/B-O formation versus B-Cl/Si-O cleavage (*44*–*50*) corresponding to the overall bond metathesis process. To our surprise, depending on the tabulated data, the resulting reaction enthalpy ranged from slightly exothermic by −3 kcal/mol to endothermic by 17 kcal/mol. The Si-O bond energy seems particularly influenced

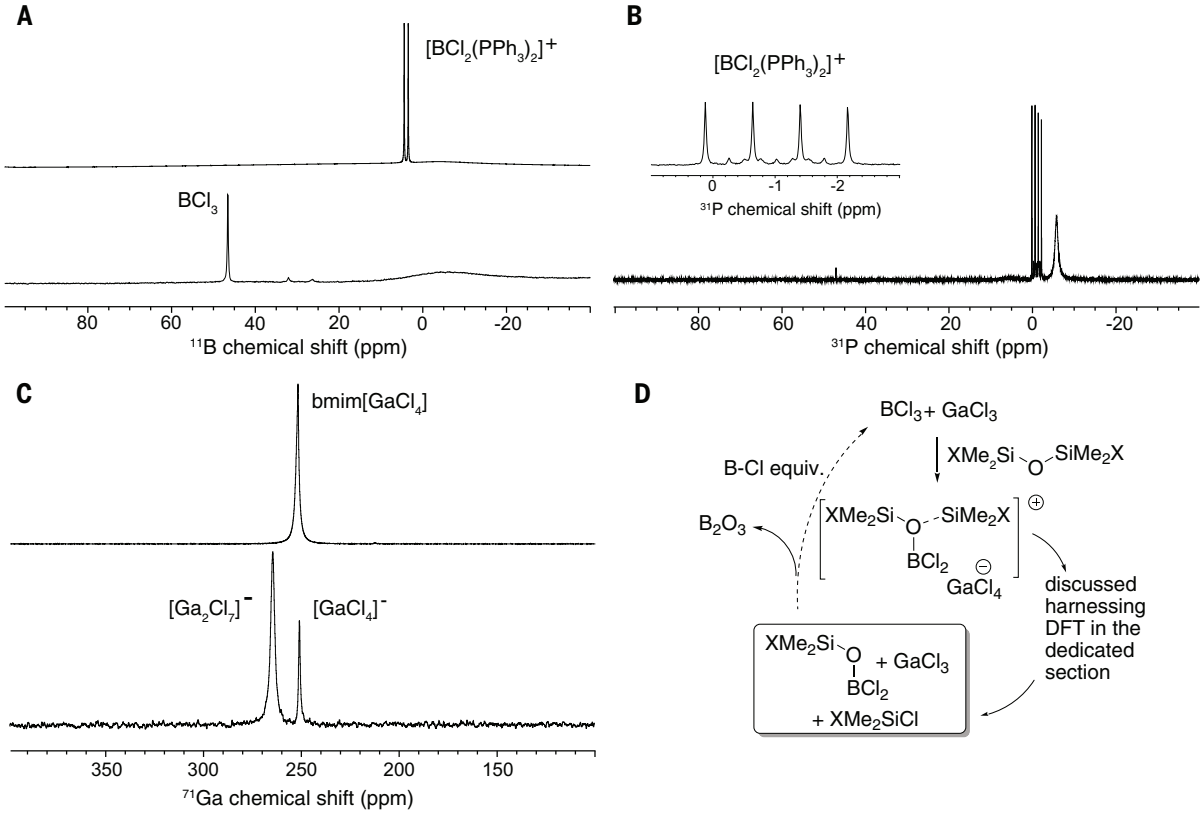

Fig. 4. Multinuclear NMR spectra of active species and postulated mechanism of depolymerization. Triphenylphosphine was used to trap reactive $+BCl_2$ cation generated from 1:1 BCl_3:$GaCl_3$ mixture (PPh_3:BCl_3:$GaCl_3$ in a 2:1:1 ratio). (**A**) ^{11}B-NMR, CD_2Cl_2, 25°C. (**B**) ^{31}P-NMR, CD_2Cl_2, 25°C. (**C**) ^{71}Ga-NMR, CD_2Cl_2, 25°C. (**D**) Postulated mechanism of the depolymerization reaction. X represents Cl (chlorine) or polydimethylsiloxane backbones.

by the molecular environment, which prompted us to seek insights from molecular modeling at the DFT level.

Mechanistic investigation by DFT

By performing calculations at the DFT level (see details in SM), we were able to rationalize the reactivity of $GaCl_3$ and/or BCl_3 with D_3 (Fig. 5), thus elucidating the depolymerization mechanism. In the first instance, the lack of reactivity of $GaCl_3$ alone is explained by the high Gibbs free energy barrier required for the Si-O/Si-Cl bond metathesis (**TS_1-Ga** ~31 kcal/mol) and its endergonicity (Fig. 5A). In the case of BCl_3, boron oxophilicity weakens the Si-O bond enough to halve the activation energy of the Si-O/Si-Cl bond metathesis to 15 kcal/mol (**TS_1-B**; Fig. 5B) and to thermodynamically favor Si-Cl and O-BCl_2 formation as detected by NMR spectroscopy. The following O-B-O cyclization via **TS_2-B** is endergonic by ~6 kcal/mol, and the subsequent chlorination and associated second Si-O cleavage (**TS_3-B**) is kinetically prevented relative to the experimental conditions. The energetics of these two steps thus hinder the reaction to proceed further, in line with experimental results. For both Lewis acids, when used independently, Si-O/Si-Cl bond metathesis transition states **TS_1-Ga** and **TS_1-B** feature distorted square-pyramidal geometries at Si (Fig. 5C), a pattern that differs when both $GaCl_3$ and BCl_3 are combined (vide infra).

In addition, we calculated bond dissociation energies on an opened D_3 molecule by BCl_3 (see fig. S67 and table S5) and obtained an exothermic value of –15 kcal/mol for the transformation of B-Cl/Si-O to B-O/Si-Cl bonds, a very different value from the enthalpy (ΔH) calculated or approximated from average tabulated enthalpies and in better agreement with the experimental results.

When D_3 reacts with both BCl_3 and $GaCl_3$, the formation of $GaCl_4^-$ by Cl transfer from B to Ga upon O-B bond formation is virtually barrierless and thermodynamically favored (~2 kcal/mol via **TS_0-GaB**), with a gain of ~4 kcal/mol over the Lewis adduct. This exchange reaction is driven by boron's preference to form B-O over B-Cl bonds, consequently weakening the (B)O-Si bond and raising the cationic character of the vicinal silicon atoms (*34*). This boron-to-gallium Cl transfer reaction also affects the geometry at Si that evolves from tetrahedral to distorted trigonal pyramid. The character of the Si center approaches a silylium cation, which could be crucial to promote the chloride transfer (*34*). From this geometry, the Si can undergo an O-to-Cl exchange mediated by an attack of $GaCl_4^-$ at both Si apical positions of a transient and hypervalent trigonal bipyramid (**TS_1-GaB_{syn}** and **TS_1-GaB_{anti}** in Fig. 5E; see also fig. S68). The Gibbs free energy barrier for the O-to-Cl exchange is lowered by 6 kcal/mol when Cl and O are trans to each other. In contrast to the BCl_3 case, the formation of new B-O bonds continues (**TS_2-GaB**) at the expense of Cl release by B and transient capture by $GaCl_3$, which again weakens the adjacent O-Si bonds to yield Me_2SiCl_2 (**TS_3-GaB_{anti}**), lowering this barrier by almost 10 kcal/mol in comparison to BCl_3. Interestingly, the promotion of such type of superelectrophilic intermediates by $GaCl_3$ has been suggested by DFT studies (*51*). Futher investiation of these associations of chlorinated Lewis acids could pave the way to other challenging transformations.

Outlook

The universal chemical depolymerization for silicones we have described here holds some potential for industrialization, bearing appropriate collecting and sorting of silicone waste. Securing identified waste streams will help this Ga/B-based technology. Industrial separation of (methyl)chlorosilanes is already a mature technology, which is done on very

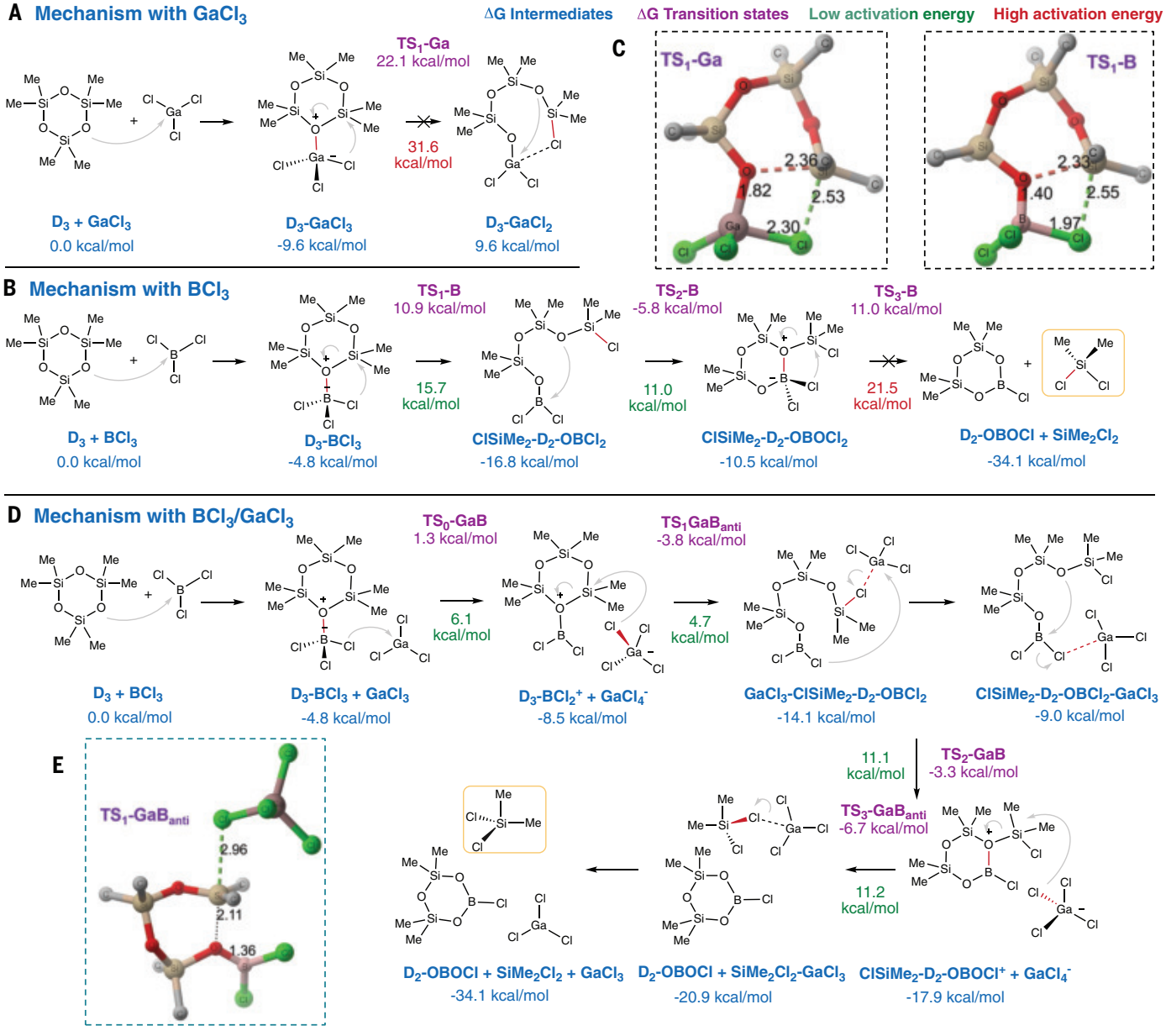

Fig. 5. DFT simulations of the formation of Me_2SiCl_2 from D_3. (**A**) Reaction with $GaCl_3$ alone. (**B**) Reaction with BCl_3 alone. (**C**) Corresponding transition states for Si-O cleavage and Cl-Si formation. (**D**) Reaction with both $GaCl_3$ and BCl_3. (**E**) Corresponding transition state with T_1-GaB anti conformation (for T_1-GaB syn, see fig. S68). DFT basis sets and method are as follows: Gaussian 16; M06; C, H (def2-SVP); B, O, Si (def2-SVPD); Cl (ECP10MWB+1p+2d); Ga (ECP28MWB,VTZ); SMD (CH_2Cl_2). ΔG, Gibbs free energy.

large scale by the silicone manufacturers. Adding a new feedstock to the industrial fractional distillation cascade appears straightforward. We provide proof of concept for a fed-batch semicontinuous process to produce the (methyl)chlorosilanes with discrete addition of waste (see fig. S25 and corresponding discussion in supplementary text section "Catalyst recycling") with strong potential for $GaCl_3$-based catalytic system reuse (or continuous use), through appropriate process ecodesign. Reuse or recycling of boron oxide will also be critical, with some potential harnessing of $SiCl_4$ (*40*). This work paves the road for the circular economy of silicon but also highlights an original reactivity through Ga-B synergy.

REFERENCES AND NOTES

1. J. E. Mark, *Acc. Chem. Res.* **37**, 946–953 (2004).
2. Grand View Research, "Silicone market size, share & trends analysis report by product (fluids, gels, resins, elastomers), by end-use (electronics, transportation, construction, healthcare, industrial processes, energy), by region, and segment forecasts, 2024 – 2030" (Report GVR-1-68038-063-7, Grand View Research, 2023); https://www.grandviewresearch.com/industry-analysis/silicone-market.
3. L. Shi *et al.*, *Science* **381**, 1011–1014 (2023).
4. N. S. Sarai *et al.*, *Science* **383**, 438–443 (2024).
5. L. T. J. Korley, T. H. Epps III, B. A. Helms, A. J. Ryan, *Science* **373**, 66–69 (2021).
6. I. Vollmer *et al.*, *Angew. Chem. Int. Ed.* **59**, 15402–15423 (2020).
7. F. Zhang *et al.*, *Science* **370**, 437–441 (2020).
8. R. J. Conk *et al.*, *Science* **377**, 1561–1566 (2022).
9. A. Rahimi, J. M. García, *Nat. Rev. Chem.* **1**, 0046 (2017).
10. G. W. Coates, Y. D. Y. L. Getzler, *Nat. Rev. Mater.* **5**, 501–516 (2020).
11. W. Zhang *et al.*, *Science* **379**, 807–811 (2023).
12. N. R. Ciccia *et al.*, *Science* **381**, 1433–1440 (2023).
13. K. P. Sullivan *et al.*, *Science* **378**, 207–211 (2022).
14. Z. Xu *et al.*, *Science* **381**, 666–671 (2023).
15. B. Rupasinghe, J. C. Furgal, *Polym. Int.* **71**, 521–531 (2022).
16. A. T. Wolf, A. Stammer, *Polymers* **16**, 2220–2531 (2024).
17. Elkem, Internal survey and calculations by Elkem Silicones of market trends, carbon footprints and life-cycle assessments; https://magazine.elkem.com/innovation-sustainability/Lower_Carbon_Circular_Safer_Silicone_Materials/.
18. N. D. Vu, A. Boulègue-Mondière, N. Durand, J. Raynaud, V. Monteil, *Green Chem.* **25**, 3869–3877 (2023).

19. W. Knott, H. Dudzik, D. Schaefer, US Patent 20200377686A1 (2020).
20. C. Allandrieu, D. Cardinaud, US Patent 5,670,689 (1997).
21. R. F. Weitkamp, B. Neumann, H.-G. Stammler, B. Hoge, *Angew. Chem. Int. Ed.* **59**, 5494–5499 (2020).
22. B. Rupasinghe, J. C. Furgal, *ACS Appl. Polym. Mater.* **3**, 1828–1839 (2021).
23. S. Enthaler, *Angew. Chem. Int. Ed.* **53**, 2716–2721 (2014).
24. P. Zhang, D. Zhang, J. Dong, G. Chen, J. Li, *Org. Process Res. Dev.* **26**, 2270–2280 (2022).
25. J. F. Hyde, *Science* **147**, 829–836 (1965).
26. P. Döhlert, S. Enthaler, *J. Appl. Polym. Sci.* **132**, 41287 (2015).
27. L. D. Pye, V. D. Fréchette, N. J. Kreidl, Eds., *Borate Glasses: Structure, Properties, Applications*, Materials Science Research, vol. 12 (Springer, 2012).
28. A. J. Becker, R. Careatti, US Patent 645803 (1975).
29. T. Sugasawa, T. Toyoda, M. Adachi, K. Sasakura, *J. Am. Chem. Soc.* **100**, 4842–4852 (1978).
30. E. Negishi, *Pure Appl. Chem.* **53**, 2333–2356 (1981).
31. H. Albright *et al*., *J. Am. Chem. Soc.* **141**, 1690–1700 (2019).
32. A. J. Davis, R. B. Watson, D. J. Nasrallah, J. L. Gomez-Lopez, C. S. Schindler, *Nat. Catal.* **3**, 787–796 (2020).
33. T. He, H. F. T. Klare, M. Oestreich, *Nature* **623**, 538–543 (2023).
34. H. F. T. Klare *et al*., *Chem. Rev.* **121**, 5889–5985 (2021).
35. J. N. Lee, C. Park, G. M. Whitesides, *Anal. Chem.* **75**, 6544–6554 (2003).
36. M. R. Alexander, F. S. Mair, R. G. Pritchard, J. E. Warren, *Appl. Organomet. Chem.* **17**, 730–734 (2003).
37. H. Schmidbaur, W. Findeiss, *Angew. Chem. Int. Ed.* **3**, 696 (1964).
38. The depolymerization of T units is thus reported for the first time, giving $MeSiCl_3$ and $(MeSiCl_2)_2O$ in a yield of 10 and 50%, respectively. As for nomenclature, the M moiety possesses one Si-O bond (and three Si-C bonds in PDMS), the D moiety has two Si-O bonds, the T moiety has three Si-O bonds, and the Q moiety has four Si-O bonds (such as in silica).
39. A mixture of oligomers of $Cl(Ph_2SiO)_xSiPh_2Cl$, including Ph_2SiCl_2, for the recycling of copolymer 14 was found, indicated by the appearance of NMR resonances at 7.75 (dd) and 7.50 (m) ppm in ^1H NMR analysis, as evidenced by fig. S36. It is likely that recovering the Ph_2SiCl_2 quantitatively would necessitate harsher reactive distillation conditions.
40. W. H. Schechter, US Patent Application 2983583 (1961).
41. K. Matuszek, S. Coffie, A. Chrobok, M. Swadźba-Kwaśny, *Catal. Sci. Technol.* **7**, 1045–1049 (2017).
42. A. W. Douglas *et al*., *Tetrahedron Lett.* **35**, 6807–6810 (1994).
43. S. Coffie *et al*., *Angew. Chem. Int. Ed.* **54**, 14970–14973 (2015).
44. T. L. Cottrell, *The Strengths of Chemical Bonds* (Butterworths Publications Ltd., ed. 2, 1958).
45. B. deB. Darwent, National Standard Reference Data Series, National Bureau of Standards, NSRDS-NBS 31 (1970); https://srd.nist.gov/NSRDS/NSRDS-NBS31.pdf.
46. S. W. Benson, *J. Chem. Educ.* **42**, 502 (1965).
47. J. A. Kerr, *Chem. Rev.* **66**, 465–500 (1966).
48. R. Walsh, "Bond dissociation energies in organosilicon compounds," University of Reading; https://www.gelest.com/wp-content/uploads/technical_library/10BondDiss.pdf.
49. R. Becerra, R. Walsh, in *Organosilicon Compounds: Experiment (Physico-Chemical Studies) and Applications*, V. Y. Lee, Ed. (Academic Press, 2017), pp. 79–113.
50. LibreTexts Chemistry, Bond energies; https://chem.libretexts.org/Bookshelves/Physical_and_Theoretical_Chemistry_Textbook_Maps/Supplemental_Modules_(Physical_and_Theoretical_Chemistry)/Chemical_Bonding/Fundamentals_of_Chemical_Bonding/Bond_Energies.
51. S. Yang, C. Bour, V. Gandon, *ACS Catal.* **10**, 3027–3033 (2020).
52. N. Đ. Vũ *et al*., Data from: Gallium-catalyzed boron-assisted recycling of silicone waste yields key chlorosilanes. Dryad (2025); https://doi.org/10.5061/dryad.xpnvx0krx.

ACKNOWLEDGMENTS

We acknowledge financial support from BPI France (French State and Région Auvergne-Rhône-Alpes with project PSPC Régions REPOS). We also thank L. Vovelle (Elkem Silicones) for enlightening discussions regarding recycling and the grand-scale fate of waste and for his constant support and leadership throughout our efforts to make silicone circularity a reality. We thank V. Henryon and *Activation* for the scale-up of this recycling process. We thank D. Blanc for proofreading the article and F. Dupin for SEC characterization (Elkem Silicones). We also thank the entire REPOS consortium for stimulating discussions on circular economy and particularly on the circularity of silicones. Finally, we thank N. Oueslati for preliminary solid-state NMR experiments on the CP2M in-house 500Mz apparatus. Finally, the CCIR of ICBMS is acknowledged for a generous allocation of computational resources and providing technical support. **Funding:** This project was funded within a joint framework between the State under the Future Investment Program and the Aura Region (Région Auvergne-Rhône-Alpes) under the acronym REPOS. We also thank the CNRS, Activation, and Elkem Silicones for providing equipment and raw materials for the project. **Author contributions:** Conceptualization: J.R., V.M.; Methodology: N.Đ.V., V.M., J.R.; Resources: A.B.-M., N.D., M.B., R.L.; NMR characterization: D.G., A.B.; DFT calculation: S.R.-G., M.-E.L.P.; Visualization: N.Đ.V., V.M., J.R.; Project administration: J.R., V.M., J.M.; Supervision: J.R., V.M., J.M.; Writing – original draft: N.Đ.V., V.M., J.R., with participation of all authors; Writing – review & editing: N.Đ.V., V.M., J.R., with participation of all authors. **Competing interests:** N.Đ.V., A.B.-M., N.D., J.R., and V.M. are the inventors on patent application WO2023222749A1, released on 23 November 2023. The other authors declare no competing interests. **Data and materials availability:** All data, including spectroscopic characterization of all compounds and materials and the basis for DFT calculations, are available either in the SM (processed) or in the Dryad repository [(*52*); includes all spectroscopic (multinuclear liquid- and solid-state NMR) and chromatographic raw data as a compressed file named "NMR_raw_data_+chromato.zip" and all xyz Cartesian coordinates from calculations at the DFT level as a compressed file named "cartesian_coordinates_mech-model.zip"].

SUPPLEMENTARY MATERIALS

science.org/doi/10.1126/science.adv0919
Materials and Methods
Supplementary Text
Figs. S1 to S69
Tables S1 to S5
References (*53*–*65*)
Movie S1

Submitted 4 December 2024; accepted 27 February 2025
10.1126/science.adv0919

EXOPLANETS

Microlensing events indicate that super-Earth exoplanets are common in Jupiter-like orbits

Weicheng Zang[1,2]*, Youn Kil Jung[3,4]*, Jennifer C. Yee[2], Kyu-Ha Hwang[3], Hongjing Yang[1,5], Andrzej Udalski[6], Takahiro Sumi[7], Andrew Gould[8,9], Shude Mao[5,1]*, Michael D. Albrow[10], Sun-Ju Chung[3], Cheongho Han[11], Yoon-Hyun Ryu[3], In-Gu Shin[2], Yossi Shvartzvald[12], Sang-Mok Cha[3,13], Dong-Jin Kim[3], Hyoun-Woo Kim[3,11], Seung-Lee Kim[3], Chung-Uk Lee[3]*, Dong-Joo Lee[3], Yongseok Lee[3,13], Byeong-Gon Park[14], Richard W. Pogge[9,15], Xiangyu Zhang[8], Renkun Kuang[1,16], Hanyue Wang[17], Jiyuan Zhang[1], Zhecheng Hu[1], Wei Zhu[1], Przemek Mróz[6], Jan Skowron[6], Radosław Poleski[6], Michał K. Szymański[6], Igor Soszyński[6], Paweł Pietrukowicz[6], Szymon Kozłowski[6], Krzysztof Ulaczyk[18], Krzysztof A. Rybicki[6,12], Patryk Iwanek[6], Marcin Wrona[6,19], Mariusz Gromadzki[6], Fumio Abe[20], Richard Barry[21], David P. Bennett[21,22], Aparna Bhattacharya[21,22], Ian A. Bond[23], Hirosane Fujii[20,24], Akihiko Fukui[25,26], Ryusei Hamada[7], Yuki Hirao[27], Stela Ishitani Silva[21], Yoshitaka Itow[20], Rintaro Kirikawa[7], Naoki Koshimoto[7], Yutaka Matsubara[20], Shota Miyazaki[28], Yasushi Muraki[20], Greg Olmschenk[21], Clément Ranc[29], Nicholas J. Rattenbury[30], Yuki Satoh[7,31], Daisuke Suzuki[7], Mio Tomoyoshi[7], Paul J. Tristram[32], Aikaterini Vandorou[21,22], Hibiki Yama[7], Kansuke Yamashita[7]

Exoplanets classified as super-Earths are commonly observed on short-period orbits, close to their host stars, but their abundance on wider orbits is poorly constrained. Gravitational microlensing is sensitive to exoplanets on wide orbits. We observed the microlensing event OGLE-2016-BLG-0007, which indicates an exoplanet with a planet-to-star mass ratio roughly double the Earth-Sun mass ratio, on an orbit longer than Saturn's. We combined this event with a larger sample from a microlensing survey to determine the distribution of mass ratios for planets on wide orbits. We infer that there are ~0.35 super-Earth planets per star on Jupiter-like orbits. The observations are most consistent with a bimodal distribution, with separate peaks for super-Earths and gas giants. We suggest that this reflects differences in their formation processes.

Information about the formation and evolution of planetary systems is encoded in the distribution of exoplanet masses and orbital separations. Many exoplanets have been observed on short-period orbits (P < 1 year, where P is the orbital period), including large numbers of super-Earths (planets larger than Earth but smaller than Neptune) (*1*–*4*). This terminology is qualitative, so different classes of exoplanet can be defined in terms of planetary radius, planetary mass, or planet-star mass ratio (q), depending on the observing technique. We classify Earth-like and super-Earth planets as those with $\log q < -4.5$. For longer-period orbits (P > 1 year), only the frequency of larger planets (gas giants and ice giants) has been determined (*5*–*7*). The population of smaller planets, including super-Earths, on orbits with P > 1 year is poorly constrained. Microlensing is sensitive to such planets (Fig. 1).

Gravitational microlensing occurs when a foreground object (referred to as the lens) passes between an observer and a background object (the source). This focuses the light from the source, causing a transient apparent increase in the source light curve (its brightness as a function of time). For microlensing events in

which both the lens and source are stars, this brightening typically lasts several months. If the lens star is orbited by a planet with a suitable alignment, an additional brightening is superimposed on the light curve, lasting days or hours. Super-Earth planets are challenging to detect with microlensing because they often cause only a small brightening of the light curve for only a few hours. Light curves measured by a single observatory have gaps due to the day-night cycle or poor weather. Therefore, detecting super-Earth planets by use of microlensing usually requires combining data from multiple observatories to provide a continuous light curve.

We analyzed data from the Korea Microlensing Telescope Network (KMTNet), which has telescopes at three widely separated sites (*8*). Each telescope provides 2 to 40 observations per night of the same target region, so the network provides densely sampled light curves (*9*–*11*). Microlensing events with planets are identified in the KMTNet data by the semi-automated pipeline AnomalyFinder (*12*, *13*).

A long-period super-Earth planet

The microlensing event OGLE-2016-BLG-0007 was initially identified as an ongoing microlensing event by the Optical Gravitational Lensing Experiment (OGLE) on 2016 February 10 (*14*, *15*). It was also observed by KMTNet and the Microlensing Observations in Astrophysics (MOA) collaboration. Our analysis of the KMTNet data with AnomalyFinder (*16*) identified an additional bump in the light curve. The light curve including data from all three groups is shown in Fig. 2. The bump has a low magnification of $A_{\rm bump} \simeq 1.09$, which peaked at time $t_{\rm bump}$ ~ 25 September 2016 at 00:00 Universal Time (UT), corresponding to ~7656.5 HJD′ (where HJD′ is the heliocentric Julian date minus 2,450,000), and lasts for $\Delta t_{\rm bump}$ ~ 2.1 days. The bump is superimposed on a standard stellar microlensing curve with parameters $(t_0, u_0, t_{\rm E})$ = (7498.4 HJD′, 1.253, 73.8 days), where t_0 is the time of the peak of the event (which correspond to ~2016 April 19 UT 21:30), u_0 is the impact parameter between the source and lens stars, and $t_{\rm E}$ is the event timescale. We investigated whether the bump was caused by a small planet orbiting the lens star.

There are three possible configurations that could produce this light curve (fig. S2). We investigated each and found that the most plausible solution (the Wide model) is a planet with a projected location more than one Einstein radius ($\theta_{\rm E}$; the characteristic spatial scale of the event) from the lens star. The two other possible configurations involve either a larger planet (higher q) located less than one Einstein radius from its star or a second (much fainter) source star rather than a planet (*17*). We modeled both of these alternate possibilities (*16*) but rule them out at high confidence ($\Delta\chi^2$ = 38.5 and 145.6, respectively) (table S1).

The Wide model indicates that the separation s between the host star and the planet is $s = 2.83 \pm 0.01\ \theta_{\rm E}$ (values are medians and 68% confidence ranges, unless otherwise stated) and the mass ratio $q = 6.79 \times 10^{-6}$ ($\log q = -5.17 \pm 0.13$). This makes OGLE-2016-BLG-0007Lb (where the final L designates the lens star and b designates the planet orbiting that star) a super-Earth planet. Its mass ratio is roughly double that of the Earth and Sun: $q_{\rm Earth} \equiv M_{\rm Earth}/M_{\rm Sun} = 3 \times 10^{-6}$, where $M_{\rm Earth}$ and $M_{\rm Sun}$ are the masses of Earth and the Sun, respectively.

We combined the microlensing parameters with a model of the distribution of stars in the Milky Way (*16*) to estimate the likely lens mass, finding $0.59^{+0.41}_{-0.30} M_{\rm Sun}$, and its distance from the Sun, finding $4.3^{+1.1}_{-1.4}$ kpc. These values imply a planet with a mass of $m_{\rm p} = 1.32^{+0.91}_{-0.67} M_{\rm Earth}$ on an orbit with semimajor axis $a = 10.1^{+3.8}_{-3.4}$ au (where au is the astronomical unit, approximately the distance from the Earth to the Sun), and period $P = 39^{+21}_{-9}$ years (Table 1).

These properties correspond to a super-Earth planet with an orbital period longer than Saturn's. Such planets are commonly produced by population synthesis models (*18*) but are absent in previous observations of normal (main sequence) stars (Fig. 1). The only other planet similar to OGLE-2016-BLG-0007Lb was found in orbit around a pulsar (*19*). We excluded planets orbiting pulsars from Fig. 1 and our discussion because the supernova that produced the pulsar would have strongly affected its local planetary system, and the detected pulsar planets might have formed after the supernova (*20*).

Mass ratio distribution from microlensing

To investigate the population of planets detected with microlensing, we combined OGLE-2016-BLG-0007Lb with the other planets identified in the KMTNet survey using AnomalyFinder. Our dataset consists of observations from KMTNet seasons 2016 to 2019. All planets with $\log q > -4$ are from the 2018 and 2019 KMTNet seasons (*13*, *21*–*23*). Planets with $\log q < -4$ are rarer, so for those mass ratios, we expanded the sample to planets identified in the 2016 to 2019 KMTNet seasons (*12*, *24*, *25*), including OGLE-2016-BLG-0007Lb. In total, our sample consists of 63 planets identified in 60 microlensing events observed with KMTNet.

To determine the sensitivity of the AnomalyFinder algorithm and KMTNet observations, we injected simulated planet signals into measured light curves from the 2018 and 2019 seasons then determined the fraction of those that were recovered by the algorithm (*16*). The sensitivity functions were calculated separately for the 2018 and 2019 seasons; we found that they are very similar, especially at $\log q < -4$ (fig. S1). KMTNet maintained the same observational setup from 2016 to 2019, with only minor changes owing to routine maintenance, so we assume 2016 and 2017 observations have a sensitivity function equal to the average of the 2018 and 2019 sensitivity functions.

We corrected the number of planet detections using the sensitivity functions for each year to determine the underlying planet distribution. This determined the planet frequency distribution from $\log q = -5.2$ to $\log q = -1.5$. The lower limit is set by OGLE-2016-BLG-0007Lb, which has a mass ratio of $\log q = 5.17$, the lowest in the sample. Over this range ($-5.2 < \log q < -1.5$), the total planet frequency is $0.65^{+0.35}_{-0.15}$ planets per star per dex (where dex is one decade in log$s$). For super-Earths, which we assume occupy the range $-5.2 < \log q < -4.5$ (the

[1]Department of Astronomy, Tsinghua University, Beijing, China. [2]Solar, Stellar, and Planetary Physics Division; Center for Astrophysics, Harvard and Smithsonian, Cambridge, MA, USA. [3]Optical Astronomy Division, Korea Astronomy and Space Science Institute, Daejeon, Republic of Korea. [4]Department of Astronomy and Space Science, National University of Science and Technology, Korea, Daejeon, Republic of Korea. [5]Department of Astronomy, Westlake University, Hangzhou, China. [6]Astronomical Observatory, University of Warsaw, Warszawa, Poland. [7]Department of Earth and Space Science, Graduate School of Science, Osaka University, Osaka, Japan. [8]Galaxies and Cosmology, Max-Planck-Institute for Astronomy, Heidelberg, Germany. [9]Department of Astronomy, Ohio State University, Columbus, OH, USA. [10]Department of Physics and Astronomy, University of Canterbury, Christchurch, New Zealand. [11]Department of Physics, Chungbuk National University, Cheongju, Republic of Korea. [12]Department of Particle Physics and Astrophysics, Weizmann Institute of Science, Rehovot, Israel. [13]School of Space Research, Kyung Hee University, Kyeonggi, Republic of Korea. [14]Center for Large Telescopes, Korea Astronomy and Space Science Institute, Daejeon, Republic of Korea. [15]Center for Cosmology and AstroParticle Physics, Ohio State University, Columbus, OH, USA. [16]Department of Engineering Physics, Tsinghua University, Beijing, China. [17]Astronomy Department, Harvard University, Cambridge, MA, USA. [18]Department of Physics, University of Warwick, Coventry, UK. [19]Department of Astrophysics and Planetary Sciences, Villanova University, Villanova, PA, USA. [20]Institute for Space-Earth Environmental Research, Nagoya University, Nagoya, Japan. [21]Exoplanets and Stellar Astrophysics Laboratory, NASA Goddard Space Flight Center, Greenbelt, MD, USA. [22]Department of Astronomy, University of Maryland, College Park, MD, USA. [23]Institute of Natural and Mathematical Sciences, Massey University, Auckland, New Zealand. [24]Department of Earth and Space Science, Graduate School of Science, Osaka University, Osaka, Japan. [25]Department of Earth and Planetary Science, Graduate School of Science, The University of Tokyo, Tokyo, Japan. [26]Instituto de Astrofísica de Canarias, La Laguna, Tenerife, Spain. [27]Institute of Astronomy, Graduate School of Science, The University of Tokyo, Tokyo, Japan. [28]Institute of Space and Astronautical Science, Japan Aerospace Exploration Agency, Kanagawa, Japan. [29]Institut d'Astrophysique de Paris, Sorbonne Université, Centre National de la Recherche Scientifique (CNRS), Paris, France. [30]Department of Physics, University of Auckland, Auckland, New Zealand. [31]College of Science and Engineering, Kanto Gakuin University, Yokohama, Japan. [32]Mount John Observatory, University of Canterbury, Lake Tekapo, New Zealand.

*Corresponding author. Email: weicheng.zang@cfa.harvard.edu (W.Z.); ykjung21@kasi.re.kr (Y.K.J.); leecu@kasi.re.kr (C.-U.L.), shude.mao@westlake.edu.cn (S.M.)

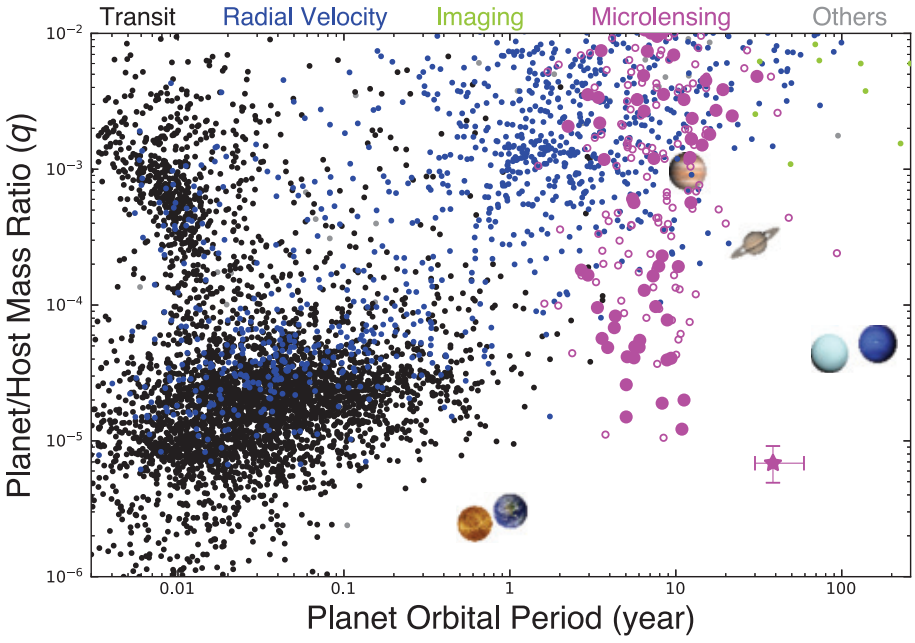

Fig. 1. Periods and mass ratios for planets detected with different methods. Data points indicate all exoplanets cataloged on 30 July 2023 (*42*) and are color-coded by detection method. The magenta star indicates OGLE-2016-BLG-0007Lb (error bars indicate 68% confidence intervals for this planet but are omitted from all other planets). Colored images indicate six Solar System planets for comparison: Venus, Earth, Jupiter, Saturn, Uranus, and Neptune. Solid magenta circles are our collated sample of planets from the KMTNet microlensing survey; open magenta circles are other planets detected with the microlensing technique. The microlensing detections include planets with mass ratios corresponding to super-Earths with Jupiter-like orbital periods.

upper limit would correspond to a ~10$M_{\rm Earth}$ planet orbiting a 1$M_{\rm Sun}$ host), there are $0.35^{+0.34}_{-0.14}$ planets per star per dex.

In Fig. 3A, we show the distribution of logarithmic mass ratios log$q$ for the planet detections and the corresponding planet distribution after correction by the sensitivity function. The bin size changes at log$q$ = –4 because four seasons (2016 to 2019) of detections were considered for log$q$ < –4, but above that, we used only the 2018 and 2019 seasons. For –6.0 < log$q$ < –5.25, we show the upper limits on the planet frequencies from Poisson statistics. We show 1σ limits because a substantial population of planets could be consistent with the nondetections.

We fit the distribution using a single power-law function

$$\frac{dN}{d\ \log\ q} = 0.18 \pm 0.03 \left(\frac{q}{10^{-4}}\right)^{-0.55 \pm 0.05} \quad (1)$$

where N is the number of planets per star, finding that it qualitatively reproduces the data. The cumulative distribution of individual detections as a function of log$q$ is shown in Fig. 3B, compared with the power-law model corrected by the sensitivity function. The slight break in the model distribution at log$q$ = –4 reflects the change in the number of observational seasons used in the analysis above and below this point.

Planet-formation theory does not predict a single power law distribution from super-Earths to gas giants. For example, in the core-accretion planet-formation scenario, runaway gas accretion occurs once a proto-planet exceeds a critical mass, causing them to rapidly grow from tens to hundreds of Earth masses (*26*–*28*). This process would produce two separate populations of planets in different mass regimes, one at ~10$M_{\rm Earth}$ and one above ~100$M_{\rm Earth}$, with a deficit between them. The alternative gravitational instability scenario produces gas giant planets through direct collapse of a protoplanetary disk (*29*) but does not produce lower-mass rocky planets, which must form through a different mechanism. This would also produce a population of gas giants (with masses above ~100$M_{\rm Earth}$) and a separate population of less massive planets.

We therefore investigated whether there is evidence for two populations in our derived mass ratio distribution. There is a sharp change in the slope of the cumulative mass ratio distribution (Fig. 3B) at log$q$ = [–3.6, –3] (also visible as a slight dip at log$q$ = [–3.5, –3] in Fig. 3A). Because log$q$ = –3.2 for a ~100$M_{\rm Earth}$ planet orbiting a 0.5$M_{\rm Sun}$ star, this is approximately where we expect the division between planets that have and have not undergone runaway gas accretion. In addition, there appear to be other changes in the slope of the cumulative mass ratio distribution at both the high (log$q$ > –2) and low (log$q$ < –5) ends (Fig. 3B). The power-law model predicts four planets with –6 < log$q$ < –5 in the KMTNet sample, but only one has been detected, which has a probability of 9% assuming a Poisson distribution.

We reproduced these features by fitting the data with a double-Gaussian function of log$q$ (Fig. 3)

$$\frac{dN}{d\ \log\ q} = \mathcal{A}_1 \times 10^{n_1 \left(\log q - \log q_{\rm peak,1}\right)^2} + \mathcal{A}_2 \times 10^{n_2 \left(\log q - \log q_{\rm peak,2}\right)^2} \quad (2)$$

which has two peaks at $\log q_{\rm peak,1} = -4.7^{+0.2}_{-0.3}$ and $\log q_{\rm peak,2} = -2.6 \pm 0.1$ (equivalent to 7.4 × $q_{\rm Earth}$ and 770 × $q_{\rm Earth}$, respectively), with amplitudes $\mathcal{A}_1 = 0.52 \pm 0.13$ and $\mathcal{A}_2 = 0.058 \pm 0.013$, and $n_1 = -0.73 \pm 0.35$ and $n_2 = -1.8 \pm 0.6$, where $n_1^{-1/2}$ and $n_2^{-1/2}$ are the effective widths of the Gaussians.

Quantitatively, the double-Gaussian is a better fit than the single-power law by $-2\Delta\ln L$ = 22.6, where $\Delta\ln L$ is the difference in the logarithmic likelihoods of the models (*16*). We calculated that the false-alarm probability p is 1.60×10^{-4} for observing a $-2\Delta\ln L$ = 22.6 preference for a double-Gaussian model if the true distribution is the power law described above (*16*). This indicates statistical preference for the double-Gaussian model over the power law model, despite the increased number of free parameters. We also regard the double-Gaussian model as more consistent with theoretical predictions because it has log$q$ peaks in the expected ranges of two classes of planets formed by runaway gas accretion.

Integrating each Gaussian separately from log$q$ = –5.2 to –1.5 yields 0.57 ± 0.13 planets per star per dex in the lower–mass ratio Gaussian and 0.053 ± 0.013 planets per star per dex in the higher–mass ratio Gaussian.

Comparison with previous work

Independent of the specific functional form of the mass ratio distribution, our results indicate an abundance of super-Earths in Jupiter-like orbits. This was not evident in previous studies of the microlensing mass ratio distribution, which found a mass ratio distribution described by a broken-power-law with a sharp break around log$q$ ~ –4 (*5*, *30*, *31*). By contrast, we found no evidence for a break at either log$q$ = –3.77 or –4.26 as found in those studies. The change in slope we identified in the cumulative mass ratio distribution did not previously appear (*5*). In fig. S9, we compare the two cumulative distributions; the previous work found an overabundance of planets from log$q$ = –3.5 to –3.0, relative to a smooth distribution, which contributed to the previous

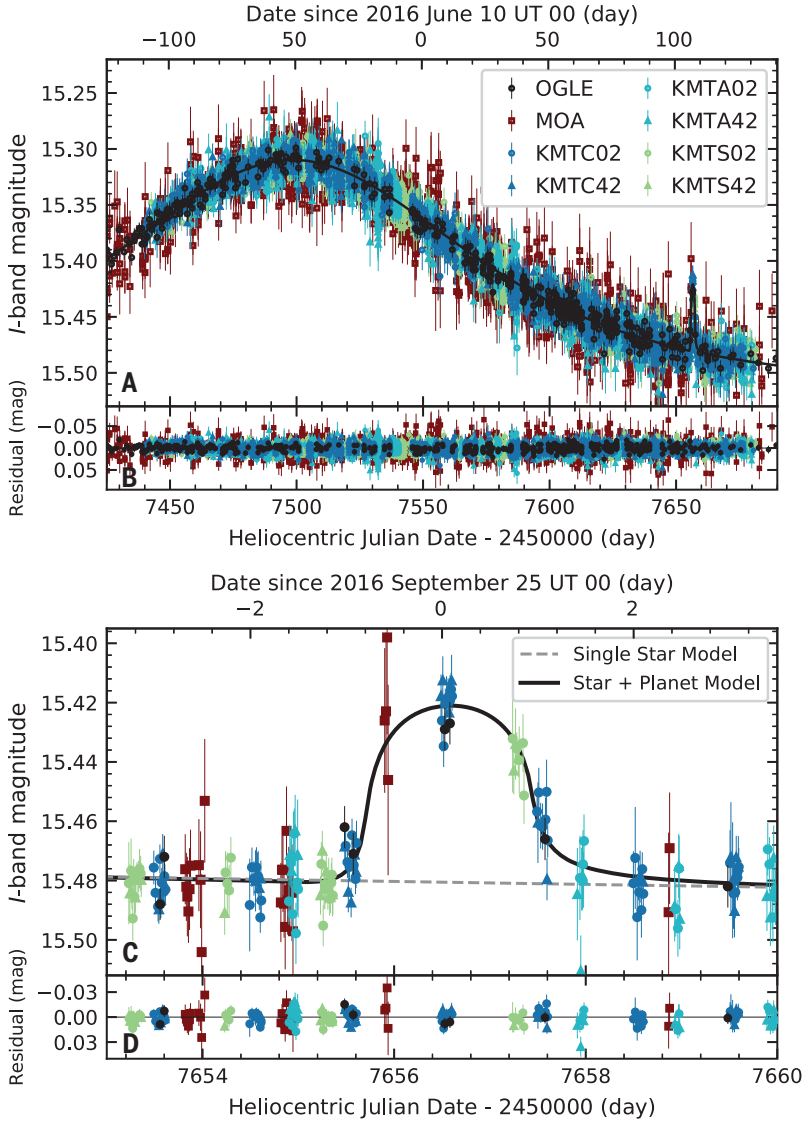

Fig. 2. Light curve of OGLE-2016-BLG-0007. Data points are color-coded by source (*16*) and shown with 1σ error bars. Lines indicate the best-fitting model light curves for a single star (gray dashed line) or a star with an orbiting planet (solid black line). (**A**) All observations of the event taken in 2016. (**C**) Zoomed view of the same light curve, showing the low-amplitude, short-duration anomaly in OGLE-2016-BLG-0007. We interpret this as indicating a planet with a mass ratio of log$q$ ~ −5. (**B** and **D**) Residuals from the best-fitting planetary model.

Table 1. Derived system parameters for OGLE-2016-BLG-0007Lb. Uncertainties are 1σ.

Parameter	Symbol	Value	Units
Planet/host mass ratio	q	$6.9^{+2.3}_{-1.9} \times 10^{-6}$	—
Planet mass	m_p	$1.32^{+0.91}_{-0.67}$	M_{Earth}
Host mass	M_{host}	$0.59^{+0.41}_{-0.30}$	M_{Sun}
Lens distance	D_L	$4.3^{+1.1}_{-1.4}$	kpc
Two-dimensional host–planet separation	$a_\perp$	$8.9^{+2.3}_{-2.9}$	au
Semimajor axis	a	$10.1^{+3.8}_{-3.4}$	au
Planet orbital period	P	39^{+21}_{-9}	year

preference for a broken power-law distribution (*5*). Differences in the methodology might contribute to these differences in the inferred distributions (supplementary text).

Our mass ratio distribution is more consistent with a previous microlensing study of only nine planets, the smallest of which had log$q$ = −4.32 (*6*). That study also did not find a change in slope in the cumulative mass ratio distribution in the range log$q$ = [−3.6, −3], but nor was there an overabundance of planets in that range. We attribute this to the low number of planets included in that study. The power-law model that study fitted to the data in the range −4.9 < log$q$ < −1.4 is consistent with our power law model though has larger uncertainties (*6*).

Another study of six microlensing planets spanning log$q$ = [−4.5, −2] found that three of those planets were in the range log$q$ = [−3.6, −3] (*32*). This is a greater proportion than we found, but we assess that the small number of planets included in that study or differences in methodology could explain the difference with our results (supplementary text).

Comparisons between microlensing results and planets detected by using the alternative radial velocity technique are complicated because the two methods are sensitive to planets on different orbits (*33*) and measure different quantities (mass m_p or $m_p \sin i$, where i is the inclination of the orbit, rather than mass ratio). In addition, the properties of most microlensing host stars are not measured, whereas radial velocity studies generally group their results by host star spectral type. We nevertheless discuss how our results compare with those from radial velocity studies (supplementary text).

Implications for planet formation

We compared our results with predictions from theoretical simulations of planet formation. A direct, quantitative comparison is challenging because the host stars of microlensing planets span a wide range of masses, and the mass of any particular host star is usually unknown or poorly constrained. Previous comparisons (*34*) have shown that the population of microlensing planets is not consistent with the theoretical predictions, especially when the simulations include the effect of planet migration (*35*, *36*).

We qualitatively compared our mass ratio distribution with predictions from simulations [(*34*), their figure 2]; we found that they are not consistent if the simulations include planet migration. However, alternative models (*37*, *38*) without migration produce two distinct populations of planets, which is qualitatively similar to our derived distribution, although the locations and heights of the peaks differ from our fitted values. Other models (*39*, *40*) without migration are also qualitatively consistent with our observations, although updated versions of those models do not form any giant planets around stars <0.5M_{Sun} (*18*). Because

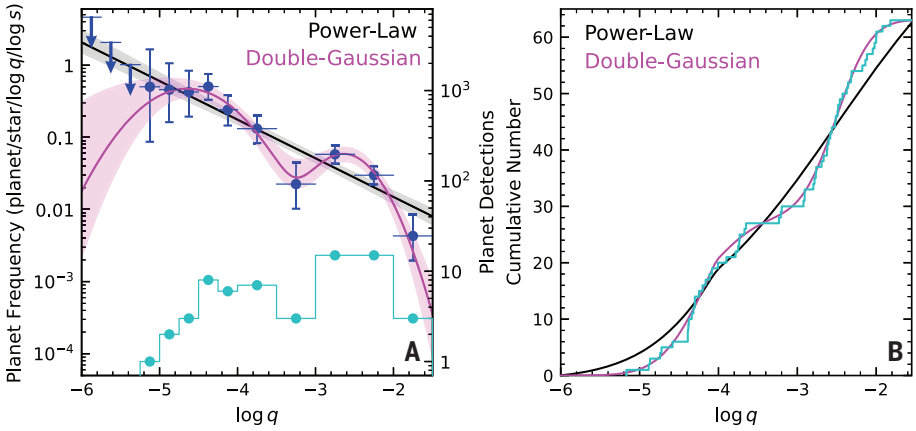

Fig. 3. Mass ratio distributions of microlensing planets from our KMTNet sample. (**A**) The observed number of planet detections (cyan; right axis) and the derived planet frequency distribution (blue; left axis) after correction by the sensitivity function (fig. S1). The horizontal lines correspond to the width of the histogram bins. Error bars indicate 1σ Poisson uncertainties and 1σ upper limits. Overlain are two models fitted to the data: a single power law (black line) and a double Gaussian (magenta line); shaded regions indicate 68% confidence intervals. (**B**) The same two fitted models multiplied by the sensitivity function and expressed as a cumulative distribution. The cyan histogram is the measured cumulative distribution from the KMTNet sample. The power law model predicts more planets in the range $-3.5 < \log q < -3$ than were detected. The double Gaussian model is also a better match to the data at both high q and low q ends of the distribution.

any type of star can produce a microlensing event, many of the events are expected to be produced by the most abundant type of star, those of $<0.5M_{\rm Sun}$. We derived a giant planet ($-4 < \log q < -1.5$) frequency of $12.3^{+3.9}_{-2.6}\%$. This can only be consistent with the latter models if the great majority of microlensing events with giant planets are produced by host stars with masses of $M_{\rm host} = 0.7M_{\rm Sun}$ and above.

We conclude that the two separate populations we identified in the mass ratio distribution indicate differentiation during the planet-formation processes. This could be explained by a single planet-formation scenario in which the two populations are produced by runaway gas accretion for planets above a mass threshold. Alternatively, the two populations could be produced by different formation mechanisms: accretion and gravitational instability (*41*).

REFERENCES AND NOTES

1. W. J. Borucki *et al.*, *Astrophys. J.* **728**, 117 (2011).
2. M. Mayor *et al.*, The HARPS search for southern extra-solar planets XXXIV. Occurrence, mass distribution and orbital properties of super-Earths and Neptune-mass planets. arXiv: 1109.2497 [astro-ph.EP] (2011).
3. R. A. Wittenmyer *et al.*, *Astrophys. J.* **738**, 81 (2011).
4. X. Bonfils *et al.*, *Astron. Astrophys.* **549**, A109 (2013).
5. D. Suzuki *et al.*, *Astrophys. J.* **833**, 145 (2016).
6. Y. Shvartzvald *et al.*, *Mon. Not. R. Astron. Soc.* **457**, 4089–4113 (2016).
7. R. Poleski *et al.*, *Acta Astron.* **71**, 1 (2021).
8. S.-L. Kim *et al.*, *J. Korean Astron. Soc.* **49**, 37–44 (2016).
9. D. J. Kim *et al.*, *Astron. J.* **155**, 76 (2018).
10. H.-W. Kim *et al.*, The KMTNet 2016 Data Release. arXiv:1804. 03352 [astro-ph.EP] (2018).
11. H.-W. Kim *et al.*, The Korea Microlensing Telescope Network (KMTNet) Alert Algorithm and Alert System. arXiv:1806.07545 [astro-ph.IM] (2018).
12. W. Zang *et al.*, *Astron. J.* **162**, 163 (2021).
13. W. Zang *et al.*, *Mon. Not. R. Astron. Soc.* **515**, 928–939 (2022).
14. A. Udalski *et al.*, *Acta Astron.* **44**, 227 (1994).
15. A. Udalski, *Acta Astron.* **53**, 291 (2003).
16. Materials and methods are available as supplementary materials.
17. B. S. Gaudi, *Astrophys. J.* **506**, 533–539 (1998).
18. R. Burn *et al.*, *Astron. Astrophys.* **656**, A72 (2021).
19. E. D. Starovoit, A. E. Rodin, *Astron. Rep.* **61**, 948–953 (2017).
20. A. Patruno, M. Kama, *Astron. Astrophys.* **608**, A147 (2017).
21. A. Gould *et al.*, *Astron. Astrophys.* **664**, A13 (2022).
22. Y. K. Jung *et al.*, *Astron. J.* **164**, 262 (2022).
23. Y. K. Jung *et al.*, *Astron. J.* **165**, 226 (2023).
24. K.-H. Hwang *et al.*, *Astron. J.* **163**, 43 (2022).
25. W. Zang *et al.*, *Astron. J.* **165**, 103 (2023).
26. J. B. Pollack *et al.*, *Icarus* **124**, 62–85 (1996).
27. J. C. B. Papaloizou, R. P. Nelson, *Astron. Astrophys.* **433**, 247–265 (2005).
28. G. A. L. Coleman, J. C. B. Papaloizou, R. P. Nelson, *Mon. Not. R. Astron. Soc.* **470**, 3206–3219 (2017).
29. A. P. Boss, *Science* **276**, 1836–1839 (1997).
30. A. Udalski *et al.*, *Acta Astron.* **68**, 1 (2018).
31. Y. K. Jung *et al.*, *Astron. J.* **157**, 72 (2019).
32. A. Gould *et al.*, *Astrophys. J.* **720**, 1073–1089 (2010).
33. C. Clanton, B. S. Gaudi, *Astrophys. J.* **819**, 125 (2016).
34. D. Suzuki *et al.*, *Astrophys. J. Lett.* **869**, L34 (2018).
35. P. Goldreich, S. Tremaine, *Astrophys. J.* **241**, 425 (1980).
36. D. N. C. Lin, J. Papaloizou, *Astrophys. J.* **309**, 846 (1986).
37. S. Ida, D. N. C. Lin, *Astrophys. J.* **604**, 388–413 (2004).
38. S. Ida, D. N. C. Lin, *Astrophys. J.* **626**, 1045–1060 (2005).
39. Y. Alibert, C. Mordasini, W. Benz, C. Winisdoerffer, *Astron. Astrophys.* **434**, 343–353 (2005).
40. C. Mordasini, Y. Alibert, H. Klahr, T. Henning, *Astron. Astrophys.* **547**, A111 (2012).
41. A. P. Boss, S. Kanodia, *Astrophys. J.* **956**, 4 (2023).
42. R. L. Akeson *et al.*, *Publ. Astron. Soc. Pac.* **125**, 989–999 (2013).
43. The VizieR database of astronomical catalogues, Strasbourg astronomical Data Center; https://doi.org/10.26093/cds/vizier.
44. F. Ochsenbein, P. Bauer, J. Marcout, *Astron. Astrophys.* **143** (suppl.), 23 (2000).
45. W. Zang *et al.*, Microlensing events indicate that super-Earth exoplanets are common in Jupiter-like orbits, Dryad (2024); https://doi.org/10.5061/dryad.ksn02v7cg.
46. M. K. Szymański *et al.*, *Acta Astron.* **61**, 83 (2011).
47. A. Claret, S. Bloemen, *Astron. Astrophys.* **529**, A75 (2011).

ACKNOWLEDGMENTS

The KMTNet system is operated by the Korea Astronomy and Space Science Institute (KASI) at three host sites of CTIO in Chile, SAAO in South Africa, and SSO in Australia. Data transfer from the host site to KASI was supported by the Korea Research Environment Open NETwork (KREONET). We acknowledge the NASA Exoplanet Archive, which is operated by the California Institute of Technology, under contract with NASA under the Exoplanet Exploration Program. We acknowledge the VizieR catalog access tool, provided by CDS, Strasbourg, France (*43*, *44*). We acknowledge computational and data storage resources provided by the Tsinghua Astrophysics High-Performance Computing platform at Tsinghua University. **Funding:** Y.K.J., K.-H.H., S.-J.C., Y.-H.R., S.-M.C., D.-J.K., H.-W.K., S.-L.K., C.-U.L., D.-J.L., Y.L., and B.-G.P. acknowledge support by KASI under the R&D program (projects 2024-1-832-00 and 2024-1-832-01) supervised by the Ministry of Science and ICT. T.S. is supported by JSPS KAKENHI grants JP24253004, JP26247023, JP16H06287, and JP22H00153. W.Za., H.Y., S.M., R.K., J.Z., and W.Zh. acknowledge support from the National Natural Science Foundation of China (grant 12133005). W.Za. acknowledges support from the Harvard-Smithsonian Center for Astrophysics through a CfA Fellowship. W.Zh. acknowledges science research grants from the China Manned Space Project, grant CMS-CSST-2021-A11. J.C.Y. and I.-G.S. acknowledge support from US NSF grant AST-2108414. Y.S. acknowledges support from BSF grant 2020740. R.P. and J.S. were funded by Polish National Agency for Academic Exchange grant "Polish Returns 2019." C.H. was funded by grants from the National Research Foundation of Korea (2019R1A2C2085965 and 2020R1A4A2002885). D.P.B., A.B., S.I.S., and G.O. were funded by NAA grants 80NSSC20K0886 and 80NSSC24M0022.

Competing interests: The authors declare that they have no competing interests. **Author contributions:** W.Za. identified the planetary anomaly in OGLE-2016-BLG-0007 and analyzed the event, conducted the frequency analysis, and wrote portions of the manuscript. Y.K.J. performed the sensitivity analysis and wrote portions of the manuscript. J.C.Y. led the writing of the manuscript and contributed to the analysis. K.-H.H. carried out the systematic search for events in the KMTNet survey and identified this event in the KMTNet data. H.Y. rereduced the KMTNet data and contributed to the analysis. A.G. is the scientific principal investigator of the KMTNet microlensing survey, contributed to the analysis, and provided feedback on the manuscript. S.M. contributed to the analysis and provided comments on the manuscript. M.D.A. contributed to the software used in this work and the analysis of data and provided comments on the manuscript. S.-J.C., Y.-H.R., I.-G.S., and Y.S. contributed to the analysis of the KMTNet data and provided comments on the manuscript. C.H. conceived of and designed the KMTNet project and contributed to the analysis. C.-U.L. is the principal investigator of KMTNet and provided comments on the manuscript. S.-M.C., D.-J.K., H.-W.K., S.-L.K., D.-J.L., Y.L., B.-G.P., and R.W.P. contributed to KMTNet operations. X.Z., R.K., H.W., J.Z., Z.H., and W.Zh. contributed to the analysis. A.U. is the principal investigator of the OGLE project and was responsible for the reduction of the OGLE data. A.U., P.M., J.S., R.P., M.K.S., I.S., P.P., Sz.K., K.U., K.A.R., P.I., M.W., and M.G. collected the OGLE photometric observations and commented on the results and on the manuscript. T.S. led the MOA project and organized the MOA observations. I.A.B. contributed to the MOA data analysis. F.A., R.B., A.B., D.P.B., H.F., A.F., R.H., Y.H., S.I.S., Y.I., R.K., N.K., Y.Ma., S.M., Y.Mu., G.O., C.R., N.J.R., Y.S., D.S., M.T., P.J.T., A.V., H.Y., and K.Y. contributed to the MOA observation and commented on the manuscript. **Data and materials availability:** Our observed light curves of OGLE-2016-BLG-0007, the pyDIA color-magnitude diagram (*16*), calculated KMTNet sensitivity functions, and a machine-readable version of our planet sample (table S3) are available at Dryad (*45*). The Dryad repository also contains the AnomalyFinder software and the codes we used for the frequency analysis and the false alarm probability calculation. The results of the population model fitting are listed in table S5. The KMTNet event tables and links to the data are available at https://kmtnet.kasi.re.kr/ulens (*9*, *10*). The OGLE-III star catalog (*16*, *46*) and limb-darkening coefficient table (*16*, *47*) are available at VizieR (*43*), respectively, at https://cdsarc.cds.unistra.fr/viz-bin/cat/J/AcA/61/83 and by searching for J/A+A/529/A75; the catalog entries we used are specified in the supplementary materials.

SUPPLEMENTARY MATERIALS

science.org/doi/10.1126/science.adn6088
Materials and Methods
Supplementary Text
Figs. S1 to S9
Tables S1 to S5
References (*48*–*122*)

Submitted 18 December 2023; accepted 25 February 2025
10.1126/science.adn6088

CHEMICAL PHYSICS

Ultrafast aqueous electric double layer dynamics

Alessandro Greco[1], Sho Imoto[1], Ellen H. G. Backus[1,2], Yuki Nagata[1], Johannes Hunger[1], Mischa Bonn[1]*

The electric double layer (EDL) is critical in electrochemical capacitors and transistors, on-water chemistry, and bioelectric technologies. Ion dynamics within the EDL define the limits for charging and discharging processes. Classical EDL models struggle at high electrolyte concentrations, and observing EDL dynamics has been challenging. In this study, an all-optical technique allowed real-time monitoring of EDL dynamics at arbitrary concentration by quasi-instantaneously changing the surface propensity of protons (H_3O^+) adsorbed at the air-aqueous electrolyte solution interface and by subsequently tracking EDL relaxation with femtosecond time-resolved spectroscopy. EDL reorganization occurred on picosecond timescales and was strongly concentration dependent. Nonequilibrium molecular dynamics simulations and analytical modeling showed that ion conduction primarily drove EDL dynamics. This research quantified EDL dynamics and identified its primary driver, providing insights for optimization of electrochemical applications.

An electrically charged surface in contact with an electrolyte solution causes the formation of an electrical double layer (EDL) (*1*, *2*). In the EDL, mobile ions in the electrolyte move to balance the charge of the surface, resulting in an inhomogeneous distribution of charges. This inhomogeneity generates substantial interfacial electric fields, which determine the double-layer capacity of electrochemical supercapacitors (*3*), regulate the functioning of electrochemical transistors (*4*), are crucial in electrocatalysis (*5*), and provide a distinctive platform for on-water chemical reactivity (*6*–*8*).

At low ion concentrations of the electrolyte, the distribution of ions near charged interfaces and their dynamics can be described well with mean-field models, such as the Gouy-Chapman and Debye-Falkenhagen models (*9*), respectively. However, the above-mentioned applications typically involve high electrolyte concentrations and surface charge densities, where these mean-field approaches fail. Nevertheless, the structure of the EDL at high electrolyte concentrations can be interrogated using both experimental (*10*–*13*) and computational methods (*14*–*16*). For example, the spatial distribution of ions near a charged interface can be inferred from the electrostatic forces of the EDL. Also, the electronic properties of interfacial silica, as determined from x-ray photoelectron spectroscopy, provide information on the absolute surface potentials, which are intimately connected to the EDL (*17*, *18*).

In contrast to the EDL structure, insights into EDL dynamics have remained elusive, despite their importance: For applications such as supercapacitors or electrosynthesis, the surface charge is not constant, and variations in surface charge cause the EDL to restructure with ions moving in response to the altered electric field. At high concentrations, this response is typically fast, as this EDL restructuring involves the displacement of ions over short distances (*19*). Such dynamics are challenging to study electrically, as the system's response is limited by characteristic resistor-capacitor times of the electrochemical assembly (*20*). Further, the dynamics may be influenced by specific interactions (*21*), which complicate the interpretation of experimental data. For example, at high electrolyte concentrations, specific interactions of ions with the interface as well as interionic and ion-water interactions can impose constraints on the ions' distribution and their mobilities. These additional constraints may counteract the forces exerted on the ions by the interfacial electric fields, raising the question of whether, even at high electrolyte concentrations, EDL dynamics are primarily driven by the conductive response to interfacial electric fields or hindered by these specific interactions.

In this work, we studied the pristine dynamics of an EDL by focusing on the air-electrolyte interface using nonlinear time-resolved vibrational sum-frequency generation (TR-vSFG) spectroscopy (*22*). vSFG (*23*) is able to indirectly probe the interfacial electric fields in the EDL through the degree of field-induced alignment of the water molecules (*24*, *25*). We used a subpicosecond temperature jump (T-jump) to induce ultrafast EDL restructuring, which we monitored in real time with TR-vSFG and which occurred on a timescale of tens of picoseconds. Molecular dynamics simulations showed that the vSFG signals were excellently suited to follow the EDL dynamics. Decomposition of the driving forces using a continuum model suggested that the ions' dynamics were governed by interfacial electric fields even at high electrolyte concentrations, which we confirmed experimentally by studying temperature and concentration-dependent EDL dynamics.

[1]Max Planck Institute for Polymer Research, Mainz, Germany. [2]Institute of Physical Chemistry, University of Vienna, Vienna, Austria.
*Corresponding author. Email: bonn@mpip-mainz.mpg.de

Molecular details of the isolated EDL structure

To study the EDL independently of electrode material and geometry, we used its spontaneous formation at the surface of acidic aqueous solutions. Solvated protons (mainly hydronium ions, H_3O^+ or D_3O^+) were stably located at the surface of a solution of HCl in H_2O (or, equivalently, DCl in D_2O) (*26*, *27*). This stabilization was due to the mismatch between the hydrogen bonding of solvated protons and that of water (*28*). As a result, solvated protons, in contrast to Cl^-, exhibited a substantial surface propensity, enriching the charge in the surface plane and attracting Cl^- counterions in the subsurface region, thereby forming the EDL (Fig. 1A).

The electric field within this EDL induced the alignment of the interfacial water molecules, which could be probed by the vSFG signal, $I(\omega)$, of the O–D stretch mode in the D_2O solution (*29*). This water alignment was directly evident in Fig. 1B from comparing O–D stretch vSFG spectra for pure D_2O, DCl solutions, and 1.0 M NaCl solution in D_2O at 10°C. The sharp ~2730 cm^{-1} peak indicated the presence of free O–D groups, and the broad band below 2650 cm^{-1} arose from H-bonded O–D groups in the EDL (*25*). Adding NaCl to water had a negligible effect on the vSFG signal because Na^+ and Cl^-, unlike H_3O^+, do not exhibit a pronounced surface activity (*14*, *30*). By contrast, the addition of DCl to D_2O reduced the free O–D peak intensity and enhanced the H-bonded O–D intensity. The reduction of the free O–D peak intensity arose from the free O–D displacement by the accumulation of D_3O^+, and the enhanced H-bonded O–D intensity indicated enhanced water alignment in the EDL (*30*) (Fig. 1A). Figure 1B shows the increase in vSFG intensity with increasing proton concentration, which was due to the increased alignment of water by an increasingly strong EDL field. The formation of the EDL was further confirmed by molecular dynamics simulations. The simulated excess charge distribution in Fig. 1C evidenced an interfacial highly positive peak attributable to the presence of H_3O^+, which was compensated by the presence of Cl^- in the adjacent region, resulting in an interfacial electric field that vanishes ~10 Å from the interface for the 1.0 M HCl solution. Lowering the HCl concentration reduced the absolute interfacial ionic densities, excess charge, and interfacial electric field, with the latter extending more deeply into the bulk.

Control of the isolated EDL structure

The adsorption free energy driving the accumulation of H_3O^+ ions and, thus, the formation of the proton peak at the air-water interface (~4 kJ/mol) (*30*, *31*) is comparable to room-temperature thermal energy (~2.5 kJ/mol).

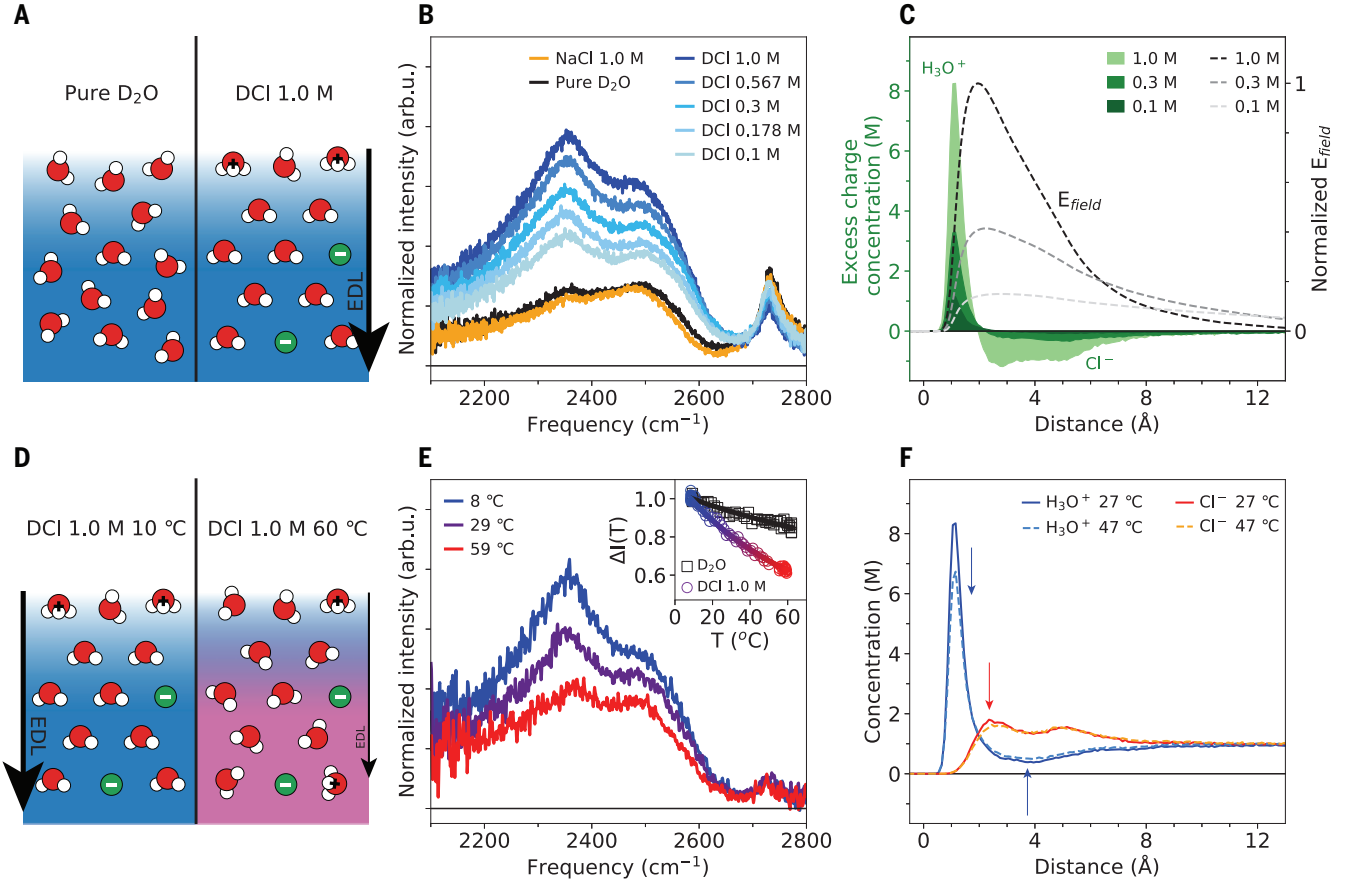

Fig. 1. Molecular details and control of the EDL structure. (**A**) Simplified molecular scheme representing the difference in the interfacial environment for pure D_2O and 1.0 M DCl. The presence of adsorbed D_3O^+ and subsurface Cl^- establishes the EDL in the DCl solution, which preferentially aligns the water molecules. (**B**) vSFG spectra in the O–D stretch frequency region of pure D_2O as well as of DCl solutions and 1.0 M NaCl solution in D_2O at 10°C testify to the enhanced water alignment with increasing proton concentration. arb.u., arbitrary units. (**C**) Simulation results: Green (left *y* axis) represents excess charge distribution for 0.1, 0.3, and 1.0 M HCl solutions. Interfacial proton adsorption caused positive excess; near-surface enhanced counterion concentration caused negative excess. Dashed lines (right *y* axis) represent resulting interfacial ionic electric field for 0.1, 0.3, and 1.0 M HCl solutions, normalized by the maximum value of the field at 1.0 M. (**D**) Simplified molecular scheme representing the temperature-induced desorption of interfacial protons and the decrease in overall water alignment. (**E**) vSFG spectra of 1.0 M DCl solution at different surface temperatures testifying to the reduced water alignment with increasing temperature. The inset shows the reduction of the normalized averaged intensity [$\Delta I(T)$] upon heating for D_2O and 1.0 M DCl. (**F**) Simulated ion distributions of H_3O^+ (blue) and Cl^- (red) at 27°C (continuous line) and 47°C (dashed line), illustrating the reduction of the EDL field at elevated temperatures.

Consequently, the interfacial proton population was expected to be sensitive to temperature (Fig. 1D). Indeed, the water alignment in the interfacial EDL of DCl (aq) as probed by vSFG was sensitive to temperature variation, as evident by a marked decrease of the vSFG intensities in the O–D stretch region with increasing temperature (Fig. 1E). In fact, the decrease in the vSFG signal was much more pronounced in the presence of DCl than in its absence (Fig. 1E, inset). Quantitatively, the decrease in the vSFG signal upon a 50°C temperature increase (Fig. 1E) resembled the changes in the vSFG signals upon a 10-fold decrease in the bulk DCl concentration (Fig. 1B), indicating that the elevated temperature caused desorption of protons from the interface. Indeed, molecular dynamics simulations showed that increasing temperature by 20°C resulted in a marked decrease in the interfacial proton density and the adjacent Cl^- ions in the EDL (Fig. 1F). Hence, upon increasing temperature, protons desorbed from the interfacial layer, which resulted in a reduction of the interfacial electric fields that aligned water molecules in the EDL.

T-jump for inducing and monitoring EDL dynamics

The thermally induced desorption of protons from the interface and rearrangement of the EDL paved the way for monitoring the EDL relaxation in real time by using a quasi-instantaneous T-jump. We achieved this T-jump with an additional infrared (IR) pump pulse capable of raising the local temperature by up to 40°C in about 1 ps. The IR pump pulse with temporal and spectral full width at half maximum of ~300 fs and ~80 cm^{-1}, respectively, and centered at 2490 cm^{-1} was in resonance with the O–D stretch band of D_2O. The impulsively excited O–D stretch mode rapidly relaxes through bending (centered at ~1200 cm^{-1}) and libration (centered at ~600 cm^{-1}) modes, which transfer energy to thermally accessible low-frequency modes centered at ~<200 cm^{-1} (*32*–*34*). The new equilibrium at elevated temperatures, with adjusted hydrogen bonding strengths and water orientation, is reached in about 1 ps. Thus, the excitation leads to quasi-instantaneous heating of the outermost few micrometers of the aqueous solution (*35*, *36*). The nanometer-thick EDL region was therefore homogeneously heated. We followed the thermally induced changes to the interfacial water by recording the vSFG spectra as a function of time after the IR pump pulse. Figure 2A shows the vSFG spectrum 209 ps after excitation with a 22.4 μJ

pulse, at which point the system had relaxed and reached a steady state (see supplementary materials). This spectrum overlapped the spectrum of the electrolyte solution heated at 50°C. The inferred ~40°C temperature increase corresponded well with calculations considering the IR absorption and the specific heat of water (see supplementary materials).

To analyze the thermally induced dynamics, we monitored the time-dependent average ratio of excited to unexcited vSFG intensities across the 2330 to 2580 cm^{-1} region (Fig. 2B). For pure D_2O the change in vSFG intensity after excitation occurred in 1 ps, with the vSFG signal being reduced by ~15% (Fig. 2B, inset): The temperature increase triggers weakening of the H-bonded network (*37*) and readjustment of water organization and orientation, achieved in about 1 ps. By contrast, the 1.0 M DCl solution showed a decaying vSFG intensity for tens of picoseconds after the T-jump. Thus, in the presence of an EDL (see supplementary materials), the water alignment probed with vSFG responded slowly, which was indicative of EDL relaxation.

To verify the origin of this slow response, we carried out nonequilibrium molecular dynamics (NEMD) simulations of the HCl solution with the instantaneous T-jump. Figure 2C displays the time evolution of the ion distributions along the surface normal. After an instantaneous increase of the temperature, the distributions of both ions rearranged on a timescale of tens of picoseconds, with interfacial protons clearly desorbing from the interface. The gradual reduction of the interfacial excess charges implied that the interfacial electric fields decrease with time. Indeed, the transient interfacial surface potential $\phi_{surface}^{NEMD}$ (i.e., the integrated interfacial electric field) calculated from MD simulations shown in Fig. 2D decreased with time after the T-jump until it equilibrated at longer delay times. Notably, Fig. 2D reveals that the overall interfacial water alignment ΔP_z, calculated from the water dipole vector's z projection, aligns with the surface potential dynamics. This correlation indicates that water molecules in the EDL rapidly adjust to interfacial electric fields, as water reorientation (~1 ps) (*38*, *39*) is much faster than ion redistribution (tens of picoseconds). Thus, the vSFG spectral intensity determined by the water orientation serves as a real-time indicator of interfacial electric fields during EDL relaxation, even under transient conditions: The time-dependent spectra of the TR-vSFG experiments could directly monitor the EDL relaxation process in real-time.

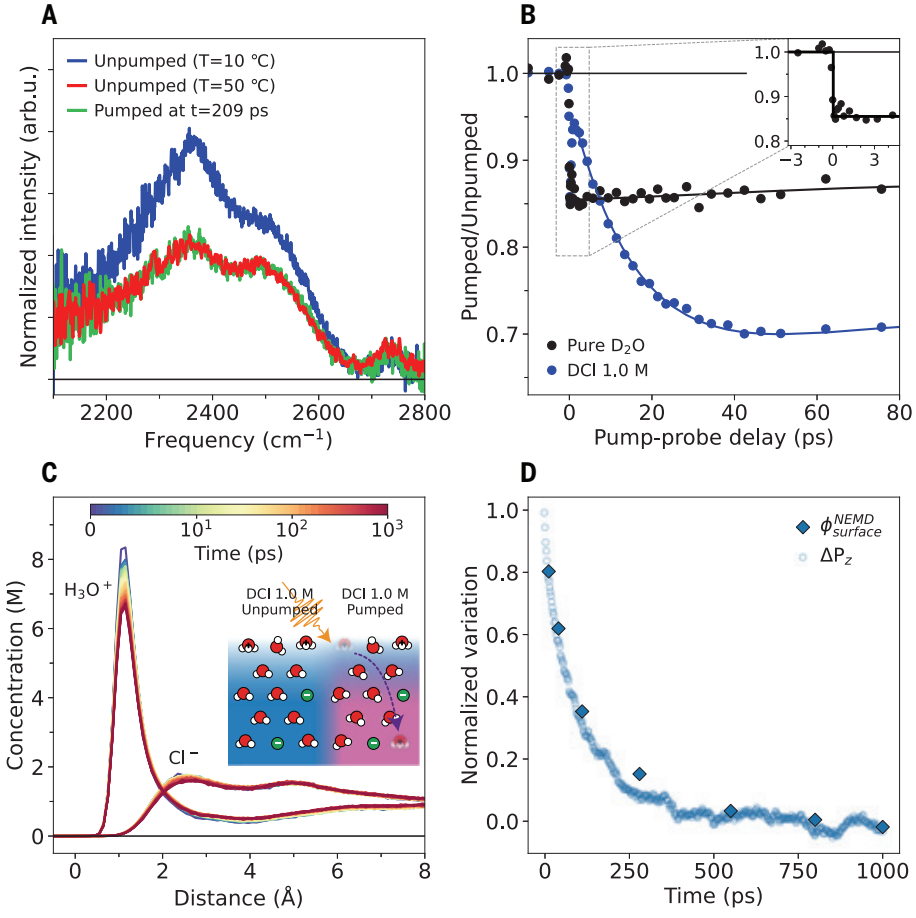

Fig. 2. Effect of the T-jump on ions and water alignment. (**A**) Time-resolved vSFG spectra of 1.0 M DCl solution before and 209 ps after the T-jump. The unexcited heated spectrum of 1.0 M DCl solution at 50°C is shown as a red line to show the comparison of the static heated data and time-resolved data. (**B**) Time-resolved traces of the integrated vSFG spectra excited with ~20.0 μJ of excitation energy. Solid lines show fits using eq. S1 from the supplementary materials. The inset highlights the 1-ps variation of the time-resolved trace of D_2O due to the T-jump (black line to guide the eye). (**C**) Time evolution of the ion distributions from NEMD simulations and simplified molecular scheme representing the thermally induced proton desorption following the T-jump. (**D**) Time-dependent interfacial electric surface potential $\phi_{surface}^{NEMD}$ and depth-integrated projection of the water dipole vector along the z-direction ΔP_z from NEMD simulations after a T-jump. Both quantities are shown as the difference between their values at t = 0 and 1 ns, normalized to their initial values.

EDL dynamics is primarily driven by conduction

To dissect the different driving forces that give rise to the thermally induced rearrangement of ions in the EDL, we analytically modeled the evolution of the ion distributions obtained from the NEMD simulations using a mean-field description. The T-jump perturbs the system's equilibrium by inducing proton desorption, which alters the surface charge density, while simultaneously modifying the dielectric function and changing the Debye length. Two main driving forces act to bring the EDL back at equilibrium: (i) diffusion of the now excess concentrations caused by the altered interfacial adsorption potentials (e.g., due to interaction of ions with water) and (ii) conduction of the now excess charges in the altered interfacial electric fields (i.e., classical EDL relaxation according to the Debye-Falkenhagen model).

To discriminate between these two driving forces, we used a mean-field analytical approach based on modified Poisson-Nernst-Planck (PNP) equations (*9*, *40*, *41*), which include an adsorption potential in addition to the usual diffusion and conduction terms. This description was equivalent to the Smoluchowski (S) diffusion equation (*42*) for adsorbed charged particles, meaning that both adsorption and electrostatics contributed to the potential and gave rise to the potential of mean force. The equilibrated initial and final ion distributions were obtained from MD simulations (Fig. 1F). The Poisson-Nernst-Planck-Smoluchowski (PNPS) equations read:

$$\frac{1}{D_+}\frac{\partial c_+(z,t)}{\partial t} = \nabla\Big[\nabla c_+(z,t) + \nabla U_+(z)\frac{c_+(z,t)}{k_B T} - \frac{e}{k_B T}c_+(z,t)\nabla\phi\Big] \quad (1)$$

$$\frac{1}{D_-}\frac{\partial c_-(z,t)}{\partial t} = \nabla\left[\nabla c_-(z,t) + \nabla U_-(z)\frac{c_-(z,t)}{k_B T} + \frac{e}{k_B T}c_-(z,t)\nabla\phi\right] \quad (2)$$

$$\Delta\phi(z,t) = -\frac{F}{\varepsilon_0\varepsilon_r}[c_+(z,t) - c_-(z,t)] \quad (3)$$

Here, e is the elementary charge; k_B is the Boltzmann constant; T is the absolute temperature; ε_r and ε_0 are the relative and vacuum permittivity, respectively; and F is the Faraday constant. D_+ and D_- are the diffusion coefficients, c_+ and c_- are the time (t)– and distance (z)–dependent ion densities, and ϕ is the electrostatic potential from the ions. From the equilibrated PNPS equations, we obtained the temperature-dependent adsorption potentials for H_3O^+ and Cl^-, denoted as U_+ and U_-, respectively (Fig. 3A). U_+ had a marked minimum at $z = 1$ Å, the origin of H_3O^+ adsorption at the interface. Conversely, U_- was predominantly repulsive at the interfacial region and exhibited no marked preferential adsorption in the liquid phase. Hence, the enhanced subsurface Cl^- population (Fig. 1F) stemmed predominantly from the electrostatic attraction to interfacial protons.

Upon raising the temperature, both adsorption and electrostatic potentials varied, resulting in an instantaneous excess of protons Δc_+ and chlorides Δc_- after the T-jump (Fig. 3A). Starting from the equilibrium distribution at ambient temperature, we used Eqs. 1 to 3 to numerically evolve in time the distributions of cations c_+ and anions c_- at an elevated temperature. Through these ion distributions, we calculated the time variation of the surface potential $\phi_{surface}^{PNPS}$: In Fig. 3B, we show that using a diffusion coefficient $D_\pm = 0.13\ D_{\pm,bulk}$ in the PNPS equations, $\phi_{surface}^{PNPS}$ excellently agreed with $\phi_{surface}^{NEMD}$. We noted that the discrepancy between the experimental $D_{\pm,bulk}$ values at infinite dilution and $D_\pm$ values required to model the NEMD results presumably stemmed from a combination of finite concentration effects and an underestimation of the H_3O^+ diffusivity (which dominated the response) by the classical force field MD simulations (*43*), which did not allow for H^+ Grotthuss hopping (see supplementary materials). This notion was further supported by the faster decay of the experimentally determined variation of the water alignment (Fig. 2B) as compared to the simulated data in Fig. 2D. As we show below, using the experimental D_{bulk} at finite concentration predicted the experimentally detected EDL relaxation well. Despite these discrepancies between NEMD and experiments with respect to absolute timescales, the agreement between the NEMD and PNPS results demonstrated that the essential driving forces for the EDL restructuring could be captured by both methods well. Additionally, the PNPS modeling even allowed us to calculate the time evolution of $\phi_{surface}^{PNPS}$ of 0.1 M, for which equilibrium ion distributions could be reliably obtained from MD, but NEMD did not provide sufficient statistics to quantify the dynamics.

Having established quantitative agreement between NEMD simulations and mean-field modeling, we dissected the driving forces for the EDL relaxation. We quantified the impact of (i) diffusion and (ii) conduction by comparing the full PNPS model ($U + \phi$) with the PNPS model without conduction (U^{noC}) (see supplementary materials). Figure 3C shows the dynamics of the surface potentials $\phi_{surface}$ with and without conduction for three concentrations. For all concentrations, equilibration was substantially accelerated when conduction was included. We fit single exponential decays to the modeled evolutions of the surface potential, obtaining the total PNPS relaxation rate $k_{U+\phi}$ and the rate without conduction $k_{U^{noC}}$. By rewriting $k_{U+\phi} = k_{U^{noC}} + k_\phi$, where k_ϕ is the Debye-Falkenhagen relaxation rate (which is conduction-driven), we could quantify the contributions of the Debye-Falkenhagen relaxation to the observed dynamics. We found that $k_\phi \approx 2k_{U^{noC}}$ at all concentrations (see supplementary materials), indicating that conduction dominated the observed double-layer relaxation. Despite the complex EDL structure and pronounced adsorption potential due to specific proton-water interactions, our findings suggest that EDL dynamics can be reasonably well described by classical EDL relaxation within the Debye-Falkenhagen model framework.

Experimental EDL relaxation agrees quantitatively with Debye-Falkenhagen

To test this hypothesis, we experimentally determined the EDL relaxation using TR-vSFG

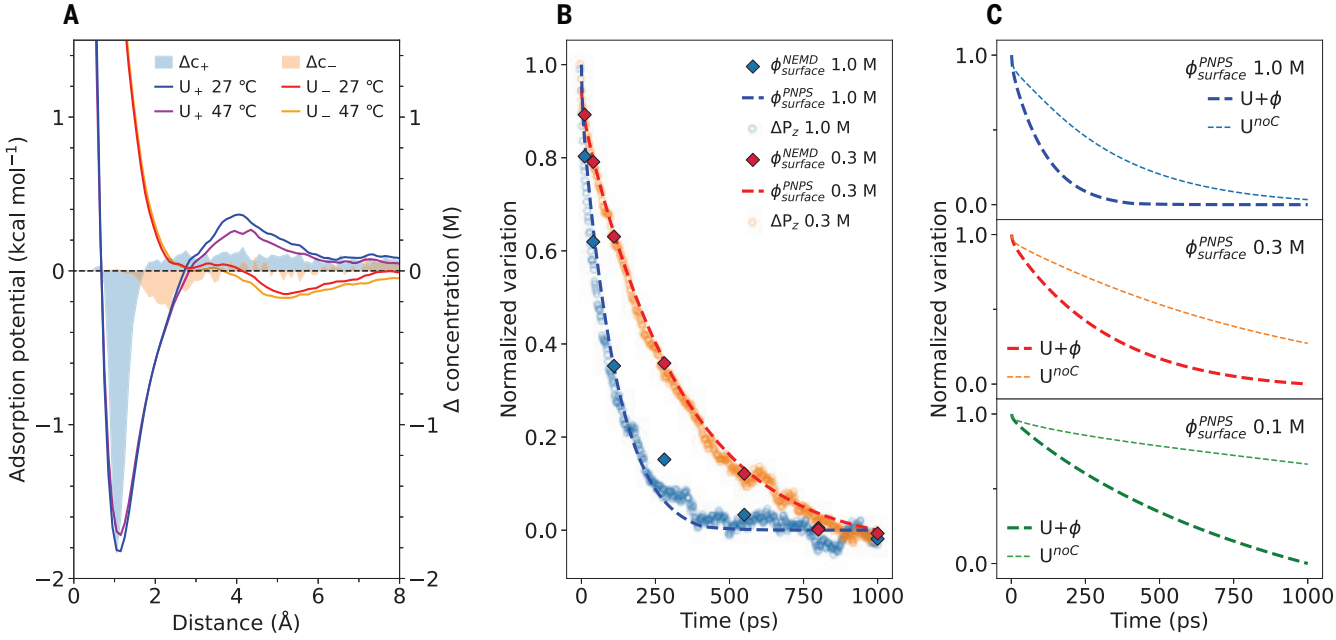

Fig. 3. Dissecting the driving forces with mean-field representation. (**A**) Adsorption potentials U_+ and U_- before and after the T-jump and variation of the ion distributions (Δ = final − initial; c_+ in light blue, c_- in orange) for 1.0 M HCl solution in H_2O. (**B**) Evolution of ΔP_z from simulation (circles) and surface potential, both from simulations (diamonds) and modeling (dashed line) for 0.3 and 1.0 M HCl solutions in H_2O. (**C**) Evolution of surface potential from the modeling with (thick dashed line) and without (thin dashed line) considering the conduction term for different HCl concentrations. In (B) and (C), quantities are shown as the difference between their values at t = 0 and 1 ns, normalized to their initial values.

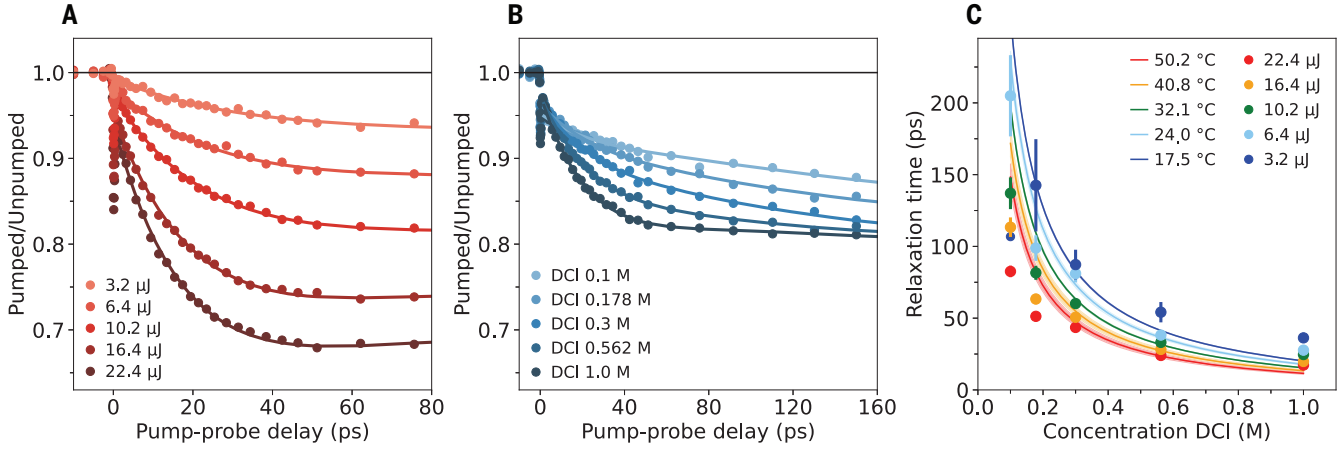

Fig. 4. Experimental EDL relaxation and Debye-Falkenhagen timescale. (**A**) Fluence dependence (or equivalently, temperature dependence) of the T-jump vSFG time trace for 1.0 M DCl solution. (**B**) Concentration dependence of the T-jump vSFG time trace at the excitation energy of 10.2 µJ corresponding to a ΔT ~ 20°C increase in local temperature. In (A) and (B), symbols correspond to transient integrated vSFG intensities, and solid lines show fits with eq. S1 to extract τ_{exp}. (**C**) Time constants and relative standard errors for the EDL dynamics (τ_{exp}, solid circles) at various excitation fluences and various DCl concentrations versus Debye-Falkenhagen relaxation times calculated at the corresponding final temperatures (τ_{DF}, lines).

with varying ionic strength (DCl concentration), varying counterion (Cl versus Br, fig. S3), and as a function of the magnitude of the T-jump (IR pump pulse energy). Figure 4, A and B, shows the temperature and concentration-dependent T-jump vSFG experiments for DCl solutions, revealing faster relaxation at higher temperatures and solute concentrations. For quantitative analysis (see supplementary materials), we extracted the experimental relaxation timescale, τ_{exp}, by fitting an exponential function to the EDL relaxation data, with the obtained relaxation time indicated by the symbols in Fig. 4C. τ_{exp} was both temperature and concentration dependent and ranged from 20 to 200 ps.

According to the Debye-Falkenhagen model, the relaxation of the EDL by redistribution of the ions is governed by the bulk mobility of the ions (their bulk diffusion coefficient D_{bulk}) and the typical screening length of the double layer (Debye length, λ_D): The Debye-Falkenhagen relaxation time could be estimated from $\tau_{DF} = \lambda_D^2/D_{bulk} = \varepsilon_0\varepsilon_r/c_{bulk}\Lambda$, where Λ is the molar conductivity of the electrolyte and c_{bulk} is the bulk concentration of the electrolyte (*9*, *40*, *44*). Note that the concentration and temperature dependence of τ_{DF} thus stemmed from the concentration and temperature dependence of ε_r, c_{bulk}, and Λ. Figure 4C illustrates that the estimated τ_{DF} values agreed well with the experimental results. Hence, although the molecular complexity of the interface and the concentration and charge density ranged far beyond the range where mean-field models, such as Gouy-Chapman and Debye-Falkenhagen, are considered applicable, the EDL relaxation was predicted with reasonable accuracy by using the simple expression for τ_{DF} with no adjustable parameters.

Our study highlighted the complex interplay between specific interactions and classical electrostatic forces in the nonideal EDL at the air-acidic solution interface. Our results demonstrated the robustness of the mean-field PNPS equations for describing EDL dynamics. For protons at the air-water interface, relevant to on-water and atmospheric chemistry, the PNPS formalism can be simplified to the Debye-Falkenhagen theory for EDL relaxation, providing accurate predictions of EDL dynamics despite its presumed inapplicability at high concentrations and surface charge densities. Also, the PNPS formalism applies broadly to EDL-based devices with solid electrodes, such as double-layer capacitors, electrochemical cells, and field-effect transistors (see supplementary materials); in conduction-driven systems, the EDL relaxation timescale is largely independent of the details of the electrode and equilibrium perturbation. Diffusion processes may dominate in some of these systems, potentials can be substantially higher than those studied in this work, and solvation effects can be rate limiting (*45*, *46*), which will cause the simplified Debye-Falkenhagen formalism to break down. Yet, our results suggest that (appropriately modified) PNPS equations may still provide an adequate description. For our system, the intrinsic limit of EDL response approximates the Debye-Falkenhagen timescale, serving as a benchmark for response time and representing the inherent high-frequency limit for the operation of these systems. This study advances our understanding of EDL dynamics at high concentrations, providing insights for the design of various electrochemical devices.

REFERENCES AND NOTES

1. G. Gonella *et al.*, *Nat. Rev. Chem.* **5**, 466–485 (2021).
2. J. Wu, *Chem. Rev.* **122**, 10821–10859 (2022).
3. M. Salanne *et al.*, *Nat. Energy* **1**, 1–10 (2016).
4. F. Torricelli *et al.*, *Nat. Rev. Methods Primers* **1**, 1–24 (2021).
5. S. J. Shin *et al.*, *Nat. Commun.* **13**, 174 (2022).
6. R. Dong, T. Zhang, X. Feng, *Chem. Rev.* **118**, 6189–6235 (2018).
7. S. Narayan *et al.*, *Angew. Chem. Int. Ed.* **44**, 3275–3279 (2005).
8. X. Song *et al.*, *J. Am. Chem. Soc.* **145**, 25910–25916 (2023).
9. J. Lyklema, *Solid-Liquid Interfaces*, vol. 2 of Fundamentals of Interface and Colloid Science (Academic Press, 1995).
10. M. Favaro *et al.*, *Nat. Commun.* **7**, 12695 (2016).
11. K. Ojha, N. Arulmozhi, D. Aranzales, M. T. M. Koper, *Angew. Chem. Int. Ed.* **59**, 711–715 (2020).
12. B. Rehl *et al.*, *J. Am. Chem. Soc.* **144**, 16338–16349 (2022).
13. C. Tian, S. J. Byrnes, H. L. Han, Y. R. Shen, *J. Phys. Chem. Lett.* **2**, 1946–1949 (2011).
14. Y. Litman, K. Y. Chiang, T. Seki, Y. Nagata, M. Bonn, *Nat. Chem.* **16**, 644–650 (2024).
15. P. Jungwirth, D. J. Tobias, *Chem. Rev.* **106**, 1259–1281 (2006).
16. D. Horinek *et al.*, *Chem. Phys. Lett.* **479**, 173–183 (2009).
17. M. A. Brown *et al.*, *Phys. Rev. X* **6**, 011007 (2016).
18. M. A. Brown, A. Goel, Z. Abbas, *Angew. Chem. Int. Ed.* **55**, 3790–3794 (2016).
19. A. M. Smith, A. A. Lee, S. Perkin, *J. Phys. Chem. Lett.* **7**, 2157–2163 (2016).
20. C. Zhao, T. Yang, S. Jin, B. Wu, *J. Phys. Chem. C* **128**, 5964–5971 (2024).
21. A. C. Forse *et al.*, *Nat. Energy* **2**, 16216 (2017).
22. J. A. McGuire, Y. R. Shen, *Science* **313**, 1945–1948 (2006).
23. Q. Du, R. Superfine, E. Freysz, Y. R. Shen, *Phys. Rev. Lett.* **70**, 2313–2316 (1993).
24. K. C. Jena, P. A. Covert, D. K. Hore, *J. Phys. Chem. Lett.* **2**, 1056–1061 (2011).
25. Y. C. Wen *et al.*, *Phys. Rev. Lett.* **116**, 016101 (2016).
26. R. Vácha, D. Horinek, M. L. Berkowitz, P. Jungwirth, *Phys. Chem. Chem. Phys.* **10**, 4975–4980 (2008).
27. H. S. Lee, M. E. Tuckerman, *J. Phys. Chem. A* **113**, 2144–2151 (2009).
28. S. Iuchi, H. Chen, F. Paesani, G. A. Voth, *J. Phys. Chem. B* **113**, 4017–4030 (2009).
29. S. Das, M. Bonn, E. H. G. Backus, *Angew. Chem. Int. Ed.* **58**, 15636–15639 (2019).
30. S. Das *et al.*, *J. Am. Chem. Soc.* **142**, 945–952 (2020).
31. K. Y. Chiang, L. Dalstein, Y. C. Wen, *J. Phys. Chem. Lett.* **11**, 696–701 (2020).
32. J. Lindner *et al.*, *Chem. Phys. Lett.* **421**, 329–333 (2006).
33. K. Ramasesha, L. De Marco, A. Mandal, A. Tokmakoff, *Nat. Chem.* **5**, 935–940 (2013).
34. S. Ashihara, N. Huse, A. Espagne, E. T. J. Nibbering, T. Elsaesser, *J. Phys. Chem. A* **111**, 743–746 (2007).

35. W. Sung, K. I. Inoue, S. Nihonyanagi, T. Tahara, *Nat. Commun.* **15**, 1258 (2024).
36. A. Greco, T. Ohto, Y. Nagata, M. Bonn, E. H. G. Backus, *J. Chem. Phys.* **161**, 174706 (2024).
37. Y. Nagata *et al.*, *Phys. Chem. Chem. Phys.* **17**, 23559–23564 (2015).
38. D. Laage, J. T. Hynes, *Science* **311**, 832–835 (2006).
39. K. J. Tielrooij, S. T. van der Post, J. Hunger, M. Bonn, H. J. Bakker, *J. Phys. Chem. B* **115**, 12638–12647 (2011).
40. M. Z. Bazant, K. Thornton, A. Ajdari, *Phys. Rev. E* **70**, 021506 (2004).
41. R. J. Hunter, *Foundations of Colloidal Science* (Oxford Univ. Press, ed. 2, 2000).
42. H. Risken, *The Fokker-Planck Equation* (Springer-Verlag, 1984).
43. T. Pongratz *et al.*, *Biophys. Chem.* **257**, 106258 (2020).
44. A. Eiberweiser, R. Buchner, *J. Mol. Liq.* **176**, 52–59 (2012).
45. A. Yamakata, M. Osawa, *J. Phys. Chem. C* **112**, 11427–11432 (2008).
46. A. Yamakata, E. Soeta, T. Ishiyama, M. Osawa, A. Morita, *J. Am. Chem. Soc.* **135**, 15033–15039 (2013).
47. A. Greco, Data files "EDL dynamics" project, Zenodo (2025); https://doi.org/10.5281/ZENODO.14796693.

ACKNOWLEDGMENTS

We are grateful to M.-J. van Zadel, F. Gericke, and H. Menges for technical support. We thank L. Bocquet, D. Maltseva, M. Grechko, L. Di Virgilio, and M. Deiseroth for fruitful discussion; S. Das for preliminary experiments; and Y. Litman and Y. Wang for sharing data. **Funding:** Funding was provided by the European Union's Horizon 2020 research and innovation program under the Marie Sklodowska-Curie grant agreement no. 811284 UHMob (A.G.), the European Union (ERC, n-AQUA, 101071937), and the MaxWater program of the Max Planck Society. **Author contributions:** Conceptualization: A.G., E.H.G.B., Y.N., J.H., M.B.; Methodology: A.G., S.I., E.H.G.B., Y.N., J.H., M.B.; Investigation: A.G., S.I.; Visualization: A.G., E.H.G.B., Y.N., J.H., M.B.; Funding acquisition: E.H.G.B., M.B.; Project administration: A.G., E.H.G.B., Y.N., J.H., M.B.; Supervision: E.H.G.B., Y.N., J.H., M.B.; Writing – original draft: A.G., Y.N., J.H.; Writing – review & editing: A.G., E.H.G.B., Y.N., J.H., M.B. **Competing interests:** The authors declare that they have no competing interests. **Data and materials availability:** All data needed to evaluate the conclusions in the paper are present in the paper or the supplementary materials. All the data in the manuscript and supplementary materials are available through Zenodo (*47*).

SUPPLEMENTARY MATERIALS

science.org/doi/10.1126/science.adu5781
Materials and Methods
Supplementary Text
Figs. S1 to S14
References (*48*–*62*)

Submitted 12 November 2024; accepted 3 March 2025
10.1126/science.adu5781

AGRICULTURE

Conventional and organic farms with more intensive management have lower soil functionality

Sophie Q. van Rijssel[1]†‡, Guusje J. Koorneef[2,3]†§, G. F. (Ciska) Veen[1], Mirjam M. Pulleman[3,4], Ron G. M. de Goede[3], Rob N. J. Comans[2,5], Wim H. van der Putten[1,6], Kyle Mason-Jones[1,7]*

Organic farming is often considered to be more sustainable than conventional farming. However, both farming systems comprise highly variable management practices. In this study, we show that in organic and conventional arable fields, the multifunctionality of soils decreases with increasing agricultural management intensity. Soil organic carbon content and bacterial biomass, respectively, were the strongest abiotic and biotic predictors of soil multifunctionality. Greater soil multifunctionality was associated with less-frequent inversion tillage and higher frequency of grass-legume cover cropping, and organic farming did not outperform conventional farming. Our results suggest that reducing management intensity will enhance soil multifunctionality in both conventional and organic farming. This implies that, in contexts where high-yielding, high-intensity agriculture prevails, the paradigm of sustainable intensification should be replaced by "productive deintensification."

Soils perform numerous ecological functions that underpin human and ecosystem health. In agricultural soils, maximized crop yield may come at the expense of soil functions, including water retention (*1*), making agriculture more sensitive to drought, or of less-efficient nutrient cycling, resulting in nutrient loss and pollution of water bodies (*2*). Intensive agricultural management can also reduce soil organic carbon (SOC) content and soil biodiversity (*3*, *4*), both strong determinants of soil functionality (*5*, *6*). Thus, increased crop yield may come at the cost of multiple functions (multifunctionality) and thus compromise soil health (*7*, *8*). The multifunctionality concept integrates soil functionality trade-offs and synergies that may otherwise be overlooked. With global soils facing multiple forms of degradation (*9*), there is a pressing need to enhance soil multifunctionality in order to produce food sustainably.

One widespread approach to improving soil health is organic farming, in which natural fertilizers and pest control are applied in place of synthetic inputs (*10*). Indeed, organic farming systems are reported to outperform conventional farming systems in numerous soil functions (*10*) and in multifunctionality overall (*11*). However, it is unclear whether functional differences are inherent to organic versus conventional farming or whether they actually originate from a combination of individual management practices that could be applied in either farming system (*12*, *13*). It is also important to understand whether agricultural management affects functions directly, or indirectly by altering the quantity or quality of SOC (*6*) or the composition of soil biological communities (*14*). Understanding the interplay between management practices, SOC, biota, and soil multifunctionality is crucial for establishing effective management targets and appropriate indicators of agricultural sustainability.

Experiments have shown how particular management practices affect soil functions; for example, it has been found that crop diversification can enhance pest control and nutrient cycling, reducing greenhouse gas emissions (*15*), and that pesticide application can affect soil enzyme activities (*16*). Comparison of multiple soil functions between sites is facilitated by aggregating the individual functions into a composite multifunctionality score (*8*, *17*). This strategy has shown that soil multifunctionality can, for example, be promoted by organic management and reduced tillage (*11*), manure application (*18*), and crop residue return (*19*).

Agricultural management is a multidimensional combination of practices, making comparisons between real farm systems challenging but nevertheless necessary for decision-making by consumers and policy-makers. The binary characterization of conventional versus organic farming has attained widespread public recognition and establishment within regulatory frameworks, despite comprising a range of different management practices (*20*). An alternative simplification is to aggregate management practices into a composite management intensity score (*13*, *21*), analogous to scoring multifunctionality. Applicable across both conventional and organic agriculture, this approach has the advantage that variability in practices is better reflected.

The aim of the present study is to examine how conventional versus organic farming, and agricultural management intensity, influence soil multifunctionality. We also determine whether these relationships can be explained by differences in the characteristics of SOC and soil microbiota. We use the term "conventional agriculture" as an analytical comparator in the sense of Sumberg & Giller (*22*), to denote farms whose practices are not organic nor self-identified as "alternative" agricultural practices,

[1]Department of Terrestrial Ecology, Netherlands Institute for Ecology (NIOO-KNAW), Wageningen, Netherlands. [2]Soil Chemistry Group, Wageningen University & Research, Wageningen, Netherlands. [3]Soil Biology Group, Wageningen University & Research, Wageningen, Netherlands. [4]International Center for Tropical Agriculture (CIAT), Cali, Colombia. [5]TNO, Geological Survey of the Netherlands, Utrecht, Netherlands. [6]Laboratory of Nematology, Wageningen University & Research, Wageningen, Netherlands. [7]Soil Microbial Interactions, Department of Geoscience, University of Tübingen, Tübingen, Germany.
***Corresponding author. Email: k.masonjones@nioo.knaw.nl**
†These authors contributed equally to this work.
‡Present address: Soil Geography and Landscape Group, Wageningen University & Research, Wageningen, Netherlands.
§Present address: Department of Terrestrial Ecology, Netherlands Institute for Ecology (NIOO-KNAW), Wageningen, Netherlands.

Table 1. Overview of soil organic carbon (SOC) quality parameters considered in the analysis.

Abbreviation	Description	Unit	Type
Total SOC	Total soil organic carbon	g C kg^{-1} soil	Size of SOC
POXC	Permanganate-oxidizable organic carbon	g C kg^{-1} soil	Size of SOC fraction
POXC:SOC	Permanganate oxidizable organic carbon, expressed as proportion relative to total SOC content	g C g^{-1} C	Proportion of SOC fraction
POMC	SOC present as particulate organic matter (POM) (>50 μm), expressed in	g C kg^{-1} soil	Size of SOC fraction
POMC:SOC	g C kg^{-1} soil or as proportion relative to total SOC content (g C g^{-1} C)	g C g^{-1} C	Proportion of SOC fraction
PyroC:SOC	Total pyrolyzable SOC, expressed as proportion relative to total SOC content (g C g^{-1} C)	g C kg^{-1} soil	Proportion of SOC fraction
MAOMC	SOC present as mineral-associated organic matter (MAOM) (<50 μm), expressed	g C kg^{-1} soil	Size of SOC fraction
MAOMC:SOC	in g C kg^{-1} soil or as proportion relative to total SOC content (g C g^{-1} C)	g C g^{-1} C	Proportion of SOC fraction
StableC:SOC	Centennially persistent SOC, expressed as proportion relative to total SOC content (g C g^{-1} C)	g C kg^{-1} soil	Proportion of SOC fraction
Bulk_CN	The organic carbon-to-total-nitrogen ratio (C:N) of the bulk soil	g C g^{-1} N	Element ratio
POMC:N	The carbon-to-nitrogen ratio (C:N) of the fraction of coarse organic matter (>50 μm), that mainly consists of POM	g C g^{-1} N	Element ratio
MAOMC:N	The carbon-to-nitrogen ratio (C:N) of the fraction of fine organic matter (<50 μm), that mainly consists of MAOM	g C g^{-1} N	Element ratio
OI	Oxygen index, a proxy for the oxygen:carbon ratio of soil organic matter	mg O_2 g^{-1} C	Element ratio
T50pyr_CH	The temperature at which 50% of the carbon has converted to volatile hydrocarbon (i.e., CH) effluents during pyrolysis.	°C	Thermal stability
T50pyr_CO2	The temperature at which 50% of the carbon has converted to CO_2 during pyrolysis	°C	Thermal stability
T50ox_CO2	The temperature at which 50% of the carbon has converted to CO_2 during oxidation	°C	Thermal stability

such as conservation or regenerative agriculture (*23*, *24*). Conventional farming represents the mainstream agricultural practices of the Netherlands, where our study was conducted. Organic practices exclude synthetic fertilizers and pesticides and are certified by "*Stichting Keur Alternatief voortgebrachte Landbouwproducten*" (SKAL) (*25*). We hypothesize that (i) organic agriculture outperforms conventional agriculture in terms of soil multifunctionality but that (ii) increasing agricultural management intensity is negatively related to soil multifunctionality in both organic and conventional farming. Furthermore, we postulate that these relationships are mediated by changes in soil biology and SOC, and we therefore hypothesize that (iii) soil biological and (iv) SOC characteristics significantly explain variation in multifunctionality by reflecting management practices.

Assessment of management intensity and soil multifunctionality

Our analysis is based on soils sampled across the Netherlands from 53 organic and conventional arable fields on two dominant mineral soil types (*26*–*29*). The sandy soils are classified as Anthrosols and clay soils as calcareous Fluvisols (*30*), with the sand or clay distinction accounting for the largest variation in pedogenic properties and therefore adopted as shorthand descriptors (fig. S1 and table S1). Sampled fields had comparable monocot crops (winter or spring wheat, barley, spelt or winter rye, or grass-legume mixtures as a representative cover crop). The organic fields varied in age from 4 to 69 years of organic management, with recently converted fields (0 to 3 years) excluded. The multifunctionality analysis integrated soil function indicators for nutrient cycling, decomposition, soil structure provision, pathogen control, and water regulation into a single multifunctionality score (materials and methods and table S2). Each indicator was scaled to the mean value for the respective soil type. Transformed indicator values were then averaged to obtain the aggregated multifunctionality score for each field (materials and methods) (*17*, *31*). We applied multiple approaches to characterize SOC and soil biota (Table 1 and table S3) and also examined whether multifunctionality relates to plant productivity using the normalized difference vegetation index (NDVI) from a previous study (*32*).

Various management practices have been previously used as management intensity indicators, including external inputs (*13*, *33*–*35*), organic residue removals (*13*, *33*), mechanical soil tillage (*4*, *33*–*35*), and narrow crop rotations (*4*, *35*). We adopted a definition of management intensity as the extent to which cropping practices alter soil processes (*34*). We used farm interviews during the sampling campaign to collect management data regarding organic matter inputs (external inputs per hectare and retention of crop residues), soil tillage (depth and frequency), and crop rotation (diversity, root and tuber crop frequency, and cover cropping) and aggregated these into a single management intensity score (materials and methods and table S4). Management practices can vary strongly and systematically by soil type, so the same approach to scaling and aggregation was applied here to each soil type separately, as for soil function indicators.

Soil multifunctionality is reduced under higher management intensity

Organic fields overall had lower management intensity scores than conventional fields [Fig. 1A; analysis of variance (ANOVA): $F_{1,49} = 14.2$, $P < 0.001$]. However, our results do not support the hypothesis that organic fields outperform conventional fields in terms of multifunctionality because this relationship was absent overall and when considering clay or sand fields separately (Fig. 1B; ANOVA $P_{ConOrg} > 0.3$). Nevertheless, there was a significant negative relationship between management intensity and multifunctionality when considering all fields together (Fig. 1C; Spearman $\rho = -0.30$, $P = 0.028$). The relationship between management intensity and multifunctionality remained significant for organic fields alone ($P = 0.033$) but not for conventional fields ($P = 0.31$) (fig. S2). Given the consistent trend in both farming systems (fig. S2; $\rho_{Org} = -0.43$, $\rho_{Con} = -0.17$), the statistical significance in the combined analysis evidently benefited from the statistical power of the larger dataset with both management systems together. Growing season NDVI of the study fields (*32*) was not correlated to soil multifunctionality (Spearman $\rho = 0.23$, $P = 0.095$). Therefore, there was neither evidence of a synergy nor a trade-off between soil multifunctionality and plant productivity.

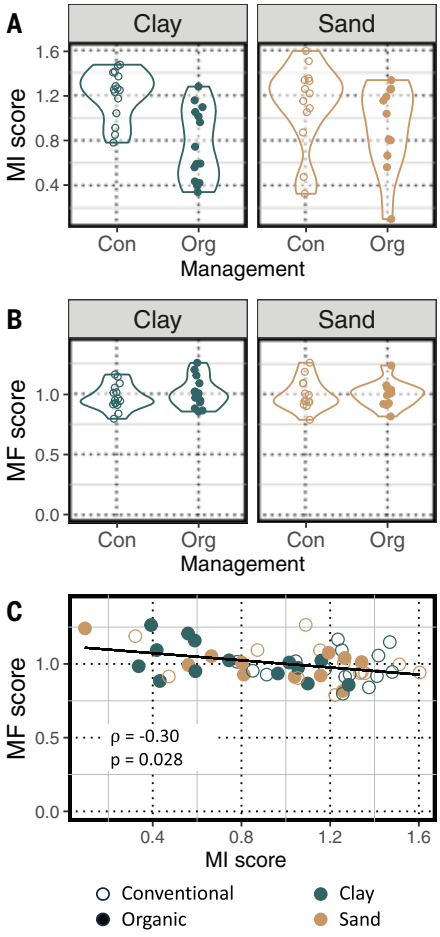

Fig. 1. Relationships between farming system, management intensity (MI), and soil multifunctionality (MF) across 53 farms in the Netherlands, on sandy and clay soils. (**A**) Organic management is less intensive than conventional management (ANOVA: $F_{1,49}$ = 14.2, P < 0.001) with no effect of or interaction with soil type. (**B**) The farming system does not, however, predict soil multifunctionality (ANOVA: not significant for farming system, soil type, and interactions). (**C**) Management intensity is negatively related to soil multifunctionality across both organic and conventional management systems (Spearman correlation illustrated with linear regression).

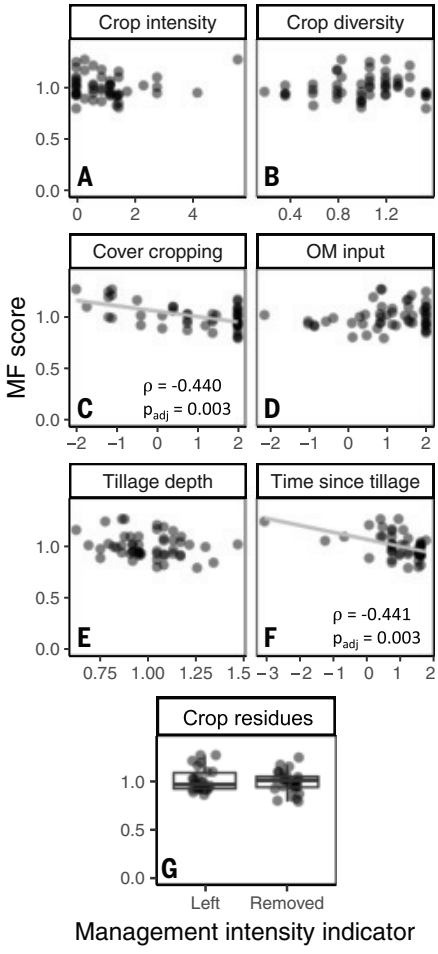

Fig. 2. Relationships between individual management intensity indicators and soil multifunctionality. (**A**) Crop intensity, determined as the frequency of root and bulb crops in the rotation. (**B**) Crop diversity in the rotation. (**C**) Grass-legume cover cropping (inverted indicator so that less cover cropping corresponds to higher intensity). (**D**) External organic matter inputs (inverted indicator). (**E**) Tillage depth. (**F**) Time since last tillage (inverted indicator). (**G**) Crop residue removal. Intensity indicators are scaled to the mean of the respective soil type.

We further analyzed the multifunctionality scores while disaggregating management intensity into its seven different component practices: crop diversity, crop intensity, percentage grass-legume in the rotation, external organic matter inputs (e.g., compost, manure), tillage depth, time since the last inversion tillage, and crop residue removal (Fig. 2; fig. S9 shows the corresponding analysis of management intensity related to individual functions). Time since the last tillage significantly increased the multifunctionality score—which remained significant when disaggregating the fields by conventional and organic management—and was marginally significant in clay soils alone (table S5). The percentage of a mixed grass-legume cover crop in the rotation also had a significant effect on multifunctionality (Fig. 2C), which was driven especially by its effect in sandy soils (table S5). External organic matter inputs, tillage depth, crop diversity, and other factors were not significantly related to multifunctionality on their own, but sensitivity analysis indicated that crop diversity, crop residue removal, and tillage depth also contributed to the strength of the observed relation (table S6).

Soil organic matter, not soil microbiota, strongly predicts multifunctionality

Although C sequestration is a soil function, we excluded biological and SOC parameters from our multifunctionality scores. By considering these parameters separately, we were able to test their hypothesized relationships to other aspects of multifunctionality. Soil multifunctionality was significantly correlated with 8 out of 16 SOC parameters, with the strongest relationship to total SOC content (Fig. 3; Spearman ρ = 0.63, P_{adj} < 0.001). SOC quality parameters representing the size of different SOC pools were all strongly positively correlated with multifunctionality [Fig. 3; permanganate-oxidizable C (POXC), particulate organic matter C (POMC), and mineral-associated organic matter C (MAOMC)]. However, these SOC parameters were also strongly correlated to total SOC content (fig. S5). Total SOC C:N ratio and thermal stability parameters did not show any relationships to multifunctionality. Consistent but weaker trends were observed when clay and sandy soils were analyzed separately (fig. S6), whereas relationships between SOC parameters and multifunctionality were generally insensitive to multifunctionality indicator composition (tables S7 and S8). Including SOC content as a soil function would have made the negative relationship between management intensity and multifunctionality somewhat stronger (Spearman ρ = −0.34, P = 0.014).

Soil multifunctionality did not show any correlation with biological soil parameters (fungal biomass; nematode abundance; and the composition, richness, and diversity of microbial or nematode communities; Fig. 4 and fig. S3), except for a positive relationship with bacterial biomass (Fig. 4; ρ = 0.42, P_{adj} = 0.031), which was driven by sandy soils (fig. S3; clay: ρ = 0.16, P_{adj} = 0.73, sand: ρ = 0.77, P_{adj} < 0.001). Bacterial biomass may have appeared as a significant factor owing to its positive relationship with total SOC (fig. S4; ρ = 0.38, P = 0.005). Total SOC content therefore emerged as the strongest predictor of soil multifunctionality from the wide range of biological and SOC indicators considered in our study.

Total SOC content also showed a marginally significant relationship to management intensity overall (Spearman: ρ = −0.31, P_{adj} = 0.051), as well as a direct relationship to time since tillage (fig. S7; Spearman: ρ = −0.44, P_{adj} = 0.008) and cover cropping (Spearman: ρ = −0.39, P_{adj} = 0.011). Higher management intensity was also reflected in a decline in the absolute and relative pool size of POMC (fig. S8; P_{adj} = 0.005 and 0.019, respectively) and was positively correlated with one of two indicators of pyrolytic stability (fig. S8; T50pyr_CO2, P_{adj} = 0.019). Of these, POMC pools corresponded to higher multifunctionality (Fig. 3) and were strongly correlated to

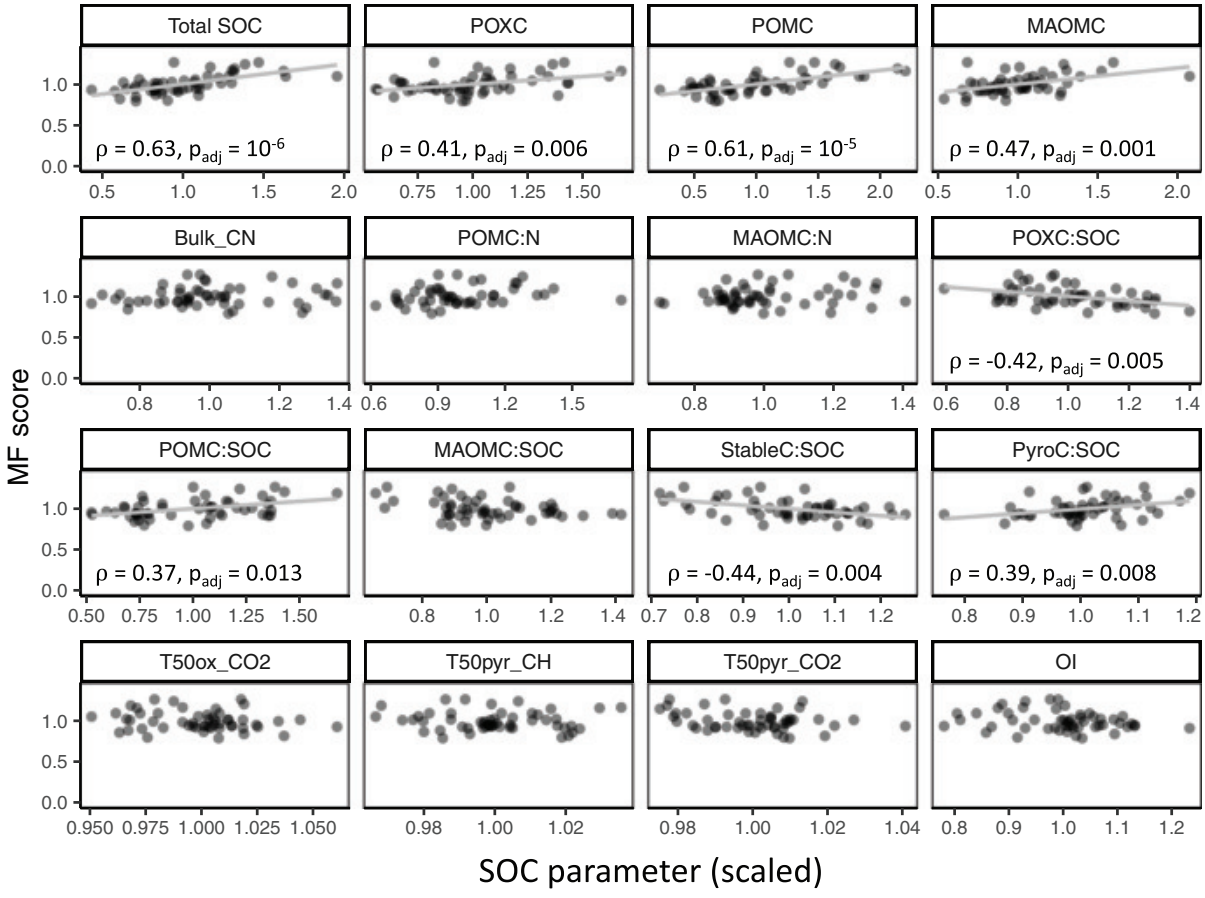

Fig. 3. Relationships between soil organic carbon parameters and soil multifunctionality (MF score). Soil organic matter parameters (Table 1) are scaled to the mean of the respective soil type, consistent with the scaling applied to the multifunctionality indicators. Total SOC: Total soil organic carbon in the bulk soil; POXC: pool size of permanganate-oxidizable C; POMC: pool size of particular organic matter C; MAOMC: pool size of mineral-associated organic matter C; Bulk_CN: C:N ratio of bulk soil; POMC:N: C:N ratio of POM; MAOMC:N: C:N ratio of MAOM; POXC:SOC, POMC:SOC, and MAOMC:SOC, respectively: POXC, POMC, and MAOMC as proportions of total SOC; StableC:SOC: centennially persistent SOC predicted from RockEval measurements as proportion of total SOC; PyroC:SOC: pyrolyzable SOC as proportion of total SOC; T50ox_CO2: temperature for 50% conversion of SOC to CO_2 during oxidation; T50pyr_CH: temperature for 50% conversion of SOC to volatile hydrocarbons during pyrolysis; T50pyr_CO2: temperature for 50% conversion of SOC to CO_2 during pyrolysis; OI: oxygen index. Significant (nonparametric) Spearman correlations are illustrated by linear regression lines.

total SOC content (fig. S5). Direct effects of management were therefore strongly reflected in SOC parameters, which in turn appears to influence multifunctionality.

The composition of aggregated indicators for management intensity and multifunctionality is crucial in such analyses. A sensitivity analysis examined the effect of omitting individual functions or management indicators. In most cases, the relationship between management intensity and multifunctionality was conserved with at least marginal significance (Spearman: $\rho = -0.24$ to -0.37; $P = 0.006$ to 0.088). However, two parameters (percentage grass-legume cover in the rotation, and time elapsed since the previous tillage) were essential to the identified trend, and the removal of either resulted in the loss of the significant relationship (table S6). By contrast, exclusion of external organic matter input greatly enhanced the strength and significance of the relationship between management intensity and soil multifunctionality (Spearman $\rho = -0.37$, $P = 0.006$). This finding was confirmed by repeating the sensitivity analysis without considering external organic matter inputs: The significance of the relationship was then robust to the removal of other functions or management intensity indicators (Spearman $\rho = -0.29$ to -0.42; $P = 0.001$ to 0.029) except for cover cropping ($\rho = -0.24$, $P = 0.083$).

Discussion

Our aggregated metric of management intensity was a better predictor of soil multifunctionality than the organic/conventional dichotomy, suggesting that reductions in management intensity can potentially improve soil functionality in both farming systems. However, there was a difference between the two systems, because organic farming had a lower average management intensity score than conventional farming, as well as a wider variation of management intensities (coefficient of variation of 0.42 and 0.26 for organic and conventional, respectively). The wide range of organic management intensities may explain why organic systems together did not have significantly higher multifunctionality overall. This variability may also explain why the relationship between management intensity and multifunctionality remained significant for organic farms when these were analyzed separately, but not for conventional farms. We do not conclude that multifunctionality is unresponsive to management intensity in conventional fields but foresee that conventional farmers will need to explore novel approaches to reduce their management intensity to enhance soil multifunctionality.

Although sensitivity analysis confirmed that multiple components of agricultural practice and soil functionality contribute to the broader relationships, the approach masks underlying mechanisms that may require targeted investigation to demonstrate individual effectiveness.

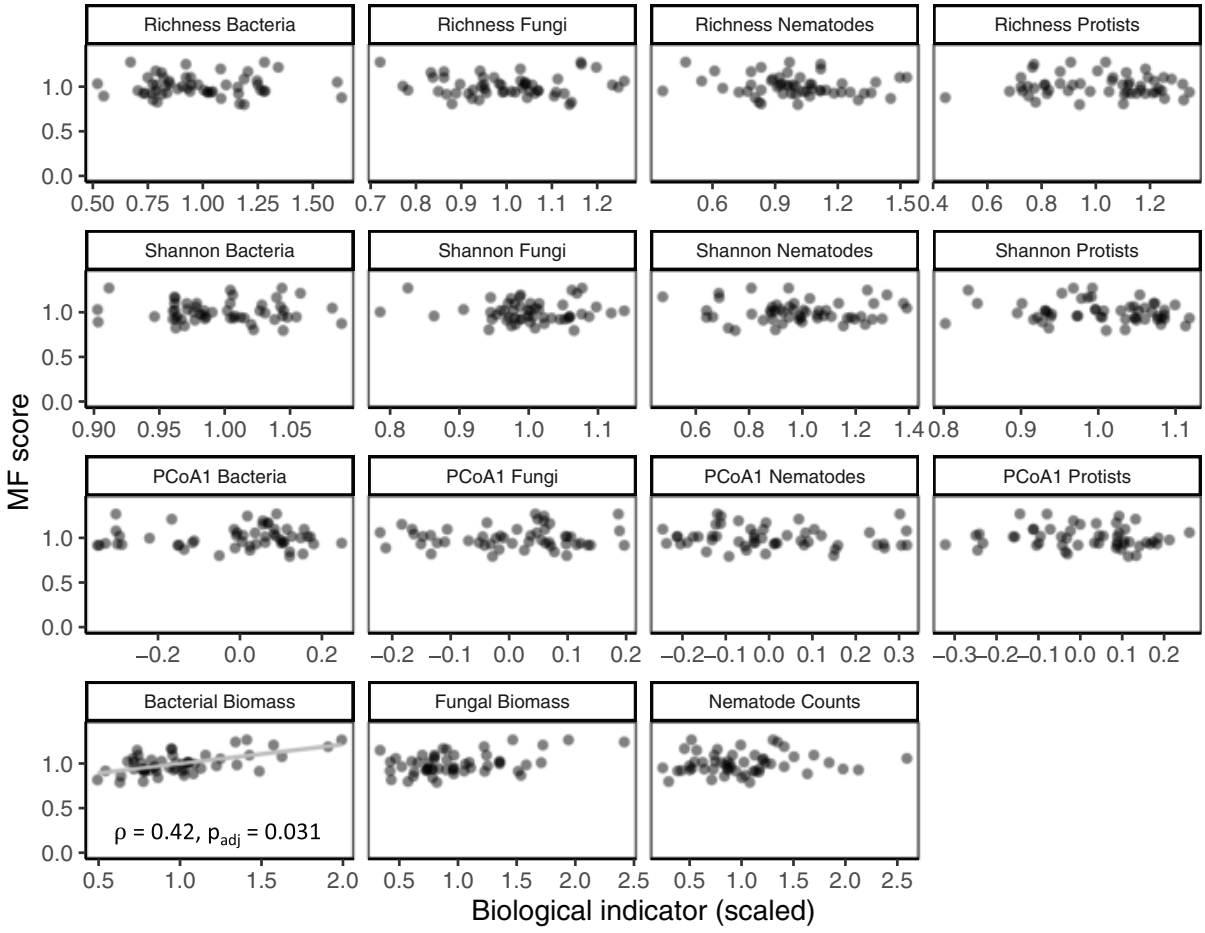

Fig. 4. Relationships between soil biological parameters and soil multifunctionality. Biological parameters are scaled to the mean of the respective soil type, consistent with the scaling applied to the multifunctionality indicators. Significant (nonparametric) Spearman correlations are illustrated by linear regression lines.

Reduced tillage frequency and the use of grass-legume cover crops influenced multifunctionality most, suggesting that these practices will contribute to greater soil health (*5*) in both organic and conventional agriculture. Our results support less-intensive management to increase soil health in high-yielding agricultural land. In this context, the paradigm of sustainable intensification may be contradictory because management intensification undermines soil multifunctionality. We propose that "productive deintensification" is a more appropriate aim, meaning "an optimization of yield while reducing management intensity."

Locating this study in the Netherlands has implications for the scale of management intensity that we observed, and our results and conclusions should be seen in the context of high-intensity, high-yielding agriculture prevailing in northwestern Europe. In particular, several components of management intensity may be considerably lower in regions where agriculture is less industrialized (*36*). By contrast, both organic and conventional arable farms in the Netherlands have historically received considerably more animal manure than in many other regions (*37*). Furthermore, relationships between management intensity and yield are expected to vary between contrasting regions. Although no region can represent the variability of agricultural practice globally, the inverse relationship we observed between management intensity and multifunctionality across a large dataset suggests a general relevance for comparable contexts.

The weak relationship between soil biodiversity and multifunctionality contrasts with several other studies (*38*, *39*), but such relationships are not consistently observed within a single climatic region (*40*). Larger fauna, not considered here, may influence multifunctionality (*5*). However, these organisms strongly influence soil microbial communities (*41*), and we found little correspondence between microbial abundance and multifunctionality or between diversity and multifunctionality. Our results also indicate that biodiversity is less important for multifunctionality than the functions provided by the biotic community (*42*), which might be better characterized by metagenomic or metatranscriptomic analysis or food-web structure (*43*).

We observed robust associations between SOC properties and soil multifunctionality (tables S7 and S8), with total SOC contents, followed by POMC content, as the strongest predictors. Notably, POMC content (and marginally total SOC) was also negatively related to management intensity, corroborating the responsiveness of this pool to management (*44*) and suggesting that it may be an important mediator of management effects. Our results support the straightforward use of total SOC content as an integrative indicator of soil multifunctionality that is not only easily and widely measured but also the best predictor among a wide range of SOC properties (*29*).

If soil multifunctionality is enhanced by reducing management intensity, the question arises whether yield can be simultaneously sustained to preserve productivity and farm economic viability. This is particularly relevant when considering increasing regulatory restrictions on fertilizer inputs and pesticides. Crop differences, variable allocation to harvested biomass, and confounding weed cover make NDVI a coarse proxy for yield. Nonetheless, as an approximation of plant productivity (*32*),

NDVI did not show any significant relationship to management intensity or multifunctionality. We also note that some fields achieved high scores across multiple multifunctionality indicators, several of which support plant productivity. This finding suggests that stringent trade-offs need not arise between multifunctionality and yield. Confirming this will require empirical work to verify causal relationships between practices and functions, in which long-term consequences for agronomic and environmental performance are monitored. Ultimately, soil multifunctionality will need to be optimized under local environmental conditions to enhance the sustainability of food production systems. Our results suggest that this might be best achieved not by targeting sustainable intensification but rather productive deintensification.

REFERENCES AND NOTES

1. P. Bescansa, M. J. Imaz, I. Virto, A. Enrique, W. B. Hoogmoed, *Soil Tillage Res.* **87**, 19–27 (2006).
2. A. Balmford *et al*., *Nat. Sustain.* **1**, 477–485 (2018).
3. R. Lal, *Glob. Change Biol.* **24**, 3285–3301 (2018).
4. M. A. Tsiafouli *et al*., *Glob. Change Biol.* **21**, 973–985 (2015).
5. R. E. Creamer, J. M. Barel, G. Bongiorno, M. J. Zwetsloot, *Soil Biol. Biochem.* **166**, 108561 (2022).
6. E. Hoffland, T. W. Kuyper, R. N. J. Comans, R. E. Creamer, *Plant Soil* **455**, 1–22 (2020).
7. J. Lehmann, D. A. Bossio, I. Kögel-Knabner, M. C. Rillig, *Nat. Rev. Earth Environ.* **1**, 544–553 (2020).
8. M. J. Zwetsloot *et al*., *Eur. J. Soil Sci.* **72**, 1640–1654 (2021).
9. Food and Agriculture Organization of the United Nations, *Status of the World's Soil Resources: Main Report* (FAO, 2015).
10. P. Maeder *et al*., *Science* **296**, 1694–1697 (2002).
11. R. A. Wittwer *et al*., *Sci. Adv.* **7**, eabg6995 (2021).
12. V. Tardy *et al*., *Soil Biol. Biochem.* **90**, 204–213 (2015).
13. M. R. Felipe-Lucia *et al*., *Proc. Natl. Acad. Sci. U.S.A.* **117**, 28140–28149 (2020).
14. F. T. de Vries *et al*., *Proc. Natl. Acad. Sci. U.S.A.* **110**, 14296–14301 (2013).
15. X. Yang *et al*., *Nat. Commun.* **15**, 198 (2024).
16. W. Riah *et al*., *Environ. Chem. Lett.* **12**, 257–273 (2014).
17. P. Manning *et al*., *Nat. Ecol. Evol.* **2**, 427–436 (2018).
18. X. Li *et al*., *Agric. Ecosyst. Environ.* **353**, 108539 (2023).
19. J. Li *et al*., *Geoderma* **430**, 116340 (2023).
20. C. Shennan *et al*., *Annu. Rev. Environ. Resour.* **42**, 317–346 (2017).
21. L. Kehoe *et al*., *Divers. Distrib.* **21**, 1308–1318 (2015).
22. J. Sumberg, K. E. Giller, *Glob. Food Secur.* **32**, 100617 (2022).
23. R. Francaviglia, M. Almagro, J. L. Vicente-Vicente, *Soil Syst.* **7**, 17 (2023).
24. L. Schreefel, R. P. O. Schulte, I. J. M. De Boer, A. P. Schrijver, H. H. E. Van Zanten, *Glob. Food Secur.* **26**, 100404 (2020).
25. Skal Biocontrole, "Skal Reglement Certificatie en Toezicht" (2021); https://www.skal.nl/assets/wetgeving-nl/Skal-R11-Reglement-Certificatie-en-Toezicht.pdf.
26. S. Q. van Rijssel *et al*., *Mol. Ecol.* **31**, 4017–4030 (2022).
27. S. Q. van Rijssel *et al*., Nematode and protist responses to conversion from conventional to organic arable farming. SSRN [Preprint] (2024); https://papers.ssrn.com/sol3/papers.cfm?abstract_id=4882625.
28. G. J. Koorneef *et al*., Understanding the effects of organic versus conventional farming on soil organic carbon characteristics– a chronosequence study. SSRN [Preprint] (2024); https://ssrn.com/abstract=4797577.
29. G. J. Koorneef *et al*., *Soil Biol. Biochem.* **196**, 109507 (2024).
30. FAO, *World Reference Base for Soil Resources 2014* (Food and Agriculture Organization of the United Nations, 2015).
31. F. T. Maestre *et al*., *Science* **335**, 214–218 (2012).
32. L. Serrano-Grijalva *et al*., *Glob. Change Biol.* **30**, e17461 (2024).
33. B. S. Griffiths *et al*., *Ecol. Indic.* **69**, 213–223 (2016).
34. B. Karimi *et al*., *Sci. Rep.* **9**, 3812 (2019).
35. L. Armengot *et al*., *Agron. Sustain. Dev.* **31**, 699–707 (2011).
36. G. N. Falconnier *et al*., *Outlook Agric.* **52**, 311–326 (2023).
37. P. Panagos *et al*., *Sci. Total Environ.* **853**, 158706 (2022).
38. M. Delgado-Baquerizo *et al*., *Nat. Commun.* **7**, 10541 (2016).
39. S. Jiao, Y. Lu, G. Wei, *Glob. Change Biol.* **28**, 140–153 (2022).
40. Y. Guo, T. Xu, J. Cheng, G. Wei, Y. Lin, *Sci. Total Environ.* **772**, 145010 (2021).
41. A. S. Grandy, W. R. Wieder, K. Wickings, E. Kyker-Snowman, *Soil Biol. Biochem.* **102**, 40–44 (2016).
42. M. M. Pulleman, W. De Boer, K. E. Giller, T. W. Kuyper, *Outlook Agric.* **51**, 75–90 (2022).
43. E. Morriën *et al*., *Nat. Commun.* **8**, 14349 (2017).
44. A. Jilling *et al*., *Geoderma* **359**, 114001 (2020).
45. S. Q. Van Rijssel *et al*., Dataset for: Conventional and organic farms with more intensive management have lower soil functionality, Version 1.0, Zenodo (2025); https://doi.org/10.5281/zenodo.11650269.

ACKNOWLEDGMENTS

We thank C. Weser and G. Koetsenruijter for helping with sample collection and all the farmers for participating in the study. We thank L. Serrano and R. Ochoa Huesco for providing access to NDVI data. **Funding:** This research was supported by Dutch Research Council grant NWO-Groen ALWGR.2015.5 (W.H.v.d.P., R.N.J.C.). **Author contributions:** Conceptualization: S.Q.v.R., G.J.K., M.M.P., G.F.V., R.G.M.d.G., R.N.J.C., W.H.v.d.P., K.M.-J.; Funding acquisition: R.N.J.C., W.H.v.d.P.; Investigation: S.Q.v.R., G.J.K., W.H.v.d.P., K.M.-J.; Methodology: S.Q.v.R., G.J.K., M.M.P., G.F.V., R.G.M.d.G., R.N.J.C., W.H.v.d.P., K.M.-J.; Project administration: R.N.J.C., W.H.v.d.P.; Supervision: G.F.V., R.G.M.d.G., M.M.P., R.N.J.C., W.H.v.d.P.; Visualization: S.Q.v.R., G.J.K., K.M.-J.; Writing – original draft: S.Q.v.R., G.J.K., G.F..V., R.G.M.d.G., W.H.v.d.P., K.M.-J.; Writing – review & editing: S.Q.v.R., G.J.K., M.M.P., G.F.V., R.G.M.d.G., R.N.J.C., W.H.v.d.P., K.M.-J. **Competing interests:** The authors declare that they have no competing interests. **Data and materials availability:** All data and R code for the analysis is publicly available after manuscript acceptance at Zenodo (*45*). Sequencing data have been submitted to the European Nucleotide Archive (accession no. for 16S and ITS: PRJEB41305; for 18S: PRJEB84927).

SUPPLEMENTARY MATERIALS

science.org/doi/10.1126/science.adr0211
Materials and Methods
Figs. S1 to S7
Tables S1 to S8
References (*46*–*114*)
MDAR Reproducibility Checklist

Submitted 19 June 2024; accepted 13 March 2025
10.1126/science.adr0211

SIGNAL TRANSDUCTION

Bottom-up reconstruction of functional death fold signalosomes reveals a requirement for polymer stability and avidity

Mauriz A. Lichtenstein[1]†, Fakun Cao[1]†, Finn Lobnow[1]†, Paulina Dirvanskyte[1], Daniel Weyhenmeyer[1], Anna Kulesza[1], Elke Ziska[1], Randal Halfmann[2], Marcus J. Taylor[1]*

Protein polymer scaffolds composed of death fold (DF) proteins are critical to the formation of signalosomes in immune signaling. The biophysical properties that these polymeric scaffolds require for signal transduction are not clearly defined. Here, we engineered single-component DF signalosomes. We found that functionality depends on the stability provided by the DF polymer, which could also be achieved with a bacterial DF domain, a synthetic filament-forming domain, and amyloid-like sequences. This demonstrates the importance of polymer stability and inducibility irrespective of the motif's origin. By varying the number of included TRAF6 interaction motifs, we demonstrate that avidity is a tunable property that can control the amplitude of signaling outputs. This work lays out a reductionist framework to elucidate the required signaling properties through polymeric scaffolds by adjusting their assembly kinetics, stability, and avidity.

As cells navigate the informational content of their environment, accurately interpreting extracellular signals and transducing them intracellularly is critical for survival. A recurrent regulatory theme in signal transduction is the compartmentalization of biochemical reactions into multiprotein complexes called signalosomes (*1*–*3*). To understand how cells sense and respond to chemical inputs, we need to understand how signalosomes assemble, recruit, and activate effector proteins. Signalosomes in the innate immune system use molecular scaffolds; after a trigger, protein monomers in solution undergo cooperative assembly into higher-order filaments (*3*–*6*). The polymeric filaments at the core of these signalosomes are composed of death fold (DF) domain superfamily proteins or Toll-interleukin-1 receptor (TIR) domain–containing proteins (*7*, *8*), two ancient protein domains found in both bacteria and eukaryotes (*9*, *10*). The signaling output of these signalosomes is determined by the effector proteins recruited to this scaffold, because the oligomers form concentrated foci of effector binding sites (*11*). Many DF-containing proteins have binding motifs for the E3 ubiquitin ligases of the tumor necrosis factor receptor associated factors (TRAF) family (*12*), and TRAF6 activation serves as a convergence point for

[1]Max Planck Institute for Infection Biology, Berlin, Germany. [2]Stowers Institute for Medical Research, Department of Biochemistry and Molecular Biology, University of Kansas Medical Center, Kansas City, MO, USA.
***Corresponding author. Email: taylor@mpiib-berlin.mpg.de**
†These authors contributed equally to this work.

multiple innate immune signaling scaffolds. TRAF6 mediates lysine 63–linked polyubiquitination, culminating in the activation of IκB kinase (IKK) and inflammatory signaling through the transcription factor nuclear factor κB (NF-κB) (*13*). These unifying structural features may indicate that signaling scaffolds at the core of signalosomes have a common signal transduction mechanism.

If innate immune oligomeric scaffolds have a shared signaling mechanism, then a core set of biophysical properties likely governs their signaling output. However, despite shared mechanistic features, innate immune signaling scaffolds are diverse. Although signalosomes commonly feature open-ended filamentous assemblies, such as in the Rig-1-like receptor complex (*14*) or the caspase recruitment domain-containing protein 11–B cell lymphoma 10–mucosa-associated lymphoid tissue lymphoma translocation protein 1 (CBM) complex (*15*), others feature stoichiometrically defined oligomers, such as in the myddosome. They can also consist of variable combinations of DF- or TIR domain–containing proteins and function from distinct cellular locations (*11*, *16*, *17*). This diversity has made it difficult to define the necessary biophysical properties and the minimal number of components required to assemble a functional scaffold. Over the past decades, detailed mechanisms of signalosome function were determined by mutational or interaction studies. These top-down approaches can characterize the biochemical and cell biological diversity that operates at individual signalosomes. However, to determine how these signalosomes converge on TRAF6 and NF-κB signaling, we need to define unifying design principles spanning all signaling scaffolds. We therefore took a bottom-up approach: building a simplified signaling system that can be used to reconstruct the behavior of signaling scaffolds de novo.

A single chimeric protein can functionally replace a three-component innate immune signalosome

Because protein domains encode functional properties, by rearranging these domains and creating a minimal functioning signaling unit, we can identify which core properties are needed for signalosome function. We aimed to do this by reducing a multiprotein signalosome to its core components by creating chimeric fusion proteins. For our model system, we chose the myddosome, a three-component signalosome composed of MyD88, IRAK4, and IRAK1. Upon Toll-like receptor (TLR) and interleukin 1 receptor (IL-1R) activation, MyD88 is recruited and forms TIR:TIR complexes with the receptor. This leads MyD88 DF domains to oligomerize and assemble with IRAK4/IRAK1 DF domains to form the filamentous myddosome (*18*, *19*). TRAF6 is recruited to the myddosome through TRAF6-binding motifs (T6BMs) in IRAK1 (Fig. 1A), sharing the amino acid sequence PxExxZ (*12*) (where Z is an aromatic or acidic residue). Ultimately, this leads to proinflammatory NF-κB signaling. To create an orthogonal reaction system to test the chimeric proteins, we created a triple-knockout (3xKO) cell line for MyD88, IRAK4, and IRAK1 in EL4 mouse lymphoma cells that also expressed TRAF6 tagged with mScarlet (fig. S1, A and B). The 3xKO cells cannot signal in response to IL-1 stimulation (fig. S1C), so any restoration of IL-1 signaling activation upon expression of chimeric proteins would show reconstitution of a functioning signaling pathway. To determine the unifying design principles spanning all innate immune signaling scaffolds, we designed a system restricted to their common features: the ability to read out information from receptors and the presence of DF domains and T6BMs.

We created three chimeric fusion proteins containing all or some of these features. We fused full-length MyD88 to the C terminus of IRAK1 that contains three T6BMs, creating a single chimeric MyD88 protein (Fig. 1B). We called this system CHARMS (chimeric higher-order assemblies for receptor-mediated signaling). To identify the minimal sufficient scaffold, we created two further chimeric proteins: a construct consisting of the TIR domain of MyD88 fused to the T6BMs of IRAK1 (CHARMS-TIR; Fig. 1C, middle) and a version of chimeric MyD88 with the central glutamic acids of T6BM mutated to alanine (CHARMS-3xA; Fig. 1C, bottom), which abolishes the interaction with TRAF6 (*12*). We expressed CHARMS in 3xKO cells and found that it could qualitatively rescue signaling, restoring the relocation of cytoplasmic RelA to the nucleus upon IL-1 stimulation (Fig. 1C and fig. S1, D and E). Conversely, neither CHARMS-TIR nor CHARMS-3xA could restore RelA translocation (Fig. 1C and fig. S1E). Only CHARMS restored downstream signaling output, as measured by cytokine release (Fig. 1D). Therefore, successful signaling appears to depend on the DF domain and the recruitment of TRAF6. Similar to wild-type (WT) cells, 3xKO cells expressing CHARMS produced phosphorylated IKK and activated mitogen-activated protein kinase signaling in response to IL-1 (fig. S2), although with different signaling kinetics than WT cells. This shows that a single chimeric fusion protein containing just the TIR and DF domains of MyD88 and T6BM of IRAK1 contains the necessary properties required for IL-1 signaling. This system allows us to determine the essential properties required to activate TRAF6 and NF-κB.

Like IL-1Rs, TLRs can signal through myddosomes due to the homotypic interactions of the TIR domains of MyD88 and TLRs (*20*, *21*). We therefore generated bone marrow–derived macrophages from a MyD88-IRAK4 double KO (2xKO) mouse (fig. S3) and reconstituted these cells with CHARMS. The chimeric signalosome restored signaling in the 2xKO cells in response to the triggering of plasma membrane associated TLR4 and two TLRs that signal from intracellular membranes, TLR7 and TLR9 (*22*) (Fig. 1E). With this experiment, we established that our chimeric signalosome retained a key property of myddosomes: the ability to read out different receptors by interacting with TIR domains of both IL-1R and TLRs. This also shows that CHARMS can transduce signals from diverse cellular locations with distinct biochemical environments.

In cells, signalosomes that assemble around oligomeric protein scaffolds form large cytoplasmic puncta that can be detected by fluorescence microscopy (*23*, *24*). To confirm whether our chimeric proteins retain this property, we used total internal reflection fluorescence microscopy (TIRFM) and IL-1 incorporated into supported lipid bilayers (*25*). Upon IL-1 stimulation in a WT background, MyD88 forms puncta, which increase in intensity and stably recruit TRAF6 (movie S1, Fig. 1F, and fig. S4A). We only observed comparable molecular dynamics for green fluorescent protein (GFP)–tagged CHARMS with functional T6BMs (movie S2, Fig. 1G, and fig. S4). Thus, CHARMS can functionally replace the three-component myddosome in living cells. It can also assemble in response to receptor stimulation into large signalosomes that have qualitatively similar properties and signaling output to myddosomes. We conclude that CHARMS has the required biophysical properties to activate TRAF6, NF-κB, and downstream transcriptional responses.

Reconstruction of functional CHARMS signalosomes from diverse filament-forming domains

We hypothesize that CHARMS requires at least two properties for its signaling function: oligomerization into a scaffold and recruitment of an effector. Both of these properties must be controlled by receptor activation (*6*). The MyD88 TIR and DF domains can both form filamentous polymers (*19*, *26*, *27*) (Fig. 2A), suggesting a degree of functional overlap in their ability to create an oligomeric scaffold. However, given that the DF polymer is required for signal transduction (*18*, *28*) (Fig. 1, C and D, and fig. S5), it remains unclear what role the DF plays in a functional signalosome that cannot be fulfilled by the TIR domain. We therefore examined the ability of CHARMS-TIR to recruit TRAF6 in live cells using TIRFM. CHARMS-TIR assembled into cell surface puncta in response to IL-1 stimulation but recruited TRAF6 only transiently (Fig. 2, B and C, and movie S3). Thus, the DF domain appears to be required for stable recruitment of TRAF6 to the signalosome scaffold.

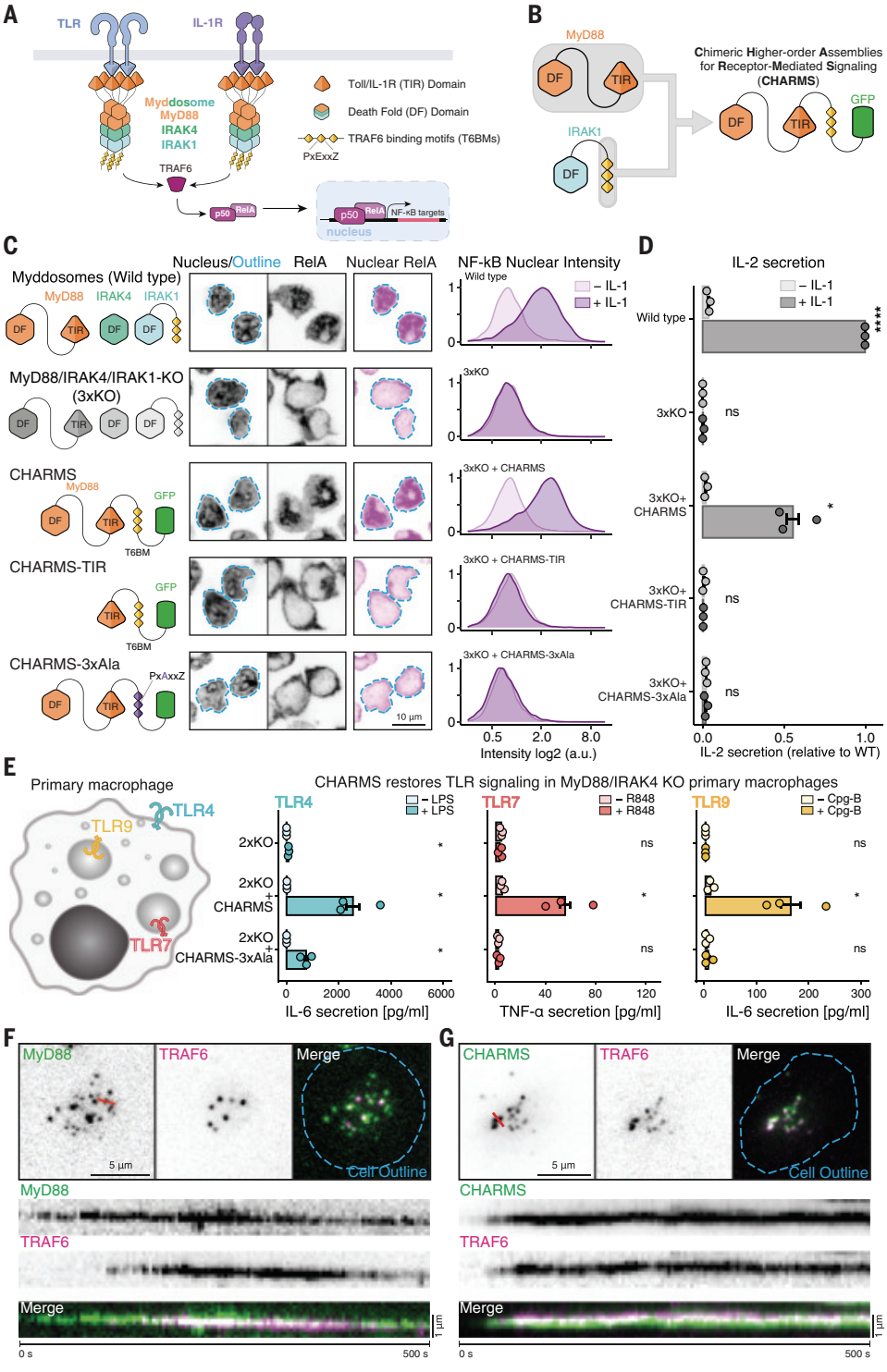

Fig. 1. Single-component CHARMS has behavior and signaling output similar to that of a three-component innate immune signalosome. (**A**) The myddosome is a three-component signalosome that assembles and transduces signals in response to TLR and IL-1R stimulation. Critical to myddosome functionality are the TIR domain, DF domain, and T6BMs. The formation of this signalosome leads to the recruitment and activation of TRAF6, resulting in NF-κB (p50/RelA) translocation to the nucleus. (**B**) We created CHARMS, a fusion protein combining MyD88 and the IRAK1 C terminus with 3xT6BMs (PxExxZ), to study innate immune signalosome design principles. (**C**) Restoration of NF-κB activation in response to IL-1 in 3xKO cells expressing CHARMS. Left, schematic diagram of the different CHARMS variants tested. Middle, confocal micrographs showing the localization of RelA after IL-1 stimulation. Dashed cyan outline superimposed on the Hoechst images shows a segmented nuclear outline used to measure RelA nuclear staining (third column). Scale bar, 10 μm. Right, quantification of the RelA nucleus intensity in unstimulated and IL-1–stimulated cells. Distributions of RelA nuclear intensity composed of measurements taken from 1138 to 7789 cells. (**D**) Restoration of cytokine release in response to IL-1 stimulation in 3xKO cells expressing CHARMS. We used the enzyme-linked immunosorbent assay (ELISA) to measure IL-2 release in WT and 3xKO cells expressing CHARMS variants. IL-2 release was normalized to that of stimulated WT cells and baseline corrected using unstimulated 3xKO ($n = 3$ independent replicates measured per cell line). (**E**) Reconstitution of CHARMS in primary macrophages derived from MyD88$^{-/-}$, IRAK4$^{-/-}$ (2xKO) mice restores TLR signaling from the plasma membrane and intracellular membranes. Schematic diagram depicts primary macrophages with the subcellular localization of the TLRs tested. Plots show IL-6 or tumor necrosis factor α (TNF-α) release after stimulation with TLR4, TLR7, or TLR9 agonists ($n = 3$ independent replicates measured per cell line). TLR4 was stimulated with 100 ng/ml lipopolysaccharide for 4 hours, and TLR9 was stimulated with 1 μM Cpg-B (ODN1668) for 6 hours to measure IL-6 secretion. TLR7 was stimulated with 50 ng/ml Resiquimod (R848) for 8 hours to measure TNF-α secretion. (**F** and **G**) IL-1–triggered assembly of CHARMS into plasma membrane–associated puncta that recruit TRAF6. TIRF images show the recruitment of mScarlet-TRAF6 to WT myddosomes (right) and CHARMS assemblies in cells undergoing IL-1 stimulation. Scale bar, 5 μm. Kymograph analysis shows an example of myddosome formation (left) and CHARMS assembly (right) that recruit TRAF6. Kymograph was taken from the red line overlying the MyD88 and CHARMS images. Scale bar, 1 μm. *$P < 0.05$, ****$P < 0.0001$. Bars represent mean ± SEM. Statistical significance was determined using an unpaired t test.

If the DF domain encodes a discrete biochemical property required for signaling, then we would expect that it would be similar in distantly related members of the DF superfamily. We chose a bacterial DF homolog, referred to as the bacterial death fold (bDF) domain, which, based on AlphaFold predictions, forms helical filaments similar to the DF domain of MyD88 (*19*) (Fig. 2, A and D, and fig. S6A and B). CHARMS-bDF formed puncta that recruited TRAF6 for extended periods of time (Fig. 2D and movie S4). Thus, a bacterial homolog of the DF contains the requisite properties for scaffold formation that allows it to be functionally interchangeable with a mammalian DF,

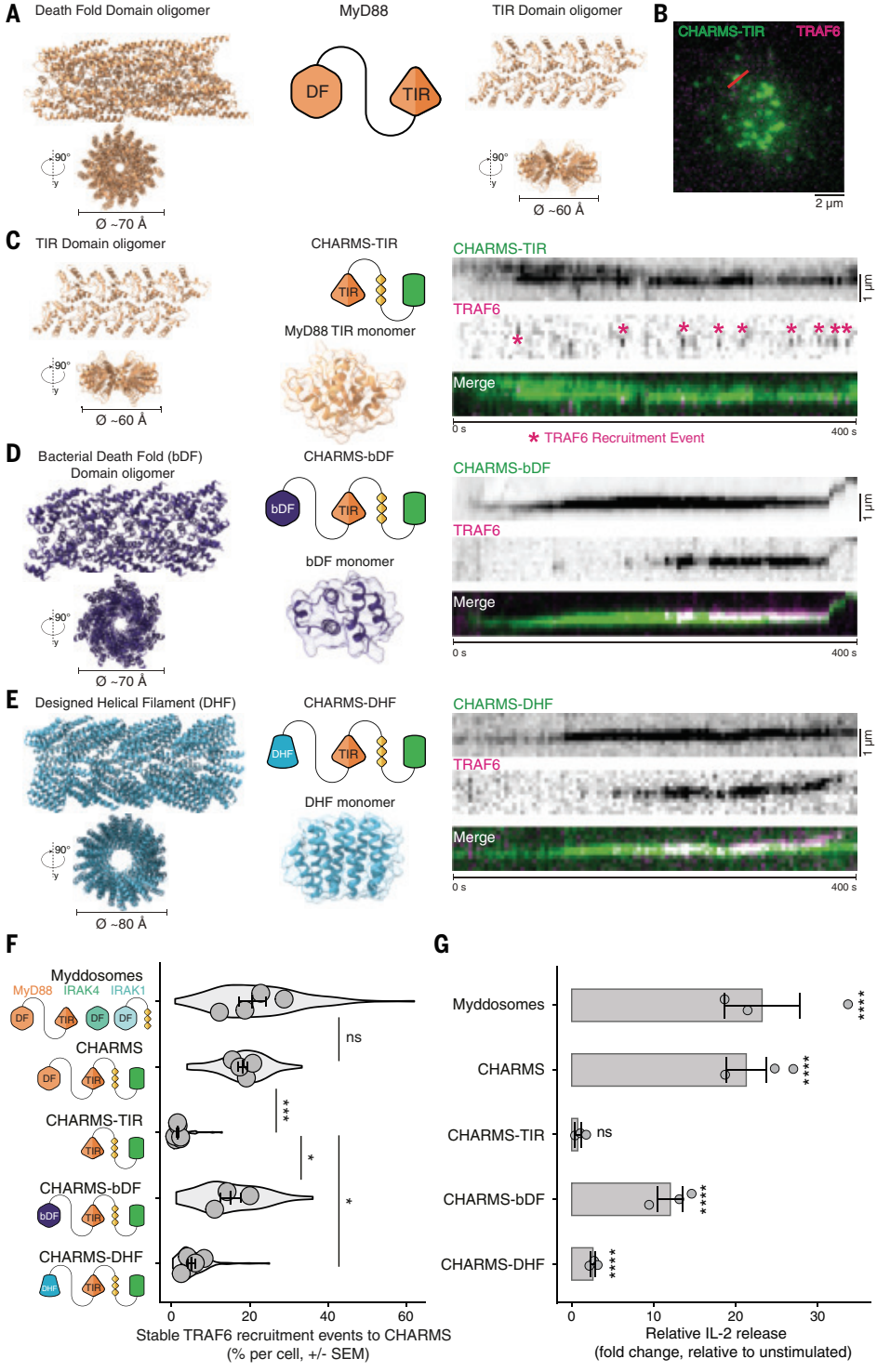

Fig. 2. Functional replacement of the DF domain by distantly related bacterial homologs or synthetic filament-forming domains. (**A**) MyD88 is composed of two domains that can form filamentous polymers: the death domain and the TIR domain. Shown are the solved helical filament MyD88-DF domain structure (PDB: 6I3N) and the AF2-predicted filament of MyD88 TIR domains. (**B** to **E**) TIRF microscopy was used to analyze TRAF6 recruitment to CHARMS variants reconstituted in live cells. Shown is a TIRF image of the merged CHARMS-TIR and mScarlet-TRAF6 channels, the red line overlay corresponds to where the kymograph in (C) was taken. Scale bar in (B), 2 µm. (C) CHARMS-TIR, which is solely composed of the MyD88-TIR domain fused to T6BMs, only transiently recruits TRAF6. Left, AF2 prediction of the individual domain and two views of the predicted filamentous polymer [same structure as in (A)]. Right, kymograph analysis showing transient mScarlet-TRAF6 recruitments to CHARMS-TIR signalosomes in 3xKO cells. Magenta asterisks on TRAF6 kymographs highlight TRAF6 recruitment events. Kymographs derived from red line–overlaid TIRF images in (B). Scale bar, 1 µm. (D) CHARMS-bDF, a construct containing a bDF domain homolog from *Nostoc* sp. 106C (NCBI WP_339376820.1), restored stable TRAF6 recruitment. Left, AF2 prediction of the individual domain and two views of the predicted filamentous polymer. Right, kymograph analysis shows stable mScarlet-TRAF6 recruitment to CHARMS-bDF signalosomes in 3xKO cells. Scale bar, 1 µm. (E) CHARMS-DHF, a construct containing a synthetic filament-forming domain [(*29*) PDB: 6E9X], restored stable TRAF6 recruitment. Left, structure view of the individual DHF domain and two views of the filamentous polymer. Right, kymograph analysis shows stable mScarlet-TRAF6 recruitment to CHARMS-DHF signalosomes in 3xKO cells. Scale bar, 1 µm. (**F**) Quantification of stable TRAF6 recruitment events (≥40 s) to CHARMS signalosomes. Shown is the percentage of total TRAF6 recruitment events that were stable per cell. Violin plots show the distribution of stable TRAF6 recruitment events per individual cell across replicates. Mean percentages of stable TRAF6 ± SEM were 20.6 ± 3.5%, 18.2 ± 1.1%, 1.6 ± 0.2%, 15.1 ± 2.6%, and 5.0 ± 1.0% for WT, CHARMS, CHARMS-TIR, CHARMS-bDF, and CHARMS-DHF respectively. Data points superimposed on the violin plots show the mean of individual experimental replicates (n = 4, 4, 6, 3, and 5 independent experimental replicates for cells expressing myddosomes, CHARMS, CHARMS-TIR, CHARMS-bDF, and CHARMS-DHF, respectively). (**G**) Reconstitution of CHARMS-bDF and CHARMS-DHF restored IL-2 release in 3xKO cells in response to IL-1 stimulation. Enzyme-linked immunosorbent assay (ELISA) measurements of IL-2 release in EL4-MyD88-GFP/mScarlet-TRAF6 cells expressing all myddosome components (referred to as WT in the figure) and 3xKO cells expressing CHARMS variants. The IL-2 release is shown as a fold change in the amount of IL-2 released in IL-1–stimulated cells compared with that released from control unstimulated cells. WT, CHARMS, and CHARMS-TIR ELISA data are the same as presented in Fig. 1C and are shown here for comparison with CHARMS-bDF and CHARMS-DHF. Bars represent mean ± SEM (n = 3 independent experimental replicates). *P < 0.05, ***P < 0.001, and ****P < 0.0001. Statistical significance was determined using unpaired t test.

suggesting a wider conservation across this ancient superfamily.

If the propensity to form helical polymers is conserved within members of the DF superfamily that assemble signalosomes (*7*), then this structural feature may underpin the domain's functionality. Therefore, unrelated protein domains that form qualitatively similar helical structures in response to a stimulus should be able to functionally replace the DF domain. To test this, we replaced the DF domain with an in silico–designed helical filament (DHF) (*29*). CHARMS-DHF restored stable TRAF6 recruitment in response to IL-1 stimulation (Fig. 2E and movie S5). Direct comparison of all constructs showed that introducing a filament-forming domain increased the percentage of long-lived (≥40 s) recruitment events compared with that observed in the presence of CHARMS-TIR (Fig. 2F and fig. S6, C and D). Such partial restoration of long-lived TRAF6 recruitment corresponded to partial restoration of cytokine release in response to IL-1 (Fig. 2G and fig. S6E). Together, these results show that CHARMS composed of diverse filament-forming oligomers contributes to stable TRAF6 recruitment and signal transduction. Therefore filament-forming oligomers must contain part of the requisite biophysical properties required for designing a functional signalosome.

Stability is an emergent property of polymeric scaffolds and is a requirement for signal transduction

Although the TIR domain can form oligomeric assemblies in response to IL-1, these are not sufficient to recruit TRAF6 and transduce signaling (Fig. 1, C and D, and Fig. 2, C and F). Therefore, the DF, bDF, and DHF filament-forming domains must share another property that emerges from their capacity to oligomerize and allow prolonged TRAF6 recruitment with downstream signaling. One shared property of the DHF and many structurally characterized DFs is high polymer stability (*29*, *30*). If oligomer stability is a property provided solely by the DF and is essential for signal transduction, then we would expect it to be absent from the nonfunctional CHARMS-TIR. We therefore used fluorescence recovery after photobleaching (FRAP) to compare protein turnover within these assemblies. CHARMS, CHARMS-bDF, and CHARMS-DHF formed stable assemblies with no monomer turnover; by contrast, CHARMS-TIR had monomer turnover (Fig. 3, A to E). We conclude that, alongside oligomerization and effector recruitment, an additional property required for signalosome functionality is polymer stability.

Although a single TIR domain could not create a stable scaffold, stability can be enhanced by increasing the valency of interactions. Therefore, we created a CHARMS consisting of a tandem dimer of TIR domains (CHARMS-2xTIR; fig. S7). CHARMS-2xTIR could form puncta that display high stability (fig. S7, A and B) and stably recruit TRAF6 (fig. S7C). We conclude that by enhancing oligomer stability, a nonfunctional CHARMS can be converted into a functional signalosome. However, this CHARMS variant is no longer under receptor control and is constitutively active (fig. S7D).

It has been proposed that DF polymers mimic the static higher-order structures of amyloid filaments (*30*), and amyloids can functionally replace a DF in a receptor-activated cell death pathway (*31*). To determine whether DFs and amyloids are functionally interchangeable because of their ability to form stable polymers, we used a synthetic sequence consisting of varying numbers of threonine-alanine (TA) dipeptide repeats (Fig. 3F and fig. S8A). This motif assembles into amyloid-like filaments with a stability that increases with repeat number across the range of 10 to 20 (*32*, *33*), allowing us to test how the emergence of polymer stability relates to signaling. We found that increasing the number of TA repeats leads to a loss of FRAP recovery (Fig. 3, H to J). In parallel, this also increases TRAF6 recruitment and signaling output upon receptor stimulation (Fig. 3G; fig. S8, B to D; and movies S6 and S7), suggesting that polymer stability is intrinsically linked to signalosome functionality. We conclude that the individual domains of proteins that multimerize into functional scaffolds that activate TRAF6 and NF-kB are interchangeable as long as they together have a set of emergent properties. These properties of oligomerization, high stability, and effector recruiting function must be controlled by receptor activation.

Signaling output can be titrated by changing the number of effector recruiting motifs

Given that signaling output is a tunable response across many signaling systems (*34*), we investigated which properties could achieve this. One property that could control signaling output is the density of T6BMs on the CHARMS scaffolds. The number of T6BMs varies in signaling effectors; for example, IRAK1, IRAK2, and IRAK3 each have three, two, and one T6BMs, respectively (*12*). Because TRAF6 multimerization is required for further signal transduction (*35*), the number of T6BMs potentially controls the cooperative oligomerization and size of TRAF6 multimers. Thus, depending on the number of T6BMs, signalosomes might have different recruitment kinetics, thereby affecting how inputs are amplified. Our designed CHARMS monomers had three effector binding sites (Figs. 1C and 2). We tested whether the signaling output could be modulated by lowering or increasing the T6BM multiplicity on the monomer (Fig. 4A). At the molecular level, the probability of TRAF6 recruitment increased with CHARMS signalosome size (fig. S9). Therefore, by changing the TRAF6 recruitment kinetics, we might change how signalosomes transduce the input from the receptor into a downstream response (Fig. 4A). To test this, we created a synthetic TRAF6 effector recruiting domain containing one, three, or five T6BMs (Fig. 4B and fig. S10). All of these constructs form puncta and recruit TRAF6 (Fig. 4B and movie S8); however, the TRAF6 recruitment to the CHARMS is modulated by the multiplicity of T6BMs. Increased the multiplicity of binding motifs results in the formation of larger TRAF6 multimers associated with the CHARMS scaffold (Fig. 4C and fig. S11, A and B) and also increases the stability of TRAF6 recruitment (Fig. 4D and fig. S11, C and D). In addition, the efficiency and kinetics of TRAF6 recruitment are directly modulated by the multiplicity of binding motifs (Fig. 4E and fig. S11, A, B, and E to G). Finally, increasing the multiplicity of T6BMS elevates cytokine secretion (Fig. 4F and fig. S12, A to C). Adding more T6BMs enhances signaling output in other CHARMS variants, but cannot restore function to inactive variants (fig. S12, D to F). Thus, signaling output can be amplified by increasing the number of effector binding motifs on the scaffolds.

Discussion

A major goal of biology is to understand how functional biological systems are assembled from their chemical constituents. Our results help to reveal fundamental features of innate immune signalosomes. We engineered a chimeric fusion of MyD88 with T6BMs, referred to as CHARMS, and discovered that this single protein fusion could functionally replace the three-component myddosome (Fig. 1). The DF domain of CHARMS is critical to signal transduction but can be functionally replaced by distant bacterial DF homologs or even synthetic sequences that form either amyloid or non-amyloid filaments (Figs. 2 and 3). We defined two key parameters for functionality. First, CHARMS require a high kinetic stability to recruit TRAF6 assemblies capable of transducing downstream signals (Fig. 3). Second, the local density of T6BMs within CHARMS controls the properties of TRAF6 recruitment and presents a way to influence downstream signaling output (Fig. 4). Like many innate immune signalosomes, CHARMS is composed of a DF oligomer and transduces signals through TRAF6 to the NF-κB pathway (*11*). Therefore, the biophysical and biochemical parameters that we identified as being critical to CHARMS function may operate across a range of innate immune signaling cascades.

We showed that a bacterial DF domain can transduce information in a mammalian innate immune signaling pathway. This supports the idea that DF proteins have the requisite

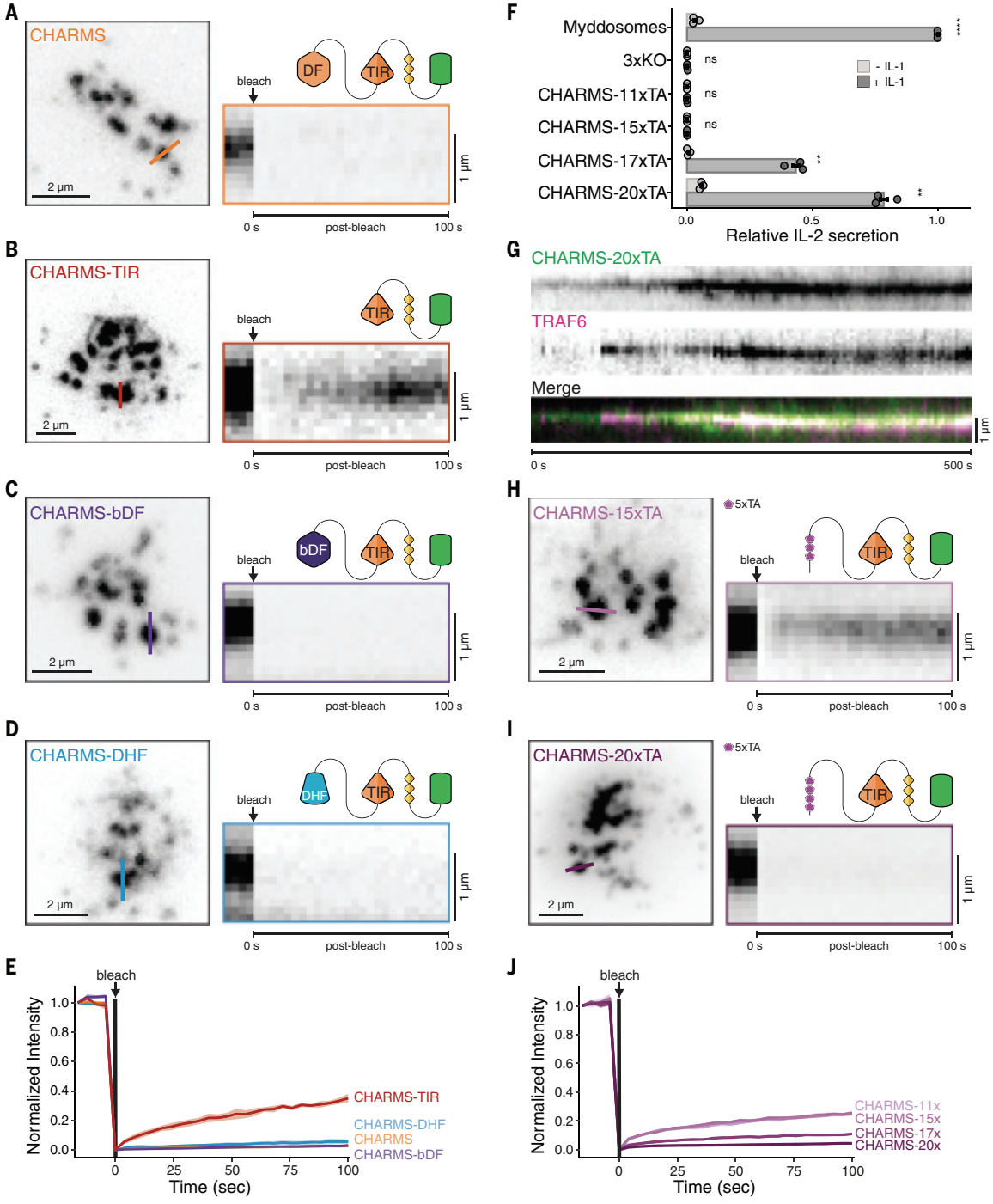

Fig. 3. DF domains or synthetic filaments provide high stability that is associated with functional CHARMS signalosomes. (**A** to **D**) FRAP analysis of CHARMS variants. Left, TIRF images of the CHARMS signalosomes before photobleaching. The orange line on the TIRF images denotes the CHARMS assembly subjected to photobleaching. Scale bars, 2 µm. Right, kymograph analysis of the photobleached region. Kymographs derived from colored lines overlying the TIRF images (left panel). Scale bars, 1 µm. (**E**) Quantification of the FRAP data showing recovery of CHARMS-TIR but not of other constructs. Lines represent the mean, and the shaded area corresponds to ±SEM. Means were calculated from three independent replicates with nine or more regions of interest photobleached per replicate. (**F**) ELISA measuring IL-2 release in WT and 3xKO cells expressing CHARMS-Poly xTA variants. IL-2 release was normalized to that of stimulated WT cells and baseline corrected using unstimulated 3xKO cells. Bars represent mean ± SEM ($n = 3$ independent experimental replicates measured per cell line). (**G**) Kymograph analysis showing stable mScarlet-TRAF6 recruitment to CHARMS-20xTA signalosomes in 3xKO cells. Scale bar, 1 µm. (**H** and **I**) FRAP analysis of CHARMS-Poly xTA variants. Left, TIRF images of the CHARMS signalosomes before photobleaching. The orange line on the TIRF images denotes the CHARMS assembly subjected to photobleaching. Scale bars, 2 µm. Right, kymograph analysis of the photobleached region. Kymographs derived from colored lines overlying the TIRF images (left panel). Scale bars, 1 µm. (**J**) Quantification of the FRAP data showing that recovery decreases as the length of the Poly xTA repeat increases. Lines represent the mean of experimental replicates, and the shaded area corresponds to ± SEM. Measurements were taken from three independent replicates with ≥16 regions of interest photobleached per replicate. $^{**}P < 0.01$, $^{***}P < 0.001$, and $^{****}P < 0.0001$. Statistical significance was determined using an unpaired t test.

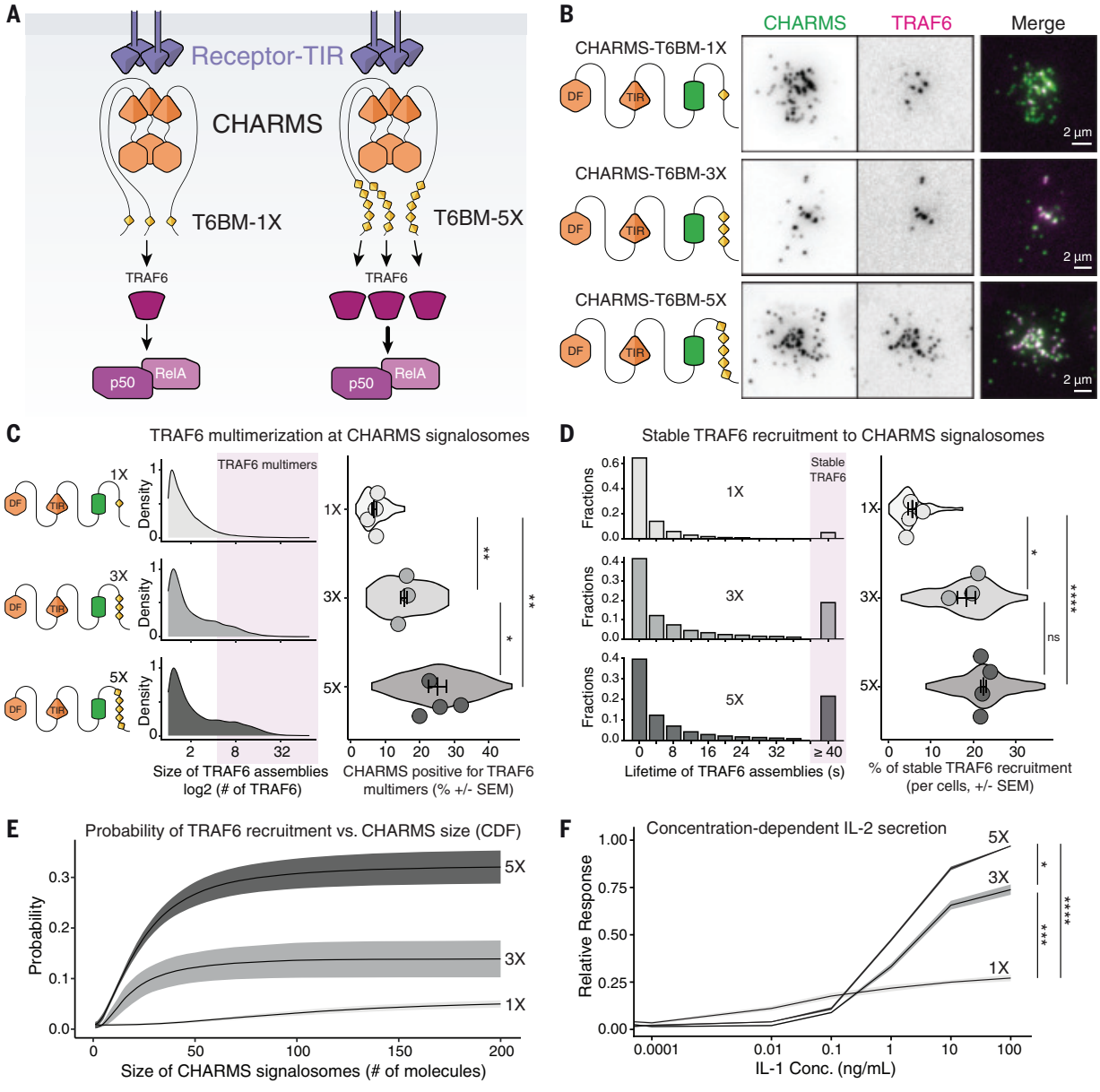

Fig. 4. The avidity of binding sites to TRAF6 is tunable and can modulate signalosome properties and signaling output. (**A**) CHARMS connect to TRAF6 through T6BMs, and this connection is required for TRAF6 activation and NF-κB signaling. We propose that varying the number and density of T6BMs on CHARMS scaffolds could change how the signalosome converts and amplifies the input from the receptor into a downstream response. (**B**) We designed CHARMS with one, three, and five T6BMs (PxExxZ): CHARMS-1x (top), CHARMS-3x (middle), and CHARMS-5x (bottom), and reconstituted them into 3xKO cells. TIRF imaging confirmed that all three CHARMS variants could recruit TRAF6. Scale bars, 2 μm. (**C**) Greater multiplicity of T6BMs increases the size of TRAF6 assemblies associated with CHARMS. Left, schematic diagram of CHARMS with one, three, and five T6BMs. Middle, density plot of the number of TRAF6 assemblies on CHARMS. Light magenta shaded area represents TRAF6 assemblies designated TRAF6 multimers (≥4.5 TRAF6 molecules). Right, quantification of the percentage of CHARMS signalosomes associated with TRAF6 multimers. Violin plots show the distribution of individual cell measurements. Colored dots superimposed on violin plots correspond to the average value per cell across independent experimental replicates. Quantifications are from n = 3 to 4 replicates with 13 to 37 cells measured per replicate. (**D**) Multiplicity of T6BMs enhances the stability of TRAF6 at CHARMS signalosomes. Left, histograms show the lifetime distribution of TRAF6 recruitment to CHARMS signalosomes. Light magenta shaded area is the sum of all events with a lifetime >40 s, which represents stable TRAF6 association with CHARMS. Right, quantification of the percentage of long-lived (≥40 s) recruitment out of all TRAF6 recruitment events. Violin plots show the distribution of individual cell measurements. Colored dots superimposed on violin plots correspond to the average value per cell across independent experimental replicates. Quantifications are from n = 3 to 4 replicates with 13 to 37 cells measured per replicate. Bars in (C) and (D) represent mean ± SEM. (**E**) The multiplicity of T6BMs enhances the probability of TRAF6 recruitment. Cumulative distribution function (CDF) showing the probability of TRAF6 recruitment versus the size of CHARMS signalosomes. (**F**) The multiplicity of the T6BMs on CHARMS changes cytokine release. ELISA was used to measure IL-2 release to an IL-1 stimulation dose response. Grayscale lines show the mean of three independent experimental replicates, and shaded areas correspond to ± SEM. *P < 0.05, **P < 0.01, ***P < 0.001, and ****P < 0.0001. Statistical significance was determined using unpaired t test [(C) and (D)] and one-way ANOVA with Tukey's correction (E).

properties for accurate and inducible signaling, a key requirement for immune signaling, which must detect and respond to threats to cell viability. This possibly explains the frequency of DF domains in innate immune signalosomes (*36*, *37*) and the discovery of bacterial DFs in putative phage defense systems (*10*). The requirement for a stable scaffold to activate TRAF6 could explain why receptor tyrosine kinases (RTKs), G protein–coupled receptors, and T and B cell receptors activate NF-κB signaling through DF-containing signaling adaptors (*38*). Although the tyrosine kinase signaling networks in RTKs and T and B cell receptors can form signalosomes with liquid-like properties and appreciable molecular turnover (*39*, *40*), the static nature of some DF polymers might be crucial for anchoring TRAF6 to these dynamic signalosomes, thereby facilitating NF-κB activation. In future studies, the CHARMS system could be adapted to investigate how these signaling pathways, composed of signalosomes with different physical properties, are functionally linked.

We found that synthetic proteins that assemble into qualitatively similar helical filaments can assemble functional signalosome as well. This is possibly attributed to the similar helical oligomer structure, in which internal subunits, by virtue of having multiple buried interfaces, have lower off-rates and disassembly can only proceed from the ends (*7*, *19*, *29*). Although the MyD88 TIR domain also forms filaments (*26*, *27*), these assemblies are unstable and insufficient to support signal transduction. By contrast, an amyloid sequence that can form stable polymers is able to functionally rescue a DF and assemble a scaffold that can activate TRAF6 (Fig. 3). These findings suggest that it is the emergent property of polymer stability, rather than helical assemblies per se, that determines functionality within a signaling scaffold. Our finding that this property requires receptor activation is consistent with models showing that innate immune signaling scaffolds use cooperative assembly and "seeded" nucleation to create metastable systems primed for activation (*3*, *5*, *6*, *30*).

One implication of our results is the likelihood that unrelated protein folds might have acquired equivalent properties to amyloid and DF domains through convergent evolution. If so, then the assembly of oligomeric scaffolds may represent a more widespread mechanism in biology than currently recognized, serving as a fundamental strategy for signal transduction. This work raises the possibility that these properties could be created synthetically, opening up the ability to construct synthetic or orthogonal signalosomes.

We have shown here that it is possible to control the signaling output of a signalosome by varying the multiplicity of effector binding sites (Fig. 4). It has been proposed that DF oligomers function as high-avidity scaffolds that concentrate signaling effectors, thereby compartmentalizing them within a signalosome (*7*, *11*). Our results support this model and also demonstrate that avidity is tunable and can influence the conversion and amplification of an input into a downstream output. We found that avidity changed the degree to which a given input is amplified, which might explain why the number of T6BMs varies across different signaling effectors (*12*).

REFERENCES AND NOTES

1. G. Werlen, E. Palmer, *Curr. Opin. Immunol.* **14**, 299–305 (2002).
2. M. Bienz, *Trends Biochem. Sci.* **39**, 487–495 (2014).
3. H. Wu, *Cell* **153**, 287–292 (2013).
4. P. R. Vajjhala, T. Ve, A. Bentham, K. J. Stacey, B. Kobe, *Mol. Immunol.* **86**, 23–37 (2017).
5. J. D. Nanson, M. H. Rahaman, T. Ve, B. Kobe, *Semin. Cell Dev. Biol.* **99**, 96–114 (2020).
6. A. Rodríguez Gama, T. Miller, R. Halfmann, *Biophys. J.* **120**, 1150–1160 (2021).
7. R. Ferrao, H. Wu, *Curr. Opin. Struct. Biol.* **22**, 241–247 (2012).
8. S. Nimma, T. Ve, S. J. Williams, B. Kobe, *Curr. Opin. Struct. Biol.* **43**, 122–130 (2017).
9. S. Li, M. K. Manik, Y. Shi, B. Kobe, T. Ve, *Curr. Opin. Microbiol.* **74**, 102316 (2023).
10. G. Kaur, L. M. Iyer, A. M. Burroughs, L. Aravind, *eLife* **10**, e70394 (2021).
11. J. C. Kagan, V. G. Magupalli, H. Wu, *Nat. Rev. Immunol.* **14**, 821–826 (2014).
12. H. Ye *et al*., *Nature* **418**, 443–447 (2002).
13. L. Deng *et al*., *Cell* **103**, 351–361 (2000).
14. F. Hou *et al*., *Cell* **146**, 448–461 (2011).
15. Q. Qiao *et al*., *Mol. Cell* **51**, 766–779 (2013).
16. N. J. Gay, M. F. Symmons, M. Gangloff, C. E. Bryant, *Nat. Rev. Immunol.* **14**, 546–558 (2014).
17. C. Odendall, J. C. Kagan, *Microbes Infect.* **19**, 229–237 (2017).
18. S.-C. Lin, Y.-C. Lo, H. Wu, *Nature* **465**, 885–890 (2010).
19. M. C. Moncrieffe *et al*., *Structure* **28**, 281–289.e3 (2020).
20. R. Ferrao, J. Li, E. Bergamin, H. Wu, *Sci. Signal.* **5**, re3 (2012).
21. K. A. Fitzgerald, J. C. Kagan, *Cell* **180**, 1044–1066 (2020).
22. G. M. Barton, J. C. Kagan, *Nat. Rev. Immunol.* **9**, 535–542 (2009).
23. S. L. Latty *et al*., *eLife* **7**, e31377 (2018).
24. A. Rodriguez Gama, T. Miller, J. J. Lange, J. R. Unruh, R. Halfmann, *eLife* **11**, e79826 (2022).
25. R. Deliz-Aguirre *et al*., *J. Cell Biol.* **220**, e202012071 (2021).
26. M. T. B. Clabbers *et al*., *Nat. Commun.* **12**, 2578 (2021).
27. T. Ve *et al*., *Nat. Struct. Mol. Biol.* **24**, 743–751 (2017).
28. J. George *et al*., *J. Biol. Chem.* **286**, 1341–1353 (2011).
29. H. Shen *et al*., *Science* **362**, 705–709 (2018).
30. H. Wu, M. Fuxreiter, *Cell* **165**, 1055–1066 (2016).
31. X. Cai *et al*., *Cell* **156**, 1207–1222 (2014).
32. W. D. Chang, M.-J. Yoon, K. H. Yeo, Y.-J. Choe, *Mol. Cell* **84**, 4334–4349.e7 (2024).
33. H. Kimbrough, J. Jensen, T. Miller, J. J. Lange, R. Halfmann, A tunable affinity fusion tag for protein self-assembly. bioRxiv 633037 [Preprint] (2025); https://doi.org/10.1101/2025.01.14.633037.
34. J. E. Purvis, G. Lahav, *Cell* **152**, 945–956 (2013).
35. Q. Yin *et al*., *Nat. Struct. Mol. Biol.* **16**, 658–666 (2009).
36. H. H. Park *et al*., *Annu. Rev. Immunol.* **25**, 561–586 (2007).
37. J. D. Nanson, B. Kobe, T. Ve, *J. Leukoc. Biol.* **105**, 363–375 (2019).
38. C. Jiang, X. Lin, *Immunol. Rev.* **246**, 141–153 (2012).
39. X. Su *et al*., *Science* **352**, 595–599 (2016).
40. C.-C. Lin *et al*., *Mol. Cell* **82**, 1089–1106.e12 (2022).
41. Data for: M. A. Lichtenstein *et al*., Bottom-up reconstruction of functional death fold signalosomes reveals a requirement for polymer stability and avidity, Zenodo (2025); https://doi.org/10.5281/zenodo.11183886.
42. Data for: M. A. Lichtenstein *et al*., Bottom-up reconstruction of functional death fold signalosomes reveals a requirement for polymer stability and avidity, Zenodo (2025); https://doi.org/10.5281/zenodo.11656330.
43. Data for: M. A. Lichtenstein *et al*., Bottom-up reconstruction of functional death fold signalosomes reveals a requirement for polymer stability and avidity, Zenodo (2025); https://doi.org/10.5281/zenodo.13772517.
44. Data for: M. A. Lichtenstein *et al*., Bottom-up reconstruction of functional death fold signalosomes reveals a requirement for polymer stability and avidity, Zenodo (2025); https://doi.org/10.5281/zenodo.13865553.
45. Data for: M. A. Lichtenstein *et al*., Bottom-up reconstruction of functional death fold signalosomes reveals a requirement for polymer stability and avidity, Zenodo (2025); https://doi.org/10.5281/zenodo.14615509.
46. Data for: M. A. Lichtenstein *et al*., Bottom-up reconstruction of functional death fold signalosomes reveals a requirement for polymer stability and avidity, Zenodo (2025); https://doi.org/10.5281/zenodo.14615999.
47. Data for: M. A. Lichtenstein *et al*., Bottom-up reconstruction of functional death fold signalosomes reveals a requirement for polymer stability and avidity, Zenodo (2025); https://doi.org/10.5281/zenodo.14616190.

ACKNOWLEDGMENTS

We thank the Advanced Medical Bioimaging Core Facility, Charité Universitätsmedizin Berlin, for help with FRAP data acquisition and spinning disk confocal microscopy; U. Klemm, M. Primke, D. Groine, and B. Raupach for assistance with breeding transgenic mouse lines; A. Zychlinsky for providing the MyD88 KO mouse line; O. Majer for advice on working with primary mouse macrophages; R. Patnala and A. Fabritius for advice on figure design and scientific illustrations; L. Fritz-Laylin for comments on figure design; S. Reber and D. Simpson for critical reading of the manuscript; I. Patten for assistance in preparing the manuscript; and K. Lattig for genotyping of transgenic mice and ELISA assays. **Funding:** This work was supported by the Max Planck Society (M.J.T.), the Deutsche Forschungsgemeinschaft (project 499533619 to M.J.T.), and the National Institute of General Medical Sciences of the National Institutes of Health (R01GM130927 to R.H.). **Author contributions:** M.J.T. conceived and supervised the study and designed and cloned the initial CHARMS constructs. E.Z. characterized the 3xKO cell lines and performed experiments in bone marrow progenitor cells from 2xKO mice with CHARMS, ELISA assays of TLR signaling in primary macrophages, and initial characterization of CHARMS in 3xKO cells. M.A.L. characterized the gene-edited 3xKO cell line expressing mScarlet-TRAF6, reconstituted and engineered 3xKO cells expressing CHARMS, designed CHARMS variants, and performed ELISA, FRAP, and microscopy analysis of CHARMS-expressing cells. F.L. performed in silico structural analysis of bacterial death domain homologs and conducted ELISA and microscopy analysis with CHARMS-bDF. F.C. performed RelA staining and confocal microscopy analysis of RelA nuclear localization, conducted FRAP analysis of CHARMS, and performed microscopy analysis of CHARMS variants. P.D. isolated 2xKO bone marrow progenitor cells, performed transient immortalization, and collected FRAP and microscopy data. A.K. performed IL-1 dose responses to compare CHARMS with different multiplicities of T6BMs. M.A.L., F.C., F.L., and P.D. analyzed and visualized the data. R.H. conceived the synthetic amyloid experiments. F.C., F.L., and D.W. characterized and analyzed the CHARMS poly xTA contructs. M.J.T., R.H., M.A.L., F.C., F.L., E.Z., and P.D. wrote the manuscript. **Competing interests:** M.J.T. has research projects sponsored by Kymera Therapeutics that are unrelated to the subject matter of this manuscript. Kymera Therapeutics had no involvement in this study. The authors declare no competing interests. **Data and materials availability:** All data are available in the main manuscript or the supplementary materials. All cell lines and plasmids are available upon request. Original code to analyze the data are publicly available at https://github.com/MJ-Taylor-Lab/Analysis-CHARMS. Primary data are publicly available at Zenodo (*41*–*47*).

SUPPLEMENTARY MATERIALS

Submitted 13 May 2024; accepted 14 March 2025
10.1126/science.adq3234

ZEOLITES

Aluminum distribution and active site locations in the structures of zeolite ZSM-5 catalysts

Przemyslaw Rzepka[1,2,3]*, Thomas Huthwelker[4], Jiri Dedecek[1], Edyta Tabor[1], Milan Bernauer[1,5], Stepan Sklenak[1], Kinga Mlekodaj[1]*, Jeroen A. van Bokhoven[2,3]*

Zeolites have exceptional catalytic performance in oil refining and chemical synthesis that can be attributed to their well-defined porous structures that host active sites. This study pinpoints the exact locations of aluminum atoms in ZSM-5 structures—a key zeolite catalyst. Aluminum siting governs catalytic efficiency in acid and redox processes. Anomalous x-ray powder diffraction (AXRPD) at the aluminum K-edge probes the long-range order of aluminum atoms within the ZSM-5 frameworks, precisely quantifying both isolated aluminum atoms and Al(-O-Si-O-)$_x$Al sequences (aluminum pairs). Supported by nuclear magnetic resonance studies, AXRPD unambiguously determines the crystallographic organization of aluminum pairs, recognized spectroscopically as α, β, and γ sites, linking their distribution to superior catalytic activity in propene oligomerization. This combined approach provides essential insights for optimizing zeolite catalysts and enhancing their performance.

Zeolites, which are used as heterogeneous acid catalysts in oil refining and fine chemical production (*1*–*6*), have robust crystalline structures with well-defined, interconnected pores (*3*, *7*). The zeolite frameworks consist of tetrahedrally coordinated silicon (Si) and aluminum (Al) atoms (collectively T atoms) linked by oxygen (O) bridges, which can be arranged into various geometries and form distinct channel systems with distinctive adsorption and catalytic properties (*8*–*10*). Currently, 265 zeolite framework topologies have been identified (*11*).

The distribution of Al atoms within zeolites is a critical parameter that defines the performance of catalytically active centers (*1*, *12*). The negative charge introduced by Al atoms on the zeolitic lattice must be balanced by extra-framework counterion species that serve as active sites and exhibit acid (protons and cations) and redox (transition metal ions) activity (*13*–*16*). In Al-rich zeolites (Si/Al < 6), Al-O-Si-O-Al sequences form so-called Al pairs that dominate the structural organization of a framework that can bind divalent cations. In Si-rich zeolites (Si/Al > 10), Al atoms can be present as isolated Al atoms, Al pairs, and close Al atoms. Single Al atoms can stabilize monovalent species; Al(-O-Si-O-)$_2$Al sequences acting as Al pairs are balanced by bare divalent cations or host nearby monovalent species, such as nearby protons in acid sites (*4*, *16*–*20*). When close Al atoms are present, Al(-O-Si-O-)$_3$Al sequences can accommodate aqua complexes of divalent cations in a hydrated form of zeolite. For Si-rich zeolites, the distribution of Al can be influenced by synthesis conditions (*14*, *21*–*23*), which offers a robust tool for optimizing the zeolite performance (*24*)

Zeolite ZSM-5, one of the most common heterogeneous catalysts, clearly demonstrates that Al siting governs catalytic reaction mechanisms, as exemplified in methanol-to-olefins processes (*24*–*27*). Al concentrated at channel intersections favors the aromatic-based cycle, whereas Al located within the channels promotes the formation of linear products (*24*, *25*, *28*). Another acid-base reaction influenced by Al distribution is propene oligomerization, where two reported Si-rich ZSM-5 samples with similar chemical compositions but differing populations of Al pairs exhibited distinct catalytic properties (*17*, *24*, *29*, *30*). The superior performance of Al pair–rich samples in this reaction has been attributed to the assured proximity of protons, which influence alkoxide formation, as well as to repulsive forces that facilitate product release (*1*, *12*, *17*, *20*, *31*). The presence of Al pairs also plays a pivotal role in the ethanol transformation pathway over zeolite ZSM-5. Operando spectroscopy studies revealed that Al pair–rich ZSM-5 promotes a dissociative reaction pathway, where close protons associated with Al pairs first dehydrate ethanol to ethene, which is subsequently converted to butane (*20*). Ethoxyl intermediates formed in Al pair–rich ZSM-5 contribute to C-C bond formation. By contrast, ZSM-5 with a high fraction of isolated Al atoms favors an associative pathway for ethanol dehydration (*20*). Additionally, Al pairs in zeolites (ZSM-5, FER, and MOR) stabilize transition metal ions, which serve as active centers in redox catalysis (*32*–*37*). Bare Fe(II) or Co(II) cations enhance the catalytic activity of zeolite catalysts in hydrocarbon-selective catalytic reduction and N_2O decomposition, the latter being used to probe the presence of associated Al pairs (*30*).

To gain full understanding of the catalytic process, a comprehensive recognition and structural characterization of Al organization is essential. Spectroscopic studies conducted for the Al pair–rich ZSM-5 sample fully exchanged with Co(II) hexa aqua complex have identified typical sites for divalent cobalt cations at two distinct locations: the elongated 6-rings formed from two-folded 5-rings (α site) and at the 5- or deformed 6-rings (β site) (*18*, *22*, *30*, *38*). The α sites, which account for 40 to 50% of the total Co loading, are believed to be located at the walls of the straight channels (*30*, *39*). The β sites, representing 50 to 60% of the Co, were suggested to be situated in the sinusoidal channels (*30*, *38*). Additionally, a minor boat-shaped γ site, formed from the 5- and 6-membered rings, was speculated to be present in the sinusoidal channels (*30*, *38*).

Understanding the relationship between Al distribution, T site–dependent reactivity, and catalytic performance remains one of the greatest challenges in zeolite science. By quantitatively identifying Al siting and correlating it with performance, this work provides a foundation for further exploration of how Al organization influences active site formation and reaction mechanisms, not only in ZSM-5 but also in other zeolite catalysts. Advancing this knowledge will be crucial for the rational design of next-generation zeolite-based materials with tailored properties for industrial applications.

Anomalous x-ray powder diffraction methodology

A multispectroscopic approach engaging the Co(II) hexa aqua complex as a probe for Al pairs in zeolites enables an indirect approximate estimation of their quantity and provides insights into the local geometry of bare Co(II) cations and their coordinated Al sites (*40*). However, the discrimination of Al from Si in zeolite frameworks and recognizing T site–dependent reactivity of zeolites is still challenging because there is no general method that can identify directly which T sites in a zeolite framework structure are occupied by Al. Although a number of techniques have been applied—including ^{27}Al multiquantum solid-state nuclear magnetic resonance spectroscopy (MQ MAS NMR) (*41*, *42*), x-ray absorption spectroscopy (XAS) (*43*), and x-ray standing waves (*44*)—so far, no universal method enables unequivocal identification.

The Al substitution for Si is usually only partial, and the scattering power of these two elements is similar (13 versus 14 electrons). Therefore, we have developed an anomalous x-ray powder diffraction (AXRPD) methodology (*45*) that leverages resonant scattering across the Al K-edge (1.56 keV) to highlight

[1]J. Heyrovsky Institute of Physical Chemistry of the CAS, Prague, Czech Republic. [2]Institute for Chemical and Bioengineering, ETH Zurich, Zurich, Switzerland. [3]Paul Scherrer Institute, Center for Energy and Environmental Sciences, PSI, Villigen, Switzerland. [4]Paul Scherrer Institute, Center for Photon Science, Villigen, Switzerland. [5]Department of Inorganic Technology, University of Chemistry and Technology, Prague, Czech Republic.
*Corresponding author. Email: przemyslaw.rzepka@jh-inst.cas.cz (P. R.); kingapatrycja.mlekodaj@jh-inst.cas.cz (K.M.); jeroen.vanbokhoven@chem.ethz.ch (J.A.v.B.)

Al positions in a structure. The x-ray energy is set either near or far from the Al K-edge, conditions referred to as near- and off-resonance. The x-ray atomic scattering factor $f = f_0 + f_1 + i \times f_2$ of an element primarily depends on its number of electrons f_0. Under the near-resonance conditions, the complex contributions $f_1 + i \times f_2$ of the scattering become meaningful and markedly alter the scattering power of Al, whereas the scattering power of other elements, such as silicon and oxygen, remains unchanged. These shifts induce variations in the structure factors originating from the lattice planes containing T sites occupied by Al.

Structural information in the specific lattice plane (hkl) can be quantified by the square of its structure factor (F_{hkl}), which in turn is proportional to the relative intensity of the corresponding reflection (I_{hkl}). Hence, the differences in Bragg reflection intensities measured at off- and near-resonance energies allow for the most unequivocal assignment of Al to T atoms in the framework structure to date. Spectroscopic methods are short-range probes that can only report on the local environment around the Al position, whereas AXRPD collects information on the long-range structural order of the Al distribution and can quantitatively locate Al positions within the periodic framework.

To date, this technique has been exploited to identify elements with absorption edges within diffraction-suitable energy ranges, such as Sr (16.1 keV), Rb (15.2 keV), Se (12.7 keV), Cu (8.98 keV), and Fe (7.11 keV) (*46*–*49*). The familiar approach has also been applied in multi-wavelength anomalous diffraction (MAD) to enhance the structural determination of biological macromolecules (*50*). As detailed in the supplementary materials, AXRPD experiments conducted at the PHOENIX beamline (https://www.psi.ch/en/sls/phoenix) at the Swiss Light Source (SLS) synchrotron facility have enabled operations in the soft energy ranges using a previously developed setup (*45*). At the K-edge (1.56 keV), the x-ray beam is fully absorbed after penetrating a few tens of micrometers of a zeolite sample, so these experiments were performed in reflection geometry inside a vacuum chamber. The Si drift single-photon–counting diode detector (*51*) effectively reduced the background noise from post-edge fluorescence emission by discriminating inelastic scattering.

Experimental results

ZSM-5 zeolites belong to the MFI topology, featuring a framework structure with 12 T atoms organized by *Pnma* symmetry into a three-dimensional (3D) network of intersecting 10-membered ring straight and sinusoidal channels. The primary object of this study was two ZSM-5 samples with similar Si/Al ratios (15.1 and 18.1) but different organizations of Al atoms, as the samples contained 82% and 9% of Al pairs, respectively. The Al distributions were optimized through selected synthesis conditions (details provided in the supplementary materials). The one enriched in Al pairs is referred to as high–Al pair ZSM-5 (HAP-ZSM-5), and the one with low concentration of Al pairs is called low–Al pair ZSM-5 (LAP-ZSM-5). We aimed to gain a better understanding of the long-range order organization of Al atoms in these two ZSM-5 structures and to learn how this organization influences their propensity for propene oligomerization.

Our refinement of AXRPD data collected from H-forms of HAP-ZSM-5 and LAP-ZSM-5 structures followed a preestablished protocol (*45*); refinement details (tables S1 and S2), profile fits (figs. S3 to S5), and crystallographic information files (CIFs) are available in the supplementary materials. The data analysis strategy involved multiple refinements with a common structure model that had a single set of profile parameters, refined using Topas software (*52*), to simultaneously fit all diffraction datasets from different energy levels. Given that the diffraction limit at 1.56 keV corresponds to a d-spacing of ~4 Å, data from conventional measurements were integrated with those at energies near the x-ray absorption edge to accurately determine the Al concentration at the already refined positions of T atoms.

Therefore, before assigning Al to T sites, the orthorhombic (*Pnma* space group) structure parameters were meticulously refined with conventional diffraction data collected in transmission mode (0.5-mm capillary) at a wavelength of 0.708597 Å (E = 17.5 keV) on the Materials Science beamline at the SLS (*53*). The peak shape was modeled by pseudo-Voight function with additional asymmetry. The background was evaluated through linear interpolation between selected points using the program Lines (*54*). The diffraction patterns calculated from the refined structural models fit the observed data well (figs. S3 and S4) and showed no evidence of monoclinic distortions (*55*). The possible guest molecules were determined by inserting two "dummy" oxygen atoms and optimized with simulated annealing, which is a global optimization algorithm particularly well suited for locating the foreign species inside the porous materials (*56*). Once the model converged, the structure parameters were fixed and concurrently used with datasets collected across the Al K-edge at 1500 eV (off-resonance) and at 1550 eV, 1555 eV, and 1560 eV (near-resonance).

Initially, profile parameters for AXRPD data (scale factor, peak profile, specimen displacement, and axial model) were fitted. Scale factors were first estimated by using a previously established approach (*45*) that involved normalized μ_E, the attenuation coefficients for the sample composition at specified energies, and I_0, the incoming photon flux (eq. S1). Subsequently, the scales were individually refined. The common instrumental function was defined by pseudo-Voight function with an additional asymmetry (*52*). The background was defined through linear interpolation between selected points (*54*). Once the profile parameters converged, they were fixed, and only the Al occupancies were refined. Al occupancies were initially set as 6.36 and 5.30 Al atoms evenly distributed between 12 T sites of HAP-ZSM-5 and LAP-ZSM-5 structure models, respectively, and refined using all datasets simultaneously. The uncertainties of Al occupancies on individual T sites were determined by bootstrap methods (*57*, *58*).

Figure 1 highlights the subtle yet important changes in structure factors calculated for HAP-ZSM-5 and LAP-ZSM-5 structure models, which arose from variations in the Al scattering form factor at different energies across the Al K-edge. Because F_{hkl} for each reflection shifted specifically with photon energy, and a sufficient number of distinct reflections were registered, the atomic parameters of the structure could be refined to achieve the best fit to the observed data, allowing the precise determination of Al organization.

The Al organization was cross-referenced with refined Co positions in HAP-ZSM-5 (figs. S5 and S6). The structure, intrinsically loaded with Co(II) hexa aqua complexes (fig. S8), maintained its orthorhombic order (fig. S7). The positions of bare divalent Co sites point out the locations of associated Al pairs. The high-resolution x-ray powder diffraction (HR-XRPD) data were measured in transmission mode (0.5-mm capillary) at a wavelength of 0.3543 Å on beamline ID-22 at the European Synchrotron Radiation Facility (ESRF) (*59*). In the course of the Rietveld analysis, the peak shape in the diffraction data was modeled as a 2Θ-dependent convolution of Lorentzian and Gaussian functions with added asymmetry. Anisotropic peak broadening was described by using spherical harmonics, and the background was defined through linear interpolation between selected points (*54*). The three distinct Co(II) positions were identified by using a simulated annealing algorithm (*60*) and were subsequently refined.

Aluminum distributions

The AXRPD studies revealed that LAP-ZSM-5 had Al concentrated at the T12 site and dispersed across several other sites located at the intersection of the straight and sinusoidal 10-membered ring (10MR) channels (Fig. 2). This distribution corroborated previous studies and the synthesis conditions (*17*, *30*). Only 0.9(1) Al atoms occupying adjacent T8 sites may form Al pairs organized in an Al(-O-Si-O-)$_2$Al sequence. Al at T8 sites accounts for ~8% of the total Al loading, which is near the reported 9% of Al pairs in this sample (*17*, *30*).

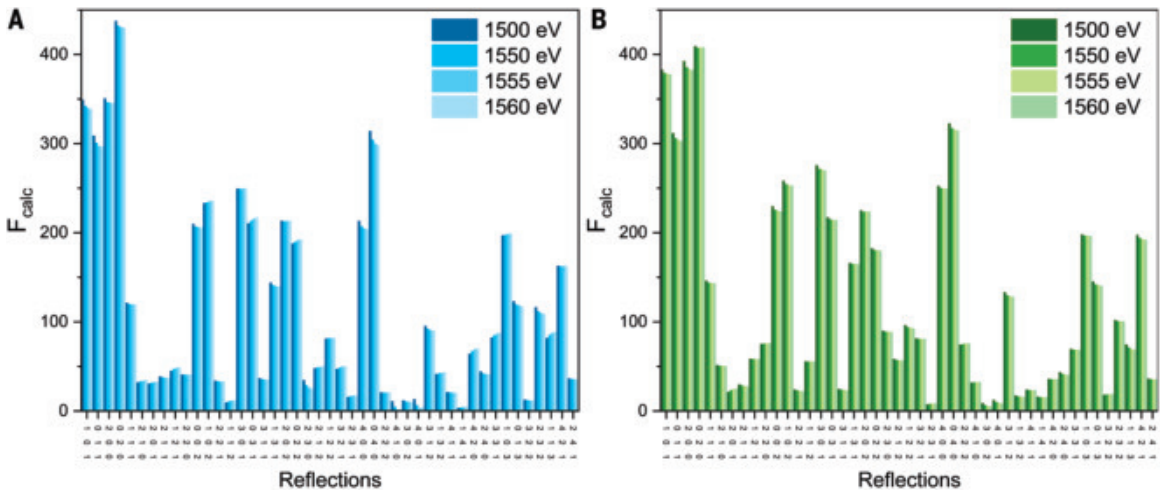

Fig. 1. Structure factors for ZSM-5 structure models. (**A** and **B**) Comparison of the structure factors (F_{hkl}) at different energies across Al K-edge calculated for high–Al pair ZSM-5 (HAP-ZSM-5) (A) and low–Al pair ZSM-5 (LAP-ZSM-5) (B).

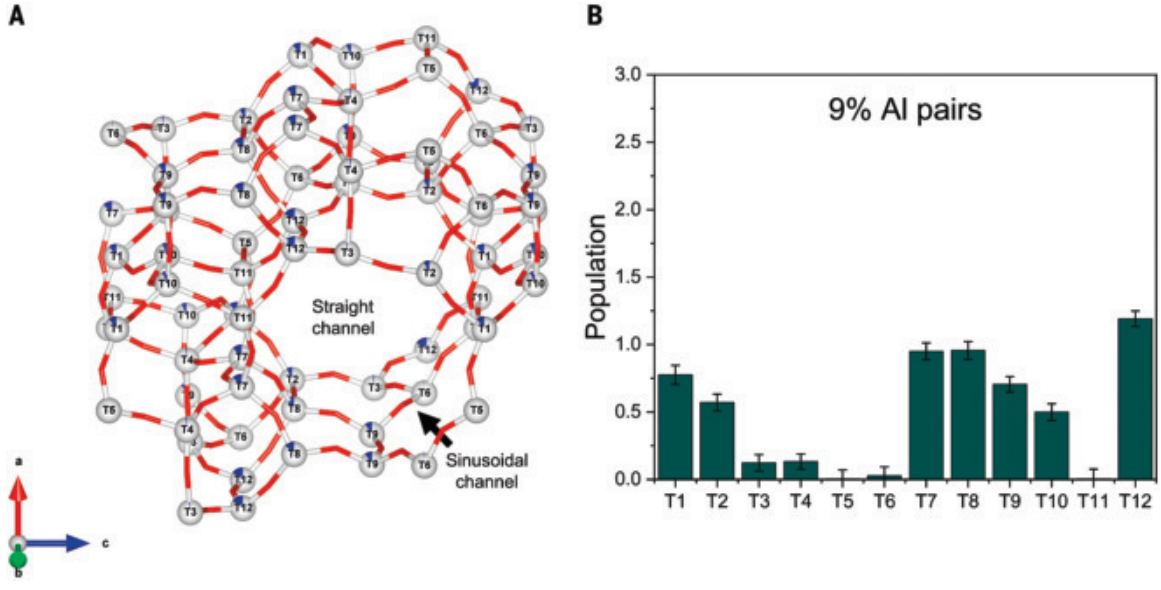

Fig. 2. Al distribution among T sites within the LAP-ZSM-5 framework structure. (**A**) [010] projection of the MFI-type framework structure. (**B**) The distribution of Al across 12 T sites.

In HAP-ZSM-5, 1.2(1) Al atoms emerge at adjacent T8 sites, positioned on opposite sides of the twisted 6-ring located at the intersection of the straight and sinusoidal channels (Fig. 3A). This Al pair coordinated 0.55(6) cobalt atom at the Co2 position, as determined by Rietveld refinement, situated in the plane of the ring and constituting the β site (Fig. 3C). This finding aligned with the electronic structure described in previous studies (*17*, *38*, *61*, *62*), but the location differed. Additionally, siting for the β′ site was established by 0.9(1) Al atoms occupying T4 and T10 or T4 and T11 sites, respectively (Fig. 3B), arranged in Al-O-Si-O-Al sequences within the 5-ring (Fig. 3C). The corresponding Co3 site, with 1.0(1) Co occupancy, was isolated from large-port voids. An Al pair at T8 and T11 was separated by an -O-Si-O- bridge within the 6-ring, which was further interlinked by silicon occupying the T3 site (Fig. 3B). This arrangement exhibited siting of Co1 in the α site, which is situated slightly above the ring plane (Fig. 3C), although less elevated than previously reported for bare divalent cations in the α positions of MOR and FER structures (*39*).

The Al organization aligned well with the three refined Co positions at the expected α and two β sites. Located at the T4, T8, T10, and T11 sites, Al-O-Si-O-Al sequences accounted for 84(8)% of the total Al, closely matching the reported 82% (17, 26), with excess Al at T4 emerging as a single Al species (Fig. 3D). Among Al pairs, 31(4)% were situated at α sites within the straight channels, 40(5)% occupy β sites at the channel intersections, and 28(5)% are β′ sites confined within the lattice.

NMR studies

The presence of Al-O-Si-O-Al sequences engaged in α and β′ sites substantially contradicted previous studies (*40*, *42*, *63*) because this type of Al organization was recognized predominantly in ZSM-5 zeolites with Si/Al ratio of <9 (*64*). To investigate this issue, a solid-state NMR experiment (details provided in the supplementary materials) was conducted on the HAP-ZSM-5 sample (Fig. 4) and LAP-ZSM-5 (fig. S1). The

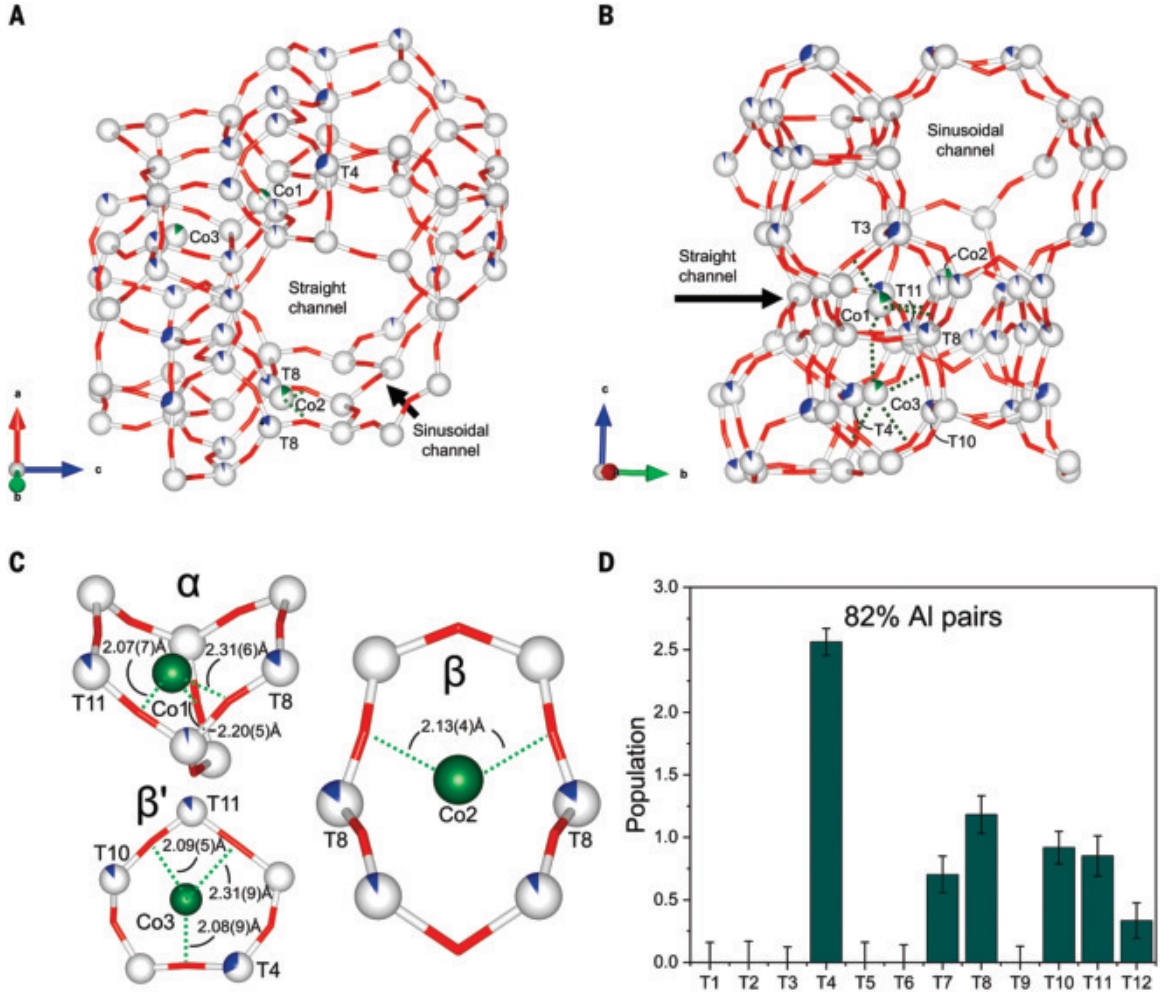

Fig. 3. Al distribution among T sites within the HAP-ZSM-5 framework structure. (**A** and **B**) [010] (A) and [100] (B) projections of the MFI-type framework structure enriched in Al pairs at adjacent T8-T8, T8-T11, and T4-T10/T11 sites. The remaining single Al atoms predominantly occupied the T4 site. (**C**) α- and β-type siting for Co(II) cations counterbalancing Al pairs. (**D**) The distribution of Al across 12 T sites.

resonance at ~55 parts per million (ppm) observed at the ^{27}Al MAS NMR spectrum corresponded to tetrahedral Al atoms located in T sites (Fig. 4A). The resonance at ~0 ppm characteristic for octahedral Al atoms was not detected, ruling out the substantial presence of extra-framework Al.

The ^{29}Si MAS NMR spectrum of the sample aligned well with reported spectra of Si-rich ZSM-5 materials and is presented along with its fit in Fig. 4B. The spectrum was dominated by resonances above −110 ppm, which we attributed to Si(4Si) atoms (Si atoms with exclusively Si neighbors), and by resonances between −102 and −108 ppm, corresponding to Si(3Si,1Al) atoms (Si atoms with one Al neighbor). The final component of the spectrum comprised resonances below −101 ppm, which could correspond either to Si(3Si,1OH) atoms or Si(2Si,2Al) atoms (Si atoms with two Al neighbors). To attribute this component, a cross-polarization experiment was conducted (fig. S2), which indicated the presence of various SiOH atoms (silanols on the external surface of the zeolite crystals or defects of the framework). However, the Si/Al_{FR} ratio estimated from the ^{29}Si MAS NMR spectra by using eq. S2 deviated from the Si/Al ratio obtained from chemical analysis for HAP-ZSM-5 when only Si(3Si,1OH) atoms were considered (Si/Al_{FR} 17.9 versus Si/Al 15.1). Both values were in good agreement when the possible presence of Si(2Si,2Al) was considered (Si/Al_{FR} 14.8 versus Si/Al 15.1). This result suggests that a notable portion of the resonance below −101 ppm arose from Si(2Si,2Al) atoms (*65*).

The presence of Si(2Si,2Al) atoms in the investigated HAP-ZSM-5 suggested that a small fraction (up to 20%) of Al atoms are organized in Al-O-Si-O-Al sequences. The resonances below −101 ppm were not found in ^{29}Si MAS NMR spectra of LAP-ZSM-5 (fig. S1). Notably, the potential contribution of the Si(2Si,2Al) resonance in the ^{29}Si MAS NMR signal below −101 ppm for Si-rich ZSM-5 zeolites has typically been omitted in previous investigations (*40*, *42*, *63*, *64*). The combined studies involving AXRPD and NMR provide meaningful insights into this matter.

Discussion

The organization of Al in ZSM-5 zeolites and its periodic distribution provide valuable insights into catalytic mechanisms, particularly in Brønsted-acid and redox processes involving transition metal ions. In both structures examined, Al was concentrated at T sites within channel intersections. The influence of the Al pair fraction in ZSM-5 zeolite on propene oligomerization was studied using in situ Fourier transform infrared (FTIR) spectroscopy to monitor formation of intermediates, transition states, and products over Al atoms and associated protons—identified as the active centers—along with gas chromatography for product detection and quantification (*17*, *18*). FTIR results showed that propene adsorption led to the faster formation of H-bonded species and alkoxides in samples with a high fraction of single Al atoms. Such samples, however,

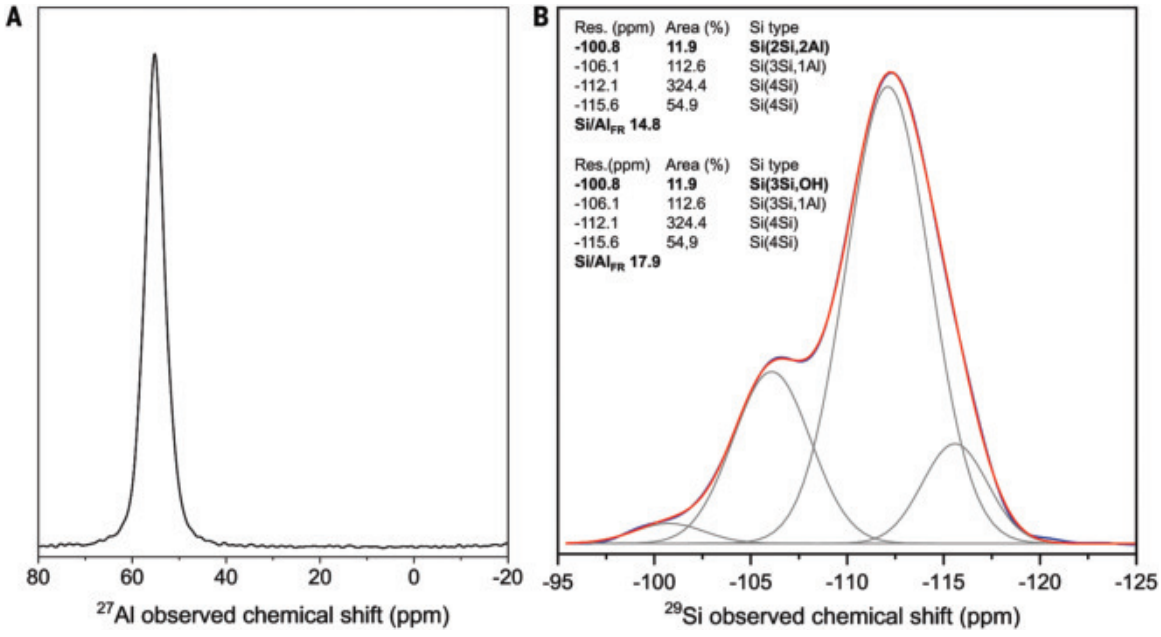

Fig. 4. Al coordination. (**A** and **B**) ^{27}Al MAS NMR spectrum (A) and ^{29}Si MAS NMR spectrum (blue) (B) together with spectrum fit (gray for components, red for cumulative curve) registered for HAP-ZSM-5.

revealed superior activity, as shown in fig. S9A, with high C4 to C9 oligomer production. In situ FTIR spectroscopy combined with catalytic tests revealed that oligomerization products stabilized over Al pairs and associated protons, where Al atoms spaced 5 to 6 Å apart facilitated desorption owing to repulsive forces from positively charged alkoxides (*17*, *18*). Additionally, protonation kinetics—crucial for product release and active center regeneration—were faster in Al pair–rich samples, highlighting the role of close protons stabilized by Al-O-Si-O-Al sequences at intersections (β sites) and within straight channels (α sites) compared with isolated Al atoms occupying similar T positions. At higher reaction temperatures (above 340°C), aromatic products form on all ZSM-5 catalysts. However, higher conversion levels are achieved, and secondary aromatization processes dominate on the HAP-ZSM-5 catalysts (fig. S9B). The siting of Al pairs, directly linked to high activity, is now unambiguously pinpointed by AXRPD.

These findings confirm that spectroscopic studies correctly identify cationic sites; however, their precise positions within the periodic structure were incorrect. Traditionally, the localization of Al atoms in zeolites has been investigated using established methods, such as ultraviolet-visible and FTIR spectroscopies of Co-containing zeolites, chemical analysis, and ^{27}Al and ^{29}Si MAS NMR studies. Although these methods provide valuable information, they are short-range probes that often offer only an estimate of quantification and insights into the local structure around Al positions, which leads to imprecise conclusions about the crystallographic locations of Al within the zeolite framework. Unlike spectroscopic methods, AXRPD at the Al K-edge provides fully quantitative information on the long-range order of Al distribution. Thus, AXRPD is an appropriate technique for revising and accurately pinpointing Al positions in the framework structures of zeolites, whether they emerge as isolated Al atoms, Al pairs, or close Al sites.

REFERENCES AND NOTES

1. D. E. Perea *et al.*, *Nat. Commun.* **6**, 7589 (2015).
2. Q. F. Lin *et al.*, *Science* **374**, 1605–1608 (2021).
3. Y. Chai *et al.*, *Science* **368**, 1002–1006 (2020).
4. B. C. Knott *et al.*, *ACS Catal.* **8**, 770–784 (2018).
5. Q. Zhang, S. Gao, J. Yu, *Chem. Rev.* **123**, 6039–6106 (2023).
6. E. G. Derouane *et al.*, *Catal. Rev. Sci. Eng.* **55**, 454–515 (2013).
7. J. Pérez-Ramírez, C. H. Christensen, K. Egeblad, C. H. Christensen, J. C. Groen, *Chem. Soc. Rev.* **37**, 2530–2542 (2008).
8. Q. Zhang, J. Yu, A. Corma, *Adv. Mater.* **32**, e2002927 (2020).
9. M. Dusselier, M. A. Deimund, J. E. Schmidt, M. E. Davis, *ACS Catal.* **5**, 6078–6085 (2015).
10. U. Olsbye *et al.*, *Angew. Chem. Int. Ed.* **51**, 5810–5831 (2012).
11. C. Baerlocher, L. B. McCusker, Database of Zeolite Structures (2014); http://www.iza-structure.org/databases/.
12. R. Gounder, E. Iglesia, *Angew. Chem. Int. Ed.* **49**, 808–811 (2010).
13. A. B. Pinar, L. Gómez-Hortigüela, L. B. McCusker, J. Pérez-Pariente, *Chem. Mater.* **25**, 3654–3661 (2013).
14. J. R. Di Iorio, C. T. Nimlos, R. Gounder, *ACS Catal.* **7**, 6663–6674 (2017).
15. S. Schallmoser *et al.*, *J. Catal.* **316**, 93–102 (2014).
16. R. Gounder, E. Iglesia, *J. Am. Chem. Soc.* **131**, 1958–1971 (2009).
17. M. Bernauer *et al.*, *J. Catal.* **344**, 157–172 (2016).
18. E. Tabor, M. Bernauer, B. Wichterlová, J. Dedecek, *Catal. Sci. Technol.* **9**, 4262–4275 (2019).
19. C. T. Nimlos *et al.*, *Chem. Mater.* **32**, 9277–9298 (2020).
20. K. Gołąbek *et al.*, *Commun. Chem.* **3**, 25 (2020).
21. K. Mlekodaj *et al.*, *Chem. Mater.* **33**, 1781–1788 (2021).
22. J. Dědeček, E. Tabor, S. Sklenak, *ChemSusChem* **12**, 556–576 (2019).
23. J. R. Di Iorio, R. Gounder, *Chem. Mater.* **28**, 2236–2247 (2016).
24. C. Li *et al.*, *ACS Catal.* **8**, 7688–7697 (2018).
25. T. Liang *et al.*, *ACS Catal.* **6**, 7311–7325 (2016).
26. S. Wang *et al.*, *ACS Catal.* **8**, 5485–5505 (2018).
27. S. S. K. Kim, G. Park, M. H. Woo, G. Kwak, S. S. K. Kim, *ACS Catal.* **9**, 2880–2892 (2019).
28. S. Ezenwa *et al.*, *J. Am. Chem. Soc.* **146**, 10666–10678 (2024).
29. J. Dedecek, V. Balgová, V. Pashkova, P. Klein, B. Wichterlová, *Chem. Mater.* **24**, 3231–3239 (2012).
30. J. Dědeček, D. Kaucký, B. Wichterlová, O. Gonsiorová, *Phys. Chem. Chem. Phys.* **4**, 5406–5413 (2002).
31. P. del Campo *et al.*, *ACS Catal.* **10**, 11878–11891 (2020).
32. P. Sazama *et al.*, *Appl. Catal. B* **189**, 65–74 (2016).
33. J. Bin Lim, J. Shin, N. H. Ahn, I. Heo, S. B. Hong, *Appl. Catal. B* **267**, 118710 (2020).
34. M. Sunil Kumar *et al.*, *Fuel* **344**, 128125 (2023).
35. E. Tabor *et al.*, *Appl. Catal. B* **240**, 358–366 (2019).
36. Z. Sobalik *et al.*, *Microporous Mesoporous Mater.* **146**, 172–183 (2011).
37. P. Sazama *et al.*, *J. Catal.* **312**, 123–138 (2014).
38. D. Kaucký, A. Vondrová, J. Dědeček, B. Wichterlová, *J. Catal.* **194**, 318–329 (2000).
39. L. Drozdová, R. Prins, J. Dědeček, Z. Sobalík, B. Wichterlová, *J. Phys. Chem. B* **106**, 2240–2248 (2002).
40. J. Dědeček, Z. Sobalík, B. Wichterlová, *Catal. Rev. Sci. Eng.* **54**, 135–223 (2012).
41. J. A. van Bokhoven, D. C. Koningsberger, P. Kunkeler, H. van Bekkum, A. P. M. Kentgens, *J. Am. Chem. Soc.* **122**, 12842–12847 (2000).
42. S. Sklenak *et al.*, *Angew. Chem.* **119**, 7424–7427 (2007).
43. A. Vjunov *et al.*, *J. Am. Chem. Soc.* **136**, 8296–8306 (2014).
44. J. A. van Bokhoven *et al.*, *Nat. Mater.* **7**, 551–555 (2008).
45. A. B. Pinar *et al.*, *J. Am. Chem. Soc.* **143**, 17926–17930 (2021).
46. C. Pichon *et al.*, in *Recent Advances in the Science and Technology of Zeolites and Related Materials Part B*, E. van Steen, M. Claeys, L. H. Callanan, Eds., vol. 154 of *Studies in Surface Science and Catalysis* (Elsevier, 2004), pp. 1641–1648.
47. A. Goldbach, M.-L. Saboungi, L. Iton, D. L. Price, *Chem. Commun.* **1999**, 997–998 (1999).
48. J. Wieser *et al.*, *Angew. Chem. Int. Ed.* **63**, e202407395 (2024).
49. K. D. Finkelstein, Q. Shen, S. Shastri, *Phys. Rev. Lett.* **69**, 1612–1615 (1992).
50. W. A. Hendrickson, *Science* **254**, 51–58 (1991).
51. R. L. Owen, J. M. Holton, C. Schulze-Briese, E. F. Garman, *J. Synchrotron Radiat.* **16**, 143–151 (2009).
52. A. A. Coelho, *J. Appl. Cryst.* **51**, 210–218 (2018).
53. P. R. Willmott *et al.*, *J. Synchrotron Radiat.* **20**, 667–682 (2013).
54. S. Smeets, Lines, version 1.4.0, Zenodo (2021).
55. M. Ardit, A. Martucci, G. Cruciani, *J. Phys. Chem. C* **119**, 7351–7359 (2015).
56. S. Smeets *et al.*, *J. Am. Chem. Soc.* **138**, 7099–7106 (2016).
57. B. Efron, R. Tibshirani, *Stat. Sci.* **1**, 54–75 (1986).
58. T. J. DiCiccio, B. Efron, *Stat. Sci.* **11**, 189–212 (1996).
59. A. Fitch *et al.*, *J. Synchrotron Radiat.* **30**, 1003–1012 (2023).
60. A. A. Coelho, *J. Appl. Cryst.* **33**, 899–908 (2000).
61. J. Dědeček, D. Kaucký, B. Wichterlová, *Chem. Commun.* **2001**, 970–971 (2001).
62. J. Dědeček *et al.*, *Stud. Surf. Sci. Catal.* **174**, 781–786 (2008).
63. J. M. Thomas, J. Klinowski, *Adv. Catal.* **33**, 199–374 (1985).
64. C. A. Fyfe, G. C. Gobbi, G. J. Kennedy, *J. Phys. Chem.* **88**, 3248–3253 (1984).

65. G. Engelhardt, U. Lohse, E. Lippmaa, M. Tarmak, M. Mägi, *Z. Anorg. Allg. Chem.* **482**, 49–64 (1981).
66. P. Rzepka, K. Mlekodaj, XRPD, Fcalc, NMR and UV-Vis data for ZSM-5, data set, Zenodo (2025).

ACKNOWLEDGMENTS

We thank the SLS at the Paul Scherrer Institute and Villigen PSI for provision of beamtime at the Phoenix beamline. P.R. further acknowledges the MS beamline at SLS for conducting the ex situ capillary measurements and V. Paunović (PSI) for insightful discussions. The authors also thank C. Dejoie from ID22 at ESRF for collecting ex situ data on Co-ZSM-5 and V. Pashkova from the Czech Academy of Sciences for her help with sample preparation. P.R. acknowledges the Czech Science Foundation under project 25-18196M. K.M. and E.T. thank the Czech Science Foundation for project 24-14387L and the National Science Centre, Poland (grant no. 2022/47/I/ST4/00607). J.A.v.B. acknowledges the Swiss National Science Foundation under grant 200021_178943 for financial support. This work was additionally supported by the project "The Energy Conversion and Storage," funded under project no. CZ.02.01.01/00/22_008/0004617 through the Johannes Amos Comenius Programme, call for Excellent Research. **Funding:** This study was supported by ETH Zurich and PSI Villigen internal funding; the Swiss National Science Foundation, grant 200021_178943; the Czech Science Foundation, grants 25-18196M and 24-14387L; Johannes Amos Comenius Programme, grant CZ.02.01.01/00/22_008/0004617; and the National Science Centre Poland, grant 2022/47/I/ST4/00607. **Author contributions:** Conceptualization: J.A.v.B., P.R., K.M.; Funding acquisition: J.A.v.B., P.R., K.M., E.T., J.D.; Investigation: P.R., K.M., T.H., M.B.; Methodology: P.R., T.H., J.A.v.B., J.D., K.M.; Validation: P.R., J.A.v.B., K.M., J.D., S.S.; Writing – original draft: P.R., K.M.; Writing – review & editing: J.A.v.B., P.R., K.M., J.D., T.H., E.T. **Competing interests:** The authors declare that they have no competing interests. **Data and materials availability:** All processed data are available in the main text or the supplementary materials. Raw data are available at Zenodo (*66*).

SUPPLEMENTARY MATERIALS

science.org/doi/10.1126/science.ads7290
Supplementary Text
Figs. S1 to S9
Tables S1 to S4

Submitted 26 August 2024; resubmitted 14 November 2024
Accepted 12 March 2025
10.1126/science.ads7290

NATURAL HISTORY

Hawaiian caterpillar patrols spiderwebs camouflaged in insect prey's body parts

Daniel Rubinoff*, Michael San Jose, Camiel Doorenweerd

Lepidoptera is the most herbivorous of all the insect orders, with predatory caterpillars globally comprising less than 0.13% of the nearly 200,000 moth and butterfly species. Here, we report a species in which caterpillars are carnivorous inhabitants of spider's webs, feeding on the arthropods that they find there. This Hawaiian lineage also boasts an unprecedented and macabre practice of decorating its portable larval home with the body parts of the spider prey it harvests from the web where it resides. Phylogenomic data suggest that the origin of this unique spider cohabitant is at least six million years old, more than one million years older than Hawaii's current high islands. After decades of searching, only one species has been discovered, and it is restricted to 15 square kilometers of a single mountain range on the island of Oʻahu, meaning that other members of the lineage have disappeared from older islands. Conservation action to save this globally unique lineage is imperative and overdue.

Hawaii's geographic isolation has fostered the evolution of an array of unusual invertebrates, including spiders that spear prey from the air (*1*), terrestrial rather than aquatic damselfly nymphs (*2*), caterpillars that hunt snails (*3*), amphibious caterpillars (*4*), and caterpillars that ambush prey (*5*). Now, the "bone collector" caterpillar (Fig. 1) adds an additional dimension with a bizarre housekeeping regimen not reported for any other insect (*6*) and an ecology not recorded elsewhere in the order Lepidoptera. These newly discovered caterpillars are the first known to depend on spider webs, using only those located in tree hollows, logs, or rock cavities and never leaving their immediate vicinity. Carnivorous caterpillars are an extremely rare evolutionary phenomenon, and although caterpillars and spiders are common in the same environments all over the world, only this single caterpillar lineage in Hawaii is known to have made the leap to spider cohabitation.

Bone collector caterpillars crawl through the jumble of web and detritus (Fig. 2) and opportunistically eat any weakened or recently deceased insects they come across (e.g., cached spider prey), even chewing through silk to reach their meal if need be. Because they exclusively rely on cobwebs in enclosed spaces (not sheet webs), they can access the full three-dimensional space of the webs. We have identified body parts belonging to more than six different families of insect attached to the silk caterpillar cases, suggesting that they are adaptable scavengers and predators. In captivity, the caterpillars will attack and eat any live, slow moving, or immobilized insect prey, and they will even cannibalize each other (movie S1). This usually limits one caterpillar per web in the wild because a larger individual would make a quick meal of a smaller neighbor.

When decorating their silken portable cases, the caterpillars are particular. Body parts are carefully measured for size before the caterpillar weaves them into its collection. Each prospective new addition is rotated and probed with its mandibles several times, and parts that are too large are chewed down to a size that will fit its case. If denied access to arthropod

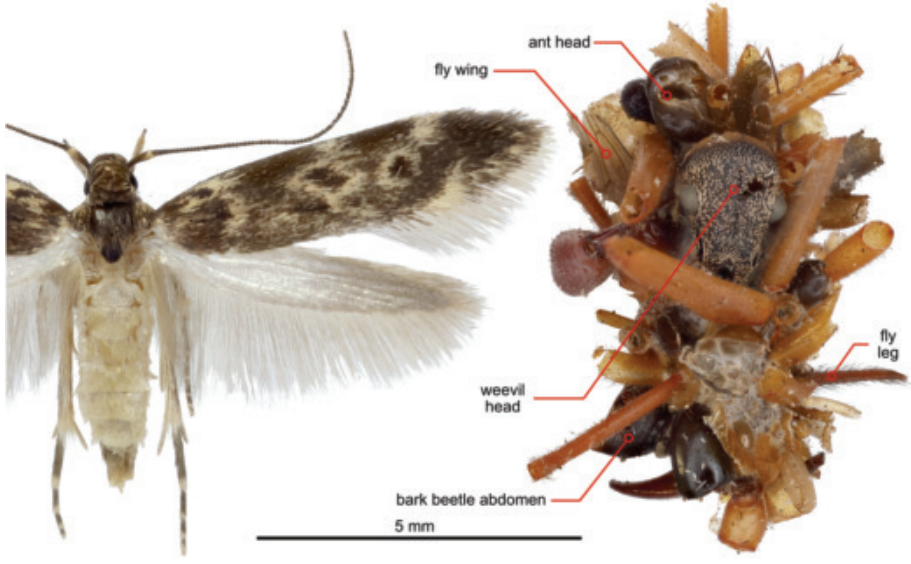

Fig. 1. Pinned adult female (left) of the bone collector caterpillar and portable case (right) in which the larva resides decorated with body parts from ants, bark beetles, weevils, and flies. Unlabeled parts are all host spider integument that has been shed.

Department of Plant and Environmental Sciences, Entomology Section, University of Hawai'i at Mānoa, Honolulu, HI, USA.
***Corresponding author. Email: rubinoff@hawaii.edu**

body parts in captivity, the caterpillars do not accept other bits of detritus, suggesting that they recognize and exclusively use corpses in nature and that this decoration is important to their survival. Given the context, it is possible that the array of partially consumed body parts and shed spider skins covering the case forms effective camouflage from a spider landlord; the caterpillars have never been found predated by spiders or wrapped in spider silk. Bone collector caterpillars have been recorded from the webs of at least four different species of spider in three different families, none of which is native to Hawaii, so adaptability to non-native elements is likely crucial to their persistence. Many of Hawaii's ecosystems are now dominated by non-native species, and dependence on native spiders would have made the survival of the bone collector lineage even more tenuous. Still, these caterpillars are only rarely encountered; >22 years of fieldwork and >150 field surveys in the area where they occur have yielded only 62 individuals, and most apparently suitable spider webs do not host them.

Fig. 2. Rotting wood log broken open to expose a bone collector caterpillar resting on a clump of webbing next to a non-native spitting spider (*Scytodes* sp.) with its egg sac. The web is partially obscured by termite and other wood-boring insect frass.

Ancient origins

The bone collector caterpillar belongs to *Hyposmocoma*, an endemic genus of small moths that is one of the most ecologically diverse adaptive radiations on the planet and, at 14 million years old, one of Hawaii's oldest (*7*). The genus contains >350 species occurring from the splash zones of the tropical shorelines to frigid alpine deserts on volcanic slopes >3200 m high, with each species typically restricted to a part of a single volcano on a single island (*8*, *9*). As shown by phylogenomic inference from 38 loci and subsequent molecular dating, there are nine major lineages of *Hyposmocoma*, most between 9 and 15 million years old, far older than the oldest current high island of Kaua'i (Fig. 3). The bone collector species is the only one known of its kind, representing a monotypic lineage without a sister species. Although it is related to the other carnivorous lineage of *Hyposmocoma*, their ancestors diverged more than 5 million years ago.

Uncertain future

Hawaii is an "extinction capital" of the world, with ongoing catastrophic losses of endemic flora and fauna [e.g., (*10*)]. This phenomenon extends to the archipelago's endemic invertebrate species, although their disappearances have gone largely undocumented. Despite >100 years of entomological surveys, the bone collector species has only been found in a 15-km^2 area of mesic forest in the Wai'anae mountain range on the island of O'ahu. Typically, an endemic Hawaiian lineage will contain multiple species with similar habits distributed across at least part of the archipelago [e.g., (*11*, *12*)], but no other member of the bone collector lineage has been found. Phylogenomic analysis shows that the bone collector lineage is at least 6 million years old, >3 million years older than the island of O'ahu (Fig. 3) (*13*). This suggests that the bone collector lineage once occurred on older islands such as Kaua'i or Nihoa, from which an ancestor dispersed to O'ahu. This ecology likely

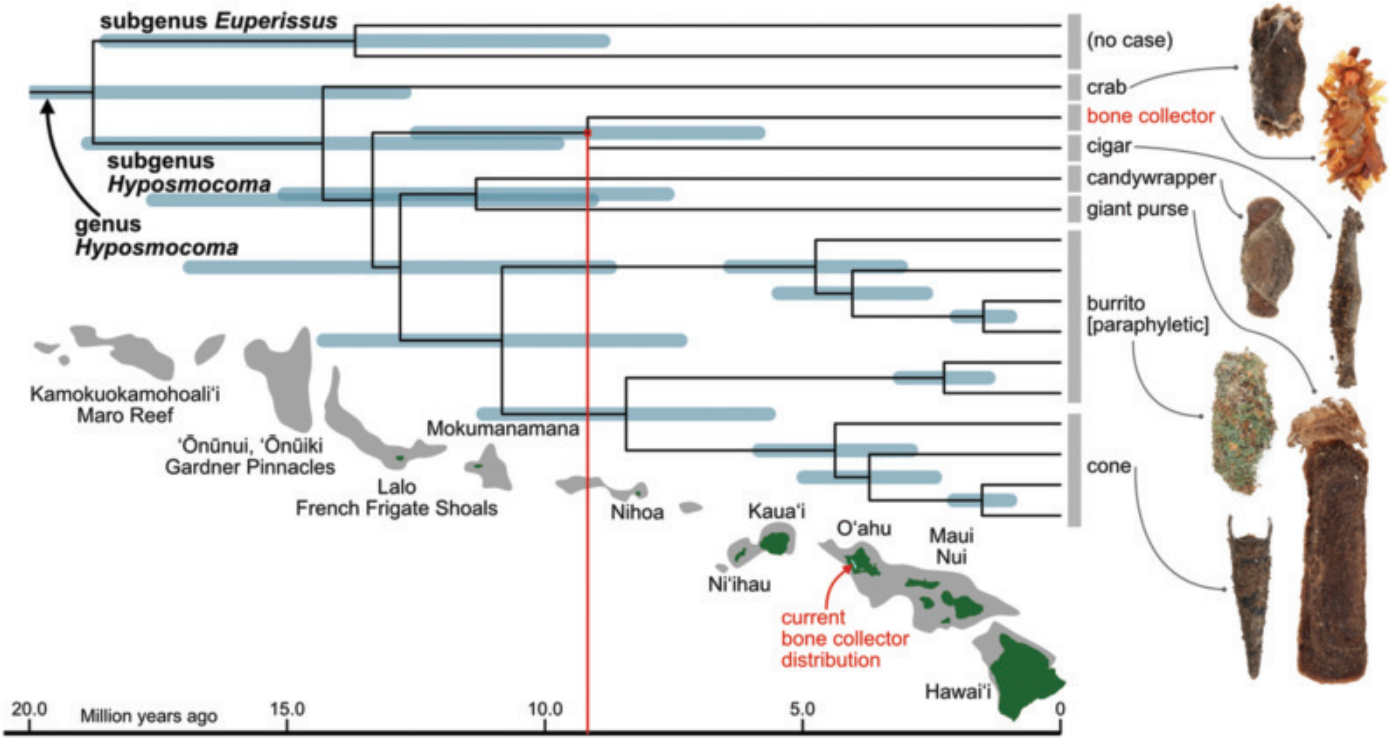

Fig. 3. Molecular phylogeny of *Hyposmocoma* lineages based on 38 genes and 82,875 aligned base pairs. The phylogeny was molecularly calibrated using age estimates from Kawahara *et al*. (*17*); 95% highest posterior density confidence intervals for the molecular dating estimates for nodes are indicated with blue bars. Outgroups are cropped, and the full tree is shown in the supplementary materials. Different lineages are indicated by their larval case type (*8*), and exemplar cases are shown on the right. Bone collector and cigar case species are the only ones that are carnivorous. Current terrestrial areas of the Hawaiian Island chain are shown in dark green; shallows that were once above sea level are shown in gray. The islands are placed along the timescale according to age and geographic position.

evolved on a now-subsided island in the Northwest Hawaiian Island chain, as did many lineages of *Hyposmocoma* (*8*) and other Hawaiian insects [e.g., *Drosophila* (*14*, *15*)]. The current range of the bone collector lineage is now limited to a single species holding on in a fragment of isolated forest that is increasingly beset with invasive species, exemplifying the vulnerability of many endemic Hawaiian insects and the ecosystems on which they depend. Although the bone collector species is able to use non-native spider hosts, it is still rarely found and its range is limited to a small area on one mountain on a single island. Population numbers may not be stable, and many factors leading to native insect decline in Hawaii (*10*) may also be affecting it, including introduced predators such as ants and parasitic wasps. It is unclear when bone collector caterpillars may have disappeared from Kaua'i, but it was before they could be discovered and may have been due to anthropogenic causes, as has been the case with most of Hawaii's historic extinctions [e.g., (*16*)]. Without conservation attention, it is likely that the last living representative of this lineage of carnivorous, body part–collecting caterpillars that has adapted to a precarious existence among spider webs will disappear.

REFERENCES AND NOTES

1. R. G. Gillespie, *Nature* **355**, 212–213 (1992).
2. S. Jordan, C. Simon, D. Polhemus, *Syst. Biol.* **52**, 89–109 (2003).
3. D. Rubinoff, W. P. Haines, *Science* **309**, 575 (2005).
4. D. Rubinoff, P. Schmitz, *Proc. Natl. Acad. Sci. U.S.A.* **107**, 5903–5906 (2010).
5. S. L. Montgomery, *GeoJournal* **7**, 549–556 (1983).
6. G. D. Ruxton, M. Stevens, *Biol. Lett.* **11**, 20150325 (2015).
7. R. G. Gillespie *et al.*, *J. Hered.* **111**, 1–20 (2020).
8. W. P. Haines, P. Schmitz, D. Rubinoff, *Nat. Commun.* **5**, 3502 (2014).
9. C. Doorenweerd, K. A. Austin, D. Rubinoff, *Proc. Hawaii. Entomol. Soc.* **55**, 29–44 (2023).
10. M. Medeiros *et al.*, *Proc. Hawaii. Entomol. Soc.* **45**, 149–166 (2013).
11. H. R. L. Lerner, M. Meyer, H. F. James, M. Hofreiter, R. C. Fleischer, *Curr. Biol.* **21**, 1838–1844 (2011).
12. D. H. Hembry *et al.*, *Q. Rev. Biol.* **96**, 247–296 (2021).
13. J. Y. Lim, C. R. Marshall, *Nature* **543**, 710–713 (2017).
14. S. M. Beverley, A. C. Wilson, *J. Mol. Evol.* **21**, 1–13 (1984).
15. P. O'Grady, R. DeSalle, *BioEssays* **40**, e1700246 (2018).
16. A. G. Boyer, *Divers. Distrib.* **14**, 509–517 (2008).
17. A. Y. Kawahara *et al.*, *Proc. Natl. Acad. Sci. U.S.A.* **116**, 22657–22663 (2019).
18. DNA sequence alignments, software scripts, and result files for: D. Rubinoff, M. San Jose, C. Doorenweerd, Hawaiian caterpillar patrols spiderwebs camouflaged in insect prey's body parts, Dryad (2025); https://doi.org/doi:10.5061/dryad.p8cz8wb1d.
19. Data for: A. Kawahara *et al.*, Phylogenomics reveals the evolutionary timing and pattern of butterflies and moths. Dryad (2019); https://doi.org/10.5061/dryad.j477b40.

ACKNOWLEDGMENTS

We thank the Army Natural Resource Program on O'ahu, Hawai'i Department of Land and Natural Resources, Kunia Loa Ridge Farmlands, R. Peralta, C. King, J. Matsunaga, T. Anuhealii, W. Haines, K. Austin, S. Pote, J. Reil, M. Haubner, S. Schachat, D. Nitta, T. Reisland, S. Geib, J. Dupuis, P. Krushelnycky, and R. Gillespie for research permits, assistance, and/or advice. **Funding:** This project was funded in part by USDA Cooperative State Research, Education and Extension (CSREES) project HAW00942-H, administered by the College of Tropical Agriculture and Human Resources, University of Hawai'i at Mānoa. **Author contributions:** D.R. led project conception and contributed to fieldwork, analyses, and writing. M.S. led analyses and contributed to writing and fieldwork. C.D. contributed to fieldwork, analyses, and writing. **Data and materials availability:** All DNA sequence alignments, software scripts, and result files are available on Dryad (*18*). The raw sequencing reads used for this study are available on NCBI GenBank Bioproject PRJNA1143550. The original sequence data used in (*17*) are available at Dryad (*19*).

SUPPLEMENTARY MATERIALS

science.org/doi/10.1126/science.ads4243
Materials and Methods
Fig. S1
Table S1
References (*20*–*30*)
MDAR Reproducibility Checklist
Movie S1

Submitted 12 August 2024; resubmitted 5 December 2024
Accepted 26 February 2025
10.1126/science.ads4243

ELECTROCHEMISTRY

Polyoxometalated metal-organic framework superstructure for stable water oxidation

Kaihang Yue[1,2,3]†, Ruihu Lu[4]†, Mingbin Gao[5]†, Fei Song[6], Yao Dai[1], Chenfeng Xia[2], Bingbao Mei[6], Hongliang Dong[7], Ruijuan Qi[8], Daliang Zhang[9], Jiangwei Zhang[10]*, Ziyun Wang[4]*, Fuqiang Huang[11]*, Bao Yu Xia[2,12]*, Ya Yan[1,3]*

Stable, nonprecious catalysts are vital for large-scale alkaline water electrolysis. Here, we report a grafted superstructure, MOF@POM, formed by self-assembling a metal-organic framework (MOF) with polyoxometalate (POM). In situ electrochemical transformation converts MOF into active metal (oxy) hydroxides to produce a catalyst with a low overpotential of 178 millivolts at 10 milliamperes per square centimeter in alkaline electrolyte. An anion exchange membrane water electrolyzer incorporating this catalyst achieves 3 amperes per square centimeter at 1.78 volts at 80°C and stable operation at 2 amperes per square centimeter for 5140 hours at room temperature. In situ electrochemical spectroscopy and theoretical studies reveal that the synergistic interactions between metal atoms create a fast electron-transfer channel from catalytic iron and cobalt sites, nickel, and tungsten in the polyoxometalate to the electrode, stabilizing the metal sites and preventing dissolution.

Water electrolysis is a critical technology for renewable energy conversion and storage (*1*–*7*). Commercial systems require efficient, stable, and earth-abundant catalysts, particularly for alkaline water oxidation, in which first-row (*3d*) transition-metal (oxy)hydroxides have shown promise over the past decades (*8*–*13*). However, achieving the required activity and stability at industrial-scale current densities remains challenging, primarily due to the substantial overpotential needed to drive water oxidation at the desired current densities. Under these operational conditions, the active phase, typically metal (oxy)hydroxides, often degrades due to dissolution of catalytic metal sites or phase segregation (*14*–*16*). One critical limitation arises from the inherently weak interactions between metal atoms and oxygen, rendering active metal sites susceptible to dissolution in the electrolyte. Additionally, the high potential for water oxidation can induce localized structural distortions in the catalyst, resulting in mechanical degradation, such as the peeling of active sites or phases (*14*, *17*). Despite various strategies to enhance activity and stability, achieving sustained, long-term operation at high current densities under

[1]State Key Laboratory of High Performance Ceramics and Superfine Microstructure, Shanghai Institute of Ceramics, Chinese Academy of Sciences, Shanghai, China. [2]School of Chemistry and Chemical Engineering, State Key Laboratory of Materials Processing and Die & Mould Technology, Key Laboratory of Material Chemistry for Energy Conversion and Storage (Ministry of Education), Hubei Key Laboratory of Material Chemistry and Service Failure, Wuhan National Laboratory for Optoelectronics, Huazhong University of Science and Technology (HUST), Wuhan, China. [3]Center of Materials Science and Optoelectronics Engineering, University of Chinese Academy of Sciences, Beijing, China. [4]School of Chemical Sciences, University of Auckland, Auckland, New Zealand. [5]National Engineering Laboratory for Methanol to Olefins, Dalian Institute of Chemical Physics, Chinese Academy of Sciences, Dalian, China. [6]Shanghai Synchrotron Radiation Facility, Shanghai Advanced Research Institute, Chinese Academy of Sciences, Shanghai, China. [7]Center for High Pressure Science and Technology Advanced Research, Shanghai, China. [8]Key Laboratory of Polar Materials and Devices (MOE), Department of Electronics, East China Normal University, Shanghai, China. [9]Multiscale Porous Materials Center, Institute of Advanced Interdisciplinary Studies and School of Chemistry and Chemical Engineering, Chongqing University, Chongqing, China. [10]College of Energy Material and Chemistry; Inner Mongolia Key Laboratory of Low Carbon Catalysis, Inner Mongolia University, Hohhot, China. [11]State Key Lab of Metal Matrix Composites, School of Materials Science and Engineering, Shanghai Jiao Tong University, Shanghai, China. [12]Center for Next-Generation Energy Materials and School of Chemical Engineering, Sungkyunkwan University (SKKU), Seobu-ro, Jangan-gu, Suwon, Gyeonggi-do, Republic of Korea.
***Corresponding author. E-mail: zjw11@tsinghua.org.cn (J.Z.); ziyun.wang@auckland.ac.nz (Z.W.); huangfq@sjtu.edu.cn (F.H.); byxia@hust.edu.cn (B.Y.X.); yanya@mail.sic.ac.cn (Y.Y.)**
†These authors contributed equally to this work.

future industrial conditions remains a formidable challenge (*18*–*20*).

In this work, we report a grafted superstructure of MOF@POM derived from the self-assembly of a metal-organic framework (MOF) and polyoxometalate (POM), followed by an electrochemical transformation into monolayer CoFe oxyhydroxides (CoFe-LDH) grafted onto POM. The transformation involves a two-dimensional (2D) CoFe-MOF precursor undergoing phase transitions to form monolayer CoFe-LDH grafted on POM while also serving as a reservoir of predefined active metal sites (Co and Fe) under water oxidation conditions. The resulting catalysts exhibit substantial activity and stability in water electrolysis, achieving a low overpotential of 178 mV at a current density of 10 mA cm^{-2}. When incorporated into an anion exchange membrane water electrolyzer (AEMWE), the system delivers a current density of 3 A cm^{-2} at an applied voltage of 1.78 V, meeting the US Department of Energy's (DOE's) 2025 target for 2035 AEM technologies (1.8 V at 3 A cm^{-2}) (*21*). Furthermore, the AEMWE demonstrates stable operation for >5140 hours at a current density of 2 A cm^{-2} under ambient conditions. In situ electrochemical investigations combined with computational studies reveal that interactions between metal atoms, including W, Ni, Co, and Fe, establish a rapid electron-transfer channel. This channel facilitates efficient electron transport from CoFe catalytic sites to electrodes, protecting the catalytic sites from dissolution. Additionally, the Ni interlayer functions as an elastic deformation interlayer, stabilizing the active metal (oxy)hydroxide phase. These synergistic effects contribute to substantial improvements in both the activity and durability of AEMWE systems.

Synthesis and structural examination

The synthesis of MOF@POM involves a dual-template assembly process (fig. S1). First, a CoFe-MOF forms through the self-coordination of Fe^{3+} and Co^{2+} with 1,4-benzenedicarboxylic acid (*11*), chosen for its layered structure, which promotes axial growth and enhances the interaction and stability of POM-Ni-MOF stacking. This formation process is accompanied by the decomposition of symmetric PW_9-Ni_4 into a trilacunary Keggin anion, $[PW_9O_{34}]^{9-}$ (PW_9) (*22*–*26*). Subsequently, the CoFe-MOF reassembles with PW_9, facilitated by the Ni–O bridge, to form the innovative MOF@POM superstructure (Fig. 1A). Ab initio molecular dynamics simulations corroborate this self-assembly process of MOF with POM, revealing a gradual decrease in surface energy, as evidenced by the reducing distance between the Ni atoms in POM and the O atoms in MOF during self-assembly (figs. S2 and S3). Scanning electron microscopy (SEM) images display a petal-like morphology for MOF@POM (Fig. 1B), which exhibits a more uniform and ordered arrangement compared with the pure MOF (fig. S4). Atomic force microscopy (AFM) measurements confirm a monolayer thickness of 3.54 ± 0.18 nm for MOF@POM (Fig. 1C), in contrast to the pure MOF monolayer thickness of 1.73 ± 0.17 nm, highlighting the successful grafting of POM (fig. S5). Furthermore, spherical aberration–corrected transmission electron microscopy (TEM) reveals thin lamellar structures (fig. S6). High-resolution TEM (HRTEM) images, coupled with selected area electron diffraction (SAED) patterns (Fig. 1D), highlight the crystalline facets within the MOF@POM, with a crystalline spacing of 0.63 nm, consistent with the pure MOF (fig. S7). X-ray diffraction (XRD) results corroborate this observation of the (200) and (001) facets for the MIL-53 MOF (fig. S8), confirming the presence of the MOF within the MOF@POM superstructure (*27*). Fourier transform infrared (FTIR) spectroscopy also validates the presence of characteristic absorption peaks of PW_9 within the MOF@POM superstructure (fig. S9) (*22*). Thermogravimetric analysis of MOF@POM and the pure MOF reinforce these findings. The presence of POM enhances the mass retention of the MOF (fig. S10). High-angle annular dark-field scanning transmission electron microscopy analysis of MOF@POM, coupled with elemental mapping (fig. S11 and table S1), provides definitive evidence of the uniform distribution of Co, Fe, Ni, C, O, P, and W within the superstructure.

Full-range synchrotron pair distribution function (PDF) analysis provides a detailed view of the atomic structure of MOF@POM (fig. S12). Further validation is achieved by fitting the PDF data to a structural model based on Fig. 1A. This fit shows excellent agreement ($R^2 \approx 0.88$) with the experimental results, confirming the presence of the MOF@POM superstructure (Fig. 1E). Each peak in Fig. 1E corresponds to specific atom pairs within the model (table S2). For instance, peak 1 corresponds to the distance between the O–W and O–Ni atom pairs. The correlation of the O–W pair across multiple peaks (1 to 16) provides evidence for the long-range order of the MOF@POM superstructure. Partial-PDF (p-PDF) analysis further characterized the MOF@POM structure. A

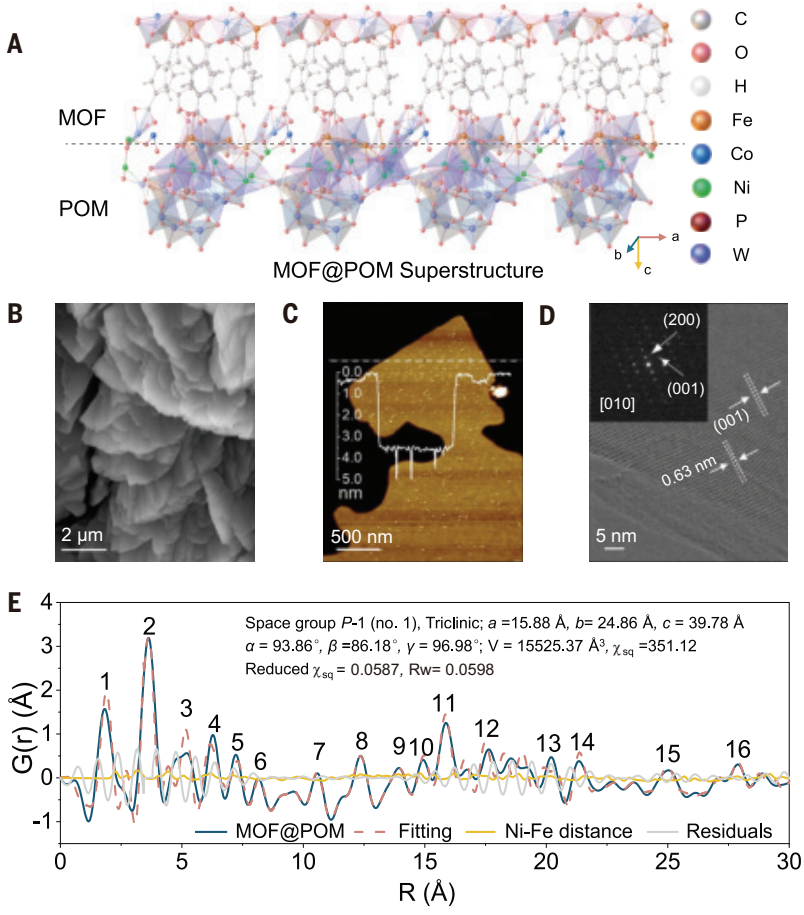

Fig. 1. Structural characterization. (**A**) Mercury-visualized structure model of the MOF@POM superstructure. (**B**) SEM image of MOF@POM. (**C**) AFM image of MOF@POM. (**D**) Spherical aberration-corrected TEM image of MOF@POM. Inset shows the SAED pattern. (**E**) Full-range synchrotron PDF analysis for MOF@POM, with the corresponding Rietveld refinement and the calculated partial PDF patterns of the Ni–Fe distance.

comparison of the p-PDF results with a structural model focused on the Ni–Fe interaction (fig. S13) reveals excellent agreement between the theoretical and experimental Ni–Fe distances. This alignment supports the hypothesis that the characteristic W–O peaks observed in the FTIR spectra originate from POM semiclusters. Moreover, this agreement between the p-PDF data and the structural model suggests a specific attachment motif for the POM moiety to the MOF. This attachment primarily occurs through the intermediary Ni sites. Accordingly, the crystal structure can be described as follows: The Ni atom acts as a bridge connecting the metal node layer of the MOF with the W–O layer of PW_9. This linkage is further stabilized by Ni–O interactions between two Ni atoms, resulting in a robust superstructure substrate that anchors the POM clusters.

Water oxidation performance

Cyclic voltammetry (CV) measurements reveal the exceptional activity of MOF@POM for water oxidation. Considering the significant impact of the metal ratio of Fe and the proportion of POM on the catalytic performance (figs. S14 and S15) (*28*–*30*), the optimized MOF@POM demonstrates a very low overpotential of only 178 mV at a current density of 10 mA cm^{-2} (Fig. 2A). This performance surpasses that of the pure MOF (203 mV) and commonly used CoFe-LDHs (250 mV) and NiFe-LDHs (220 mV). The low water oxidation current density observed for pure POM highlights the crucial role of the synergetic effect achieved through grafting in the MOF@POM superstructure (fig. S16). Analysis of the turnover frequency (TOF) calculated using the actual active site numbers obtained from the CV curves (fig. S17) indicates that the TOF of Co and Fe (TOF_{Co+Fe}) in MOF@POM is 78 times higher that of pure MOF at the overpotential of 200 mV (fig. S18). Consequently, the mass activity of MOF@POM is >7 times greater than that of pure MOF (fig. S19). The Tafel slopes for CoFe-LDHs and NiFe-LDHs are 42.9 and 45.5 mV dec^{-1}, respectively, at 1.50 V versus the reversible hydrogen electrode (RHE) (fig. S20), which align with the 46 mV dec^{-1} reported for oxidized Ni, Co, and Fe electrodes in alkaline conditions (*31*). This indicates that the rate-determining step involves the formation of a superoxy (–OOH) intermediate. For MOF and MOF@POM, the Tafel slopes decrease to 37.0 and 27.7 mV dec^{-1}, respectively, which can be attributed to the in situ formation of single-layer LDHs (*32*) and POM grafting. The lowest Tafel slope observed for MOF@POM suggests a significant enhancement in catalytic OER activity (*2*, *33*–*35*). Electronic conductivity is a critical factor for determining catalyst activity (*7*, *36*, *37*). Combined results of electrochemical impedance spectroscopy and ultraviolet photoelectron spectroscopy reveal that MOF@POM has the lowest charge-transfer resistance among the tested samples (figs. S21 and S22). Two-probe resistivity measurements confirm that the electrical conductivity of MOF@POM is higher than that of pristine MOF (fig. S23). This indicates that POM grafting provides a more efficient electron-transfer pathway within the MOF, leading to a significant increase in the TOF of the Co and Fe sites. Moreover, under a three-electrode system, MOF@POM demonstrates exceptional stability, showing negligible degradation for 1000 hours at a current density of 100 mA cm^{-2} (fig. S24 and S25). This performance is quite competitive with previously reported catalysts for water oxidation (tables S3 and S4).

Furthermore, the AEMWE cell constructed with MOF@POM exhibits a significantly lower voltage requirement than the cell constructed

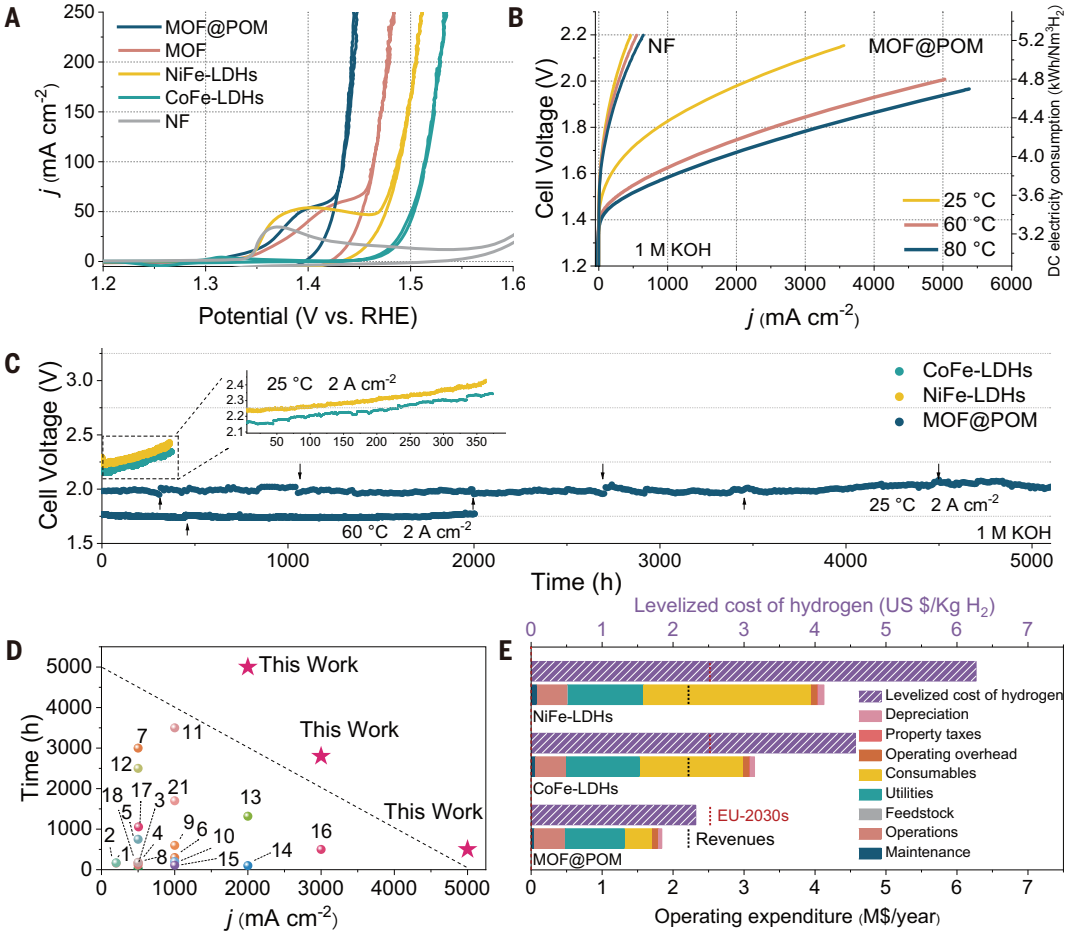

Fig. 2. Electrochemical measurements. (**A**) CV curves of MOF, MOF@POM, and the reference samples. (**B**) Polarization curves of the AEMWE cell using MOF@POM as the anode (AEM: Sustainion X37-50 Grade T, cathode: 20% Pt/C). (**C**) Long-term durability of the AEMWE cell at 2 A cm^{-2} (AEM: Sustainion X37-50 Grade T, cathode: 20% Pt/C, electrolyte: 1 M KOH). At the positions indicated by the arrows, the fresh electrolyte was replaced in the electrolyzer. (**D**) Relationship between current and time during continuous long-term durability tests in AEMWE using different electrocatalysts (the references are given in table S7). (**E**) Economic analysis of the operational costs of different catalysts and the leveled cost of hydrogen production.

from pure MOF. At 25°C, a current density of 1 A cm^{-2} is achieved with a cell voltage of only 1.83 V for MOF@POM, whereas the pure MOF cell requires nearly 1.97 V (Fig. 2B and figs. S26 to S27). The results obtained from focused ion beam scanning electron microscopy demonstrate that the performance differences between the two are not attributable to the contact interface between the catalyst and the current collector (fig. S28). Even under simulated real-world operation conditions (1 M KOH, 60° to 80°C), MOF@POM displays exceptional activity, achieving a current density of 2 A cm^{-2} with a very efficient cell voltage of only 1.69 V at 80°C (corresponding to an energy consumption of 4.04 kWh Nm^{-3} H_2). Increasing the cell voltage to 2.0 V enables a current density exceeding 5.5 A cm^{-2} (at this point, the background current of pure Ni foam is only 0.23 A cm^{-2}). By comparison, a mere 1.78 V is sufficient to achieve a current density of 3 A cm^{-2}, surpassing the ambitious AEM future 2035 requirements (1.8 V at 3 A, mentioned in the DOE 2025 target) (Fig. 2B) (*21*).

A rigorous stability evaluation revealed the excellent durability of MOF@POM in AEMWE. The MOF@POM cell shows a decay rate of only 0.015 mV h^{-1} after 2000 hours of operation at 1 A cm^{-2}, meeting the DOE 2025 target (*21*). By contrast, the decay rate of the pure MOF cell reaches nearly 1 mV h^{-1} within the first 300 hours at the same current density, after which it degrades further, exceeding 4 mV h^{-1} (fig. S29). This highlights the significant role of the grafted POM in enhancing the catalytic stability of MOF@POM. Compared with the CoFe-LDH and NiFe-LDH catalysts synthesized using typical methods, the MOF@POM exhibits higher stability. At 25°C, MOF@POM maintains a current density of 2 A cm^{-2} for 5140 hours with a minimal decay rate of 0.02 mV h^{-1}. By contrast, these metal (oxy)hydroxides show a significant decay rate within 100 hours (Fig. 2C). This exceptional stability is maintained even at elevated temperatures (60°C). Moreover, MOF@POM exhibits commendable stability at higher current densities (3, 5, and 10 A cm^{-2}) for extended durations (3000, 500, and 200 hours, respectively), with minimal performance fluctuations, suggesting potential adaptability to fluctuating green electricity (figs. S30 to S32). Analysis of the decay rates across the current density range of 1 to 10 A cm^{-2} reveals a slow linear ($y = 0.0067 + 0.0075x$, with a coefficient of determination $R^2 \approx 0.96$) decay for MOF@POM at lower current densities (up to 5 A cm^{-2}). However, the decay rate transitions to exponential ($y = 0.111e^{0.3067x}$, with a coefficient of determination $R^2 \approx 0.99$) at higher current densities (10 A cm^{-2}) (fig. S33). This behavior contrasts with the rapid linear decay observed for CoFe/NiFe-LDHs at 2 A cm^{-2} (Fig. 2C) and the exponential decay of the pure MOF at 1 A cm^{-2} (fig. S29). These findings suggest that a structurally stable catalyst exhibits a linear decay profile within a specific current density range, whereas unstable structures experience exponential decay.

The exceptional stability of MOF@POM during AEMWE operation is evidenced by its superior preservation of active sites. To gain insight into the behavior of active metal sites during AEMWE operation, the S number, which reflects the stability of active sites based on metal dissolution in the electrolyte, was calculated (table S5) (*38*). MOF@POM exhibits the highest S number, surpassing those of CoFe-LDHs, NiFe-LDHs, and even the MOF by a significant margin (fig. S34), which indicates that MOF@POM loses fewer active sites during water oxidation. The activity stability factor, which correlates the rate of metal dissolution with the O_2 production rate, was also used (figs. S34 and S35) (*14*, *39*). The activity stability factor of MOF@POM is nearly an order of magnitude greater than that of the pure MOF, CoFe-LDHs, and NiFe-LDHs. This finding experimentally supports the exceptional stability of the POM-grafted CoFe (oxy)hydroxide (table S6).

Techno-economic analysis

The performance merits of MOF@POM were further evaluated by considering both the activity and durability of the AEMWE. Compared with existing electrocatalysts, MOF@POM demonstrates superior stability and efficiency across a range of current densities (Fig. 2D, figs. S36 and S37, and table S7). A preliminary techno-economic analysis (TEA) was conducted to explore the economic and sustainability benefits of MOF@POM-based AEMWE systems (Fig. 2E and supplementary note). This analysis considers factors such as annual operating expenditure and the levelized cost of hydrogen (LCOH). The TEA calculations demonstrate that MOF@POM results in the lowest annual operating expenditure and highest profitability compared with the CoFe-LDHs and NiFe-LDHs catalysts, showing negative revenue projections. Considering a 10-year lifetime for 100 m^2 AEMWEs operating at 2 A cm^{-2}, MOF@POM enables green hydrogen production at a competitive LCOH of US$2.324 per kg H_2, which is lower than the European Commission's 2030 target (<$2.5 per kg H_2). Compared with MOF@POM, the TEA results for the CoFe-LDHs and NiFe-LDHs systems yield significantly higher LCOHs. Furthermore, an AEM electrolyzer in the laboratory assembled with a MOF@POM anode (5 × 5 cm^2) can achieve a current of 70 A (2.8 A cm^{-2}) at a voltage of 1.98 V at 25°C, demonstrating the scalability of the MOF@POM catalyst for large-scale applications (fig. S38).

Investigation of structural evolution

We systematically investigated the structural transformation of MOF@POM during the water oxidation process. After complete activation of MOF@POM during water oxidation, MOF@POM (MOF@POM-act) maintains its excellent structural integrity, whereas the pure MOF (MOF-act) undergoes significant degradation and structural collapse (fig. S39). HRTEM images reveal subtle changes in the lattice stripes, consistent with the formation of CoFe-related metal (oxy)hydroxide, the catalytically active phase (fig. S40). XRD characterization corroborates these observations, showing that the MOF@POM structure transitions from its initial state to a mixed state of MOF and hydroxide, ultimately forming the desired CoFe-related metal (oxy)hydroxides (Fig. 3A and fig. S41) (*40*). Furthermore, AFM measurements confirm a significant reduction in the lamellar thickness of MOF@POM from 3.54 ± 0.18 to 1.47 ± 0.20 nm upon ligand detachment (fig. S42). In situ Raman spectroscopy provides real-time insights into surface structure changes (Fig. 3B and fig. S43). As the applied potential increases, characteristic Raman peaks associated with organic components at 1611, 1422, 633, and 376 cm^{-1} diminish. At a potential of 1.53 V versus RHE, these peaks nearly disappear, replaced by new peaks (540 to 465 cm^{-1}), indicating the formation of hydroxyl oxide species (*41*). This transformation occurs only upon an applied potential, underscoring its dependence on water oxidation (fig. S44). Unlike the pure MOF, the surface state of MOF@POM transitions to metal (oxy)hydroxide only after ~5 min at a voltage of 1.63 V versus RHE (Fig. 3B). This behavior aligns well with the results from in situ FTIR spectroscopy (fig. S45). This phenomenon was further corroborated by x-ray photoelectron spectroscopy of MOF-act and MOF@POM-act after the stability test (figs. S46 and S47). The emergence of a new peak in the O 1s spectrum corresponding to M–OH and an increase in the valence state for Co and Fe confirms the in situ conversion of MOF@POM to a metal (oxy)hydroxide-grafted POM catalyst during water oxidation.

The MOF@POM-act superstructure was further validated through PDF analysis and detailed investigations of its atomic and periodic structural relationships. The detected PDF of MOF@POM-act demonstrates excellent alignment with the model presented in Fig. 3C (fig. S48). The preservation of PW_9 clusters in the MOF@POM-act superstructure was further confirmed through the p-PDF of Ni–Fe (fig. S49A). Detailed analysis of Ni–Ni interlayer atomic distances reveals two primary contributions from bond pairs (Fig. 3C): one originating from a single PW_9 cell (marked in pink) and another from interactions between two PW_9 cells (marked in green). The peaks before 9 Å, such as Ni_1–Ni_2, correspond to Ni sites within a single PW_9, whereas a distinct contribution at 9.12 Å indicates interactions between multiple POMs. The most pronounced

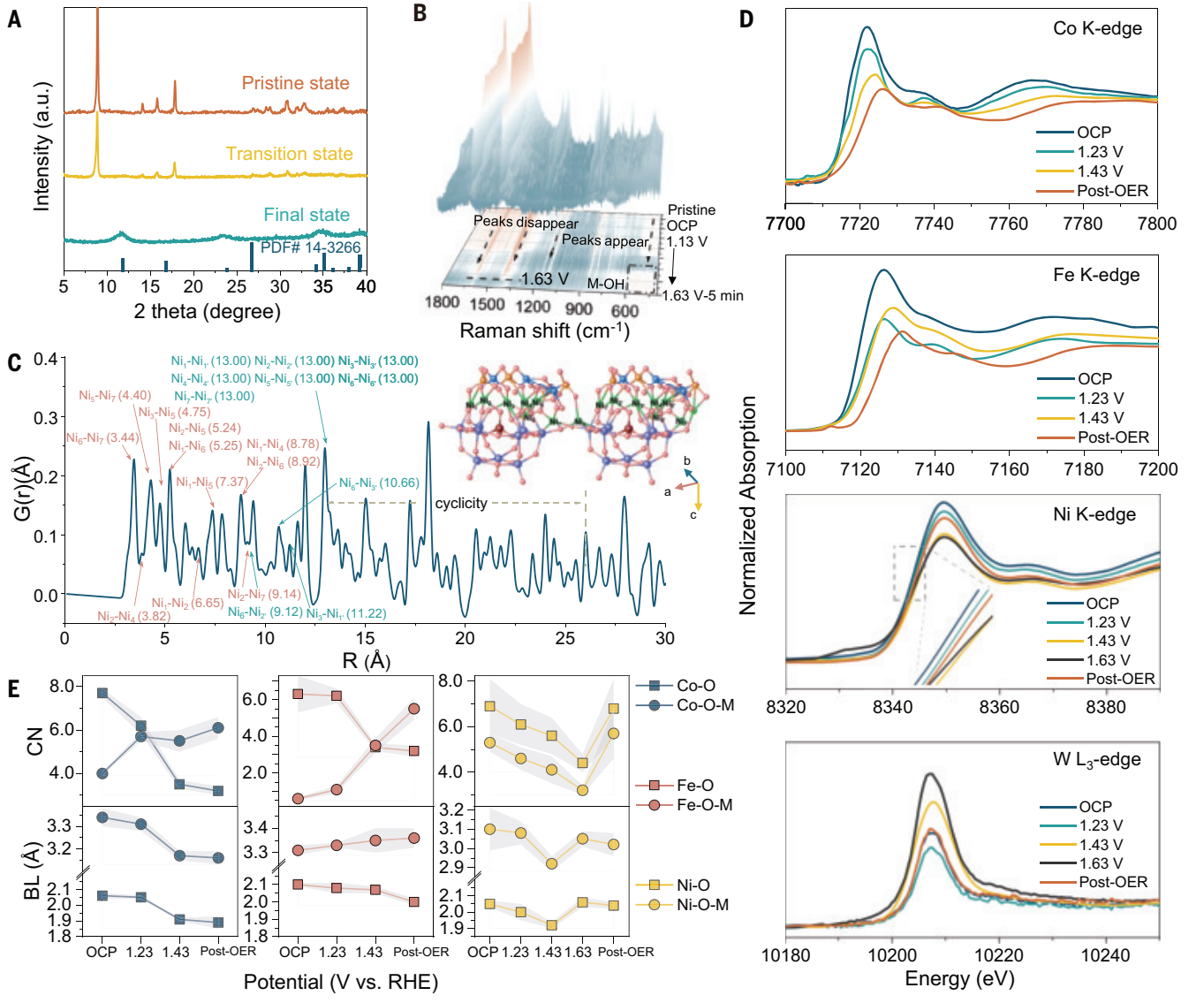

Fig. 3. Structural evolution. (**A**) XRD comparison of MOF@POM in different states during the water oxidation. (**B**) In situ Raman spectra of MOF@POM during the water oxidation process. (**C**) p-PDF fitting of Ni-Ni in MOF@POM-act. (**D**) XANES spectra of Co, Fe, Ni, and W at different potentials of MOF@POM. (**E**) Variation in the bond lengths and coordination numbers of the Co (Fe, Ni)–O and Co (Fe, Ni)–O–M coordination shells obtained from the XAS absorption spectra of MOF@POM during water oxidation.

inter-POM atomic contribution appears at 13 Å, resulting from bond pairs across multiple POMs located at the same site. Analogous peak positions are identified at larger distances, such as the 13 Å extension to the next cell at 26 Å. A similar pattern emerges in the p-PDF of Ni-W (fig. S49B), with the distance relationships mirroring the periodic structure. These findings collectively validate that the MOF@POM-act superstructure aligns well with the monocrystalline cell.

Catalytic behavior analysis

The transformation of MOF@POM during water oxidation reveals distinct roles of Co, Fe, and Ni. The x-ray absorption near edge structure (XANES) spectrum (Fig. 3D and fig. S50) shows a rapid increase in the valence states of the Co and Fe sites as the applied potential increases (fig. S51). Extended x-ray absorption fine structure analysis (Fig. 3D and fig. S52) indicates that the coordination environments of Co and Fe transition from M–O (where M = Co or Fe) to M–OH and ultimately to M–OOH. This conclusion is supported by the observation that the M–O bond length in the MOF exceeds 2 Å, whereas it is ~1.9 Å in M–OOH (*42*). This change signifies the formation of oxyhydroxide species and confirms that Co and Fe sites on the surface of the MOF@POM catalyst transform into the genuine active phase M–OOH, which is widely recognized as the true active phase for most alkaline water oxidation catalysts (*42*). By contrast, the behavior of Ni atoms, which act as the intermediate layer in the superstructure, differs significantly during this process (Fig. 3D and fig. S52). Although Ni initially exhibits a valence increase upon potential application, this change is less pronounced. Furthermore, the Ni K-edge shifts back toward its initial position after catalyst reconstruction, indicating that the Ni sites do not transition into an irreversible Ni–OOH state, which is different from the in situ XAS data previously reported for Ni as the active site (*43*–*45*). A similar phenomenon is observed for the W sites (Fig. 3D). The final Ni–O coordination layer in the MOF@POM-act closely resembles that in the freshly prepared MOF@POM material. These observations confirm that Ni does not serve as a catalytic active

site during the water oxidation process; on the contrary, it undergoes elastic deformation during the structural transformation process. The changes in oxidation states of Ni and W observed during the water oxidation process indicate their involvement in electron transfer from CoFe sites to the electrode. Ni sites act as intermediate connectors in the upper structure, stabilizing the active phase, whereas POM primarily serves as an electron-transfer carrier (*46*, *47*), enhancing conductivity during the water oxidation process.

To provide a comprehensive understanding of the stable mechanism of metal active sites during the water oxidation process, the bonding state between adjacent metals and oxygen in the layer was analyzed. As shown in fig. S53, MOF@POM-act and MOF-act materials exhibit shorter M–M and M–O bond lengths. This result stems from the self-optimization of the catalysts during structural transformation, suggesting that metal (oxy)hydroxide has a more stable coordination environment than the initial MOF materials. After the transformation, the bond lengths of M–M and M–O remain relatively stable despite increases in applied potential. This observation is consistent with the minimal K-edge shifts detected at various voltages, indicating that the catalyst no longer undergoes significant structural changes after the reconfiguration (figs. S54 and S55). The Ni sites maintain consistent coordination numbers for M–O and M–O–M throughout this process (Fig. 3E). In particular, after the cessation of the applied potential, the coordination numbers of both M–O and M–O–M of the Ni sites nearly return to their initial state. These in situ XAS observations for Ni over the MOF@POM catalyst reveal that the Ni sites serve as elastic deformation modulators, preserving a stable coordination environment for the Co and Fe sites during structural transformation, as well as the water oxidation process. This role ensures sustained catalytic activity.

Theoretical calculation of catalytic mechanism

We used density functional theory to determine the effect of POM grafting on the water oxidation performance of the MOF@POM-act superstructure, especially for long-term water oxidation operation. In accordance with our p-PDF fitting of the MOF@POM-act structure and the evolved active species for the water oxidation, we constructed and modeled single-layer $Co_{0.5}Fe_{0.5}OOH$ grafted onto POM (CCDC-2421729) (Fig. 4A). A thermodynamic dissolution diagram was calculated to predict the stable phase of single-layer $Co_{0.5}Fe_{0.5}OOH$ and POM/$Co_{0.5}Fe_{0.5}OOH$ relative to dissolutive phases under high oxidative potential and pH conditions (figs. S56 to S58) (*48*). $Co_{0.5}Fe_{0.5}OOH$ on POM is more stable than bare $Co_{0.5}Fe_{0.5}OOH$ under water oxidation conditions (pH = 14). In addition, the electrochemical phase diagram (at pH = 14) confirms the enhanced stability of POM/$Co_{0.5}Fe_{0.5}OOH$ over $Co_{0.5}Fe_{0.5}OOH$ (Fig. 4B and figs. S59). As the potential increases, $Co_{0.5}Fe_{0.5}OOH$ is a thermodynamically stable phase up to 1.48 V versus RHE (Fig. 4C). Beyond this potential, phases that tend to dissolve become thermodynamically favored. Through the grafting of POM, $Co_{0.5}Fe_{0.5}OOH$ can be stabilized at potentials up to 1.80 V versus RHE. Considering the dissolution energy barrier reported in the literature (G_a = ~0.4 eV) (fig. S60), we calculated that the degradation time can be expressed as a function of the reaction energy and barrier using the Arrhenius equation (Fig. 4C). The Fe and Co sites in traditional $Co_{0.5}Fe_{0.5}OOH$ can quickly dissolve into the electrolyte at 2.0 V versus RHE. This rapid dissolution leads to low stability, often limiting the operational life of these materials to significantly less than 2000 hours. By contrast, at the same potential, introducing POM substantially suppresses the dissolution of Fe and Co sites,

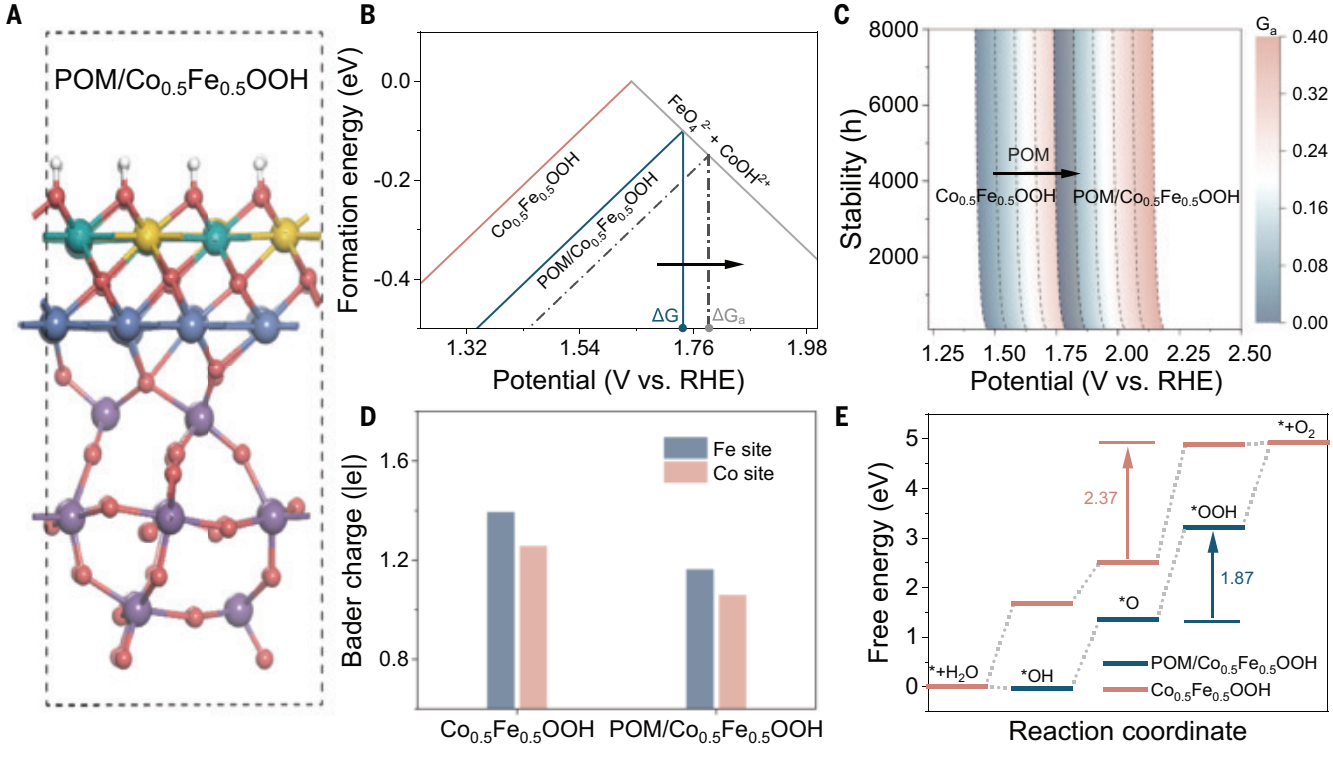

Fig. 4. Theoretical investigations. (**A**) Side view of POM-supported POM/$Co_{0.5}Fe_{0.5}OOH$. The white, red, pink, yellow, green, blue, and purple spheres represent H, O, P, Fe, Co, Ni, and W atoms, respectively. (**B**) Formation energies of the $Co_{0.5}Fe_{0.5}OOH$, POM/$Co_{0.5}Fe_{0.5}OOH$, and dissolved (FeO_4^{2-} + $CoOH^{2+}$) phases expressed as a function of potential. The dotted line shows that the dissolution barrier is greater than the reaction energy. (**C**) Stability (10% sites/dissolution rate) is a function of the working potential and dissolution barrier. (**D**) Charge state of the Fe and Co sites on $Co_{0.5}Fe_{0.5}OOH$ and POM/$Co_{0.5}Fe_{0.5}OOH$. (**E**) Free energy profile of the water oxidation on $Co_{0.5}Fe_{0.5}OOH$ and POM/$Co_{0.5}Fe_{0.5}OOH$. The arrow and number indicate the corresponding energy change in the rate-determining step (RDS).

allowing $Co_{0.5}Fe_{0.5}OOH$ to work for up to ~5000 hours, notably improving the stability of the transition metal compounds. This theoretical prediction is in good agreement with the active decay pattern observed in the experimental data (Fig. 2C). Moreover, the decay of the catalyst activity exhibits linear behavior below 2.0 V, as shown in Fig. 4C. This theoretical prediction is in good agreement with the active decay pattern collected from experimental data (Fig. 2C and fig. S33), providing an insightful methodology for the screening of highly active and stable catalysts.

In addition, we calculated the electronic structure to study the mechanism of long-term stability. According to the calculated charge difference density, electron transfers from the Ni atom to the $Co_{0.5}Fe_{0.5}OOH$ reduce the charge state of the Fe and Co sites for catalyzing the water oxidation (Fig. 4D and fig. S61). This effectively prevents Fe and Co sites from the high-charge state to overoxidation during the water oxidation process, thereby mitigating their dissolution. Conversely, a high–water oxidation overpotential (corresponding to low activity) forces the Fe and Co sites to catalyze the water oxidation at relatively high potentials, which is also a reason for overoxidation. Diminishing the impact of potential on the dissolution of Fe and Co atoms is a way to improve stability. We analyzed the water oxidation activity of $Co_{0.5}Fe_{0.5}OOH$ with and without POM by calculating the free energy change of the water oxidation (Fig. 4E). The highest energy change of 2.37 eV occurs during the *OOH formation step on $Co_{0.5}Fe_{0.5}OOH$, indicating a greater energy requirement for *OOH formation compared with other intermediates (*35*). This is consistent with the tested Tafel slopes, suggesting that *OOH formation is the rate-determining step, with an associated overpotential of 1.14 V. By contrast, POM/$Co_{0.5}Fe_{0.5}OOH$ displays a lower overpotential of 0.64 V for the same rate-determining step. This suggests that Fe and Co sites in POM/$Co_{0.5}Fe_{0.5}OOH$ facilitate water oxidation at lower potentials, ensuring stable water oxidation operation. These theoretical findings support the durability of POM-stabilized $Co_{0.5}Fe_{0.5}OOH$ during long-term water oxidation operation.

Conclusions

In summary, we report a robust superstructure by constructing a POM-coordinated MOF through targeted grafting, aiming to solve the dissolution and corrosion issue of the crucial metal (oxy)hydroxide active sites responsible for alkaline water oxidation. We have shown the high stability and activity of this catalyst in the AEMWEs. Implementing it in industry that can contribute to a sustainable green hydrogen production will critically rely on the development of membrane fabrication, truly affordable electricity, and the maturity of the hydrogen energy industry chain.

REFERENCES AND NOTES

1. X. Wang *et al*., *Nature* **611**, 702–708 (2022).
2. L. Chong *et al*., *Science* **380**, 609–616 (2023).
3. W. Shi *et al*., *Science* **387**, 791–796 (2025).
4. C. Baeumer *et al*., *Nat. Mater.* **20**, 674–682 (2021).
5. X. Zheng *et al*., *Proc. Natl. Acad. Sci. U.S.A.* **118**, e2101817118 (2021).
6. K. Yue *et al*., *Energy Environ. Sci.* **14**, 6546–6553 (2021).
7. E. Fabbri *et al*., *Nat. Mater.* **16**, 925–931 (2017).
8. B. Zhang *et al*., *Science* **352**, 333–337 (2016).
9. L. Magnier *et al*., *Nat. Mater.* **23**, 252–261 (2024).
10. A. Bergmann *et al*., *Nat. Catal.* **1**, 711–719 (2018).
11. S. Zhao *et al*., *Nat. Energy* **1**, 16184 (2016).
12. S. Yuan *et al*., *Nat. Mater.* **21**, 673–680 (2022).
13. M. S. Burke *et al*., *J. Phys. Chem. Lett.* **6**, 3737–3742 (2015).
14. D. Y. Chung *et al*., *Nat. Energy* **5**, 222–230 (2020).
15. H. Liu *et al*., *Joule* **7**, 558–573 (2023).
16. F. M. Li *et al*., *Adv. Mater.* **34**, e2200840 (2022).
17. C. Kuai *et al*., *Nat. Catal.* **3**, 743–753 (2020).
18. Z. Li *et al*., *Joule* **8**, 2920–2937 (2024).
19. S. Z. Oener, A. Bergmann, B. R. Cuenya, *Nat. Synth.* **2**, 817–827 (2023).
20. F.-Y. Chen, Z.-Y. Wu, Z. Adler, H. Wang, *Joule* **5**, 1704–1731 (2021).
21. National Renewable Energy Laboratory (NREL), "U.S. Department of Energy Hydrogen Program: 2022 Annual Merit Review and Peer Evaluation Meeting; June 7-8 2022" (NREL, 2023); https://www.osti.gov/biblio/1990033
22. Q. Yin *et al*., *Science* **328**, 342–345 (2010).
23. I. A. Weinstock, R. E. Schreiber, R. Neumann, *Chem. Rev.* **118**, 2680–2717 (2018).
24. L. Vilà-Nadal, L. Cronin, *Nat. Rev. Mater.* **2**, 17054 (2017).
25. G. Paille *et al*., *J. Am. Chem. Soc.* **140**, 3613–3618 (2018).
26. Y. Shimoyama, N. Ogiwara, Z. Weng, S. Uchida, *J. Am. Chem. Soc.* **144**, 2980–2986 (2022).
27. D. Salionov *et al*., *Nat. Commun.* **13**, 3762 (2022).
28. M. B. Stevens, C. D. M. Trang, L. J. Enman, J. Deng, S. W. Boettcher, *J. Am. Chem. Soc.* **139**, 11361–11364 (2017).
29. L. Trotochaud, S. L. Young, J. K. Ranney, S. W. Boettcher, *J. Am. Chem. Soc.* **136**, 6744–6753 (2014).
30. Y. Ou *et al*., *Nat. Commun.* **14**, 7688 (2023).
31. M. E. G. Lyons, M. P. Brandon, *J. Electroanal. Chem.* **641**, 119–130 (2010).
32. F. Song, X. Hu, *Nat. Commun.* **5**, 4477 (2014).
33. D. Zhou *et al*., *Chem. Soc. Rev.* **50**, 8790–8817 (2021).
34. W. H. Lee *et al*., *Nat. Commun.* **13**, 605 (2022).
35. H. N. Nong *et al*., *Nature* **587**, 408–413 (2020).
36. M. B. Stevens *et al*., *Nano Res.* **12**, 2288–2295 (2019).
37. R. A. Krivina *et al*., *Adv. Mater.* **34**, e2203033 (2022).
38. S. Geiger *et al*., *Nat. Catal.* **1**, 508–515 (2018).
39. A. Li *et al*., *Nat. Catal.* **5**, 109–118 (2022).
40. S.-P. Zeng *et al*., *Nat. Commun.* **14**, 1811 (2023).
41. M. W. Louie, A. T. Bell, *J. Am. Chem. Soc.* **135**, 12329–12337 (2013).
42. S. Zhao *et al*., *Nat. Energy* **5**, 881–890 (2020).
43. P. Acharya *et al*., *J. Phys. Chem. C* **127**, 11891–11901 (2023).
44. D. Wang *et al*., *J. Phys. Chem. C* **119**, 19573–19583 (2015).
45. D. F. Abbott *et al*., *J. Mater. Chem. A* **6**, 24534–24549 (2018).
46. Y.-S. Xia *et al*., *Nat. Synth.* **3**, 406–418 (2024).
47. I. A. Weinstock, *Chem. Rev.* **98**, 113–170 (1998).
48. R. R. Rao *et al*., *Nat. Catal.* **3**, 516–525 (2020).
49. K. Yue *et al*., Polyoxometalated metal-organic framework superstructure for stable water oxidation, Dryad (2025); https://doi.org/2010.5061/dryad.hqbzkh2021t2029.

ACKNOWLEDGMENTS

We thank the staff of the BL20U1/BL17B/BL01B beamline of the Shanghai Synchrotron Radiation Facility (SSRF) and the staff of the 1W2B beamline of the Beijing Synchrotron Radiation Facility (BSRF) for assistance during data collection; the East China Normal University Multifunctional Platform for Innovation (004) for the TEM measurements; and Y. Chen for help with the XAFS measurements. All density functional theory calculations were performed at the New Zealand eScience Infrastructure (NeSI) high-performance computing facilities. **Funding:** This work was supported by the National Natural Science Foundation of China (grants 22325901 and 22279159), the National Key Research and Development Program of China (grants 2021YFA1600800 and 2021YFA1501000), the Natural Science Foundation of Shanghai (grant 22ZR1471900), the Research Plan of International Collaboration Fund for Creative Research Teams (ICFCRT) of NSFC (grant W2441008), and the Shanghai Rising-Star Program (grant 22QA1410300). The computational study was supported by the Marsden Fund Council from Government Funding (grant 21-UOA-237) and a Catalyst: Seeding General Grant (22-UOA-031-CGS) managed by Royal Society Te Apārangi. **Author contributions:** Y.Y. and B.Y.X. conceived and supervised the project. K.Y., Y.Y., and B.Y.X. synthesized and characterized the materials and analyzed the data. Z.W. and B.Y.X. supervised R.L. and M.G. during the theoretical calculations. J.Z. and K.Y. performed the PDF measurements. K.Y., Y.Y., B.Y.X., F.S., H.D., and B.M. performed the XAFS measurements. C.X., R.Q., and D.Z. performed the TEM measurements. Y.D. assisted K.Y. and Y.Y. with the AEMWE tests. F.H. suggested the catalytic mechanism. Y.Y., K.Y., R.L., and B.Y.X. wrote and revised the manuscript. All authors have read the manuscript and agree with its content. **Competing interests:** The authors declare no competing interests. **Data and materials availability:** Pair distribution function data and electrochemical data are available at Dryad (*49*).

SUPPLEMENTARY MATERIALS

science.org/doi/10.1126/science.ads1466
Materials and Methods
Supplementary Text
Figs. S1 to S66
Tables S1 to S21
References (*50*–*129*)

Submitted 31 July 2024; resubmitted 3 December 2024
Accepted 12 March 2025
10.1126/science.ads1466

THE DEPARTMENT OF PATHOLOGY
WAYNE STATE UNIVERSITY SCHOOL OF MEDICINE

The Department of Pathology in the Wayne State University School of Medicine (**https://pathology.med.wayne.edu/**) is expanding its high-impact research program and is seeking outstanding candidates who are addressing fundamental and/or translational scientific questions that complement the department's existing strengths. A current area of focus is the molecular pathogenesis of human diseases. Additional areas of interest include cancer biology, metabolism, and inflammation.

These tenure-track positions are expected to be filled at the **assistant professor level**. A competitive start-up package will be provided, commensurate with the candidate's experience and accomplishments. Successful candidates will be expected to establish an extramurally funded, internationally recognized research program and contribute to graduate and medical education as well as departmental and university service. Numerous opportunities for scientific collaboration are available within the department and across the institution.

Candidates holding a PhD and/or MD (or equivalent degrees) with a strong record of research productivity are encouraged to apply. For more information and to submit your application, please visit **https://hr.wayne.edu/jobs?utm_source=jobs.wayne.edu (Posting #req2618 and #req2619)**. Application materials should include a cover letter, a research statement (1–3 pages), a teaching philosophy, and a curriculum vitae.

Our department has a longstanding tradition of providing high-quality education and pioneering research training for medical and graduate students in our PhD and MD-PhD programs. A distinctive strength of our graduate programs is the integration of rigorous research training with a broad understanding of the clinical aspects of human disease pathogenesis.

Wayne State University is a premier public research university located in the heart of Detroit, offering students from all backgrounds a rich, high-quality education. Our strong commitment to excellence, collaboration, integrity, diversity, and inclusion creates exceptional opportunities for educational and professional success in today's global society. We strongly encourage applications from women, individuals from underrepresented groups in biomedicine, and others who share our commitment to diversity and inclusion. Wayne State University is an affirmative action/equal opportunity employer.

The metropolitan Detroit area, with a population of approximately four million, offers many outstanding residential communities, excellent public and private K–12 schools, a vibrant cultural and recreational scene, and proximity to other major institutions of higher education.

AFPI

These positions will serve as key members of AFPI's Office for Fiscal and Regulatory Analysis (OFRA) team, working directly with senior members of OFRA to help advance its quantitative portfolios in fiscal and regulatory fields. These positions will be good fits for those passionate about building tools and applying them to advance public policy.

RESEARCH SCIENTIST

What you would do: Develop quantitative analyses to support OFRA's scorekeeping operations and enhance the understanding of various policy issues. Use open source and other modeling resources to analyze policy proposals and apply policy and academic research relating to methods and key assumptions. Develop and maintain a variety of quantitative models encompassing econometric and statistical models, simulations, and machine learning and deep learning methods. Operate with discretion in an environment that requires information security.

Qualifications include:

- 8+ years of relevant, quantitative research experience after PhD degree or equivalent
- Strong experience with team-based software development and principles
- Strong programming ability in Python, R, or other common programming languages
- Deep expertise in econometrics, statistics, simulations, machine learning, or deep learning—preferably multiple from the list

QUANTITATIVE RESEARCH ASSOCIATE

What you would do: Develop quantitative analyses to support OFRA's scorekeeping operations and enhance the understanding of various policy issues. Use open source and other modeling resources to analyze policy proposals and apply academic research relating to methods and key assumptions. Develop and maintain a variety of quantitative models encompassing econometric and statistical models, simulations, and machine learning and deep learning methods. Support senior staff with cross-cutting research efforts. Operate with discretion in an environment that requires information security.

Qualifications include:

- A doctoral degree in a quantitative field
- Strong experience with team-based software development and principles
- Strong programming ability in Python, R, or other common programming languages
- Deep expertise in econometrics, statistics, simulations, machine learning, or deep learning—preferably multiple from the list
- Ability to maintain productive, collaborative, and collegial relationships with staff and external stakeholders and uphold the public reputation of the organization

PLATFORM ENGINEER

What you would do: Develop server applications, APIs, local tools, and libraries to support data scientists and economists in their analysis. Design, manage, and maintain cloud-based infrastructure and resources, particularly: compute, networking, storage, serverless functions, vector data storage and processing. Manage IAM and ensure security best practices. Design and maintain monitoring, logging, and CI/CD tools and pipelines.

Qualifications include:

- Strong experience and familiarity with team-based software development and principles
- Solid programming ability in Python and preferably several other languages
- Deep expertise in managing resources within at least one major cloud platform
- Machine learning or statistics experience is a plus
- A strong interest in pursuing interdisciplinary research
- Excellent attention to detail

SOFTWARE ENGINEER

What you would do: Develop applications and libraries to support data scientists and economists in modeling and policy forecasting. Build reactive frontends that meet modern performance and accessibility standards. Work with Python and JavaScript to provide backends that are well-tested and secure. Communicate with users to fix issues and develop new features. Operate with discretion in an environment that requires information security.

Qualifications include:

- Strong experience and familiarity with team-based software development and principles
- Solid programming ability in JavaScript, HTML, CSS, and Python
- A good eye for web design and interface usability
- Machine learning or statistics experience is a plus
- Excellent interpersonal skills and communication skills (both oral and written)

For additional information on these opportunities, please visit:
https://americafirstpolicy.com/careers

By **Jasmine Gabriel Hughes**

Healing waters

It's 5:25 a.m. on a Thursday and my alarm goes off. I sluggishly get up from bed, add several layers of clothing, and make my way toward the chilly River Cam for my first ever race. As I get closer to the boathouse, doubt and fear start to bubble up. Can I really do this? But when my paddle touches the water, a calmness washes over me. I take it one stroke at a time; if I mess up, I just breathe and keep going. The mindset I've developed as a rower keeps me focused and in control—and as we zip down the river, I realize it's helped me regain my confidence as a scientist, too.

As a child, I was convinced that a career in global health was for me. I dreamt of becoming a doctor and biomedical researcher, envisioning myself as a sort of Black Lara Croft, fearless and daring—except instead of searching for artifacts, I'd create groundbreaking cures and treat patients all around the world.

But as the years progressed, my dream seemed increasingly unattainable. During college, I was one of the only Black students in my STEM courses. It was hard to see myself in a field in which so few people from my background were represented.

As a first-generation student, I also struggled to find guidance on how to reach my career goal. Unlike many of my peers, I did not have family members or connections who were doctors or scientists. I was often told my dream was too ambitious: I wanted to become both a neuroimmunology researcher and a neurosurgeon, helping people in low- and middle-income countries. But my undergraduate advisers were skeptical and suggested I focus on just one field of study.

These experiences shook my confidence and left me questioning my plans. Even after I started my Ph.D., I often felt I didn't belong there. And I was plagued with doubts about the two massive projects I had taken on. I felt so overwhelmed by everything I would have to do over the next 3 years that I struggled to even get started.

But things changed after I started rowing.

I initially joined my college's boat club as a way to fully immerse myself in the student experience and develop a community away from home. It seemed like a fun and exciting new opportunity—and I soon found it to be an empowering one, too.

Rowing suffers from the same lack of diversity as biomedical research, with very few Black women rowers at my university. When I joined the boat club, I was nervous I would stand out or the rowing community wouldn't accept me—the same feeling I experienced in science. But despite my initial fears, I was embraced by my fellow rowers, who not only gave me support and guidance to improve my technique, but also made me feel appreciated and valued. As a result, when I'm having my doubts about belonging in science, I now reflect on the fact I'm already doing something I once thought would be impossible for me.

"Within a couple months of starting to row, I'd found a new level of confidence."

Rowing also helped me develop discipline and a new approach for tackling difficult tasks. At first, I felt overwhelmed by what seemed like unattainable goals, such as rowing nonstop for 2 kilometers in less than 8 minutes. But I realized that by breaking these goals down into smaller steps, I was able to set mini-milestones that were much less intimidating and more feasible.

I began to use a similar strategy in my Ph.D.: By viewing my projects as a series of small goals, they became much more manageable. During the process of designing my first lab experiment, for instance, I started to stress over the complexity of all the procedures involved. But instead of giving in to the fear of being inadequate, I began to focus on how I could make sure each step was successful. Within a couple months of starting to row, I'd found a new level of confidence—both on the water and in the lab.

On that early Thursday morning on the river, I'm so focused on my strokes that I'm surprised when a loud blowhorn goes off. As I catch my breath, it starts to dawn on me that I've completed my first race. And suddenly, my future career as physician-scientist finally begins to seem attainable, too. ■

Jasmine Gabriel Hughes is a Ph.D. student at the University of Cambridge.

ILLUSTRATION: ROBERT NEUBECKER

myIDP ScienceCareers
INDIVIDUAL DEVELOPMENT PLAN

Features in myIDP include:

- Exercises to help you examine your skills, interests, and values.
- 20 career paths with a prediction of which ones best fit your skills and interests.
- A tool for setting strategic goals with optional reminders to keep you on track.
- Articles and resources to guide you through the process.
- Options to save materials online and print them for further review and discussion.
- A certificate of completion for users that finish myIDP.

Start planning your future today!
myIDP.sciencecareers.org

In partnership with:

FASEB
Federation of American Societies for Experimental Biology

UMASS University of Massachusetts Medical School

UCSF University of California San Francisco

UIC

BURROUGHS WELLCOME FUND